



TECHNISCHE
UNIVERSITÄT
WIEN
Vienna University of Technology

Unterschrift BetreuerIn

DIPLOMARBEIT

Commissioning and Evaluation of a Fallback Planning Module for Proton and Photon Radiotherapy

ausgeführt am Atominstitut
der Technischen Universität Wien

unter der Anleitung von
Univ.Prof. Dipl.-Ing. Dr.techn. Dietmar Georg
und
Mag. Barbara Knäusl, PhD,
Dipl.-Ing. Wolfgang Lechner, PhD

durch
Gloria Mirescu
0827464

Dezember 2016

Unterschrift StudentIn

Statutory Declaration

I hereby declare on my honor to have written the present thesis independently, solely with the support of the listed literature references and to have submitted its content to no other examination authority.

(place, date)

(signature)

Contents

Acknowledgements	iv
List of Figures	v
List of Tables	vi
Glossary	vii
Abstract	ix
1 Introduction	1
1.1 Purpose and Aim	1
1.2 Radiation Therapy	2
1.2.1 Definition and Purpose	2
1.2.2 Historical Background	2
1.3 Physics of Radiation Therapy	6
1.3.1 Basics	6
1.3.2 Interaction of Ionizing Radiation with Matter	9
1.4 External Beam Photon Therapy	17
1.4.1 Linear Accelerators	17
1.4.2 Photon Beam Formation and Shaping	19
1.4.3 Physical Characteristics of Megavoltage Photon Beams	21
1.4.4 Photon Beam Dose Calculation Algorithms	25
1.4.5 Planning and Treatment Techniques	27
1.4.6 Gamma-Index Analysis	31
1.5 Literature on Beam Commissioning	32
2 Materials and Methods	34
2.1 Beam Model Creation	34
2.1.1 Methods	34
2.1.2 Materials	36
2.2 Independent Verification of the Beam Model	36
2.2.1 Materials	36
2.2.2 Methods	37
2.3 Treatment-Delivery Verification	39
2.3.1 Materials	39
2.3.2 Methods	40
2.4 FB vs. mVMAT Plan Comparison	42
2.5 Beam Model Comparison	42
2.5.1 Materials	42
2.5.2 Methods	43
2.6 Statistical Analysis	43
3 Results	45
3.1 Emergent Beam Models	45
3.2 Independent Verification	46
3.3 Treatment-Delivery Verification	55
3.4 Beam Model Comparison	57
3.5 FB vs. mVMAT Plan Comparison	61

4 Discussion	66
4.1 Beam Modeling	66
4.2 Beam Model Verification	67
4.3 FB vs. mVMAT Plan Comparison	69
4.4 Beam Model Comparison	70
5 Conclusions and Outlook	71
References	73
A Machine Reports	76
A.1 FF Machine	76
A.2 FFF Machine	97
B Complete Results of Independent Verification	117
B.1 MATLAB Verification	117
B.2 Point Dose Verification	137
B.3 Output Factor Verification	149
C Complete Results of Treatment-Delivery Verification	152
D Complete Results of Beam Model Comparison	155

Acknowledgements

“Gratitude is not only the greatest of virtues, but the parent to all others.”

(Marcus Tullius Cicero, 3 January 106 BC – 7 December 43 BC)

On that note, let me begin by first thanking my official supervisor, Prof. Dietmar Georg and my co-supervisors, Barbara Knäusl, PhD and Wolfgang Lechner, PhD for their guidance and, above all, their patience. In addition, I would like to thank Dr. Thomas Schreiner, Rolf Seemann, PhD and Prof. Markus Stock for making it possible for me to perform the work related to this thesis at MedAustron. Special thanks are extended to Gabriele Kragl, PhD for her cheerful readiness to help and share her expertise and also to Florine Enengl, for her assistance in the creation of Fallback plans and her pleasant company while working late.

On a personal level, I am immensely grateful to my family for supporting me throughout the time it took me to get to the finish line. Special thanks go out to my sister who has been a constant source of inspiration and strength and has been with me through both good and bad times.

“I am thankful to all those who said NO to me. It’s because of them that I did it myself.”

(Albert Einstein, 14 March 1879 – 18 April 1955)

Having finally grasped Einstein’s meaning, I also wish to thank those who have not exactly made it easy for me throughout the course of my studies. Ironically, it is because of those people that I now am a better physicist than I originally thought I could be.

List of Figures

1.1	Timeline of clinical, technological and biological advances in radiotherapy [1]	5
1.2	Basic schematical setup of X-ray tube [2].	8
1.3	The two mechanisms of X-ray production [2].	8
1.4	Filtered and unfiltered bremsstrahlung spectra [3].	9
1.5	Energy deposition of 6 MV photons, protons and carbon ions.	10
1.6	Example of non-constant HVLs for a photon beam exhibiting a photon spectrum [4].	11
1.7	Photon attenuation [5].	12
1.8	Sketch of a scattering process to demonstrate the solid angle and scattering angle [3].	13
1.9	Photoelectric effect [3].	14
1.10	Kinematics of Compton scattering [3].	15
1.11	Schematics of a modern-day linear accelerator [5].	18
1.12	Beam as produced with (red) and without flattening filter (blue) [6].	20
1.13	PDD curves in water for several megavoltage photon beams: from ^{60}Co γ -rays to 25 MV X-rays [7].	22
1.14	Build-up effect [3].	23
1.15	Beam profiles.	24
1.16	Flowchart of the two planning methods.	27
1.17	Example of DVHs [4].	28
2.1	Final dose computation in RayPhysics on a 30 cm \times 30 cm \times 30 cm water phantom with a beam of field size 15 cm \times 15 cm using the 10 MV FFF beam model.	37
2.2	Computed and measured PDD curve for a 10 MV FF beam of field size 15 cm \times 15 cm and spatial distribution of γ -values as provided by the MATLAB code.	38
2.3	Setup for QA plan irradiation at the AKH Vienna: the Versa HD linac and the Delta ⁴ phantom.	39
2.4	Example of isodose distribution of a 10 MV FF QA plan, calculated for a patient from the LR contingent.	41
2.5	Setup for QA plan irradiation at the LKH Wiener Neustadt: the Clinac120 and the Delta ⁴ phantom.	43
3.1	CR profile for a 40 cm \times 40 cm field size of the 6 MV FF beam model, where the “steps” in the out-of-field region can be observed.	45
3.2	CR profile for a 40 cm \times 40 cm field size of the 6 MV FFF beam model, demonstrating the “steps” in the out-of-field region.	46
3.3	Examples of good (a) and bad (b) agreement between measured and computed PDDs.	49
3.4	Examples of good (a) and bad (b) agreement between measured and computed cross-plane (CR) profiles.	50
3.5	Examples of good (a) and bad (b) agreement between measured and computed in-plane (IN) profiles.	51
3.6	Differences between measured and calculated output factors for the FF linac models.	53
3.7	Differences between measured and calculated output factors for the FFF linac models.	54
3.8	Example of isodose distributions of plans used in the treatment-delivery verification.	56
3.9	Transversal view of dose distributions of LR plans created with the Versa HD beam model (a and c) and the Clinac120 generic beam model (b and d).	59
3.10	DVH of Versa HD (VHD) plan vs. Clinac120 (C120) plan for an HR patient (HR12). Continuous lines represent the plan created with the Versa HD beam model and dashed lines represent the plan created with the Clinac120 beam model.	60
3.11	Transversal view of dose distributions of LR FB and mVMAT plans.	62
3.12	DVH of FB plan vs. mVMAT plan for a LR patient (LR01). Continuous lines represent the mVMAT plan and dashed lines represent the FB plan.	63

List of Tables

2.1	Null and alternative hypotheses of the statistical tests performed throughout this thesis.	44
3.1	Average γ_{mean} and $\gamma_{<1}$ for PDD curves.	47
3.2	Average γ_{mean} and $\gamma_{<1}$ for lateral profiles.	47
3.3	Average point dose and percental difference relative to measurement for various SSDs.	48
3.4	Average difference (in %) between measured and computed output factors.	52
3.5	Average median dose deviation and local GPR for LR patients.	55
3.6	Statistical analysis of LR results.	57
3.7	Median dose deviations and local GPRs for plans calculated on the Delta ⁴ of a mass density of 1.19 g/cm ³	57
3.8	Average median dose deviation and local GPR for Elekta's Versa HD and Varian's Clinac120	58
3.9	Statistical analysis of beam model comparison results.	60
3.10	Average median dose deviation and local GPR for LR FB and LR mVMAT plans.	61
3.11	Average median dose deviation and local GPR for HR patients, 6 MV FF	61
3.12	Delivery time/segment [s] and gantry speed/segment [deg/s] for LR plans.	63
3.13	Delivery time/segment [s] and gantry speed/segment [deg/s] for HR plans.	64
3.14	Segmentation differences with maximum delivery time (MDT) set at 180 s on the Versa HD for a selected patient from each indication.	65
3.15	Estimated delivery time [s] for plans created with the Versa HD (VHD) and the Clinac120 (C120).	65
B.1	Results of MATLAB verification for 6 MV FF.	117
B.2	Results of MATLAB verification for 10 MV FF.	122
B.3	Results of MATLAB verification for 6 MV FFF.	128
B.4	Results of MATLAB verification for 10 MV FFF.	133
B.5	Results of point dose verification for 6 MV FF.	138
B.6	Results of point dose verification for 10 MV FF.	141
B.7	Results of point dose verification for 6 MV FFF.	144
B.8	Results of point dose verification for 10 MV FFF.	147
B.9	Results of output factor verification for 6 MV FF.	150
B.10	Results of output factor verification for 10 MV FF.	150
B.11	Results of output factor verification for 6 MV FFF.	151
B.12	Results of output factor verification for 10 MV FFF.	151
C.1	Results of treatment-delivery verification for LR 10 MV FF.	152
C.2	Results of treatment-delivery verification for LR 6 MV FF.	153
C.3	Results of treatment-delivery verification for LR 6 MV FFF.	153
C.4	Results of treatment-delivery verification for LR 10 MV FFF.	154
C.5	Results of treatment-delivery verification for HR 6 MV FF.	154
D.1	Results of beam model comparison for HR 6 MV FF.	155
D.2	Results of beam model comparison for LR 6 MV FF.	155

Glossary

3D-CRT	three-dimensional conformal radiotherapy
AKH Wien	Allgemeines Krankenhaus der Stadt Wien
CAX	central axis
DD	dose deviation
DICOM	Digital Imaging and Communications in Medicine
DMLC	dynamic MLC
DTA	distance-to-agreement
DVH	dose volume histogram
EBRT	external beam radiotherapy
FB	Fallback plan
GPR	gamma(-index) passing rate
HDR	high dose rate
HVL	half value layer
IMAT	intensity-modulated arc therapy
IMRT	intensity-modulated radiotherapy
LDR	low dose rate
LET	linear energy transfer
linac	linear accelerator
LKH Wr. Neustadt	Landeskrankenhaus Wiener Neustadt
MLC	multileaf collimator
MRI	magnetic resonance imaging
MU	monitor unit
mVMAT	manually created VMAT plan
NTCP	normal tissue complication probability
OAR	organ-at-risk
PDD	percentage depth dose
PET	positron emission tomography
PTV	Planning Target Volume
QA	quality assurance
RBE	relative biological effectiveness
RF	radiofrequency
SAD	source to axis distance

SBRT	stereotactic body radiotherapy
SMLC	segmental MLC
SSD	source to surface distance
TCP	tumor control probability
TPS	treatment planning system
VMAT	volumetric modulated arc therapy

Abstract

In the last few decades, technological advancements in the field of radiation therapy have made it possible to exploit the higher precision of charged particles (ions) owed to their distinctive Bragg peak.

A new facility making use of particle beams, MedAustron, the first of its kind in Austria will soon become operational in Wiener Neustadt, Lower Austria. It will rely on a synchrotron to accelerate protons and carbon ions and the particles will be subsequently extracted and directed towards the treatment rooms. However, in case of a synchrotron breakdown it is crucial for patients with fast-growing tumors to be able to receive their usual fraction dose without delay, which is why a few fractions of photon beam treatment are preferable to no treatment whatsoever. The treatment planning system at MedAustron, RayStation (RaySearch Laboratories AB, Stockholm, Sweden), incorporates a so-called Fallback Planning module enabling the creation of “fallback” (FB) plans which mimic the dose distribution of a given plan with a different modality and/or treatment technique. In order to be able to create and deliver photon fallback plans with the linear accelerator (linac) at the General Hospital in Vienna (AKH Wien), the Versa HD (Elekta AB, Stockholm, Sweden), the TPS must include the beam model(s) of the respective machine.

This thesis was aimed at using MedAustron’s TPS, RayStation, to create the beam models of the Versa HD linac for 6 MV and 10 MV flattened (FF) and unflattened (FFF) beams for all clinically relevant field sizes, adding up to 16 field sizes per beam model. Furthermore, once created, the beam models were independently verified using a MATLAB code and by digitally recreating the experimental setup for the measurement of basic beam data and comparing the computed and the measured doses. A treatment-delivery verification was also performed by using the finished models to create clinically acceptable plans which were then converted to quality assurance (QA) plans that were subsequently delivered to a Delta⁴-phantom, whose software performed a local γ -index analysis with 3 mm distance-to-agreement (DTA) and 3% local dose difference (DD) pass/fail criteria.

In a final verification step, the 6 MV FF beam model was compared to the generic model of Varian’s Clinac120 linac (Varian Medical Systems, Palo Alto, California, USA) using the same method employed in the treatment-delivery verification.

The four beam models created over the course of this master’s thesis have generally passed the independent γ -index analysis, showing mean $\gamma_{<1}$ -values greater than 90% for all beam models and curve types except for the inplane (IN) profiles of the 6 MV FF beam model. Average differences between computed and measured central axis point doses were found to be under 1% for all beam models. Average differences between measured and computed output factors of less than 0.35% were observed for all beam models as were individual local GPR values higher than the 90% threshold, in general, during the treatment-delivery verification. The average GPR obtained with 3% local DD and 3 mm DTA criteria were above 90% for all models and even above 95% for both FFF beam models.

All FB plans showed higher local GPRs and were therefore more accurate when delivering the planned dose, however, at the expense of the modulation and therefore the quality of the treatment plan itself.

The 6 MV FF beam model of both the Versa HD and the Clinac120 performed well for a low complexity indication such as low risk prostate carcinoma. For an indication of higher complexity (high risk prostate carcinoma), however, the generic model of the Clinac120 exhibited a low mean GPR and a high variation among the results.

To conclude, all four Versa HD beam models have thus been proven to be fit for clinical practice, the Fallback Planning Module should be further optimized before being implemented in clinical practice in contingency situations at MedAustron and the same is recommended for the generic model of Varian’s Clinac120.

1 Introduction

1.1 Purpose and Aim

The main objective of this master's thesis has been the generation of beam models using RayStation for the 6 MV and 10 MV flattened and unflattened beams produced by a Versa HD linear accelerator (Elekta AB, Stockholm, Sweden). A secondary objective has been the comparison of one of those models (6 MV FF) with the generic model of the Clinac120 (Varian Medical Systems, Palo Alto, California, USA), available in RayStation.

The realization of the main objective was achieved through several steps: the proper machine properties along with important beam parameters were entered for the Versa HD treatment machine and its measured beam characteristics were imported into the beam modeling application of RayStation, RayPhysics. The models were then obtained by performing auto-modeling steps and/or manual fine tuning for the remainder of the beam parameters, such that in the end a predominant agreement between measured and calculated curves was attained. Once the models were finished, they were verified by inputting measured and calculated curves into an in-house created MATLAB code meant to perform a γ -index analysis with 2%/2 mm acceptance criteria. A point dose verification and an output factor verification were also performed by comparing measured point doses and output factors resulting from measurements with calculated doses and the output factors resulting thereof. In a next verification step the performance of the models with VMAT planning was tested, by creating both manual and proton plans-based automatically generated Fallback VMAT plans with the new models, transforming them to QA plans and delivering them to a Delta⁴-phantom, thus enabling a GPR-analysis of the plans (3%/3 mm DD/DTA). This also enabled a direct comparison of the manually created VMAT plans (henceforth denoted by "mVMAT" plans) with the Fallback plans. Finally, the same procedure was applied with the 6 MV FF beam model of the Clinac120, making it possible to compare GPRs resulting from delivery with the Versa HD linac with those arising from delivery with the Clinac120.

The thesis starts with an ample introductory section 1, beginning with the relatively short historical background of radiation therapy, then going over the basic physics relevant for the topic at hand and slightly elaborating on the subject of external beam photon therapy and finally closing with information on the herein widely used γ -index analysis and previously published relevant literature.

The second section (2) details all the beam commissioning, verification and comparison steps and the equipment used in every stage while the next, third section (3) sums up the results for each of the stages mentioned in the previous section.

The fourth section (4) discusses the results and any questions raised by them or discoveries made in the process and the fifth and final section (5) provides a conclusion and reflection/outlook on possible ways of expansion or improvements of the work done for this thesis.

1.2 Radiation Therapy

1.2.1 Definition and Purpose

The specific branch of medicine dealing with the use of ionizing radiation in the treatment of disease is called radiation therapy (or short: radiotherapy), therapeutic radiology and, when dealing exclusively with malignant diseases, radiation oncology [7].

There are two main forms of radiotherapy: external beam radiotherapy (or teletherapy) which requires the patient to lie on the treatment couch and receive radiation from a remote source, and brachytherapy, wherein sealed radioactive sources are implanted interstitially or intracavitarily [5, 3].

The thesis at hand will only deal with the former, while the latter shall only be mentioned in the next section for the sake of completeness.

1.2.2 Historical Background

This section is mainly based on [1] for the first part and [8] for the second part, concerning radiation therapy in Austria.

Since the discovery of X-rays by Wilhelm Conrad Röntgen in 1895, natural radioactivity by Henri Becquerel in 1896 and the new radioactive element radium (Ra) by Pierre and Marie Curie in 1898, ionizing radiation has become of everincreasing importance in medicine. Soon after the discovery of their evident usability in diagnostics, the application of X-rays also for therapeutic purposes became apparent.

While the first ailments to be treated with X-rays were benign (eczema and lupus), within the next year after Röntgen's discovery malignant neoplasia were also successfully treated. In most cases, only superficial and shallow-seated tumors were irradiated, given the low energies and hence low penetration depths which could be attained at the time. However, the field rapidly evolved over the course of the following century.

The enthusiasm over the success with treating malignancies completely overshadowed the potential risks which were unknown at the time, yet the visible side effects and occasional famous cases of radiation poisoning (such as Marie Curie's) were sufficient to raise awareness on the subjects of radiation protection and dosimetry.

In the early days of radiation therapy, cancers were treated either by placing radium sources in or onto the tumor (an ancestor method of today's brachytherapy) or by single exposures to large doses provided by cathode ray tubes, making it nearly impossible to obtain satisfactory curative results without severely damaging normal tissue as well. It was soon discovered that fractionation could solve this problem, by delivering the same cumulative dose to the tumors and yet allowing enough time in between the individual fractions so as to enable the repair process in the normal tissue.

Henri Coutard introduced the concept of customized treatment intensities assigned according to the different degrees of radiation-induced skin desquamation and oral mucositis observed in individual patients. Coutard was also among the first to suspect a connection between the histologies and locations of different cancer types and their probability of being cured by means of radiotherapy. Some of Coutard's ideas are the basis for today's everyday standard practice in radiotherapy, such as beam hardening, custom immobilization and beam collimation and shaping.

With fractionation garnering increased popularity, many scientists attempted to find a time-dose relationship which would accurately model the effects of external beam radiotherapy (EBRT) on both cancerous (of different types) and normal tissue.

Much effort was also put into investigating the potential damages for normal tissue in the case of fractionation. As a consequence, several factors were found to play a role in complications incidence: fraction size, total radiation dose, tissue type as well as portion of irradiated organ(s).

In an attempt to overcome the challenges posed by sparing enough normal tissue whilst making sure the tumor receives sufficient dose, the medical and scientific community turned to new approaches to fractionation. These new approaches were hyperfractionation, accelerated fractionation and a more recent development, stereotactic radiosurgery, which was originally intended for brain tumors but was later extended to extracranial locations and called stereotactic body radiotherapy (SBRT). The idea behind hyperfractionation was delivering an increased number of fractions of small doses at smaller time intervals with the objective of achieving an increased total dose and less normal tissue complications. Accelerated fractionation, on the other hand, merely relied on reducing the overall treatment time, giving tumor cells a diminished chance of proliferating.

In stereotactic radiosurgery, a single large fraction of $\sim 15 - 20$ Gy is delivered by a few small fields to an intracranial location with millimeter accuracy. Stereotactic body radiotherapy was later performed on other body sites, where 3 fractions of 20 Gy each were found to have satisfactory results [1, 9, 3].

This re-evaluation of time-dose principles was also applied to brachytherapy (= “radiation treatment by using implanted radioactive sources”) [3]. The long-standing method of interstitial or intracavitary therapy using low dose rate (LDR) sources was to be revised in part due to technological advancements, making robotical afterloading of high dose rate (HDR) radioactive sources possible and thus shortening or completely eliminating the need for patient hospitalization. Studies have shown the LDR and HDR approaches to have similar results.

As far as X-ray production is concerned, there has also been technological progress in that field as well. The shallow penetration depths and high incurred doses by the skin have been a problem from the beginning of radiotherapy, which is why efforts have been made to increase the X-ray energies and thus their penetration depths. Low energy radiotherapy started with about 100 keV, which was doubled by 1913 thanks to the collaboration between William Coolidge and General Electric, whose method of treatment was later termed orthovoltage EBRT. Other methods of decreasing the skin dose of X-ray beams involved the usage of thin metallic sheets to filter out lower energies or firing multiple beams at different entry points, but adding up at the right depth and location. The concept of rotating beams around the tumor emerged as early as the 1920s, yet the problem of low penetration still persisted even with orthovoltage X-rays.

Supervoltage X-rays were the new goal several scientific groups were attempting to achieve. It was the same Coolidge who developed a cascade tube in 1926. Its series configuration was designed to boost electron acceleration. A 700 keV version of this invention was installed by General Electric at Memorial Hospital in New York.

An entirely different approach was being tested in 1929 by Ernest Lawrence at the University of California at Berkeley. His method involved accelerating particles with high-frequency alternating potentials. Together with his graduate student, David Sloan, Lawrence developed such a linear accelerator using 30 electrodes and Sloan continued improving this model. Other groundbreaking inventions soon followed such as Donald Kerst’s electron accelerator (called betatron) and the synchrotron, developed both in the Soviet Union by Veksler and in the Los Alamos Laboratory in the US by McMillan.

The period after World War II proved very fruitful for the field of radiation therapy. At Stanford University, Henry Kaplan managed to obtain 6 MV X-rays for the treatment of patients starting in 1956 and the 1960s saw the beginning of the installation of linear accelerators with gantries capable of 360°-rotation.

Around the same time, a new ^{60}Co teletherapy unit was rapidly gaining popularity. As its name suggested, it contained a ^{60}Co radioactive source, which produces γ -rays in the low MV range.

More recent improvements in radiotherapy have been in part due to the technological progress achieved in other (adjacent) fields: computer science and imaging. A better knowledge of tumor and neighboring organs at risk (OARs) location as well as sufficient computer resources that allow three-dimensional treatment planning have revolutionized the industry. Today’s treatment planning is performed mostly on computed-tomographical images, however, other imaging modalities such as

magnetic resonance imaging (MRI) or positron emission tomography (PET) may prove even more advantageous for some particular cases.

Beam shaping has also evolved from the previously used blocks, which were custom-shaped to fit each individual tumor, to the recently introduced multileaf collimators (MLCs). These are made up of several small metallic leaves, which are each connected to a computer-controlled motor. This new equipment combined with advanced computer algorithms and software optimizing the number, intensity and shape of each individual beam have lead to a new treatment technique called three-dimensional conformal radiotherapy (3D-CRT).

An even newer idea involved splitting the beam into smaller beamlets with different intensities or creating a checkerboard-pattern across each beam's length and width using intensity modulation. This technique called intensity-modulated radiotherapy (IMRT) made use of the aforementioned MLC and worked under the premise that the leaves could move while the beam was on.

Although the theoretical basis for IMRT was laid in the late 1970s, its physical realisation was only made possible 20 years later and also lead to a new treatment planning algorithm: inverse planning. This new algorithm starts with the dose prescribed by a radiation oncologist for the target volume and the allowed maximally tolerable doses for the surrounding OARs and then optimizes the different beam intensities and dose distributions during several iterations.

One of the latest advances in radiation therapy has been its expansion from the already well-established photon and electron therapy to particle beam therapy, especially proton beam therapy. The distinctive energy absorption profile of the proton in tissue has made proton beam therapy one of the most conformal modalities of radiotherapy. A 40-year long close collaboration between the Harvard Cyclotron Laboratory and the Massachusetts General Hospital has had a huge contribution to the existing knowledge on proton therapy.

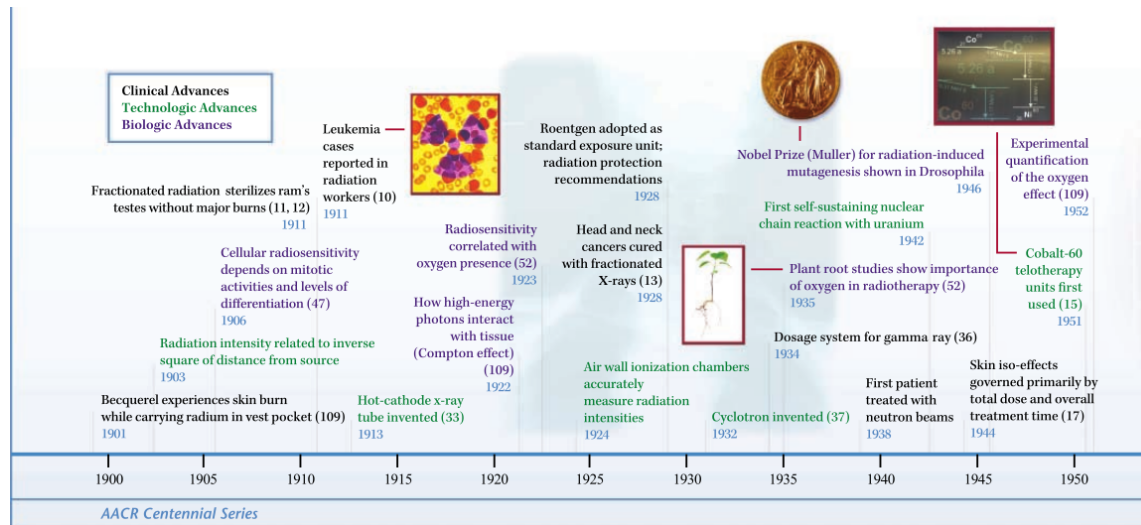
The end of the 20th century and the beginning of the 21st brought forth the novelty of ion beam therapy. The first patients were treated with ion beams as early as 1977 at the Lawrence Berkeley Laboratory. Mostly helium ions were used, yet a small minority of patients were treated with ions heavier than helium such as neon, carbon, argon and even silicon. Carbon ions have since become the most widely used ion type in ion beam therapy, having been delivered regularly to patients since 1994 in Chiba, Japan. Other facilities capable of delivering carbon ion beams have since been opening around the world and are still in planning [3].

The growing success of radiation therapy was, however, not solely owed to advances in computer science and technology. Treating a growing number of different cancer types has been increasingly effective also due to discoveries in the field of biology and the newly formed subfield of radiation biology. Perhaps the most relevant of said discoveries were the stages of cell development and the fact that radiosensitivity seemed higher in cells showing increased mitotic activity and diminished differentiation, the effect of oxygen on radiotherapy effectiveness, pinpointing the tumoricidal effects of radiation to the DNA damage and different effects of different types of ionizing radiation on tissue, which ultimately lead to the definition of the relative biological effectiveness (RBE) [1, 5].

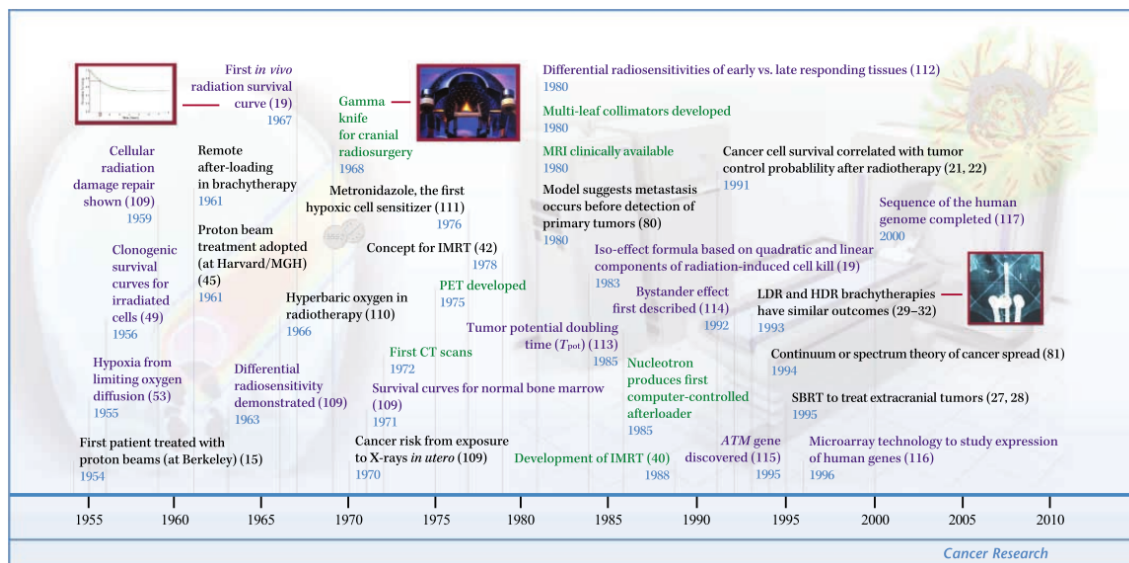
Figure 1.1 shows a timeline of all the discoveries which contributed to the evolution of radiotherapy.

The evolution of radiation therapy in Austria also started soon after the discovery of X-rays, in November 1896, when Leopold Freund, who is considered the founder of radiotherapy, conducted the first thoroughly documented therapeutic irradiation on a young girl with a hairy naevus.

Freund went on to perfect his method of fractionated radiotherapy and had other substantial contributions to the field, through his pertinent observations throughout his experiments. Among other things, he concluded that the biological effects caused by X-rays vary with the tissue type exposed to them, that there is a change in the pigmentstatus of irradiated skin and that treatments with X-rays have a cumulative effect, which manifested after $\sim 16 - 22$ h of treatment. Furthermore, Freund identified the importance of treatment session durations and that of the treatment as a whole for the avoidance of negative side effects and inferred the potential for the application of X-rays to treat diseases of internal organs.



(a) From 1900 to 1950



(b) From 1950 to the present day

Figure 1.1: Timeline of clinical, technological and biological advances in radiotherapy [1]

Though Leopold Freund wrote the first extensive textbook on radiation therapy in 1903, his was not the first book on radiotherapy ever written, since his compatriot Eduard Schiff wrote a shorter book on the therapeutic uses of X-rays as early as 1901.

Other notable contributors to the rise of radiation therapy in Austria were Robert Kienböck, Guido Holzkecht and Gottwald Schwarz.

Kienböck was the first to observe an increased radiosensitivity in cells frequently containing mitotic figures, as well as in organs with higher metabolic activity. He also published a textbook on radiotherapy which contained concepts that strongly impacted the treatment of deeply seated tumors in particular.

Holzkecht, a diagnostic radiologist at first, was motivated by Kienböck to cross over to therapeutic radiology as well and in 1902 developed the first device capable of measuring X-rays - the chromoradiometer - paving the way for exact dosimetry.

Schwarz developed the calomel-radiometer, a new device for measuring X-rays based on a chemical reaction, discovered the oxygen effect by treating with radiation therapy and using compression anemia simultaneously, combined radiotherapy with hyperthermia, observed that within a tumor some cells are more radiosensitive than others, depending on its stage in the cell cycle and proposed that a new factor called “dosage rate” be added to each dose definition.

From the inauguration of the first Austrian independent radiotherapy center in 1931 and the first university clinic for radiotherapy in 1969, new centers and facilities quickly followed and in March 1994, radiotherapy-radiooncology finally became a clinical specialization of its own.

1.3 Physics of Radiation Therapy

1.3.1 Basics

Classification

Radiation is usually classified into two categories: non-ionizing and ionizing.

Non-ionizing radiation comprises all types of electromagnetic radiation with insufficient energy per quantum as would be required to knock an electron from an atom or molecule of the target (ionization). Examples of such non-ionizing radiation are radio waves, visible light, near ultraviolet radiation, infrared photons and microwaves.

Ionizing radiation, on the other hand, does possess a quantum energy greater than the ionization potential of atoms and molecules and can therefore ionize matter [5].

This thesis deals with the use of ionizing radiation in medicine and shall therefore only focus on ionizing radiation.

Ionizing radiation can be further classified with respect to either their mode of ionization or to the density of ionization produced in the absorber [5].

Classification by mode of ionization

This criterion yields two categories of ionizing radiation: directly and indirectly ionizing.

- directly ionizing radiation: refers to charged particles such as protons, α -particles, heavy ions but also electrons, which require a one-step process to deposit their energy in the absorber via Coulomb interactions with the orbital electrons of the individual atoms in the absorber material.
- indirectly ionizing radiation: refers to neutral particles such as photons (either X-rays or γ -rays) and neutrons, which require an additional intermediate step to ionize the absorber. In a first step the neutral particle causes a charged particle to be released - an electron or electron/positron-pair for photons and a proton or heavier ion for neutrons - and the charged particle then ionizes via Coulomb interactions with the orbital electrons, as previously described [5].

Classification by density of ionization

The concept of linear energy transfer (LET) was introduced to establish the quality of a beam of ionizing radiation. It quantifies the linear rate at which the absorber medium takes in the energy of the charged particle traversing it. The ionization density is correlated with the linear energy transfer, which also leads to two categories of ionizing radiation:

- low LET (or sparsely ionizing) radiation,
- high LET (or densely ionizing) radiation.

A value of 10 keV/ μ m is the limit between the two categories. An example of low LET radiation would be photon radiation while α -particles would typically exemplify high LET radiation. For other particles (such as e.g. electrons) their energy decides whether they have sparsely or densely ionizing potential [5].

Radiation-Related Physical Quantities and Units

Regardless of its application for diagnostic or therapeutic purposes, it is universally agreed upon the fact that the radiation used in medicine needs to be accurately measured. The goal in radiotherapy is to maximize the tumor control probability (TCP) while keeping the normal tissue complication probability (NTCP) at a minimal value, which can only be achieved if the delivery of the prescribed dose is of both high accuracy and precision. For the purpose of quantifying radiation, the following physical quantities were defined [5]:

Exposure X: refers to the ability of photons to ionize air. The unit for exposure is Roentgen (R) and is defined as a charge of $2.58 \cdot 10^{-4}$ C produced per kg of air.

$$X = \frac{\Delta Q}{\Delta m_{\text{air}}} \quad (1.1)$$

Kerma K (stands for kinetic energy relaxed in matter): defined as the energy transferred from indirectly ionizing particles to charged particles per unit mass of the absorber.

$$K = \frac{\Delta E_{\text{tr}}}{\Delta m} \quad (1.2)$$

Dose D: specifies the energy absorbed per unit mass of medium. Its unit - Gray (Gy) - is defined as 1 J of energy absorbed per kg of medium.

$$D = \frac{\Delta E_{\text{abs}}}{\Delta m} \quad (1.3)$$

Equivalent dose H: a physical quantity meant to account for the different biological effects of different types of radiation [3]. It is defined as the previously introduced dose D multiplied by a radiation weighting factor w_R and has the SI unit Sievert (Sv).

$$H = D \cdot w_R \quad (1.4)$$

Activity A: used for radioactive elements to quantify their number of nuclear decay per unit of time. Its respective unit - Becquerel (Bq), amounting to 1 decay per second - was named after the discoverer of radioactivity Henri Becquerel [5, 3].

$$\mathcal{A} = \frac{dN}{dt} = -\lambda \cdot N \quad (1.5)$$

Basic Principle of X-Ray Production

Though nowadays more sophisticated equipment is used to produce X-rays for photon therapy (which will be dealt with in section 1.4.1), the principle of X-ray production remains the same and shall be covered here briefly.

Figure 1.2 shows the schematics of a simple X-ray tube.

Electrons emerge from the tungsten cathode (the negative electrode) through thermionic emission and, because of the high voltage between the cathode and the anode (the positive electrode), are accelerated towards the latter. To avoid undesired interactions inbetween, the entire setup is encapsulated by a glass envelope and under high vacuum. When the electrons reach the anode - which is essentially a copper rod with a small layer of tungsten at its end, serving as the target - they trigger the production of X-rays in their two possible forms [5, 2, 3]:

- characteristic radiation (fluorescence) and
- bremsstrahlung (which quite literally means “braking radiation” [2, 3]).

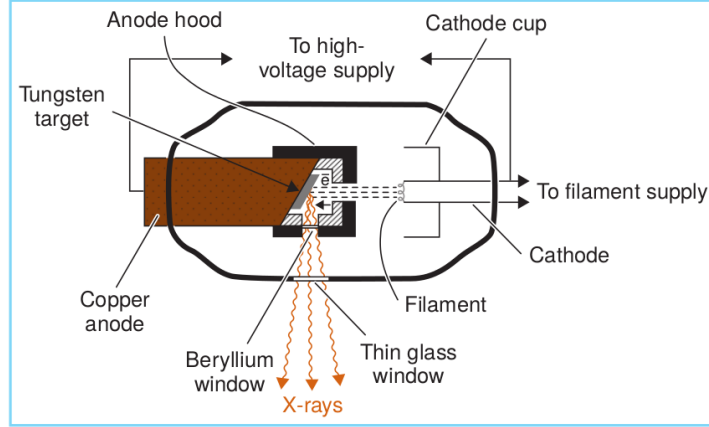


Figure 1.2: Basic schematical setup of X-ray tube [2].

Characteristic X-rays occur when the incoming electron interacts with an inner shell orbital electron and causes it to be ejected, thus ionizing the respective atom of the target material. When an electron from an outer shell occupies the vacancy left by the ejected electron, the energy difference is emitted in the form of electromagnetic radiation - characteristic radiation, since the energy of the emitted radiation is characteristic of the atom and the shell transition it emerged from [3, 2, 5].

Bremsstrahlung, on the other hand, is a form of X-rays emitted when an incoming electron gets close enough to the positively charged nucleus of the target atom to be decelerated through inelastic Coulomb interactions with it [3, 2, 5].

A schematic depiction of both production mechanisms can be observed in Figure 1.3 (from [2]).

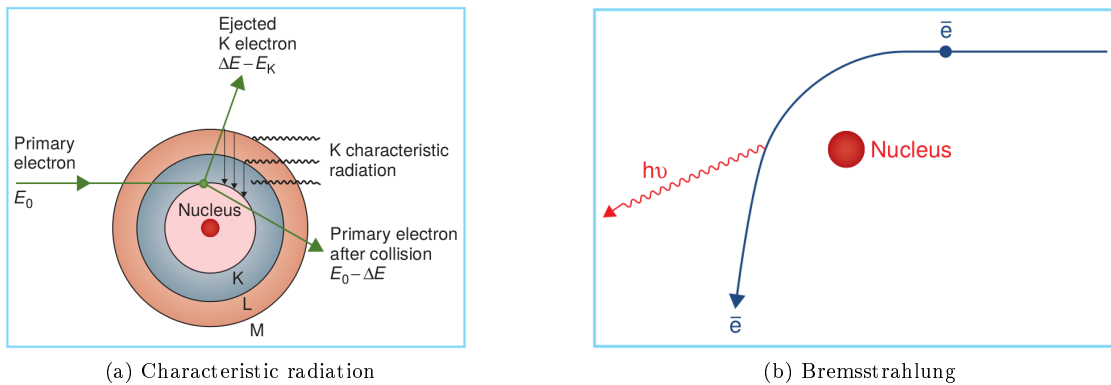


Figure 1.3: The two mechanisms of X-ray production [2].

Of the overall output of X-ray photons emitted from an X-ray tube, the majority can be accounted for as bremsstrahlung and only a small fraction of those photons make up the characteristic radiation [3, 2].

The X-ray spectrum of energies is by no means homogeneous, given that the discrete energies of characteristic radiation are superimposed to the continuous energy distribution of bremsstrahlung photons [3, 2].

Provided the beam was not filtered in any way, the calculated energy spectrum resulting from a thick target would be given by the following equation:

$$I(E) = C \cdot Z \cdot (E_m - E) , \quad (1.6)$$

where $I(E)$ stands to represent the intensity of the bremsstrahlung at energy E , Z is the atomic number of the target material, C is a constant related to the number of incoming electrons and therefore proportional to the tube current and E_m is the maximum energy of the emitted photons, which has to be equal to the maximum energy lost by the electrons hitting the target, that is in turn determined by the applied peak kV (kVp). In standard practice, however, the spectrum is attenuated both inherently and intentionally, especially to eliminate the lower energies from the spectrum. An example of spectra from a completely unfiltered beam and a beam filtered with a 2 mm thick aluminum layer is shown in Figure 1.4 (from [3]).

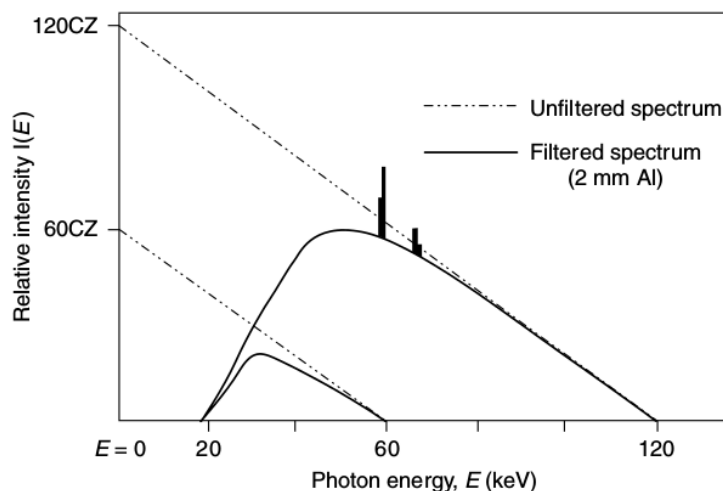


Figure 1.4: Filtered and unfiltered bremsstrahlung spectra [3].

1.3.2 Interaction of Ionizing Radiation with Matter

This thesis revolves around the beam commissioning of a photon treatment machine and will therefore only be covering the interaction of photons with matter (which for medical applications is tissue). However, the automatically generated Fallback plans are based on clinically acceptable proton plans, which have entirely different dose deposition characteristics. Suffice to say that due to the Bragg peak that protons manifest at the end of their range in matter, more precision and normal tissue sparing can be achieved with protons, provided the location of the target volume is known with sufficient accuracy.

Having said that, Figure 1.5 shows the different curves of depth-dose deposition of photons and charged particles - in this case the previously mentioned protons and the heavier carbon ions, with their typical fragmentation tail - courtesy of Dr. Hermann Fuchs.

Macroscopic Behaviour: Attenuation

In the case of a narrow monoenergetic photon beam, the number of photons N reaching a detector after passing through a filter of thickness x without being attenuated by it is given by [4]:

$$N = N_0 \cdot e^{-\mu \cdot x} , \quad (1.7)$$

where N_0 is the number of photons reaching the detector after a filter of thickness zero and μ is the *linear attenuation coefficient* which is filter material- and photon beam energy-dependent. For homogeneous media, the linear attenuation coefficient is uniform (meaning $\mu = \text{const}$) [5]. The *mass attenuation coefficient* $\frac{\mu}{\rho}$ was introduced to examine what role the atomic number might play in the attenuation phenomenon, which was achieved by eliminating the variation with material density ρ . It is a macroscopic quantity that gives the total probability of interaction of a photon of a given energy with matter, irrespective of the actual type of interaction [4].

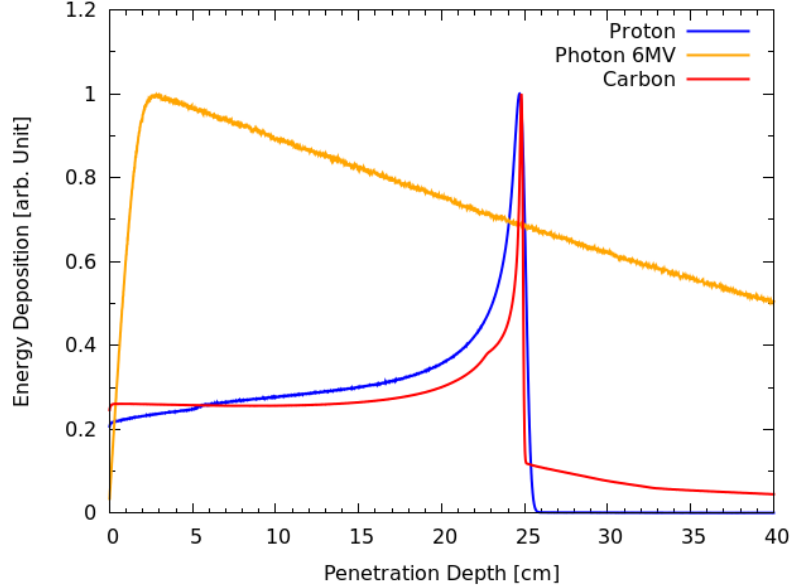


Figure 1.5: Energy deposition of 6 MV photons, protons and carbon ions.

The filter thickness reducing the intensity to half its original value, i.e. for which

$$\frac{N}{N_0} = 0.5 = e^{-\mu \cdot x_{1/2}} \quad (1.8)$$

holds true, is called the *half value layer* $x_{1/2}$ (HVL) or half value thickness [4]. In the case of monoenergetic photon beams, the intensity of the beam drops to 50% after the first HVL, to 25% after the second and so on. For any filter material, the half value layer of a photon beam indicates its power of penetration. For kilovoltage photon beams, the HVL can be used as a means to establish the quality of the respective beams [4].

As previously stated, however, the beams used in radiation therapy are not monoenergetic. When filtering a polyenergetic photon beam, the lower energetic photons - having larger attenuation coefficients - will be preferentially eliminated from the beam (beam hardening) and as a consequence, the average attenuation coefficient will decrease yet the beam's average energy will increase. With the attenuation coefficient no longer constant, the transmission curve also changes since it no longer is purely exponential. A constancy of the half value layers can no longer be observed, their thickness now depending on how much the beam has already been filtered. The ratio of the first half value layer to the second is called *homogeneity coefficient* χ and is an indicative of the degree of beam hardening arising [4, 5]:

$$\chi = \frac{HVL_1}{HVL_2}. \quad (1.9)$$

Depending on the value of the homogeneity coefficient, it contains the following information [5]:

- $\chi = 1$: the photon beam is monoenergetic;
- $\chi \neq 1$: the photon beam is polyenergetic (shows a spectral distribution);
- $\chi < 1$: the absorber material has a hardening effect on the photon beam;
- $\chi > 1$: the absorber material has a softening effect on the photon beam.

Figure 1.6 compares the attenuation of a monoenergetic beam (dashed line) and a 100 kV photon spectrum, having the same first HVL. It depicts the loss of the true exponential form of the transmission curve for a polyenergetic beam.

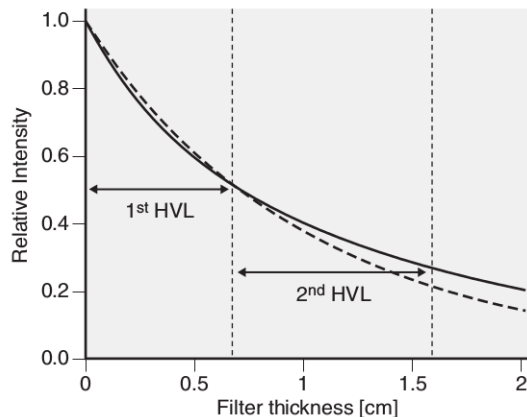


Figure 1.6: Example of non-constant HVLs for a photon beam exhibiting a photon spectrum [4].

Other coefficients relevant for radiation dosimetry are energy-related. These are used to account for [5, 4]:

- mean energy transferred from photons to charged particles (electrons and positrons) during photon-atom interactions - *linear energy transfer coefficient* μ_{tr} and its respective *mass energy transfer coefficient* μ_{tr}/ρ ;
- mean energy absorbed in the medium (in radiotherapy: biological tissue) - *linear energy absorption coefficient* μ_{ab} (often denoted by μ_{en} in literature) and its respective *mass energy absorption coefficient* μ_{ab}/ρ .

In order to determine the absorbed energy, not only the photons that have not been attenuated in the absorber, but also all non-locally absorbed energies need to be detected, i.e. energies transported away in the form of characteristic X-ray photons, scattered photons, bremsstrahlung photons or annihilation photons emerging after pair production. To that end, a broad beam geometry is better suited since the output signal of the detector will result from both a drop due to the attenuation in the absorber and an increase due to the additional radiation arising from the scattering caused by the same absorber. In this case it is only logical for the attenuation coefficient for a monoenergetic photon beam and a given absorber material to be greater than the corresponding energy absorption coefficient for the same energy and material since attenuation would now additionally account for absorption and scatter [4, 5].

The signal read by the detector for a broad beam geometry with an absorber of thickness x is given by:

$$I_B(x) = B \cdot I_N(x) , \quad (1.10)$$

where $I_N(x)$ is the signal for narrow beam geometry (discussed earlier) and B is the *build-up factor* which takes into account all the additional secondary photons being scattered into the detector. B can depend on the energy and geometry of the photon beam, on the thickness and atomic number of the absorber material and the actual quantity that is being measured such as dose, kerma, photon fluence, beam intensity etc. While for a narrow beam geometry B is obviously 1, for broad beam geometries, B is positive and can reach values of 10 or more [5]. Figure 1.7 sketches the narrow and broad beam geometries (from [5]).

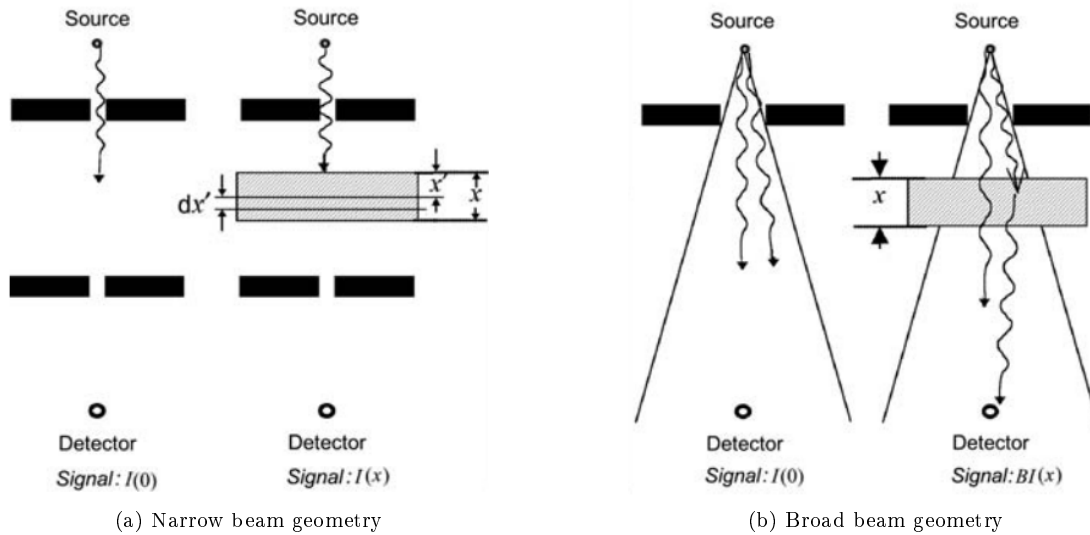


Figure 1.7: Photon attenuation [5].

Photon Interaction Cross Sections

Photons can interact with several different target entities such as atomic electrons, nuclei, atoms and molecules and their respective probabilities of interaction with those target entities are given by their cross sections σ for that particular interaction. Although the cross section indicates a probability, it usually bears the unit of an area (m^2 or in this case, because of the very small, atomic scale, barn= $10^{-28} m^2$) because it can be regarded as the cross sectional area of the target as it is being “perceived” by the incoming photon, in a plane perpendicular to its direction of incidence [3].

There are two categories of photon interactions: *absorption* and *scattering* processes.

A full absorption process requires the incoming photon to transfer all of its energy to the target entity, leading to the emission of secondary particles during or after the interaction.

The premise of a full scattering process, on the other hand, is that the interaction of an incoming photon with the target entity will lead to a change in its direction of motion, energy and momentum in accordance with the laws of relativistic kinematics [3].

Photoelectric absorption, pair and triplet production make up the main absorption processes, whereas coherent and incoherent scattering represent the main scattering processes [3].

The sum of the cross sections for all these individual processes is called the total interaction cross section σ and gives the probability that a process occurs, regardless of its type [3]:

$$\sigma = \sigma_{pe} + \sigma_{coh} + \sigma_{incoh} + \sigma_{pair} + \sigma_{trip} + \sigma_{phn} , \quad (1.11)$$

where each of the terms in the equation stands to represent the cross section for the aforementioned processes, except for σ_{phn} , which is the cross section for the nuclear photoeffect, that normally isn't of major importance but sometimes needs to be considered [3].

In order to account for anisotropic distributions of scattered photons, the *differential scattering cross section* $\frac{d\sigma}{d\Omega}$ was introduced, which assumed a dependence of the cross section on the solid angle Ω in the direction of the scattered photon. The probability that the photon is scattered into

the solid angle $d\Omega$ is given by $(d\sigma/d\Omega) \cdot d\Omega$, which means that for the *total cross section*

$$\sigma = \int_{4\pi} \frac{d\sigma(\theta, \phi)}{d\Omega} \cdot d\Omega \quad (1.12)$$

holds true, with θ being the scattering angle and ϕ an azimuthal angle, as can be deduced from Figure 1.8.

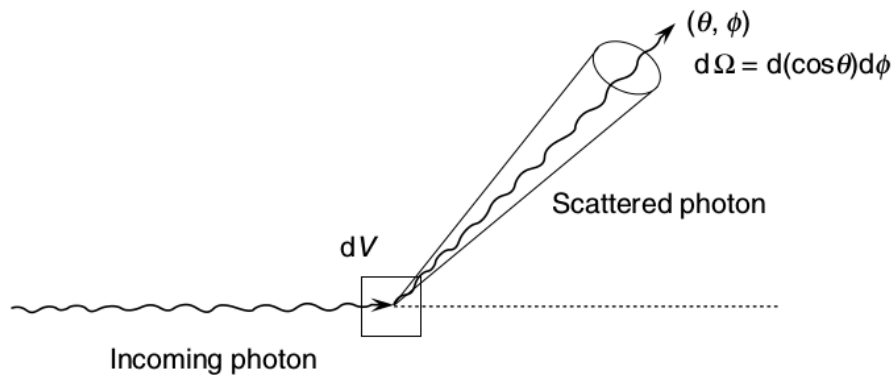


Figure 1.8: Sketch of a scattering process to demonstrate the solid angle and scattering angle [3].

It may sometimes be of use to look at the cross section differential in the energy of the scattered photon, $d\sigma/dE$ and in the case of more complex (multiple, consecutive) processes, the *double-differential cross section* $\frac{d^2\sigma}{d\Omega dE}$ is employed, as it thoroughly describes the respective interaction. This way, both the scattering angle and the scattering energy are equally considered in a scattering process [10].

Photon Interaction Processes

There are several criteria for classifying the interactions of photons with absorber atoms, namely according to:

- the type of target they interact with (either orbital electrons or nuclei);
- the type of interaction with respect to the consequences for the photon (photon disappearance/absorption or photon scattering) and
- the type of particle released as a result (either electrons or positrons) [5].

In medical physics (of which radiation physics is only a branch) and radiation dosimetry a somewhat different classification can be made, according to their importance in these fields. This leads to four distinct categories of photon interactions with absorber atoms (according to [5]):

1. interactions of major importance: photoelectric effect, Compton scattering by “free” electron and pair production (including triplet production);
2. interactions of moderate importance: Rayleigh scattering;
3. interactions of minor importance: Thomson scattering by “free” electrons, photonuclear effect and
4. interactions of negligible importance: Compton scattering by the nucleus, Thomson scattering by the nucleus, meson production and Delbrück scattering.

This thesis shall not delve into the latter two categories but will instead focus on the former two by going through each interaction and elaborating on their respective principles.

The Photoelectric Effect

This phenomenon comes to pass when an incoming photon interacts with a tightly bound orbital electron of an absorber atom, i.e. with an electron of the innermost shells (usually K, L, M or N). The energy of the photon is greater than the binding energy of the electron and is completely transferred to the latter. The electron is thus ejected from the atom with an energy E_{kin}^e equal to the photon's initial energy $h \cdot \nu$ minus the binding energy E_B^e which had to be spent in order for the electron to be released in the first place [3, 5]:

$$E_{\text{kin}}^e = h \cdot \nu - E_B^e . \quad (1.13)$$

Figure 1.9 illustrates the photoelectric effect.

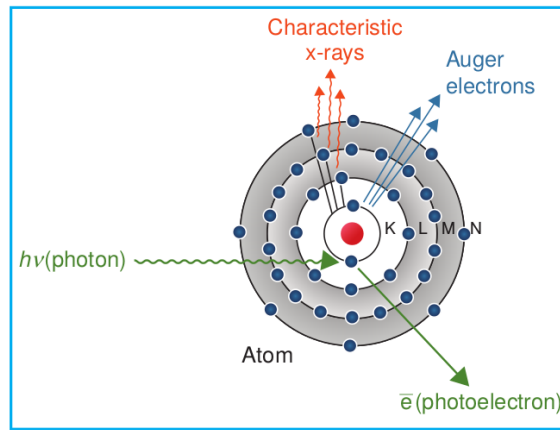


Figure 1.9: Photoelectric effect [3].

With the ejection of the photoelectron, the atom is now ionized and in an excited state. The energy it needs to shed in order to return to a stable (non-excited) state is emitted in the form of either characteristic X-rays, if the vacancy in the inner shell is filled by an electron from a shell of higher energy and the difference in energy is released as characteristic photons or Auger electrons, which are emitted if the X-rays are not emitted outwards, but are instead using their energy to release another orbital electron. The Auger electron has a kinetic energy equal to the energy released during the transition minus its binding energy [3].

The atomic number of the absorber material as well as the energy of the incident photon strongly affect the probability of photoeffect occurrence [2, 4]:

$$P \sim Z^3/E^3 . \quad (1.14)$$

The photoelectric effect is the dominating effect in water (or tissue) in the energy range below 30 keV and in lead (which is used for shielding purposes) for energies up to 500 keV, which makes it extremely important in diagnostic radiology [4].

The Compton (Scattering) Effect

In order to correctly understand the Compton effect, a short introduction on scattering processes may be of use.

The main characteristic of a photon scattering process is that the photon is not absorbed as a result of the interaction but instead changes its direction of motion. The photon may or may not lose energy during the interaction, which leads to the two categories of scattering processes: coherent (no energy loss) and incoherent (with energy loss).

The relative magnitude of the energy of the incoming photon $h \cdot \nu$ and the orbital electron's binding energy E_B determines whether the electron is tightly bound ($E_B \lesssim h \cdot \nu$) or loosely bound/"free" ($E_B \ll h \cdot \nu$) [5].

Therefore, for photon energies considerably higher than the electron binding energies, the electron is considered free and stationary at the moment of impact, which will lead to the photon losing energy upon collision, making the scattering process an incoherent one. At low photon energies, both types of scattering can occur depending on whether the photon was scattered from an individual bound electron (incoherent scattering) or from all the bound electrons as an entity, because they all scattered in phase (coherent scattering) [3].

The Compton effect is an incoherent scattering process: the incoming photon transfers part of its energy to an orbital electron of the absorber atom and causes it to be ejected, thereby ionizing the atom (see Figure 1.10).

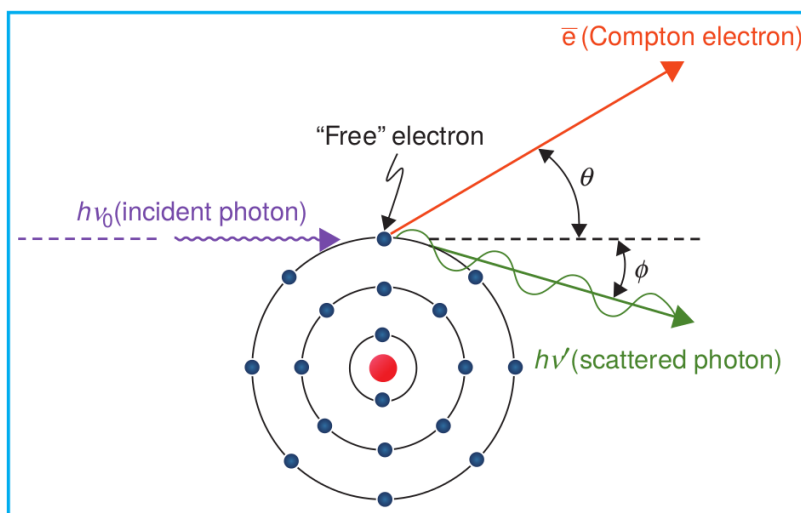


Figure 1.10: Kinematics of Compton scattering [3].

The photon emerges from the interaction on a trajectory at an angle θ relative to the the original trajectory and with a reduced energy $h \cdot \nu'$ given by the Compton equation [3]:

$$h \cdot \nu' = \frac{h \cdot \nu}{1 + \alpha(1 - \cos \theta)}, \quad (1.15)$$

where $\alpha = \frac{h \cdot \nu}{m_0 c^2}$, with m_0 being the rest mass of the electron. This leaves the ejected electron with a kinetic energy of $E_{\text{kin}}^e = h \cdot \nu - h \cdot \nu'$.

From the Compton equation one can easily deduce that there is no energy loss for the photon when it is being scattered in the forward direction ($\theta = 0^\circ$), whereas for backward scattering ($\theta = 180^\circ$), it experiences the highest energy loss, which also seems to increase with increasing photon energies, until reaching the limiting value of $m_0 c^2 / 2$ (256 keV). The limiting value for a scattering angle of $\theta = 90^\circ$ is of course $m_0 c^2$ (511 keV) [3].

The angle into which the electron is emitted relative to the direction of the incoming photon is given by [3]:

$$\cot \phi = (1 + \alpha) \cdot \tan \left(\frac{\theta}{2} \right), \quad (1.16)$$

which also implies that $\phi \leq \pi/2$ and that a backward emission of the electron is out of the question. In water, the Compton effect dominates between 100 keV and 20 MeV making it the dominant interaction in tissue for radiotherapy, since that energy range covers the photon energies frequently used in radiation photon therapy [4].

The probability of the Compton effect coming to pass depends on the electron density of a material, which is given by Z/A , with Z being the atomic number and A the mass number of an element. Given that this ratio is almost constant for all elements heavier than hydrogen, it is safe to say the Compton effect is independent of the atomic number and only depends on the physical density of the traversed material. This is extremely important in radiotherapy applied to soft-tissue malignancies since a dependence on Z would translate to a higher absorbed dose in bone compared to that absorbed in soft tissue [4].

The amount of energy transferred to the electron depends on the initial energy of the incident photon. With the increase of incident photon energy comes an increase in the average percentage of energy transferred to the electron. In the case of megavoltage photons which are employed in radiation therapy, this means that the interaction leads to the production of high energy secondary electrons that will cover a significant distance in tissue and thus contribute to the sparing of skin. This is in part also due to the dependency of the angular distribution of emitted electrons on the energy of the incident photon. The higher the photon energy the more pronounced is the electron distribution in the forward direction (relative to the incident photon's direction) [4].

Pair and Triplet Production

An electron (negatron)-positron pair can only be produced, if the energy of the incident photon exceeds the threshold value of $2m_0c^2 = 1.022$ MeV (equivalent to the rest mass of two electrons, since a positron has the same mass as an electron). According to the laws of physics, energy, charge and momentum need to be conserved, meaning that this phenomenon can only occur in the Coulomb field of another charged particle (either atomic nucleus or orbital electron), in order to provide a suitable transfer partner for part of the momentum of the photon [5]. The nucleus thus experiences a minor recoil, for which a negligible amount of energy is spent [3].

Since the photon is absorbed entirely during the process of pair production, the electron and positron are left with the kinetic energies:

$$E_{\text{kin}}^{e^-} + E_{\text{kin}}^{e^+} = h \cdot \nu - 2m_0c^2, \quad (1.17)$$

which they share equally, on average [3].

The cross section for pair production is proportional to the square of the atomic number ($\sigma_{\text{pair}} \propto Z^2$) and is of course zero below the energy threshold. Above the threshold it increases rapidly with energy [3].

Pair production need not necessarily occur in the Coulomb field of the nucleus. It may just as well occur in the electric field of an orbital electron. Having a significantly smaller mass, the recoil the electron will receive will be enough to lead to its ejection from the atomic shell. Having produced two electrons and a positron this interaction process is called triplet production. The energy threshold for triplet production is $4m_0c^2 = 2.044$ MeV, below which the cross section for triplet production is zero. Above that threshold energy, however, the cross section varies with the atomic number of the medium ($\sigma_{\text{trip}} \propto Z$), which is why its importance relative to the one of pair production decreases with increasing atomic number [3].

The electron will undergo several other interactions (collisions with atomic electrons) before losing its energy, while the positron will annihilate with a local electron, leading to the emission of two photons, each with an energy of 0.511 MeV, into opposite directions [4].

Rayleigh Scattering

This process occurs mainly when photons of low energy and absorbers of high atomic number interact with each other. The photon interacts with the absorber atom and is scattered by its bound electrons. The entire atom absorbs the transferred momentum and since it receives very little recoil energy, it is neither excited nor ionized in the process and its bound electrons subsequently return to their original states. The photon, however, is scattered into the scattering angle θ (which is usually very small) and has approximately the same energy it had upon impact.

The Rayleigh cross section exceeds the Compton cross section in the low energy region because of the collective contribution of all atomic electrons to the atomic Rayleigh cross section [5].

Rayleigh scattering is not to be confused with Thomson scattering which is also a coherent scattering process, where an incident photon as a *wave* induces a dipole oscillation in a loosely bound atomic electron and causes it to release an electromagnetic wave of the same wavelength in return [5].

1.4 External Beam Photon Therapy

As previously stated in section 1.2.2, external beam radiotherapy with photons has been the first form of radiotherapy, being introduced soon after the discovery of X-rays. Being the pioneering method additionally meant that external beam therapy has been under scrutiny longer than any other modality or technique, which in time has led to periodical improvements.

In the scope of this subsection, the treatment machines used in external beam radiotherapy will be approached, as will the mechanisms and components involved in beam formation, shaping and bending, which are relevant for the beam models. Of similar importance to creation of the beam models are the characteristics of megavoltage photon beams that are currently being used in clinical practice, which is why they will also be discussed in this subsection.

Finally, some of the most important treatment techniques used in external beam photon radiotherapy will be addressed at the end of this subsection.

1.4.1 Linear Accelerators

Medical linear accelerators (linacs) are at present the predominant machines used in radiation therapy to generate megavoltage beams [3, 5]. The foundation for the linear accelerator was laid by Ernest Lawrence in 1929 (see section 1.2.2) and saw significant improvements throughout time. The linac is a cyclic accelerator that accelerates electrons on straight (hence: linear) trajectories to kinetic energies of 4 – 25 MeV using non-conservative microwave radiofrequency (RF) fields operating at frequencies in the $10^3 - 10^4$ MHz range, mostly at 2856 MHz. For the particle energy to gradually increase, the wave and the particle need to resonate, meaning they need to move in synchrony as the RF wave continues to provide forward acceleration [5, 11].

Although the design of modern linear accelerators may vary depending on the manufacturer's preferences and the maximum kinetic energy that is to be reached by the electron beam, the components of all medical linacs can be divided into five sections:

- gantry;
- gantry stand or support;
- modulator cabinet;
- patient support assembly (treatment couch);
- control console [5].

A typical contemporary linac is depicted schematically in Figure 1.11.

Modern linacs are capable of delivering both photon and electron beams in the energy ranges of 6–25 MV and 4–22 MeV, respectively. A beam of electrons is required in any case for the generation of X-ray photons, which will be achieved by inserting a thick target of high atomic number into the beam's path. Yet, if only the electron beam is needed, a scattering foil is introduced to broaden the beam [3].

The main linac components responsible for forming and shaping the beam of electrons are:

- injection system;
- RF power generation system;
- accelerating waveguide;
- auxiliary system;

- beam transport system;
- beam collimation and beam monitoring system [5].

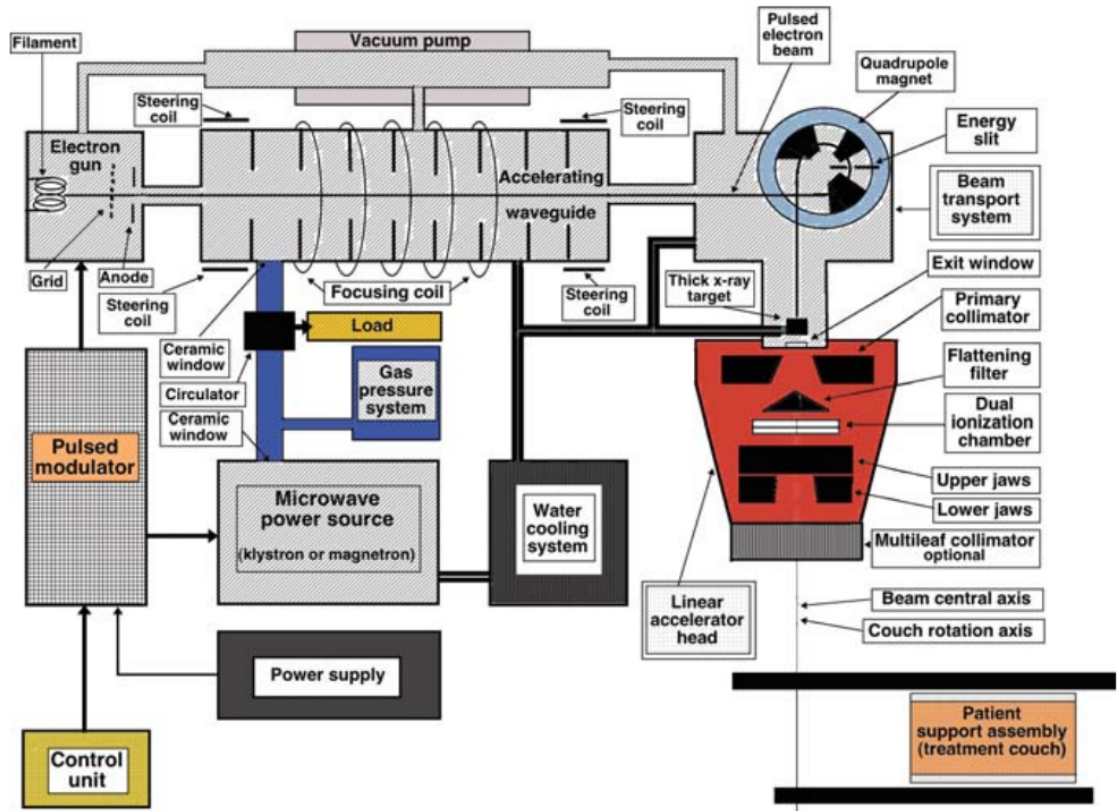


Figure 1.11: Schematics of a modern-day linear accelerator [5].

The *injection system* is responsible for providing the electrons and is merely an electrostatic accelerator popularly termed as “electron gun”. There are currently two main types of electron guns on the market: diode and triode type. They both contain a heated cathode at roughly -25 kV and a perforated grounded anode, but the triode type gun additionally contains a grid placed between the cathode and the anode. The gun operates in the following way: electrons are ejected from the heated cathode by way of thermionic emission, are then focused into a pencil beam and finally accelerated towards the anode, whose perforation allows them to be lead into the accelerating waveguide [5].

The production of high power microwave radiation needed to accelerate the electrons in the waveguide occurs in the *RF power generating system*, which is made up of two main components: the RF power source and the pulsed modulator. Medical accelerators operate in pulses in the power range of $2 - 10$ MW which can be provided by one of two possible RF power sources: the magnetron and the klystron. Magnetrons can provide peak outputs of 3 MW and are generally used in lower energy machines whereas klystrons are preferred for dual energy machines. The underlying principle of operation of both devices is accelerating and decelerating electrons in vacuum to produce the high power RF field. The short pulses of high voltage and high current are produced by the pulsed modulator [3, 5].

Perhaps the most important component of a linac is the *accelerating waveguide* which can be roughly envisioned as a copper pipe with disks (irises) having circular apertures in the center that divide the waveguide into a series of cylindrical cavities. This is the location where electrons are accelerated by being tranferred energy from the RF field.

The waveguide can be one of two available types, depending on the way the wave behaves inside: either propagating along the waveguide axis or stationary in which case they would be called travelling waveguide and standing waveguide, respectively [5, 3].

As the name indicates, the *auxiliary system* is not directly involved in the process of acceleration, however, it provides the right conditions to ensure that the clinical operation proceeds without problems. The subsystems falling into the category of auxiliary system are the water-cooling system, the vacuum-pumping system, the air pressure system and the system providing shielding against leakage radiation [5].

The task of the *electron beam transport system* is to lead the pulsed high-energy electron beam from the waveguide onto either the x-ray target (photon therapy mode) or the scattering foil (electron therapy mode) [5].

There are several different ways of bending the electron beam, in order to ensure that the output beam, be it photon or electron beam is directed at the patient. Although all methods involve the use of bending magnets, it is their number and configuration which make up the difference. Unarguably the simplest of all bending systems is the use of a simple dipole magnet to bend the beam by 90° . Such a magnet was used with regularity on earlier versions of linacs. Bending the electron beam by 270° is widely used and can be achieved through several configurations: with magnets of hyperbolic pole faces, with locally tilted pole pieces or using three 90° sectors. Another method designed to reduce the machine's vertical height is the slalom bend (or 112.5° double focusing) system, which uses two 45° sector magnets followed by a third one of 112.5° [3].

As for the *beam collimation and beam monitoring system*, let it only be said here that it is crucial in a clinical linac, since its purpose is to ensure that the prescribed dose is delivered to the patient with high numerical and spatial accuracy [5].

Since this subject is of relevance for the thesis at hand, an entire separate subsection will be devoted to it. More information can therefore be found in section 1.4.2.

1.4.2 Photon Beam Formation and Shaping

The location where the photon beam is produced or the electron beam is broadened, i.e. where either beams are prepared for clinical operation is the treatment head of the linear accelerator. Apart from its task of producing the clinical photon and electron beams, the linac head is also responsible for shaping, localizing and monitoring said beams. A linac head will usually contain the following components:

- multiple retractable X-ray targets;
- flattening filters and electron scattering foils;
- primary and adjustable secondary collimators;
- dual transmission ionization chambers;
- field defining light and range finder;
- optional retractable wedges or full dynamic wedges;
- optional multileaf collimator (MLC) [5].

Production of megavoltage clinical photon beams generally originates in a combination of target and flattening filter. The high kinetic energy electron beam is lead onto a high atomic number target, either made entirely of tungsten or a copper-tungsten laminate, thus inducing the release of bremsstrahlung radiation, whose lateral profile at these energies mainly shows a forward peak. A flattening filter is therefore used to flatten the beam by creating a profile that increases at the field edges instead of decreasing as it would normally do, due to a lacking scatter at the edges (see Figure 1.12). Flattening filters are usually circularly symmetric with designs that vary among the different manufacturers. It is precisely its design that can have a significant impact on the photon beam. A specific target/flattening filter combination is determined for each given kinetic energy of

the electron beam, meaning that the linac can hold several interchangeable flattening filters in its treatment head [5, 3].

The concept of using flattened beams for clinical applications was originally preferred to the simple unflattened beams because of the limitations on computer resources and algorithms in earlier times, but with the rapid technological advances brought on by the last decade, the scientific community seemed intent to scrutinize the capabilities of unflattened beams [12].

Recent studies [12, 13, 14, 15, 16, 17, 18, 19, 6] have revealed some advantages of flattening filter free (FFF) photon beams, such as the possibility of achieving a higher dose rate along the central beam axis along with the immediate consequence of shorter delivery times. Furthermore, a reduction of treatment head and MLC leakage and occasionally of peripheral dose for some distinct treatment techniques can be achieved. This is relevant since the object of this thesis was creating beam models not only for flattened beams but also for unflattened (FFF) beams.

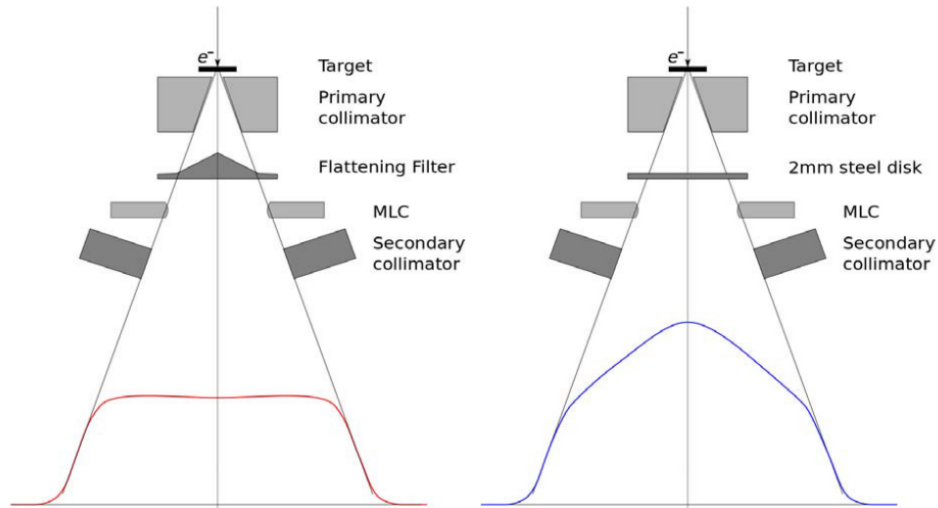


Figure 1.12: Beam as produced with (red) and without flattening filter (blue) [6].

Three collimation devices jointly collimate the photon beam: the primary collimator, the movable secondary collimator (defining the beam) and the multileaf collimator (MLC).

The circular shape of the primary collimator limits the field to a maximum circular size which is further curtailed by the secondary collimator which consists of two independent upper jaws and two independent lower jaws whose adjustable positions create either square or rectangular fields not larger than $40 \times 40 \text{ cm}^2$ at the isocenter (100 cm from the X-ray target). Finally, the newest collimation device, the MLC, enables the achievement of irregular field shapes both with efficiency and accuracy and is constituted by an array of narrow pairs of collimator leaves, each independently controlled by a small computer-controlled motor [5]. MLCs can be of three types: providing all the collimation (type A), providing collimation in conjunction with backup jaws (type B) and providing collimation together with backup jaws but being mounted externally (type C) [3]. MLC properties such as transmission, thickness, curved leaf tips and leaf tip widths, and their being connected via a so-called tongue-and-groove mechanism influence the output beam and are therefore considered during beam commissioning [20]. To make sure the right amount of dose is delivered to the patient, two separately sealed, powered and read out transmission ionization chambers are permanently embedded in the photon (and electron) beam. The chambers make up the dose monitoring system, whose task is not limited to monitoring only the dose, but also the beam's radial and transverse flatness as well as its symmetry and energy [5].

The field light and the range finder are instruments needed for a correct and reproducible positioning of the patient. They are, however, irrelevant for the beam models and shall therefore not be further discussed here [5].

Wedges are wedge-shaped pieces of aluminum, brass or lead that are inserted in front of the collimators in order to obtain a wedge-shaped intensity beam profile instead of the normal, uniform one, which may in some cases be desired [3].

They are, however, only mentioned here for the sake of completeness and will not be covered any further since the beam models which made the object of this thesis were of open fields (i.e. with no beam modifiers).

1.4.3 Physical Characteristics of Megavoltage Photon Beams

General

Even though all photon beams can be characterized using the same physical parameters, their origin, means of production and energy distinguishes the different categories they can be classified into. Depending on where they originate, the photon beams are composed of either γ -rays or X-rays, having been produced in the nuclei of radioactive elements or in a target of high atomic number that has been bombarded with high energy electrons, respectively. The production of X-rays always yields both bremsstrahlung and characteristic radiation and can occur either in X-ray tubes (for superficial/orthovoltage radiation) or, most importantly for megavoltage X-rays as used most commonly in radiation therapy, in linacs [7].

A factor of critical importance in radiotherapy is radiation dosimetry, i.e. knowing at all times what dose is received by the patient. This is achieved by reporting two different entities, one of which relating to the photon beam itself, accounted for through the number of photons and their energies and the other referring to the amount of energy deposited by the beam in different media such as air, water and biological tissue [7].

The quantities used to accurately describe the radiation beam itself are the photon fluence ϕ , defined as the number of photons dN entering a sphere with a cross sectional area dA , with its respective photon fluence rate which accounts for the photon fluence per unit time, and the energy fluence Ψ with its respective energy fluence rate, which are defined as the amount of energy dE crossing a unit area dA and the energy fluence per unit time, respectively [7].

As for the description of the dose deposition in media, it can be undertaken by using the air kerma in air, the exposure in air and the “dose to small mass of medium in air” which is to be obtained from the air kerma in air but shall not be discussed here, seeing that it is of rather little importance to megavoltage radiotherapy, being primarily used in orthovoltage and ^{60}Co teletherapy [7].

Dose to Water Formalism

Since the human body consists mostly of water and the majority of all tissue types have radiological properties similar to those of water, it is understandable that TPSs throughout history have been reporting dose distributions as dose-to-water and calculating doses by assuming all materials to be water of different densities. The dose-to-water ($D_{w,w}$) is formally defined as the dose in an infinitesimally small volume of water inside a heterogeneous medium again assumed to consist of different density water [21].

Monte Carlo methods, however, report the dose to medium with radiation transport in the medium ($D_{m,m}$). For such cases the dose-to-water concept has a different definition: the dose deposited in a particular point when an infinitesimal volume of tissue is replaced by an infinitesimal volume of water. This rationale leads to the dose to water with radiation transport in the medium - $D_{w,m}$ - a product of $D_{m,m}$ and the fraction of restricted electron mass collision stopping power, whose cutoff energy is determined by the volume size.

The restricted stopping power is obtained by dividing the energy loss per unit distance for local energy absorption by the mass density and does not include the energy carried away by energetic electrons.

Since over time clinical dose prescriptions were obtained using dose-to-water and since the radiosensitive part of the cell is made up of mostly water, it seems reasonable to continue to report dose-to-water rather than dose-to-material.

The newest version of RayStation - the TPS used for this thesis - first computes the dose-to-material (D_{mat}), i.e. the ratio of energy deposition to material mass density, and then performs a conversion to dose-to-water ($D_{\text{H}_2\text{O}}$), using the following formula [21]:

$$D_{\text{H}_2\text{O}} = D_{\text{mat}} \cdot \frac{\rho_{\text{effH}_2\text{O}}}{\rho_{\text{efftissue}}} \cdot \frac{\rho_{\text{mtissue}}}{\rho_{\text{mH}_2\text{O}}}, \quad (1.18)$$

where $\rho_{\text{effH}_2\text{O}}$ and $\rho_{\text{efftissue}}$ represent the effective densities of water and tissue, respectively and $\rho_{\text{mH}_2\text{O}}$ and ρ_{mtissue} are the mass densities of water and tissue, respectively.

Percentage Depth Dose

In radiation therapy, one is interested in the absorbed dose incurred at a certain depth along the central axis (CAX) in tissue. This quantity is given by the percentage depth dose (PDD) as follows:

$$PDD = 100 \cdot \frac{D(d)}{D(d_{\text{max}})}, \quad (1.19)$$

where $D(d)$ is the dose measured at depth d and d_{max} is the depth of maximum dose, therefore assuming a normalization to $D(d_{\text{max}}) = 100\%$. Four parameters influence the PDD: the depth in the patient/phantom, the field size, the source to surface distance (SSD) or source to axis distance (SAD), depending on the type of set-up and the photon beam energy [7, 4, 3]. For an exemplification of the latter dependency, see Figure 1.13.

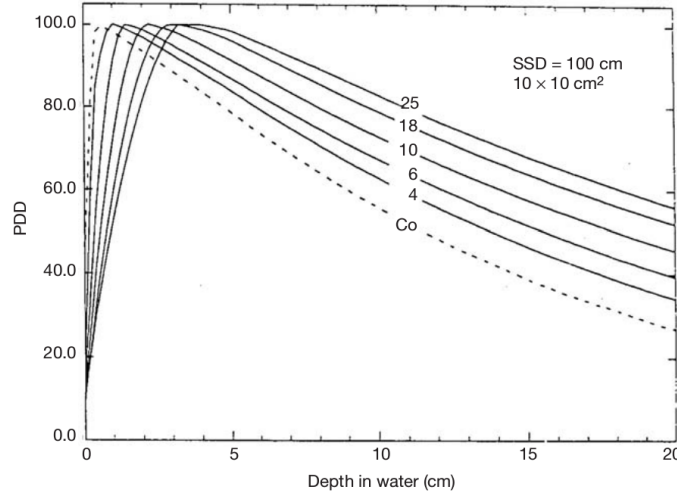


Figure 1.13: PDD curves in water for several megavoltage photon beams: from ^{60}Co γ -rays to 25 MV X-rays [7].

A PDD graph (depth dose curve) has three important parts: the build-up region, the point of maximum dose $D(d_{\text{max}})$ and the fall-off region [20, 3]. The build-up region was named after the phenomenon occurring directly beneath the skin and up to the depth of maximum dose: the build-up effect. According to this effect, the dose in this small portion of depth is higher than the surface dose, due to a lack of electronic equilibrium at shallow depths. Secondary electrons resulting from the interactions of energetic photons with the medium, mostly Compton scattering, are responsible for the absorbed dose. As stated in section 1.3.2, at these energies characteristic for megavoltage photon beams, the secondary electrons are primarily directed in the forward direction and deposit their energy further away from the actual site of interaction. The number of electrons passing through each layer of the patient/phantom and consequently the deposited dose will increase progressively until electron equilibrium is reached, which is at a depth approximately equal to the range of the electrons (see Figure 1.14).

Since secondary electrons emerging from the treatment head have also been known to influence the depth dose curve at shallow depths, different linacs will show differences in the build-up regions of their depth-dose curves. The surface dose depends on both beam energy and field size and is mainly due to electron contamination from the collimator system and especially the flattening filter. Contamination seems to increase with larger fields and more energetic beams, though collimation with MLCs can solve this problem [3].

Beyond the point of dose maximum, the primary photons are attenuated by being either absorbed or scattered out of the primary beam, resulting in the nearly exponential fall-off region of the depth-dose curve. The fall-off is also due to the inverse square law effect, according to which the dose of a beam diverging from a point source decreases in the absence of attenuators with the square of the distance from the source [4, 3].

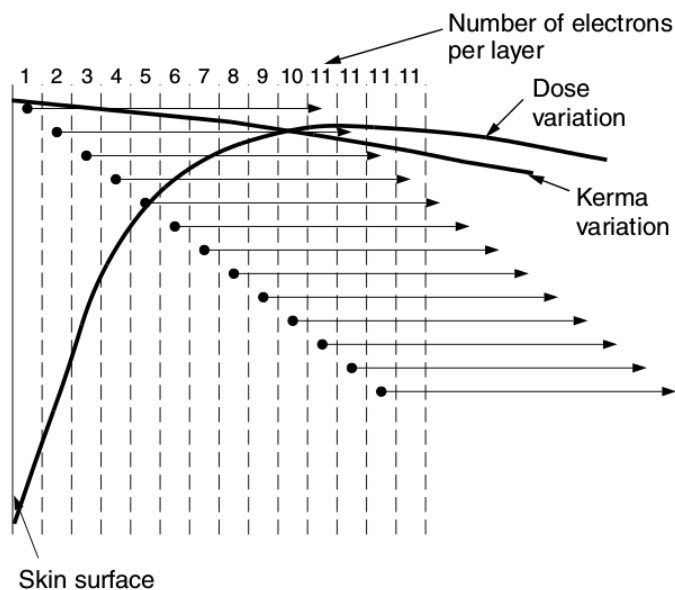


Figure 1.14: Build-up effect [3].

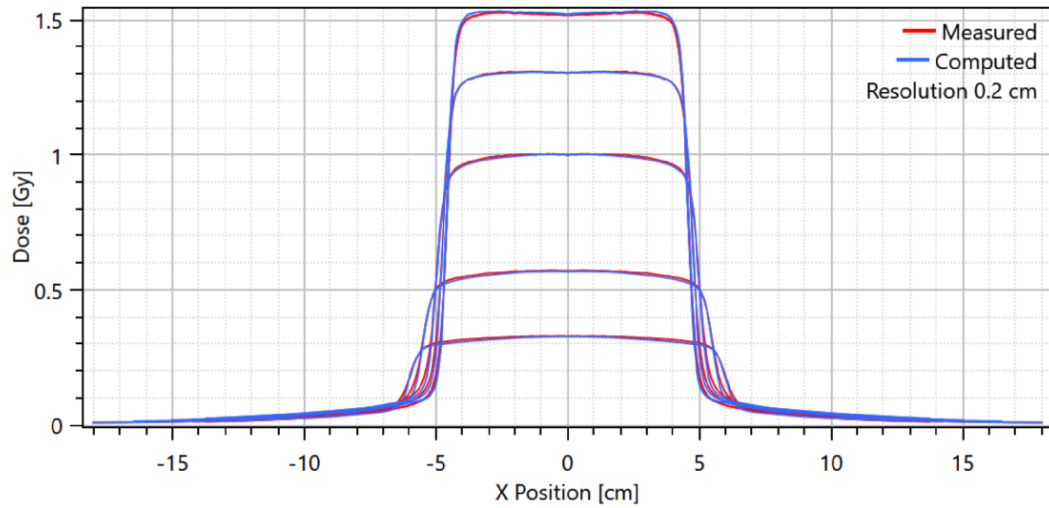
Beam Lateral Profiles

An accurate description of the dose inside the patient/phantom requires dose distributions both along the beam central axis (i.e. the PDDs) and off-axis, with the latter being supplied by the beam dose profiles.

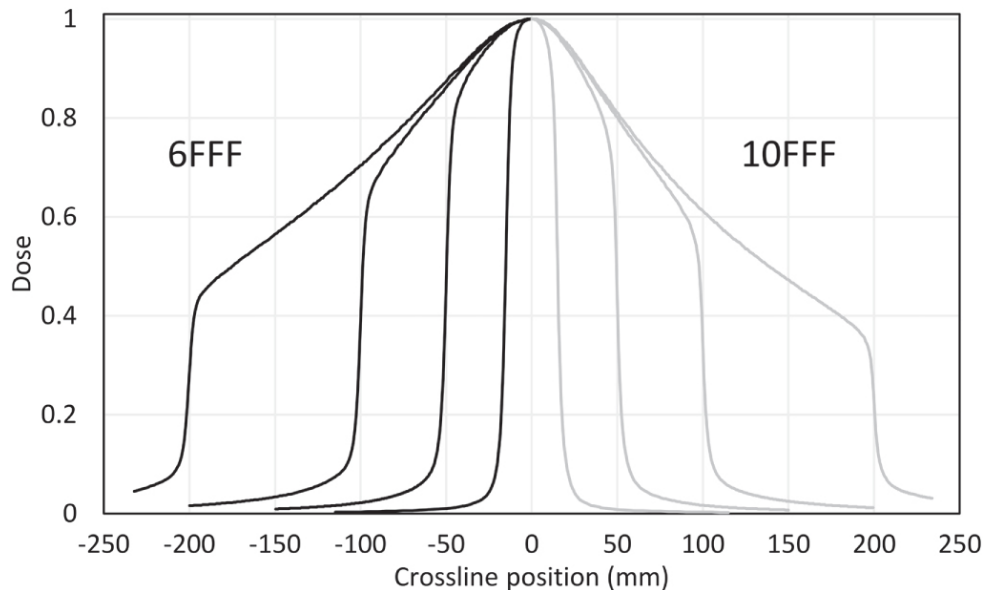
Beam profiles are measured perpendicularly to the beam CAX at a chosen depth in a phantom. The typical depths are d_{\max} and 10 cm to which those required by different treatment planning systems (TPSs) for beam commissioning are added [7]. Figure 1.15 shows examples of beam profiles, for both flattened (a) and unflattened (b) beams.

As was the case with PDD curves, beam profiles are also composed of three distinct regions: the central, penumbra and umbra regions which shall henceforth be referred to as in-field, penumbra and out-of-field, respectively, in accordance to their nomenclature in [20], whose instructions were followed in the beam commissioning process [7].

The in-field region is the central portion of the profile and is formed by dose values above 80% of the maximum dose of the curve. It is influenced by a number of aspects: the atomic number and shape of flattening filter, the energy of the electrons hitting the X-ray target and the atomic number of the target itself.



(a) Crossplane profiles for a 6 MV flattened beam of field size $10 \times 10 \text{ cm}^2$ at various depths.



(b) Beam semi-profiles for 6 and 10 MV unflattened beams of 3×3 , 10×10 , 20×20 , $40 \times 40 \text{ cm}^2$ field sizes [22].

Figure 1.15: Beam profiles.

The penumbra is defined as the region where the dose falls from a value of 80% to 20% of the maximum dose of the curve. It is formed by three components: transmission, geometric and scatter penumbra, caused by collimator transmission, finite source size and in-patient scatter, respectively. The factors influencing the total (or physical) penumbra are: source size, SSD, beam energy, source to collimator distance and depth within the phantom.

In the out-of-field region the dose is less than 20% of the maximum dose of the respective curve and stems from the little radiation that has made it past the collimator and the head shielding [20, 7]. The quality of dose profiles is assessed through three parameters that quantify field uniformity. These are: beam flatness, beam symmetry and penumbra width [20].

Flatness can obviously only be relevant for flattened beams, which only occur for field sizes greater than $4 \text{ cm} \times 4 \text{ cm}$. It measures the largest deviation from the maximum dose of the flattened profile:

$$F = \frac{D_{\max}}{D_{\min}}, \quad (1.20)$$

where D_{\max} and D_{\min} are the maximum and minimum doses, respectively, occurring within the flattened region of the profile.

The beam symmetry is given by the maximum ratio between two symmetrically spaced dose points $D(x)$ and $D(-x)$ having the CAX as the symmetry axis:

$$S = \max\left(\frac{D(x)}{D(-x)}, \frac{D(-x)}{D(x)}\right) - 1. \quad (1.21)$$

The penumbra width is self-explanatory. It is given by:

$$P = |x_{80\%} - x_{20\%}|, \quad (1.22)$$

where $x_{80\%}$ and $x_{20\%}$ represent the positions of 80% of the maximum dose and 20% of the maximum dose.

1.4.4 Photon Beam Dose Calculation Algorithms

This section shall briefly cover the algorithms that were/are used for the calculation of doses in photon radiotherapy.

The dose calculation algorithms can be categorized into three major groups: dose calculation methods based on Monte Carlo simulations, methods correcting for inhomogeneities using equivalent path length (EPL) scaling or equivalent tissue-air ratio (ETAR) and methods based on convolution techniques. All three categories will be covered in the following paragraphs with a special emphasis laid on the collapsed cone convolution (CCC) algorithm since it is the dose calculation algorithm used by the treatment planning system employed for this thesis [23].

Monte Carlo-Based Methods

Methods relying on Monte Carlo simulations for dose calculating purposes are indeed considered to be the most accurate, albeit at the expense of significantly higher calculation times. The physics behind photon and electron transport is used to determine trajectories of individual particles from which the pattern of dose deposition is then inferred. A random number generator establishes the history of every particle and does so for millions of particles. The final dose distribution is reached by adding up the energy deposition resulting from each particle's history [23].

EPL Scaling or ETAR Methods

EPL correction methods are one-dimensional and consider the electron density information along a ray's path from the source to a chosen point; changes in electron lateral transport are not modeled. Two dose calculation methods fall under this category: the ratio of tissue-air ratio method and the power law (modified Batho) method. Both account for the attenuation change in the primary dose but fail to do so for the scatter contribution, thus overestimating the dose for electron densities less than unity and underestimating it for electron densities greater than unity.

ETAR methods are based on three-dimensional electron density information emerging from CT images and are therefore also three-dimensional. Changes in primary dose are determined through ray tracing and scatter dose calculations are based on the three-dimensional density information. The methods of this category are not of high accuracy and are therefore used mainly for quick dose calculations and independent calculations to provide a rough estimate of absorbed doses or to help detect major errors [23].

Convolution Technique-Based Methods

Model-based convolution algorithms present Monte Carlo-similar accuracies while performing dose calculations in considerably less time. They are made up of two major components: the TERMA (total energy released per unit mass) and the kernel with the former standing to represent the

energy transmitted to the medium via interactions with primary photons and the latter expressing the energy deposited around a primary photon interaction site. The kernel in turn is composed of two parts: the primary kernel, calculating the primary dose, and the scatter kernel, calculating the dose from first and multiple scattering processes. The convolution of the TERMA with the kernel for any chosen point yields the dose for that particular point [23].

Tissue inhomogeneities are dealt with by scaling the kernel by radiological distances as determined from material densities given by CT images. In such cases, however, the process is no longer a convolution but a superposition of various kernels with the TERMA, because the kernel itself is not space-invariant [23].

Two of the most widely used variations of the convolution/superposition algorithm are the pencil beam convolution (PBC) and the collapsed cone convolution (CCC) techniques [23].

The pencil beam method calculates the point dose by convolving the TERMA with a pencil-shaped kernel, obtained from measured beam data. The pencil beam kernel represents the distribution of dose arising from a narrow beam entering a water phantom along the CAX. Corrections on account of inhomogeneities are achieved by using equivalent path length corrections for primary dose contributions and one-dimensional convolution along fan lines for scattered radiation. An algorithm based on the PBC is the anisotropic analytical algorithm (AAA), which relies on spatially variable convolution scatter kernels obtained from Monte Carlo simulations and on separate models for primary photons, scattered photons and contaminating electrons. A superposition of doses from the photon and electron convolutions gives the final doses [23].

Collapsed Cone Convolution Algorithm

Dose computation in RayStation is achieved through the collapsed cone dose engine, which is based on the convolution/superposition method covered exhaustively in [24].

The key to the collapsed cone convolution is to handle the primary photon transport and the secondary transport of photons and electrons originating from primary photon interactions separately. Because it takes lateral energy transport into account, yet still considers inhomogeneities, the accuracy of the collapsed cone algorithm exceeds that of the pencil beam algorithm.

Two steps are necessary to compute the dose from the energy fluence [21]:

1. determination of a TERMA distribution by tracing a ray of primary radiation through the patient, including all inhomogeneities;
2. point spread kernels collapsed along radial rays in a spherical coordinate system are then superimposed, all the while still considering inhomogeneities.

The TERMA is the product of the material- and energy-dependent linear mass attenuation coefficient and the energy fluence [21]:

$$TERMA(\bar{r}) = \int \frac{\mu(\bar{r}, E)}{\rho_m} \cdot \Psi_r(\bar{r}, E) dE, \quad (1.23)$$

where \bar{r} denotes the spatial dependence, meant to also symbolize the material-dependence for the linear mass attenuation coefficient $\frac{\mu}{\rho_m}$.

A discretization of the spectrum yields

$$\Psi(\bar{r}, E_i) = \Psi_0(E_i) \cdot \exp\left(-\int_{\bar{r}_0}^{\bar{r}} \mu(\bar{r}, E_i) dl\right) \quad (1.24)$$

for each component of the beam energy fluence, for a parallel beam at position \bar{r}_0 , with Ψ_0 denoting the energy fluence incident at \bar{r}_0 and the integration being performed along the fluence ray from the patient surface to \bar{r} . This expression can equally describe the fluence per space angle of an isotropic divergent beam [21].

As already mentioned in section 1.3.2, Compton scattering is the dominant photon interaction in radiotherapy, from which a long-range low energy photon and a short-range tissue-ionizing electron

emerge. The point spread kernel contains the statistical distribution of the energy deposit for the entire process. It is cylindrically symmetric and can be defined as “the spatial energy distribution resulting from one unit of primary energy loss at the origin from a photon energy fluence directed in the $\vartheta = 0^\circ$ direction” [21]. Point spread kernels thus give the dose distribution around a single photon interaction site in water, taking into consideration primary, first, second scatter and multiple residual dose contributions.

The final dose is the sum of all the voxel doses, which are given by the product of TERMA and the point spread kernels for each voxel.

1.4.5 Planning and Treatment Techniques

Forward Planning vs. Inverse Planning

There are two ways of approaching treatment planning: the forward planning and the inverse planning methods (see Figure 1.16).

In the former, the planner defines or is given a physician-defined target volume for which he/she then has to determine the right number of beams, their weighting, intensities and angles of incidence in order to achieve conformality, i.e. for the high value isodose volume to perfectly cover the target volume. The parameters for beam modulation are thus obtained on a trial-and-error basis or iteratively (using software programs) at best and can therefore be very labour-intensive and time-consuming, depending on the complexity of the anatomy and the quality of the patient input data [2, 4].

The latter starts from a prescribed dose for the target volume and additional constraints concerning maximum and median/mean doses allowed to the neighboring OARs and combines this information with an entered beam geometry to reach an optimal plan that best achieves all goals and constraints in the given frame. Optimization is performed by various computer algorithms, depending on the treatment planning system used [2, 4].

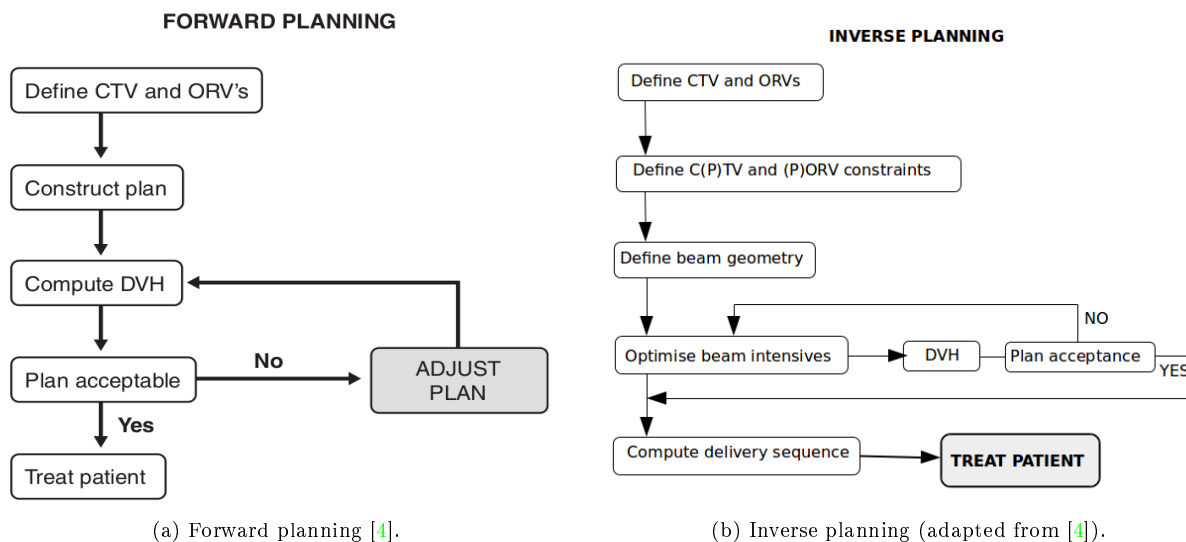


Figure 1.16: Flowchart of the two planning methods.

Treatment Plan Evaluation

Two of the most important tools for evaluating planned dose distributions are *isodose curves* and *dose volume histograms (DVHs)*.

With the help of isodose curves treatment plans can be evaluated either in a single plane or in several planes in the patient, nowadays rendered possible by modern 3-D TPSs, which can display isodose distributions not only in the axial but also in the coronal and sagittal planes [7].

The information provided by isodose curves or isodose surfaces is nothing more than what lines or surfaces share the same dose, reported as either relative (normalized) or absolute dose. The former means the dose is given as a percentage of a reference dose and the latter gives the actual dose in Gray, provided the treatment plan also includes a prescription dose [4].

It is common practice to normalize isodose curves to a reference point (e.g. the ICRU 62 reference point), meaning the dose in that particular point would represent 100%. This is done in order to enable the possibility of simultaneous assessment of both planning target volume (PTV) coverage and dose uniformity. According to [25, 26], the PTV should be covered by the 95% isodose curve while at the same time not receiving (in any one point) more than a maximum dose of 107%.

While isodose curves provide essential information on regions of uniform dose, high dose (“hot spots”) or low dose (“cold spots”), they should ideally be supplemented by dose volume histograms (DVHs) for the target volume(s) and critical structures [2].

DVHs provide quantitative information on the amount of dose absorbed by a particular percentage of volume and graphically summarizes the distribution of the entire dose within any specifically defined anatomical volume of interest [2, 4].

Two forms are used to represent DVHs: the direct (or differential) DVH and the cumulative (or integral) DVH.

In the former, the volume of a given anatomical structure receiving a dose that is within a specified dose interval is plotted against the dose, while the latter plots the volume of an anatomical structure receiving a dose greater than or equal to a certain dose against the dose. The volume itself can be represented as either a percentage of the total organ volume or the actual volume (in cm^3) [2, 27].

Over the course of time, the cumulative DVH has become the preferred form used by planners, since it facilitates the identification of the total volume affected by high or low dose [27].

Figure 1.17 exemplarily shows cumulative DVHs for a PTV (a) and an OAR (b).

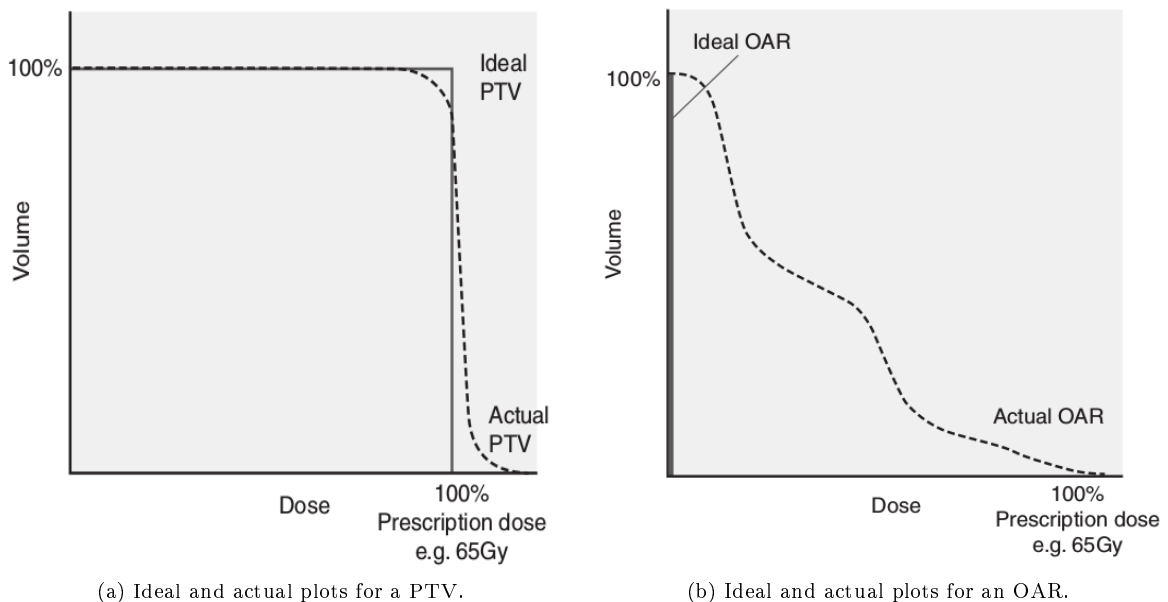


Figure 1.17: Example of DVHs [4].

Three Dimensional Conformal Radiotherapy (3D-CRT)

As can be directly inferred from the name itself, this technique heavily relies on 3D anatomic information and delivering fields that are as conformal as possible to the target volume and thus achieving the best possible compromise between maximum TCP und minimum NTCP [2].

High accuracy in the delineation process of the various target volumes and other healthy relevant structures, as well as in localizing the target volumes is of the utmost importance in 3D-CRT, considering its ultimate goal of conformity. In the end, the final treatment plan can only be as good as the individual components needed to put it together: the input patient data, image segmentation (delineation of structures in the image data), image registration, field aperture(s), dose computation, plan evaluation, plan optimization. While the advances in diagnostic imaging can vouch for high quality anatomic images, segmentation is still the most laborious and delicate process of the steps leading up to a treatment plan, mostly because of the inter-observer differences that can arise. Dose computation uses one of three types of algorithms: correction-based, model-based and direct Monte Carlo, with the latter two rapidly gaining ground over the former because of their ability to simulate the transport of radiation in three dimensions [2].

Intensity-Modulated Radiotherapy (IMRT)

Although intensity modulation had been employed prior to the actual creation of the technique named after it, this was done using wedges and compensators whose purpose was to change the beam intensity profiles in order to attain the goals of composite plans. The somewhat later emerging technique of intensity-modulated radiation therapy delivers a nonuniform fluence from any given position of the treatment beam in order to reach an optimized composite dose distribution [2].

While 3D-CRT plans are generally the result of forward planning, plans intended to be delivered via the IMRT technique are generated through inverse planning. The planner enters the treatment criteria necessary for the optimization process and the TPS then determines the optimal fluence profiles for a given set of beam directions.

Given that the linac is computer-controlled and that the fluence files are documents, the transfer can occur smoothly and the treatment machine is able to deliver the intensity-modulated beams as calculated [2].

Having said that, there is a minimum of two major systems required for the clinical implementation of IMRT:

- a TPS capable of calculating a nonuniform fluence distribution for multiple beams delivered from different angles in order to achieve maximum dose to the target volume and minimum dose to the critical normal structures;
- a delivery system (the linac) capable of delivering these nonuniform fluences as planned.

Planning involves dividing each beam into multiple beamlets for which optimum intensities/fluences or weights are determined.

The numerous computerized methods for calculating optimum intensity profiles can be of an either analytical or iterative nature, with the latter involving an optimization process called simulated annealing [2].

A component crucial for the successful delivery of IMRT plans by a linac is the multileaf collimator (MLC), since it is responsible for shaping the beam profile arbitrarily. MLCs allow IMRT delivery in three possible ways:

- using fixed gantry angles;
- using rotating fan beams (tomotherapy) and
- using rotating cone beams.

IMRT delivery for fixed gantry angles can be done using either the SMLC (segmental MLC) or the DMLC (dynamic MLC) method. The former, also called step-and-shoot, uses multiple fields to treat the patient, which have in turn been divided into subfields, delivered with uniform beam intensity levels and in a stack arrangement consecutively without the operator intervening. Its alias derives from the fact that the beam is off while the MLC leaves move on to the next subfield shape. The latter, on the other hand, moves the leaves of each leaf pair simultaneously and unidirectionally while the accelerator beam is on although the leaf velocity also differs within each leaf pair. The

variation of intensity over different points of the field is achieved by the movement of a momentarily open aperture between leaves [2].

The use of rotating fan beams is not limited to diagnostic purposes. The megavoltage version of these beams is used to treat patients slice by slice, hence the name “tomotherapy”. Intensity modulated beams (IMBs) are generated by a special collimator while the gantry rotates around the longitudinal axis of the patient and the couch is moved either one to two slices at a time or continuously, much like in a helical CT [2].

Two IMRT techniques use rotating cone beams: intensity-modulated arc therapy (IMAT) and volumetric modulated arc therapy (VMAT). Since the latter has been employed throughout the course of the work on which this thesis is based, it will be addressed separately later on.

IMAT combines step-and-shoot with DMLC: the intensity modulation sought after is achieved by superimposing the uniform intensities of the subfields which were created by the MLC along the arc of gantry rotation; the MLC moves dynamically and the beam is permanently on.

Because of the inability to deliver single treatment fields in one arc, the IMAT delivery technique proved inefficient and since no substantial improvements over other IMRT techniques could be observed, the use of IMAT remained limited [2].

Volumetric Modulated Arc Therapy (VMAT)

Though IMAT proved to be of little popularity, the idea of using rotating cone beams was not entirely given up. In IMAT, the linac dose rate stays constant over the entire motion of the gantry in an arc, even though the treatment field changes with the gantry angle. The idea of using beam intensities that also varied with gantry angles soon emerged and resulted in isodose distributions superior to those produced by gantry-static IMRT. A new technique was born, involving the delivery of rotational cone beams of variable shapes and intensities; it was given the name volumetric modulated arc therapy (VMAT). The name is also used to describe any technique combining arc therapy and variable dose rates [2].

VMAT uses a continuous motion of the gantry, all the while varying the dose rate and the shape of the treatment field (through the MLC leaves) throughout the arc. The dose is computed by sampling the delivery at a preferably high number of discrete gantry angles, which makes the velocity of MLC leaves the limiting factor. The number of samples is restricted by how fast the leaves can move to the next position within the time required to reach the new gantry angle. A solution developed by Otto, called progressive sampling is now being used to optimize VMAT delivery. It starts out by dividing the arc into a limited number of gantry angle samples and the first few iterations focus on varying the intensities and/or shapes of the respective beams. As the number of iterations continues to increase, new arc samples are added progressively in between already existing samples, with shapes interpolated between the shapes of the neighboring samples.

The most compelling argument proving VMAT efficiency is the considerable reduction of delivery time and monitor units (MUs), when compared to conventional IMRT. This is important in radiation therapy because a shorter delivery time minimizes patient motion and therefore errors due to patient motion [2].

Fallback Planning (FB)

The concept of automated fallback planning is relatively new and is still being tested in the scientific community. It is therefore not established as a universal technical term and certainly not a standard planning tool, as of yet. The work done for the present thesis comprises some use of the automated fallback planning module, which explains the necessity of its inclusion in the introductory section of this thesis.

Fallback planning is exclusively available in RayStation (the treatment planning system developed by RaySearch Laboratories AB, Stockholm, Sweden) and is an automated planning tool with the purpose of enabling the automatic generation of additional treatment plans that are to be used in contingency situations.

This means that in the eventuality of e.g. the original treatment machine becoming temporarily unavailable (due to reasons such as malfunctions, service slots or power outage), the patient would

be able to not interrupt the prescribed treatment (which is extremely important for fast-growing tumor cases) but instead be treated on a different machine, possibly even with a different modality and/or treatment technique [28].

Fallback planning converts plans, even proton or TomoTherapy plans, into photon plans using the 3D-CRT, SMLC and/or VMAT treatment techniques. This is done by a dose mimicking function that replicates the dose volume histograms (DVHs) of an indicated plan using a different machine or treatment technique and if the plan evaluation and comparison to the original plan in terms of dose statistics, dose differences, fulfillment of clinical goals and of course DVH curves is satisfactory, it can be approved for delivery. There is also the option of additional optimization, should the experienced planner think further improvements can be achieved. Since Fallback plans are intended for use in contingency situations, it is also possible to convert them back to their original plans, yet taking into consideration the dose that has been delivered inbetween with a different modality and/or technique.

The main advantage advertised by the creators of Fallback planning is the drastic reduction of planning time in emergency situations, where time is of the essence [28].

1.4.6 Gamma-Index Analysis

The concept of γ -index analysis as introduced by Low et al. in [29] will hereby be explained, since it has been widely used throughout this thesis.

In order to be able to quantitatively assess the differences between measured and computed doses and thus determine the quality of dose distribution calculations, the γ -index analysis proposes to simultaneously use the concepts of dose difference (DD) and distance-to-agreement (DTA), which have previously been used separately. Dose differences are generally used in regions of low dose gradients, where doses can be compared directly and have to be within a predetermined tolerance given as a percentage of either a reference dose point or an average over a relevant region. Typical DD criteria used clinically are 2% and 3%.

For regions of high dose gradients, it is recommended to use the distance-to-agreement, defined as the minimal distance between a measured data point and a point exhibiting the same dose value in the calculated data. DTA criteria of 2 mm and 3 mm are typically being used to establish the quality of clinically used dose distributions.

To perform a GPR-analysis, the following formula is required:

$$\Gamma(\vec{r}_m, \vec{r}_c) = \sqrt{\frac{r^2(\vec{r}_m, \vec{r}_c)}{\Delta d_M^2} + \frac{\delta^2(\vec{r}_m, \vec{r}_c)}{\Delta D_M^2}}, \quad (1.25)$$

$$r(\vec{r}_m, \vec{r}_c) = |\vec{r}_m, \vec{r}_c| \quad \delta(\vec{r}_m, \vec{r}_c) = D_c(\vec{r}_c) - D_m(\vec{r}_m) \quad , \quad (1.26)$$

where \vec{r}_m and \vec{r}_c represent the locations of a measured and a calculation point, respectively, $\delta(\vec{r}_m, \vec{r}_c)$ gives the difference between the calculated $D_c(\vec{r}_c)$ and the measured $D_m(\vec{r}_m)$ dose, Δd_M and ΔD_M are the DTA criterion and the DD criterion, respectively.

A quality index γ can now be defined as:

$$\gamma(\vec{r}_m) = \min[\Gamma(\vec{r}_m, \vec{r}_c)] \quad \forall \vec{r}_c \quad , \quad (1.27)$$

which also defines new pass/fail criteria:

$$\begin{cases} \gamma(\vec{r}_m) \leq 1, & \text{calculation passes} \\ \gamma(\vec{r}_m) > 1, & \text{calculation fails.} \end{cases} \quad (1.28)$$

Ultimately, the gamma passing rate (GPR) is nothing more than the percentage of points for which the calculation passes the acceptance criteria.

The acceptance criteria can also be visualized as spanning the surface of an ellipsoid in which case the calculated dose passes at \vec{r}_m if its surface $D_c(\vec{r}_c)$ intersects with the ellipsoid's surface.

A faster version of the γ -index calculation was made possible through an optimized search algorithm introduced in [30]. The algorithm is an iterative process that starts by defining several regions of interest (ROIs) around each point of interest. ROI 1 in the calculated dose matrix has the exact same spatial coordinates as the corresponding point in the measured dose matrix, ROI 2 contains neighboring pixel values to ROI 1, ROI 3 contains pixel values in the vicinity of ROI 2 etc. The γ -index is first calculated for ROI 1, then for a point in ROI 2 at a minimal distance to ROI 1. If the γ -index for the point in ROI 2 is smaller than the one calculated for ROI 1, γ -values for ROI 2 are further calculated and a minimum for ROI 1 and ROI 2 is sought after. This minimum is then compared to a γ -value calculated for a point in ROI 3 at a minimal distance to ROI 1 and so on, until the overall minimum γ -index is found. The γ -value is always calculated based on the DTA criterion only, i.e. by neglecting the possible dose difference. In addition to the advantage in calculation speed, the algorithm is also capable of calculating and displaying the γ -angle, which holds information on the parameter that mostly influences the γ -value.

1.5 Literature on Beam Commissioning

The purpose of beam commissioning is to virtually/digitally recreate the beam characteristics of the treatment machine with the software intended for the treatment planning process so as to ultimately enable dose calculations and therefore planning radiation treatments which will be delivered by the respective machine.

This translates to the fact that every radiation treatment facility has to undergo beam commissioning at one point, for every combination of treatment machines and treatment planning systems available in the respective facility. Since there are several treatment machine manufacturers/vendors and providers of treatment planning software, this leads to multiple possible combinations of machine and TPS, which in turn amounts to a vast pool of available literature. While it is unlikely to encounter the exact same combination of treatment unit and treatment planning software in publications, partly also due to the fact that the Versa HD linac with an Elekta Agility MLC (Elekta AB, Crawley, West Sussex, UK) is among the newest treatment machines available, a recommendable approach would be to look at publications dealing with Versa HD beam commissioning with arbitrary TPSs, at those reporting on beam commissioning performed with RayStation and those simply focusing on commissioning of flattened and unflattened beams with TPSs whose dose calculation algorithm is the same as the one used in this thesis, the collapsed cone algorithm.

Not only the same treatment machine model, but the exact same machine, whose beam models were created for this thesis, was the object of a project thesis performed by a student of the Vienna University of Technology [31]. Therein only the 6 MV FF and 6 MV FFF beam models were verified and validated, both created in iPlan (Brainlab, Feldkirchen, Germany) and showing satisfactory results.

Elekta's Versa HD with the Agility MLC has recently been reported to have been commissioned with RayStation by [22], albeit only for its FFF beams of 6 MV and 10 MV. The models are subsequently compared with models obtained with a Monte Carlo-based TPS, Monaco 5.0.

Another case where the beams of a Versa HD linac with an Agility MLC have been commissioned, but with the Pinnacle³ v9.8 (Philips Radiation Oncology Systems, Fitchburg, WI) TPS can be found in [32]. In this case the beams modeled were indeed 6 MV FF, 10 MV FF, 6 MV FFF and 10 MV FFF as well as an additional 18 MV FF beam and electron beams for four available energies. Point dose verification and treatment-delivery verification were also performed, the latter making use of IMRT QA plans and yielding an average GPR of > 99.5% with the same pass-fail criteria that were applied for the present thesis.

Pinnacle³ was also used in [33] to model the Agility MLC and was found to accurately do so. The study also used their beam model to assess the VMAT performance of the Agility MLC.

Beam modeling with RayStation has been reported in [34, 35, 36, 37]. In [34] only the MLC model for a Varian Trilogy linac equipped with a Millennium 120 MLC was optimized using RayStation (v.4.5) and its quality then verified with both global and local GPRs staying above 90% for all plan

types. A comparison of RayStation with other more established TPSs is undertaken in [35, 36, 37]. The first two compare RayStation (v3.5) with Pinnacle (v.9.2) in its ability to model Elekta's Agility MLC and MLCi and the third compares RayStation (v2.4.13) with Pinnacle (v9.0) and Eclipse (v10.0) (Varian Medical Systems) as they model the 6 MV FF photon beam of a Varian TrueBeam equipped with the Millennium 120 MLC.

The capabilities of the collapsed cone convolution (CCC) algorithm regarding dose calculations were weighed against those of a Monte Carlo code, BEAM, in [38]. The study also involved commissioning the Monte-Carlo code for a 6 MV FF beam and showed no significant discrepancies between the two for common 3D radiation therapy treatments.

In [39] the collapsed cone convolution algorithm was implemented in a TPS to perform dose calculations for 6 MV FF and 15 MV FF beam models, whose calculated PDDs and lateral dose profiles were compared to measured curves and proven to be acceptable for clinical purposes. The use of the CCC algorithm for commissioning, verification and clinical use of flattening filter free beams was first reported in [40] and was compared to Monte Carlo calculations and other reported measurements. The study proved the CCC algorithm to be perfectly capable of adequately modeling FFF beams.

2 Materials and Methods

Beam commissioning is not limited to the creation of a beam model. It also consists in the verification of its quality and agreement with the actual beam(s) it is intended to model. This entire process has been the object of this thesis and shall hereby be documented by going through each of the abovementioned stages separately and giving an account of the materials and methods used in the respective stage.

2.1 Beam Model Creation

2.1.1 Methods

The instructions in the RayPhysics Manual [20, chapter 6] were followed for the creation of the open beam models, which will be compactly covered here. The interested reader is therefore referred to [20] for a detailed look at the steps of the procedure.

RayPhysics contains a list called machine tree view of all treatment machines whose models have been introduced into the application. These can be either commissioned, uncommissioned, template machines (generic models provided by the developer of the TPS) or deprecated machines.

The first step was to choose a template machine as similar as possible to the machine that was to be commissioned and copy it so that the copied machine would appear in the section of the uncommissioned machines, which, unsurprisingly, could be edited. In order to commission beams of the same beam qualities, i.e. in this case 6 MV and 10 MV, both in flattening filter and flattening filter free mode for the same physical machine, two virtual machines were created, one of which would later contain the FFF beam models.

Editing is allowed when entering edit mode for the newly copied machine, which allows to first change the machine's name to better distinguish it from the template machine it was duplicated after or to simplify communication between different pieces of equipment. If need be, the static machine properties and optimization parameters will be edited to make the virtual machine as similar as possible to the actual machine. There are ten tabs containing the different machine properties of the machine, each tab covering properties pertaining to the same category. Since the open beam model (i.e. without a beam modifier in the beam path) was commissioned, some of these tabs are irrelevant, i.e. the blocks tab, the wedges tab and the cone tab. The machine properties which were entered for the Versa HD linac can be found in the Appendix, sections A.1 and A.2.

Next, the right beam qualities were created and any existing measured curves (part of the basic beam data) deleted in preparation of the following step: importing the correct basic beam data for the respective machine.

According to the RayStation Beam Commissioning Data Specification [41], the following data is required for photon beam commissioning:

- depth dose curves on the CAX (PDDs)
- lateral profiles (crossplane and/or inplane)
- output factors
- absolute dose calibration point for the reference field size (in this case 10 cm × 10 cm).

Lateral profiles can only be added if there is a corresponding PDD for the respective field size. While it is not required to import both cross- and inplane profiles, doing so might improve the quality of the beam models and is therefore recommended. The same applies for the field sizes: theoretically only the reference field size is absolutely necessary, with all other field sizes considered optional; however, it is important to import measured curves for all clinically relevant field sizes [41]. The beam model was therefore created for 14 square fields with a side length of 1, 2, 3, 4, 5, 6, 7, 8, 10, 14, 15, 20, 30 and 40 cm and 2 rectangular fields of 5 cm × 30 cm and 30 cm × 5 cm.

The lateral profiles at the following depths are recommended [41]: d_{\max} , 5 cm, 10 cm and 20 cm. Compliance with this recommendation was mostly upheld, although for some field sizes only 3 of these depths were available and in other cases measurements at additional depths (1.5 cm and 30 cm) were also provided.

The output factors for every field size need to be provided at curve import, with the reference field size having an output factor of 1, measured at a depth where electron contamination is no longer an issue, i.e. at 10 cm.

The dose per monitor unit (MU) is provided by the absolute dose calibration which is to be measured at a defined reference point for the reference field size and should ideally also be a depth point where electron contamination should no longer prevail (10 cm). It is imperative that the SSD used for absolute dose calibration (90 cm) be the same as that used in the dose curves and the output factors. The absolute dose was calibrated so that $0.01 \text{ Gy} \triangleq 1 \text{ MU}$. The entered resolution was 0.2 cm.

The open field curves mentioned above can only be imported after having entered the information on absolute dose calibration point. During the import process, one is prompted to enter the measurement conditions for each imported curve: the detector height and width, what type of collimation was used (both MLC and jaw) and the size of the water phantom (assuming a cubic form, which means that only the side length is needed). The output factors are also entered at this point, although not per curve, but per field size. The dimensions of the detectors refer strictly to the active volumes of said instruments and were taken from [42] for the detectors mentioned in section 2.1.2.

In a consecutive step, the model was normalized and as a consequence the dose in the reference point for the reference field size became equal for both measured and computed curves.

The last step entailed working on the beam model parameters in order to bring all computed curves in agreement with the measured ones. This was done by using auto-modeling steps and/or manual tuning. Only part of the beam model parameters were included in the auto-modeling process, meaning some were only manually tuned, which made every information on the physical machine extremely valuable.

The beam model parameters for photons can be found under four tabs, since the machine has been configured without cones, which lead to the automatic elimination of the fifth possible tab, the cone factor corrections. The four major tabs are: energy spectrum, fluence, off axis and output factor corrections.

The fluence tab parameters do influence the dose computation process. Some of these, i.e. distances to source and transmissions were manually entered according to the specifications given by the hardware manufacturer. Only two auto-modeling steps exist and were used for parameters in the fluence tab: the primary source step and the flattening filter source step. The former affects the widths of the primary source (x and y), which in turn change the penumbra region of lateral profiles and the latter affects the width and weight of the flattening filter source, whose effect is reflected over the entire lateral profile [20].

The energy spectrum tab contains two additional sub-tabs: the photons sub-tab and the electron contamination sub-tab. The two are covered by four auto-modeling steps and influence the dose computation with respect to depth, i.e. the depth-dose curves. As explained in section 1.4.3, contamination electrons influence the build-up region of the PDD, which is why they are at first switched off; the fall-off region is influenced by the photon energy spectrum on the central axis, given by mono-energetic contributions which, combined, yield a poly-energetic energy spectrum [20].

The off-axis tab deals with off-axis softening and beam profile correction, meaning it affects the lateral profiles of the beam. Off-axis softening is used to obtain agreement between measured and computed profiles over the entire depth range. It models the change caused by the flattening filter in the off-axis energy spectrum, which is correlated with the energy spectrum at radius zero. Consequently, all entries in the off-axis softening table of the FFF beam models were set to zero. Beam profile correction can create either a dip or an increase in the fluence intensity at small radii

in addition to creating fall-off at the corners [20]. Though there are auto-modeling steps for each of these parameters, which were made use of, in the end manual fine tuning was resorted to.

The output factor correction tab contains a table of correction factors that are applied to the output factors per field measure. Output factor corrections are performed in order to account for backscattering into the monitor chamber and model imperfections. It is recommended to run the output factor correction auto-modeling step often, however, manual tuning was preferred in the final steps since only minor disagreements between measured and computed model remained [20].

The RayPhysics application has an in-built fit quality calculator in order to assist during the commissioning process, i.e. to provide a guideline. RayPhysics calculates the symmetry, penumbra width and flatness for the entered measured profiles and the fit quality then assesses the agreement between the measured and computed curves as root mean square (RMS) difference. The fit quality is given for the build-up and fall-off regions (for the PDDs) and the in-field, out-of-field and penumbra regions (for the lateral profiles), respectively. If the RMS differences were within the respective tolerances (i.e. 10% for the build-up and penumbra regions, 2% for the fall-off and 3% for the in-field and out-of-field regions), or only slightly exceeded these tolerances and for a minority of cases within the PDDs and profiles, the beam parameters were no longer altered.

The final values for the photon beam model parameters of all four models (6 MV FF, 10 MV FF, 6 MV FFF and 10 MV FFF) can be found in Appendix A.1 and A.2.

2.1.2 Materials

The beams to be commissioned are produced by a Versa HD linear accelerator (Elekta AB, Stockholm, Sweden) equipped with an Elekta Agility MLC (Elekta, Crawley, West-Sussex, UK). The Versa HD linac is able to produce photon beams of 6, 10 and 18 MV and additionally beams of 6 MV and 10 MV in FFF mode. The Agility MLC contains a total of 160 leaves (80 pairs) each of a nominal width of 5 mm projected at the isocenter, capable of moving at a maximum leaf speed of 3.5 cm/s in x (crossline)-direction.

The RayStation system (RaySearch Laboratories AB, Stockholm, Sweden) includes a beam commissioning application called RayPhysics, enabling additional activities such as CT commissioning and beam 3D modeling. RayPhysics version 4.99.1.3 was used to create the beam models of the 6 MV and 10 MV flattened (FF) and unflattened (FFF) beams. The algorithm used by RayPhysics for dose computation is the collapsed cone algorithm version 3.2.

The basic beam data was measured by the staff of the Division of Medical Radiation Physics, Department of Radiation Oncology of the General Hospital in Vienna (AKH Wien) prior to the work related to the present thesis. The measurements were performed on a water-phantom using the following PTW (Freiburg, Germany) instruments: the MP3 water tank, Semiflex ionization chambers of 0.125 cm^3 for field sizes above $3\text{ cm} \times 3\text{ cm}$ and DiodeE, DiodeP and microDiamond detectors for field sizes of $3\text{ cm} \times 3\text{ cm}$ and smaller.

2.2 Independent Verification of the Beam Model

2.2.1 Materials

An in-house developed MATLAB code was used to perform a one-dimensional gamma passing rate (GPR) analysis with the criteria of 2 mm distance-to-agreement (DTA) and 2% dose deviation (DD).

The input for the MATLAB program is made up of the same basic beam data used as input for the beam model creation - in the form of Mephysto (.mcc) files - and of DICOM (.dcm) files of computed dose distributions in virtual versions of a $30\text{ cm} \times 30\text{ cm} \times 30\text{ cm}$ water phantom and a $50\text{ cm} \times 50\text{ cm} \times 50\text{ cm}$ water phantom at an SSD of 90 cm (or an SAD of 100 cm). The Beam 3D Modeling module within the RayPhysics 4.99.1.3 application was used for this purpose, since it allows using uncommissioned machine for dose computation.

Measurements performed with a PTW Farmer 30013 chamber (PTW, Freiburg, Germany) at various points of depth along the CAX and for all commissioned field sizes and SSDs ranging from 80 cm to 100 cm were also used to perform individual point dose comparisons of measured and computed values. The same application was used to yield the computed point dose values as for the MATLAB verification step. The point doses for every field size at a depth of 10 cm were additionally used to calculate the output factors, which were then compared to their respective measured values.

2.2.2 Methods

In order to independently verify the newly created model, the setup used for the measurement of the basic beam data was recreated virtually, allowing for direct comparison between measured and computed values.

Digital versions of a $30\text{ cm} \times 30\text{ cm} \times 30\text{ cm}$ and a $50\text{ cm} \times 50\text{ cm} \times 50\text{ cm}$ water phantom were imported into RayPhysics and the commissioned beam models for all beam qualities in both flattened and unflattened mode were used to compute spatial dose distributions on the phantoms, using a dose grid resolution of $0.2\text{ cm}/\text{voxel}$. An example of such a computation can be seen in Figure 2.1.

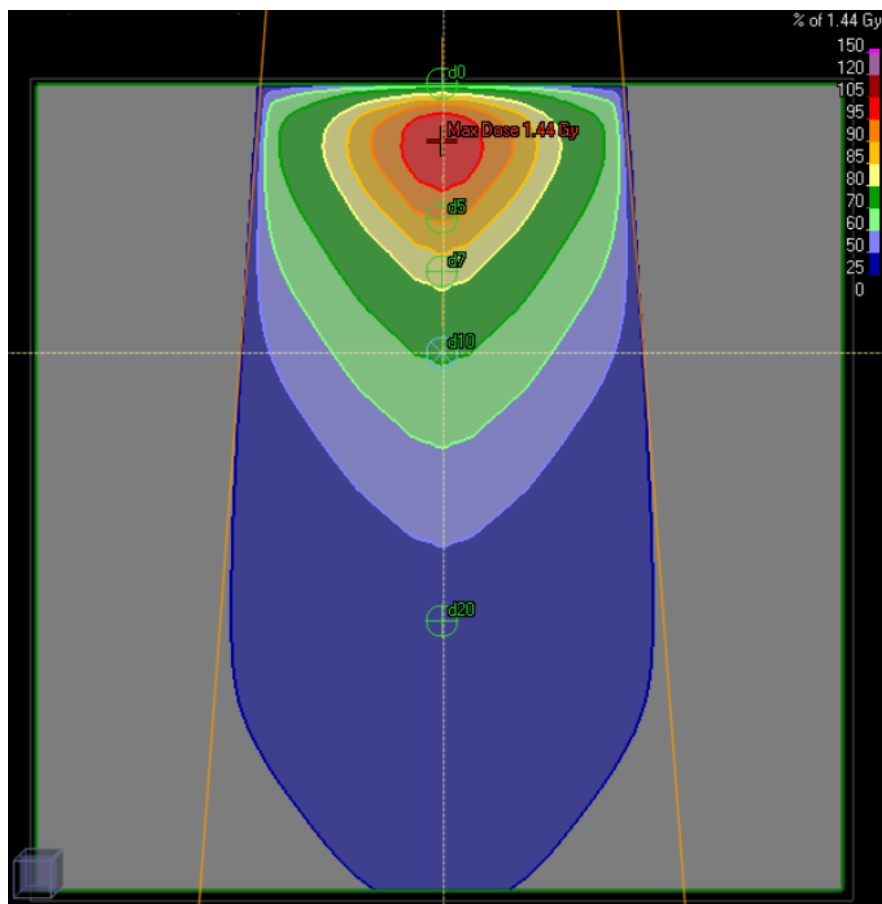


Figure 2.1: Final dose computation in RayPhysics on a $30\text{ cm} \times 30\text{ cm} \times 30\text{ cm}$ water phantom with a beam of field size $15\text{ cm} \times 15\text{ cm}$ using the 10 MV FFF beam model.

The smaller phantom was used for time-saving reasons, since the final dose computation was notably more time-consuming on the $50\text{ cm} \times 50\text{ cm} \times 50\text{ cm}$ digital water phantom. The larger phantom was therefore used for field sizes starting with $10\text{ cm} \times 10\text{ cm}$ and all other field sizes where the profile measurement was performed at higher depths, e.g. 30 cm, which would correspond to the

distal side of the 30 cm \times 30 cm \times 30 cm digital water phantom (in beam's eye view). The thus calculated dose distributions were exported as DICOM files, a file format accepted by the MATLAB program.

The MATLAB code is designed to read both the .mcc measured files and the DICOM files and to plot PDDs and lateral profiles corresponding to the available measurements from the spatial dose distribution provided in the DICOM files. A plot always contains a curve based on measurements and a curve emerging from calculations using the new beam model. In addition, the code also provides a plot of the spatial distribution of γ -values alongside a mean γ -value for the entire curve at hand and the actual GPR. The criteria chosen for the γ -index analysis were 2 mm distance-to-agreement and 2% dose deviation.

Figure 2.2 serves to demonstrate the output delivered by the MATLAB code.

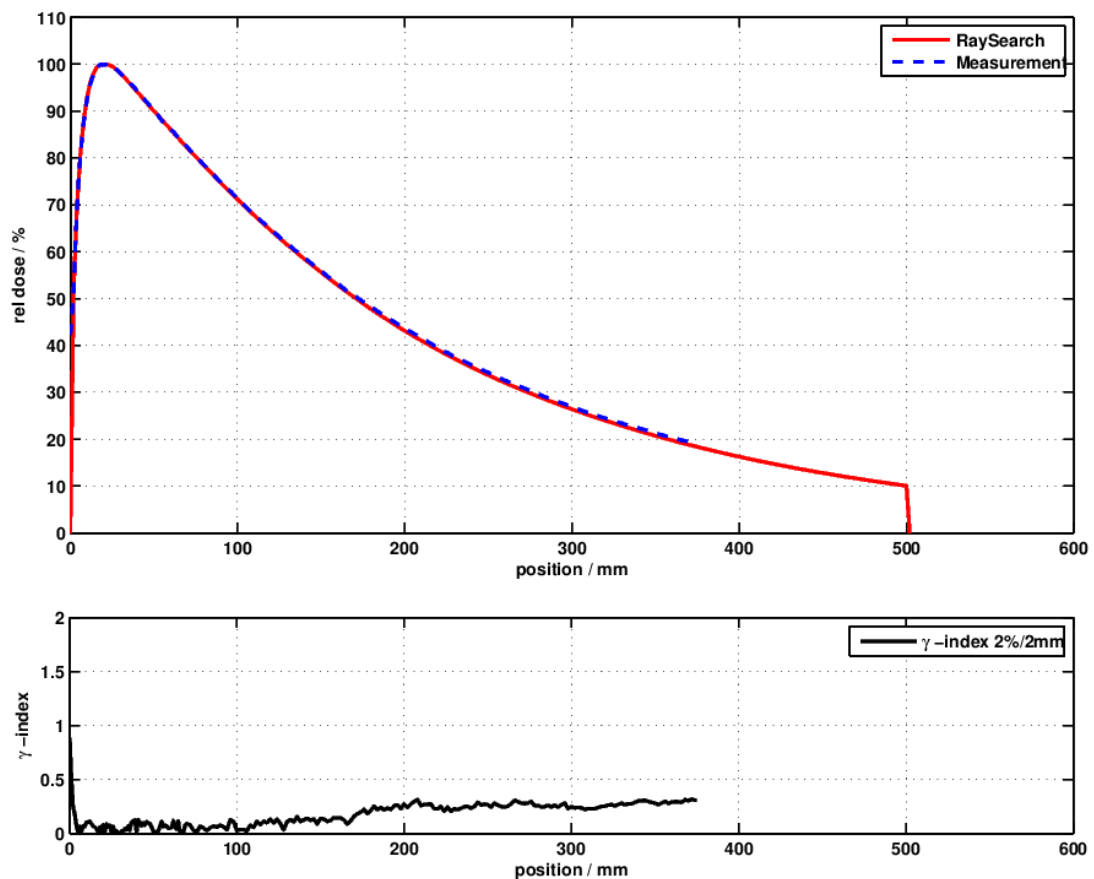


Figure 2.2: Computed and measured PDD curve for a 10 MV FF beam of field size 15 cm \times 15 cm and spatial distribution of γ -values as provided by the MATLAB code.

These computations were not only used as input for the MATLAB code but also to extract point doses at different points along the CAX in order to compare with measurements for various field sizes. Similar computations but with different SSDs were performed in order to perform the same comparative task. Finally, the output factors were calculated using the computed dose at a depth of 10 cm for all field sizes with a constant number of 100 MUs; the newly calculated output factors were compared to the ones resulting from the measurements.

2.3 Treatment-Delivery Verification

2.3.1 Materials

A patient cohort of ten patients having been diagnosed with low risk (LR) prostate carcinoma and two suffering from high risk (HR) prostate carcinoma was used for the second verification method. To this end the RayStation application within the RayStation system was used for creating clinically acceptable photon plans and to create quality assurance (QA) plans based on the original plans.

The Versa HD linear accelerator at the General Hospital of Vienna (AKH Wien/Medical University of Vienna) was then used to deliver the quality assurance plans to a Delta⁴ phantom (ScandiDos AB, Uppsala, Sweden), whose software program enabled a local GPR analysis (with acceptance criteria of 3% DD/3 mm DTA) of planned and measured doses. The measurement setup, showing the two main components, the Versa HD linear accelerator and the Delta⁴ phantom, is depicted in Figure 2.3.

The Delta⁴ phantom is a two-dimensional detector array commonly used in treatment QA measurements.

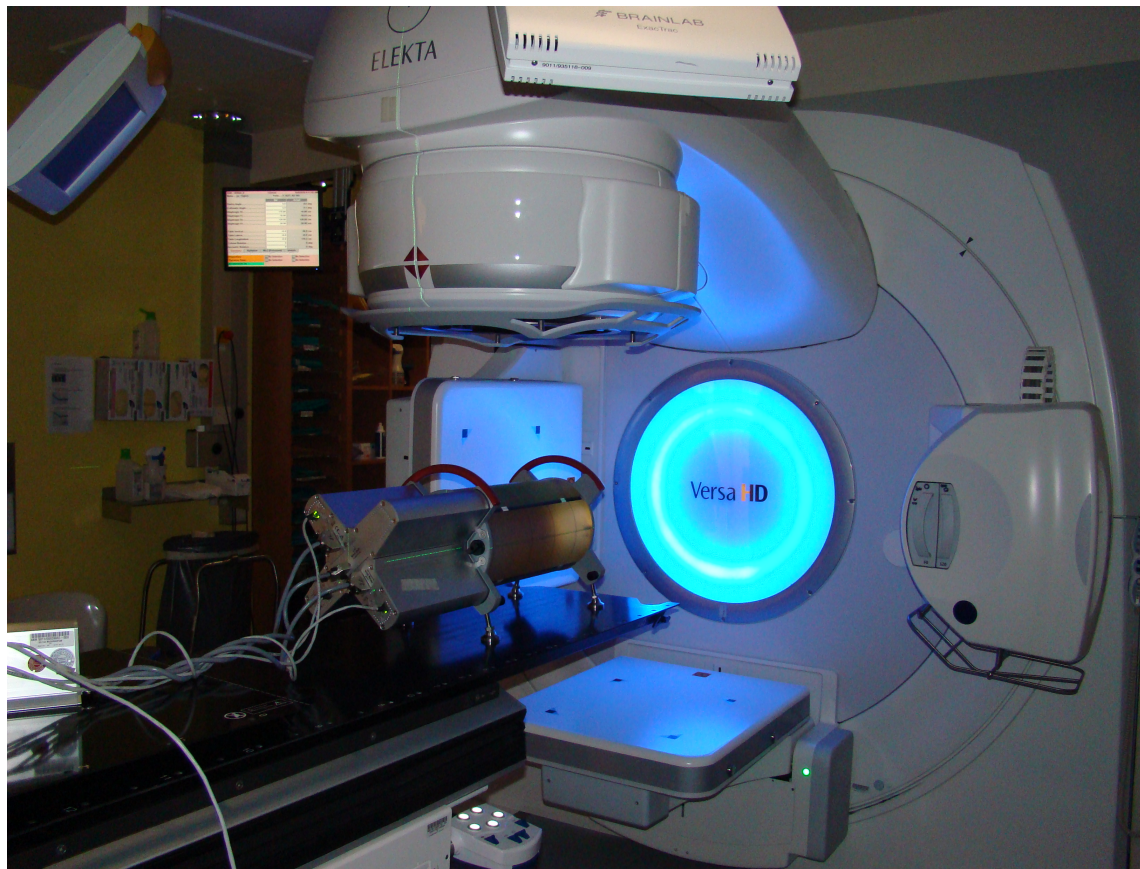


Figure 2.3: Setup for QA plan irradiation at the AKH Vienna: the Versa HD linac and the Delta⁴ phantom.

2.3.2 Methods

To verify the performance of the new beam models in clinically-similar situations, a treatment-delivery verification was undergone.

This was achieved by using the models to create treatment plans for actual clinical cases. The treatment modality was therefore photons, the treatment technique was VMAT. Plans were created both manually (termed mVMAT plans in the present thesis) and using the Fallback planning module available in RayStation. Information on the plan creation process can be found in the next section (2.4). The Fallback plans (hereafter denoted by FB) and the mVMAT plans for the HR and LR patients with the 10 MV FF beam model were created in cooperation with bachelor student Florine Enengl from the Vienna University of Technology (TU Wien).

Five plan types were created for all ten LR patients: 10 MV FF mVMAT, 10 MV FF FB, 6 MV FF mVMAT, 10 MV FFF mVMAT and 6 MV FFF mVMAT. An additional 6 MV FF FB plan was created for only four LR patients, of which only three were actually delivered. No FB plans were created for the FFF models, in order to speed up the process, which was delayed as it is due to the additional phantom calibration and machine settings required for measurements in FFF mode.

Only the 6 MV FF beam model was used for the HR patients, leading to the creation of an mVMAT and an FB plan per patient.

Overall a total of 53 LR and 4 HR plans (i.e. 57 plans altogether) were created and delivered to the Delta⁴ phantom for treatment-delivery verification.

The VMAT plans for the LR patient cohort used a single arc starting at 210° and ending at 150°, whereas the HR plans consisted of two full arcs, one from 180.1° to 180.0° going clockwise and a second going counter clockwise between the same angles.

Once created, the clinically acceptable treatment plans were recalculated on a digital Delta⁴ phantom in the QA Preparation tab of the RayStation photon planning application, thus yielding QA plans. Figure 2.4 shows an example of isodose distribution calculated for such a QA plan, i.e. on the digital Delta⁴ phantom. The plan that was converted to a QA plan was an mVMAT plan created with the 10 MV FF beam model on patient 10 from the LR PC group. The subfigures represent the different possible perspectives in RayStation: transversal, coronal and sagittal.

The digital phantom was set to have a mass density of 1.178 g/cm³ for 6 MV and 1.165 g/cm³ for 10 MV beams. These QA plans were exported along with their respective calculated doses as DICOM files and used to deliver photon beams to the actual Delta⁴ phantom. Having both the planned and the measured dose, the software of the phantom could perform a local GPR analysis, using pass/fail criteria of 3 mm DTA and 3% DD (local).

In the end, the best and worst plan for each beam model were selected according to their GPR-values and recalculated as QA plans on a Delta⁴-phantom whose mass density was overwritten with a universal value of 1.19 g/cm³. Adding the new planned dose to the already present measurements yielded new values for the median dose deviation and local GPR. This was done in order to verify whether the results were energy-dependent.

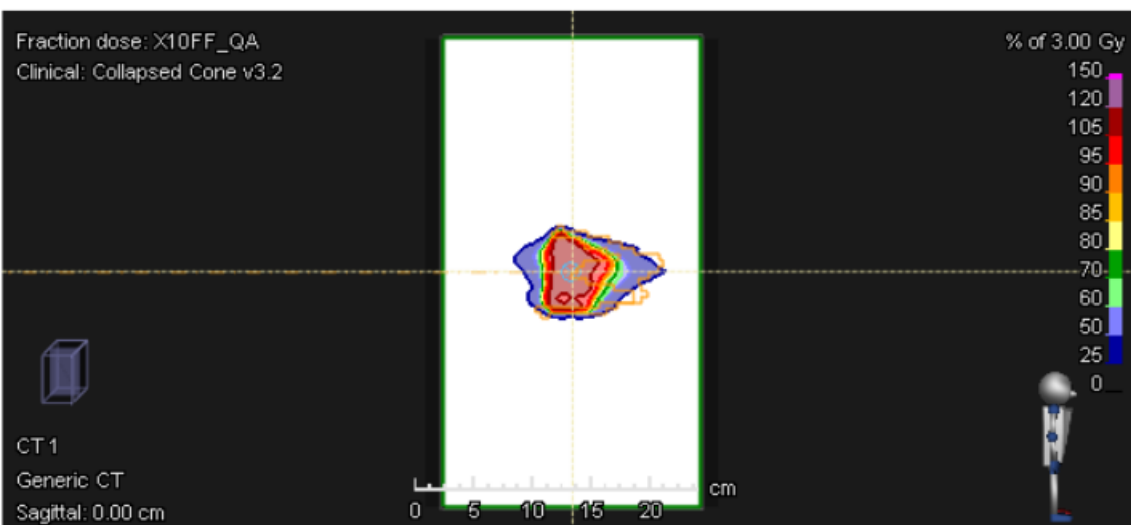
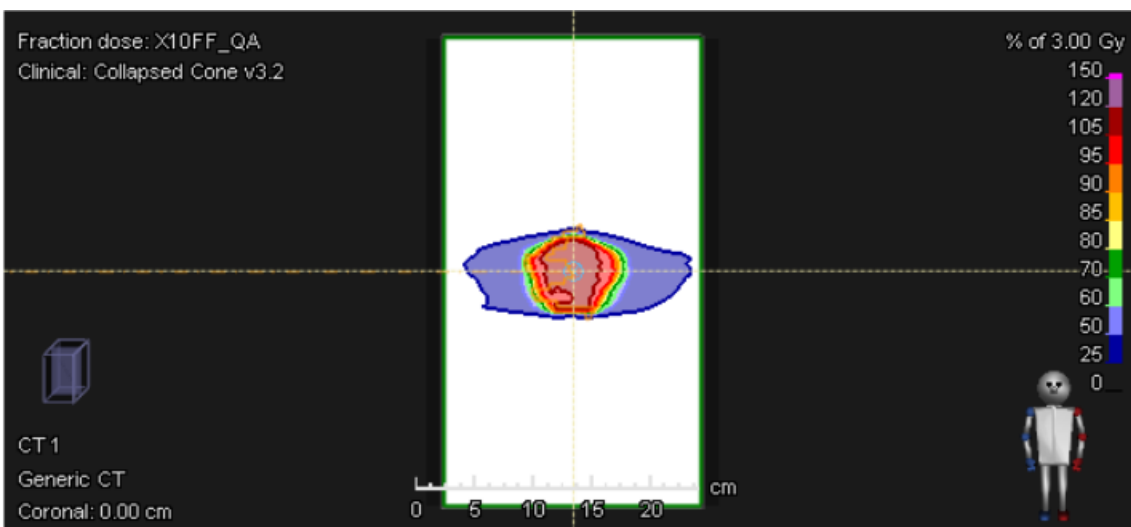
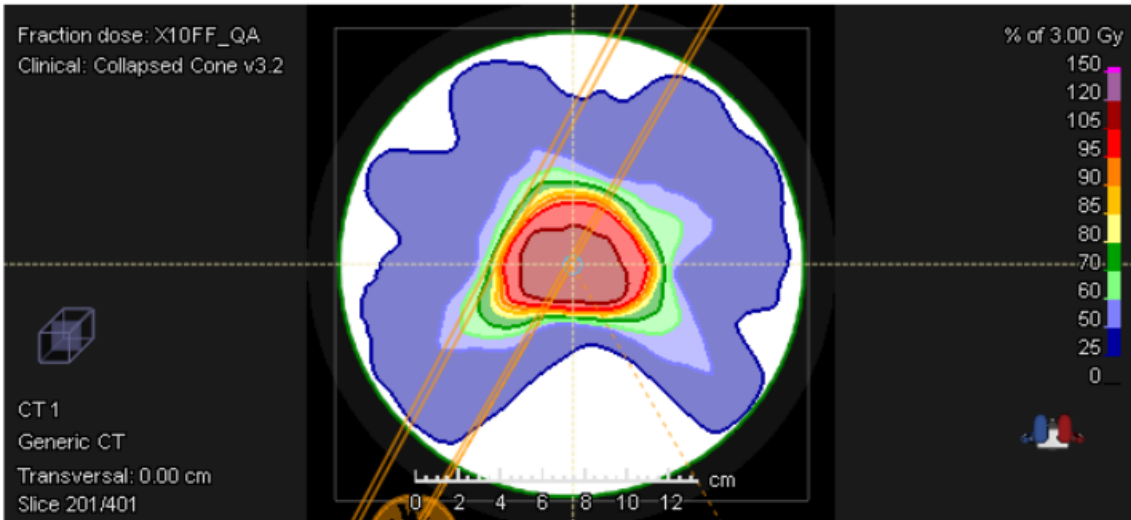


Figure 2.4: Example of isodose distribution of a 10 MV FF QA plan, calculated for a patient from the LR contingent.

2.4 FB vs. mVMAT Plan Comparison

The verification of the new beam models using QA plans was a good opportunity to compare the VMAT plans generated automatically from clinically acceptable proton plans with the VMAT plans created manually, following the normal beam geometry creation and subsequent optimization procedure. After plan delivery, the median dose deviation (in %) and the local GPR (in %) was noted for every plan, making it possible to create average values and standard deviations not only per beam quality and indication but also per plan type, thus yielding a direct comparison between the quality of mVMAT and FB plans.

The indications covered by both plan types were LR and HR prostate carcinoma, for which a median dose of 63.0 Gy was prescribed. All LR plans used a single 300°-arc, going from 210° to 150° in a clockwise rotation, whereas HR plans used two full arcs, of which the first went clockwise from 180.1° to 180.0° and the second retraced the same arc in counter clockwise rotation.

Both plan types were created in RayStation photon planning version 4.99.1.3, yet the FB plans were created using the Fallback Planning Module additionally (and exclusively) available in RayStation and the beam geometry of the finished mVMAT plans since the two types were still using the same treatment modality (i.e. photons) and technique (i.e. VMAT). The dose distribution of proton plans, however, was mimicked in order to obtain the FB plans. This is only one possibility of dose mimicking offered by the RaySearch's Fallback Planning Module, as previously explained in section 1.4.5. Fallback planning only offers limited settings, e.g. the Target vs. OAR Ratio, which was set at 0.1 and Voxel Dose Priority, whose value was set at 0.0. Maximum delivery time and gantry spacing were set to the same values entered for mVMAT plans, 90 seconds and 4.0°, respectively and the options of segment shapes optimization and segment MU optimization were checked.

2.5 Beam Model Comparison

2.5.1 Materials

Part of the results of the treatment-delivery verification were used for the beam model comparison. The remaining measurements enabling the comparison were performed with a Varian Clinac120 linear accelerator (Varian Medical Systems, Palo Alto, California, USA) at the state hospital (LKH) in Wiener Neustadt, Lower Austria.

The beam model of this particular Varian treatment machine was used for comparison since it is at the LKH Wr. Neustadt that patients will be temporarily treated with photons in case of a synchrotron breakdown at MedAustron. For this purpose, it is important to be assured of the high quality of the beam model. Given that the beam model itself is not a custom model but a generic one, i.e. it is a basic model meant to fit treatment machines of one particular machine class, its quality had to be tested.

The generic model of the Varian Clinac120 available in RayStation was created by N. Zagler, O. Hentschel and G. Kragl by entering all the machine properties corresponding to the actual machine(s), the calibration information and importing only the PDD for the reference field size of 10 cm × 10 cm along with the respective output factor and the measurement conditions. No further work was done on the model, i.e. the computed PDD corresponding to the imported one was not auto-modeled or manually tuned to fit the measured curve.

The exact same setup was used for the measurements in Wiener Neustadt (with the exception of the type of linac, of course), with the local GPR analysis again being executed by the software program of the Delta⁴phantom, with the same pass/fail criteria of 3 mm DTA and 3% local DD. Once again RayStation was used to first create clinical plans with the generic Clinac120 beam model available, which were later used to create their corresponding QA plans. Since the beam model available in RayStation only contained one beam quality, 6 MV, in FF mode, comparison was only possible for one of the four created beam models. The treatment modality was again photons, the treatment technique VMAT of the same two types: mVMAT and FB. Three of the LR patients and the same two HR patients were used for the model comparison measurements. Figure 2.5 shows the setup of the measurements performed with the Clinac120.

2.5.2 Methods

The same procedure was followed as in the case of the measurements performed in Vienna: clinical plans were created with the generic model, these were then used to create QA plans on the digital Delta⁴ phantom and these plans were then exported along with their respective doses as DICOM files. The plans (along with their respective dose distributions) were then sent on to the personnel of the LKH Wiener Neustadt to import into their own verification and Delta⁴ software in order to enable their transfer to the linac for subsequent irradiation and the ensuing GPR-analysis.



Figure 2.5: Setup for QA plan irradiation at the LKH Wiener Neustadt: the Clinac120 and the Delta⁴ phantom.

2.6 Statistical Analysis

The RayStation-internal RMS differences of the modeled curves relative to the measured curves were used as a guideline throughout the modeling process, since there are specific tolerance values for each region of the lateral profiles and PDDs that need not be exceeded. These tolerances are: 10% for the build-up and the penumbra region, 2% for the fall-off and 3% for the in-field and out-of-field regions.

During the MATLAB verification, $\gamma_{<1}$ -values of $\geq 90\%$ were indicative of good agreement and during the point dose and output factor verification, differences between measured and computed values that fell within 1% were considered as good, those falling within 2% OK and those falling within $\geq 3\%$ bad.

For the treatment-delivery verification, GPRs higher than 90% were clinically acceptable, while plans exhibiting GPRs higher than 95% and 99% were considered very good and excellent, respectively.

A one-way ANOVA (analysis of variance) was performed on the median dose deviations and local γ -passing rates obtained for the LR indication, to test (F-test) whether the means of each model's values are the same for **all** models. This was undertaken for the LR indication, since only LR plans were delivered with all four beam models. In addition to the ANOVA, double-sided t-tests were

pairwise performed on both the median dose deviation and the local γ -passing rates obtained for the LR indication with **each** of the four models, thus resulting in **six** t-tests.

Because the γ -passing rates are not normally distributed and therefore do not fulfill a condition implied by the t-test, an additional statistical test, the Mann-Whitney-Wilcoxon (U-test), not assuming any (parametric) distribution of the observations has been performed in the same pairwise manner as the t-test for both the median dose distribution results (as a means of control) and the γ -passing rate results.

T-tests were also employed to assess whether the mean median dose deviation and mean local γ -passing rate obtained with the Versa HD and the Clinac120 for both the LR and the HR indication differed in a statistically significant manner. On the basis of the same argument as above, U-tests were also performed for the same results.

Table 2.1 contains the simplified null and alternative hypotheses assumed in each of the three statistical tests.

Table 2.1: Null and alternative hypotheses of the statistical tests performed throughout this thesis.

	H_0	H_A
ANOVA	$\mu_1 = \mu_2 = \dots = \mu_n, n \geq 3$	$\mu_1, \mu_2, \dots, \mu_n$ are not all equal
t-test	$\mu_1 = \mu_2$	$\mu_1 \neq \mu_2$
U-test	$F_1(x) = F_2(x), \forall x$	$F_1(x) = F_2(x + a), a \neq 0, \forall x$

H_0 : null hypothesis,

H_A : alternative hypothesis,

μ_i : mean of sample set i,

$F_i(x)$: cumulative distribution function for the sample set i.

In all tests (F-test, t-test and U-test), the null hypothesis is rejected if and only if the observed p-value of the test statistics is lower than a level of statistical significance, hereby chosen at 5%. When multiple t-tests or U-tests are carried out, the level of statistical significance is corrected to $5/n\%$, where n denotes the number of tests (Bonferroni correction).

RStudio version 0.99.484, an integrated development environment for R, a programming language for statistical computing, was used to perform the F-test, the t-test and the U-test.

3 Results

3.1 Emergent Beam Models

As previously stated in section 2.1.1, the beam parameters that have been reached as a result of auto-modeling steps and manual tuning can be found in the Appendix of this thesis (sections A.1 and A.2), along with information on the curve fit quality of the calculated PDDs and lateral profiles as compared with the entered measured curves by the RayPhysics application itself.

The curve quality of the 6 MV and 10 MV FF models showed good agreement with the measured curves, staying mostly within the respective tolerances. The 10% tolerance for the build-up region was not exceeded (the maximum RMS difference there was 8.3% and 7.0% for the 6 MV and the 10 MV beam model, respectively), as was the case with the 2% tolerance for the fall-off region (maximum of 0.9% - 6 MV and 0.7% - 10 MV, respectively). The fit quality of the lateral profiles revealed a somewhat better agreement for the 10 MV FF model, although the results for both models were mostly within the 3% tolerance for the in-field region. However, some curve values did exceed the tolerance, mostly for very small field sizes and at larger depths or - only for the 6 MV FF model - for field sizes bigger than $15\text{ cm} \times 15\text{ cm}$. The penumbra region of the 10 MV FF model exhibited RMS differences that stayed well within the 10% tolerance. The same holds true for the 6 MV FF beam model, with the exception that in this case the 10% tolerance for the penumbra region was exceeded, for the largest field size of $40\text{ cm} \times 40\text{ cm}$ and the rectangular field of $5\text{ cm} \times 30\text{ cm}$. For both FF models the 3% tolerance of the out-of-field region was mostly observed with the few exceptions occurring for bigger field sizes. The $40\text{ cm} \times 40\text{ cm}$ field size in particular showed a higher disagreement between measured and computed curves, since the computed curves overestimated the dose in the heel and exhibited a step-like fall into the toe (see figure 3.1 below).

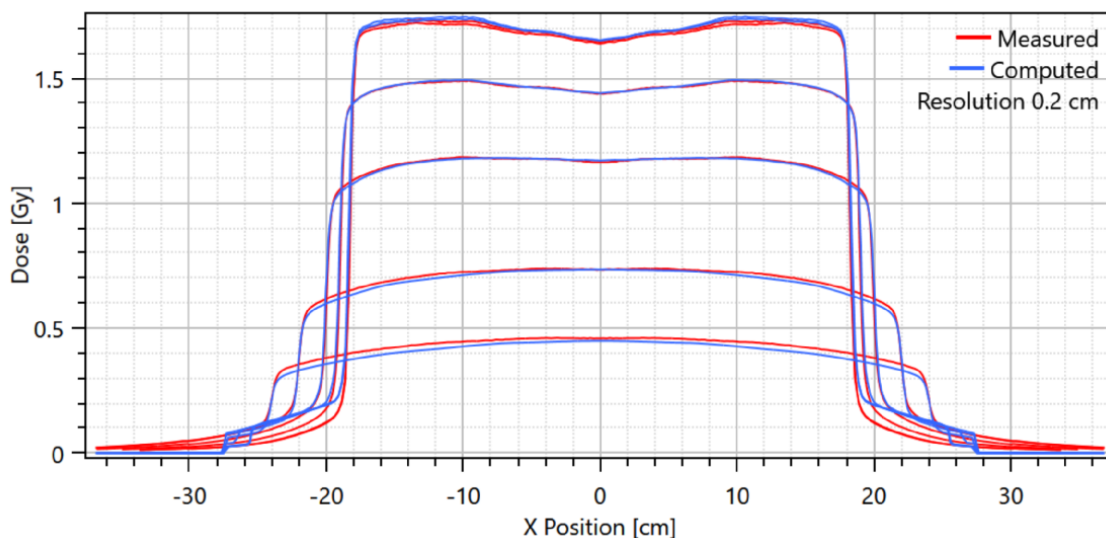


Figure 3.1: CR profile for a $40\text{ cm} \times 40\text{ cm}$ field size of the 6 MV FF beam model, where the “steps” in the out-of-field region can be observed.

As far as the FFF models were concerned, the PDDs showed a different behaviour, in that the build-up tolerance was upheld for the 10 MV FFF model, while the 6 MV FFF exhibited two small field cases where the RMS difference was in excess of the 10% tolerance. The 2% tolerance for the fall-off region, however, is never exceeded by both FFF models, thus exhibiting the same behaviour as the FF models. An exceedance of the in-field tolerance only occurs for the smallest field size of both models. The penumbra region does differentiate between the two FFF models: while for the 10 MV FFF case there is no value exceeding the 10% tolerance, for the 6 MV FFF beam model this

seems to occur for the two largest field sizes and the rectangular field size of $5\text{ cm} \times 30\text{ cm}$. Finally, the agreement in the out-of-field region for both FFF models seems to fall within the accepted limits in most cases, with a few isolated exceptions for field sizes larger than $15\text{ cm} \times 15\text{ cm}$ for the 6 MV FFF and $30\text{ cm} \times 30\text{ cm}$ for the 10 MV FFF beam model. The step-like fall in the out-of-field region of the $40\text{ cm} \times 40\text{ cm}$ profiles seems to be reoccurring in the FFF models as well, albeit not as pronounced as in the FF models, as one would expect from FFF beams (see Figure 3.2 below).

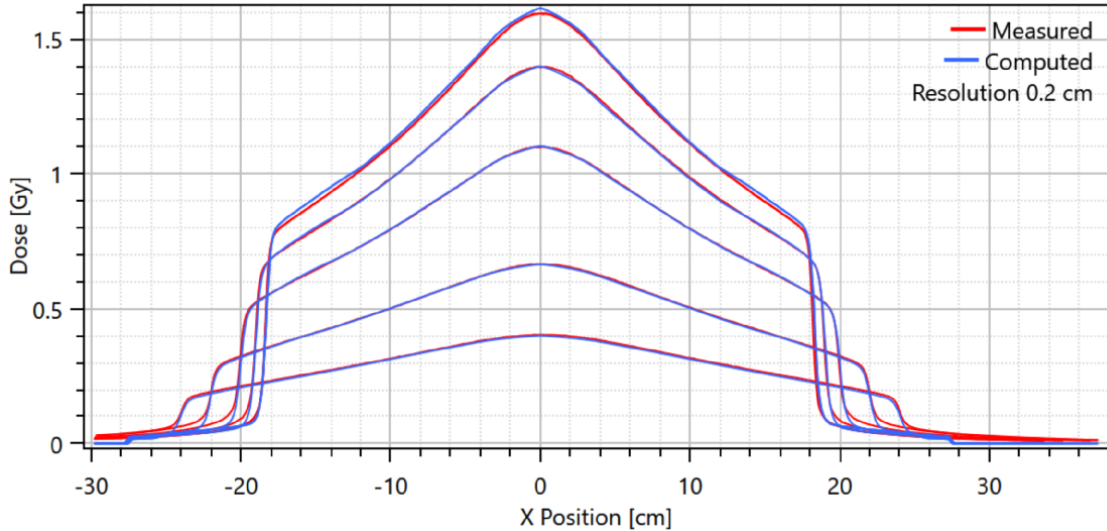


Figure 3.2: CR profile for a $40\text{ cm} \times 40\text{ cm}$ field size of the 6 MV FFF beam model, demonstrating the “steps” in the out-of-field region.

3.2 Independent Verification

The summarized results of the independent verification can be found in Table 3.1, Table 3.2 and Table 3.3. Table 3.1 and Table 3.2 contain the results of the γ -index analysis performed with the MATLAB code, the former for the PDDs and the latter for the lateral profiles. Table 3.3 presents the results of the point dose verification.

Figure 3.3 shows examples of good and bad agreement between measured and computed PDD curves. The same is shown for the lateral profiles in Figures 3.4 and 3.5, with the former dealing with crossplane profiles and the latter with inplane profiles.

The independent (i.e. outside of RayStation) MATLAB verification showed similar results when compared to the RayPhysics fit quality calculations, thus confirming the findings.

The average percentage of $\gamma_{<1}$ values for the PDDs of all four models was greater than 99%, for calculations performed both on the $30\text{ cm} \times 30\text{ cm} \times 30\text{ cm}$ digital water phantom (DWP) and on the $50\text{ cm} \times 50\text{ cm} \times 50\text{ cm}$ digital water phantom. Moreover, the average $\gamma_{<1}$ percentage values for the lateral profiles were all greater than 90%, except for the IN (inplane) profiles of the 6 MV FF beam model calculated on the $50\text{ cm} \times 50\text{ cm} \times 50\text{ cm}$ phantom and, on occasion, individual $\gamma_{<1}$ percentages were even below 50% (the lateral profiles for two of those cases are shown in Figures 3.4b and 3.5b). This was mostly found for large depths and increasingly so for larger field sizes. Moreover, all models featured a slightly better agreement between measured and computed curves for CR (crossplane) profiles.

Table 3.1: Average γ_{mean} and $\gamma_{<1}$ for PDD curves.

Beam quality + mode	30 cm \times 30 cm \times 30 cm DWP		50 cm \times 50 cm \times 50 cm DWP	
	γ_{mean}	$\gamma_{<1}$ [%]	γ_{mean}	$\gamma_{<1}$ [%]
6 MV FF	0.23 \pm 0.16	99.26 \pm 0.51	0.19 \pm 0.06	99.79 \pm 0.31
10 MV FF	0.18 \pm 0.12	99.36 \pm 0.30	0.19 \pm 0.16	99.53 \pm 1.08
6 MV FFF	0.16 \pm 0.10	99.06 \pm 0.25	0.16 \pm 0.06	99.66 \pm 0.30
10 MV FFF	0.17 \pm 0.08	99.28 \pm 0.27	0.16 \pm 0.04	99.83 \pm 0.23

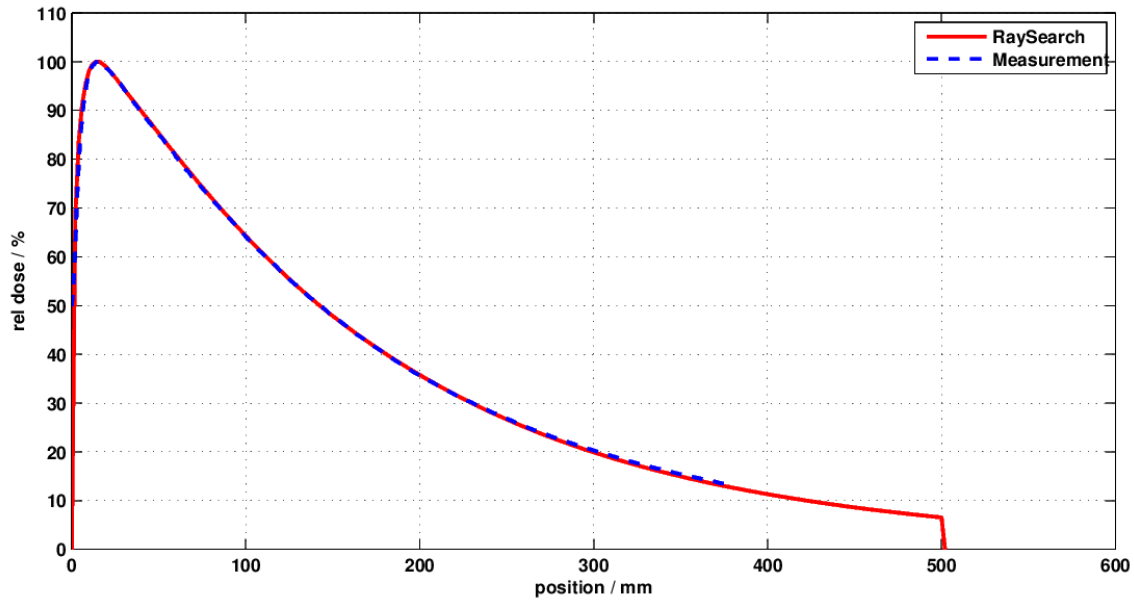
Table 3.2: Average γ_{mean} and $\gamma_{<1}$ for lateral profiles.

Beam quality + mode	Profile type	30 cm \times 30 cm \times 30 cm DWP		50 cm \times 50 cm \times 50 cm DWP	
		γ_{mean}	$\gamma_{<1}$ [%]	γ_{mean}	$\gamma_{<1}$ [%]
6 MV FF	CR	0.28 \pm 0.21	95.66 \pm 10.88	0.41 \pm 0.25	91.52 \pm 26.10
	IN	0.40 \pm 0.31	91.53 \pm 18.33	0.48 \pm 0.33	87.21 \pm 20.90
10 MV FF	CR	0.25 \pm 0.19	97.52 \pm 7.27	0.32 \pm 0.22	95.62 \pm 12.07
	IN	0.43 \pm 0.29	90.28 \pm 18.88	0.46 \pm 0.28	90.42 \pm 18.66
6 MV FFF	CR	0.30 \pm 0.27	94.92 \pm 11.84	0.37 \pm 0.16	94.25 \pm 9.38
	IN	0.40 \pm 0.29	92.93 \pm 13.64	0.39 \pm 0.18	92.76 \pm 10.86
10 MV FFF	CR	0.27 \pm 0.21	95.83 \pm 10.99	0.34 \pm 0.11	97.20 \pm 5.79
	IN	0.38 \pm 0.22	94.38 \pm 13.37	0.35 \pm 0.12	96.06 \pm 7.49

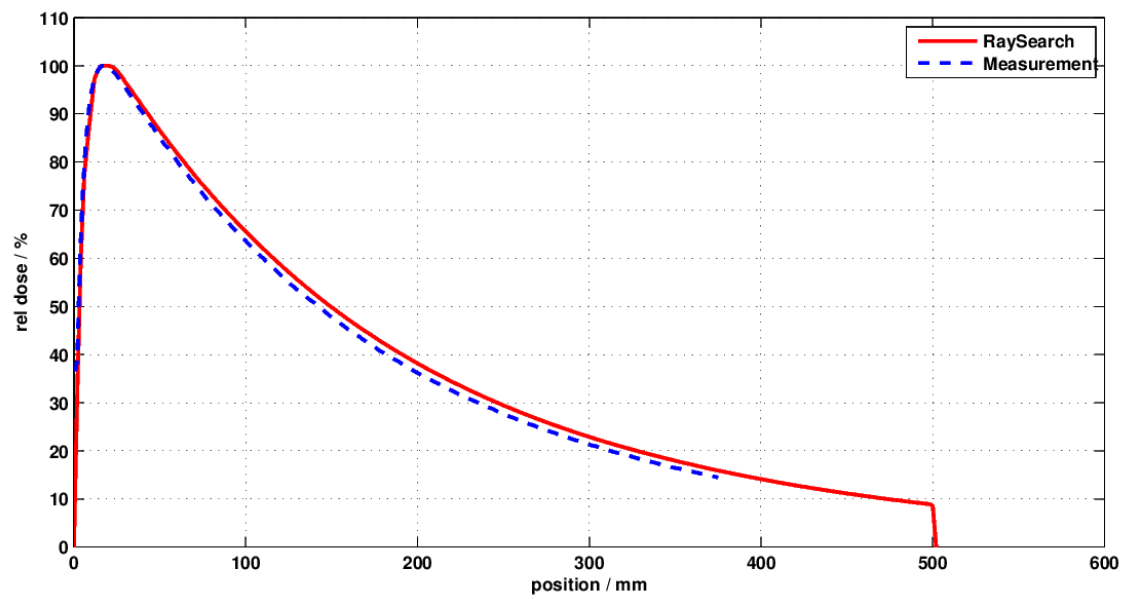
Average differences between computed and measured central axis point doses stayed under 1%, while individual values were mostly below $\pm 2\%$, with the occasional exceedance observed at small field sizes, where measurement uncertainties cannot be ruled out due to the difficulties such measurements raise.

Table 3.3: Average point dose and percental difference relative to measurement for various SSDs.

Beam quality + mode	SSD [cm]	30 cm \times 30 cm \times 30 cm DWP		50 cm \times 50 cm \times 50 cm DWP	
		Dose [Gy]	Difference [%]	Dose [Gy]	Difference [%]
6 MV FF	90	0.92 \pm 0.30	0.30 \pm 1.28	0.96 \pm 0.30	0.32 \pm 0.98
	100	0.76 \pm 0.24	0.28 \pm 0.81	0.79 \pm 0.24	0.53 \pm 0.88
	85	1.01 \pm 0.33	0.55 \pm 1.67	1.05 \pm 0.34	0.49 \pm 1.23
	80	1.12 \pm 0.41	0.54 \pm 2.43	1.16 \pm 0.40	0.43 \pm 1.88
10 MV FF	90	0.92 \pm 0.26	0.63 \pm 1.85	0.95 \pm 0.27	0.47 \pm 1.62
	100	0.77 \pm 0.21	0.78 \pm 1.33	0.79 \pm 0.21	0.79 \pm 1.11
	85	1.02 \pm 0.30	0.86 \pm 2.23	1.05 \pm 0.30	0.60 \pm 1.83
	80	1.13 \pm 0.37	0.55 \pm 3.29	1.16 \pm 0.36	-0.02 \pm 2.61
6 MV FFF	90	0.94 \pm 0.30	-0.29 \pm 0.57	0.96 \pm 0.30	-0.08 \pm 0.75
	100	0.79 \pm 0.24	0.07 \pm 0.60	0.80 \pm 0.24	0.25 \pm 0.83
	85	1.04 \pm 0.33	-0.02 \pm 0.59	1.06 \pm 0.34	0.05 \pm 0.70
	80	1.16 \pm 0.42	-0.13 \pm 0.70	1.18 \pm 0.41	-0.08 \pm 0.61
10 MV FFF	90	0.95 \pm 0.27	0.38 \pm 0.47	0.96 \pm 0.27	0.35 \pm 0.61
	100	0.79 \pm 0.22	0.40 \pm 0.66	0.80 \pm 0.22	0.61 \pm 0.53
	85	1.05 \pm 0.30	0.42 \pm 0.58	1.06 \pm 0.30	0.45 \pm 0.58
	80	1.17 \pm 0.38	-0.22 \pm 0.54	1.18 \pm 0.37	-0.14 \pm 0.59

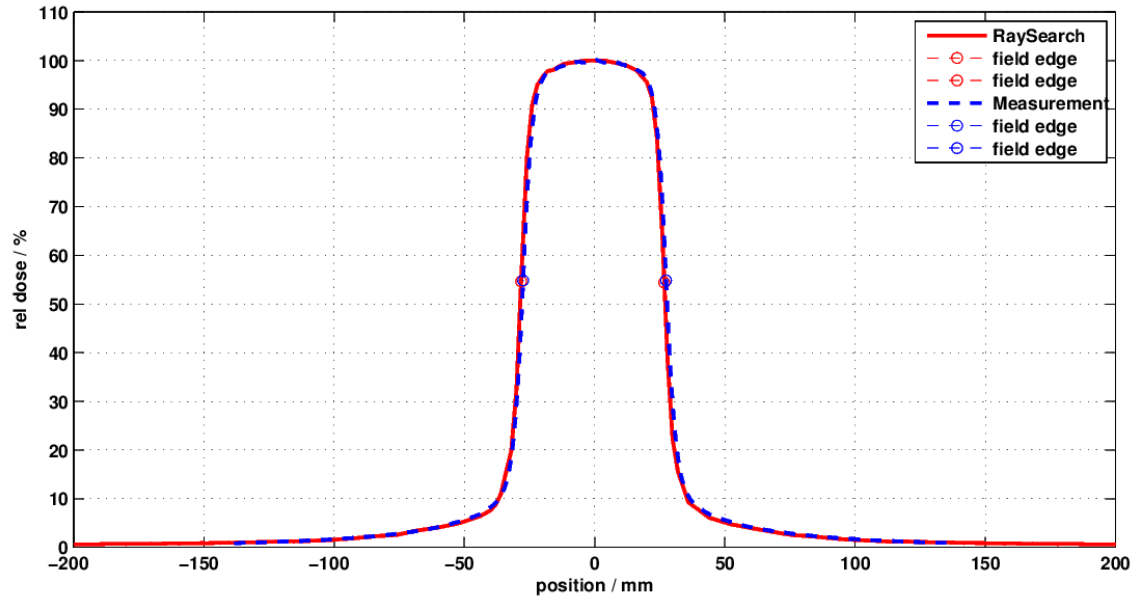


(a) 6 MV FF, field size 7 cm \times 7 cm. $\gamma_{\text{mean}} = 0.11$ and $\gamma_{<1} = 100\%$.

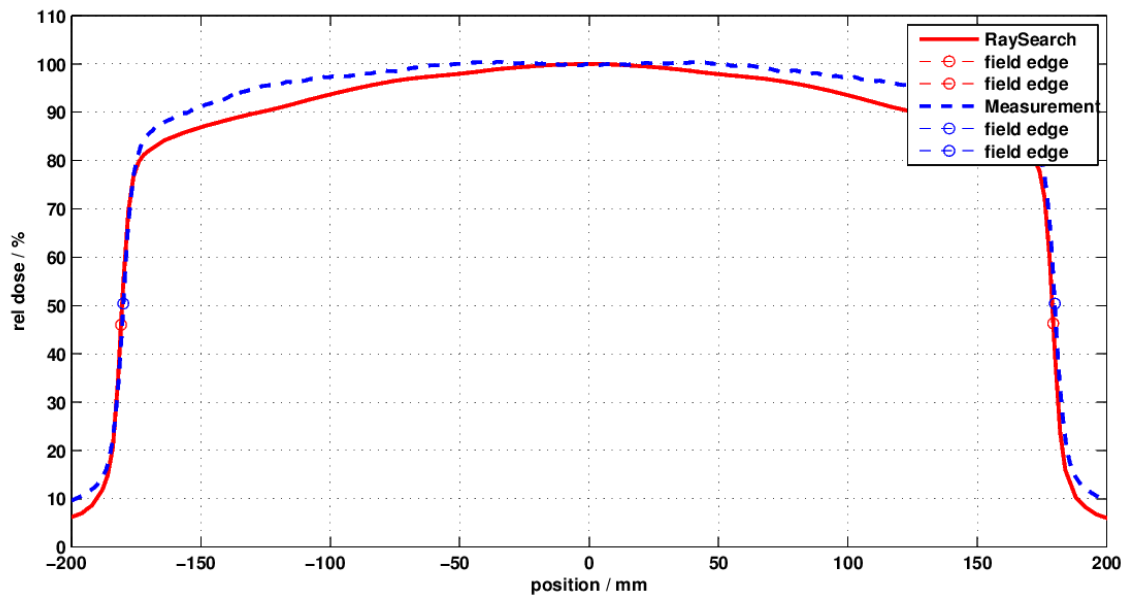


(b) 10 MV FF, field size 1 cm \times 1 cm. $\gamma_{\text{mean}} = 0.77$ and $\gamma_{<1} = 95.54\%$.

Figure 3.3: Examples of good (a) and bad (b) agreement between measured and computed PDDs.

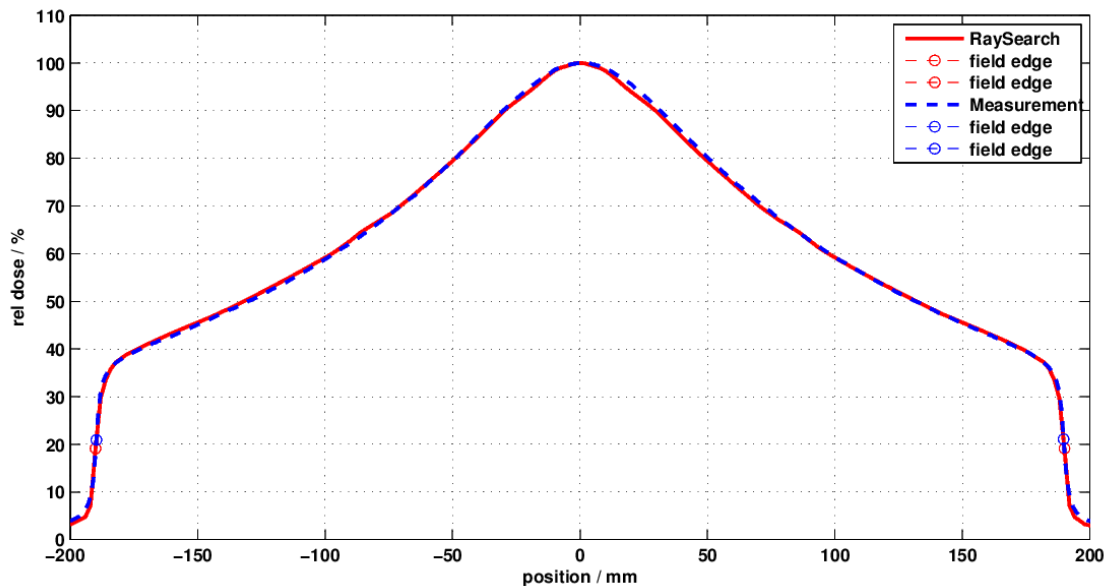


(a) 6 MV FF, field size 5 cm \times 5 cm, depth 5 cm. $\gamma_{\text{mean}} = 0.21$ and $\gamma_{<1} = 100\%$.

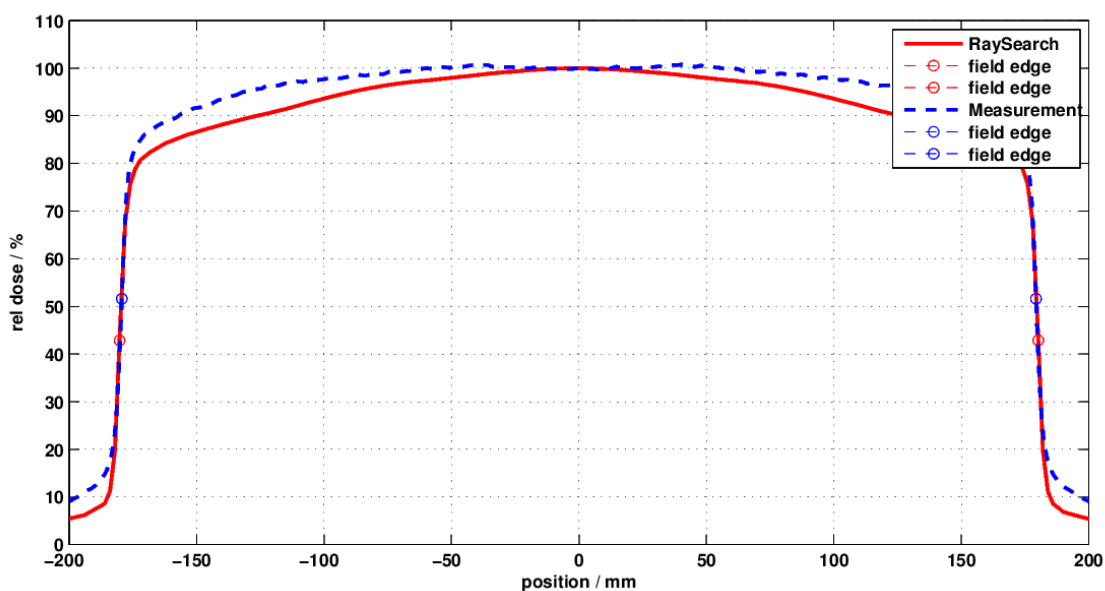


(b) 6 MV FF, field size 5 cm \times 30 cm, depth 30 cm. $\gamma_{\text{mean}} = 1.29$ and $\gamma_{<1} = 36.32\%$.

Figure 3.4: Examples of good (a) and bad (b) agreement between measured and computed cross-plane (CR) profiles.



(a) 10 MV FFF, field size 40 cm \times 40 cm, depth 5 cm. $\gamma_{\text{mean}} = 0.22$ and $\gamma_{<1} = 100\%$.



(b) 6 MV FF, field size 30 cm \times 5 cm, depth 30 cm. $\gamma_{\text{mean}} = 1.51$ and $\gamma_{<1} = 23.09\%$.

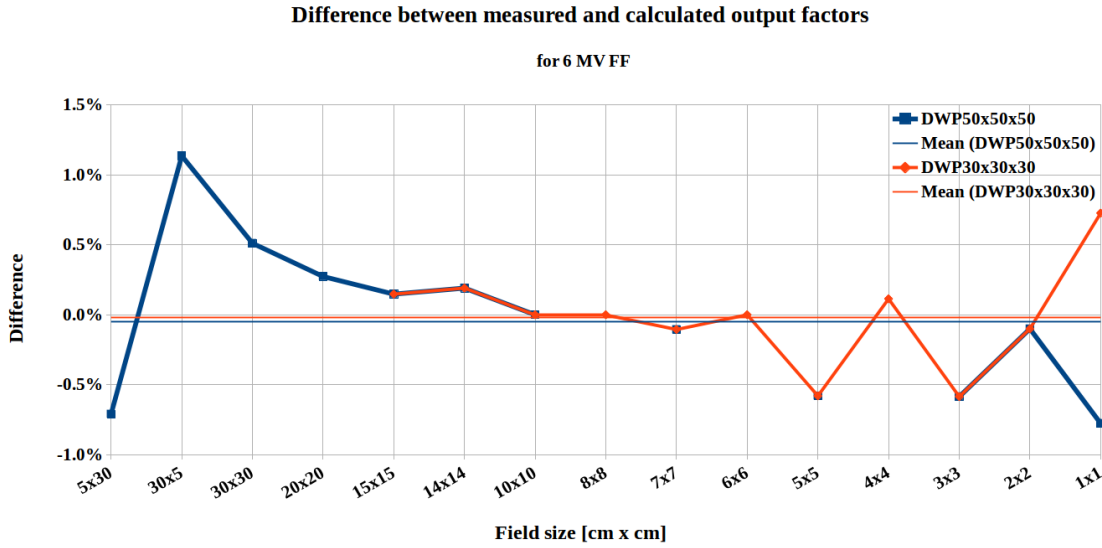
Figure 3.5: Examples of good (a) and bad (b) agreement between measured and computed inplane (IN) profiles.

Finally, since each of the models was created for 16 field sizes the results of the output factor verification are quite extensive and can therefore be found in the Appendix, section B.3. Tables B.9 through B.12 have nevertheless been used to plot the differences between the measured and the calculated output factors for each of the four models. The plots are depicted by Figures 3.6 and 3.7. The maximum such difference for each of the two FF models has been found to be 1.1% and a slightly lower value for each of the FFF models, 0.9%. The average differences, reported for both the 30 cm \times 30 cm \times 30 cm and the 50 cm \times 50 cm \times 50 cm digital water phantoms (DWPs) are outlined in Table 3.4.

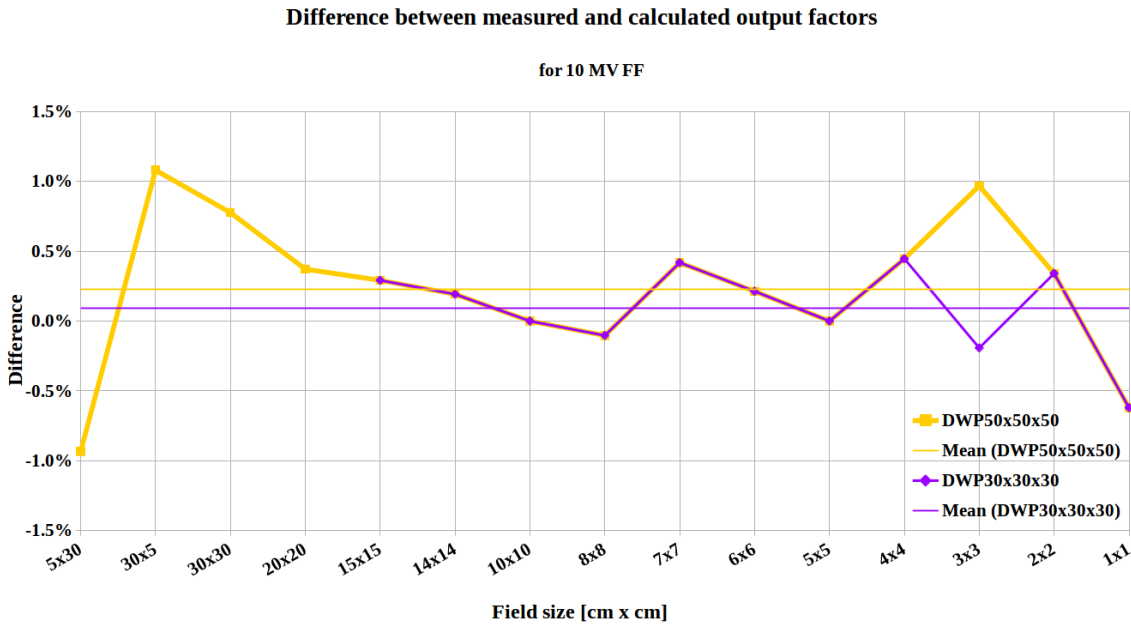
The values were obtained by averaging over 15 field sizes for each beam model.

Table 3.4: Average difference (in %) between measured and computed output factors.

Beam quality + mode	Average Difference [%] $\pm 1^{st}$ SD.	
	30 cm \times 30 cm \times 30 cm DWP	50 cm \times 50 cm \times 50 cm DWP
6 MV FF	-0.02 \pm 0.36	-0.05 \pm 0.57
10 MV FF	0.09 \pm 0.32	0.23 \pm 0.53
6 MV FFF	-0.11 \pm 0.45	-0.06 \pm 0.49
10 MV FFF	0.38 \pm 0.32	0.33 \pm 0.36

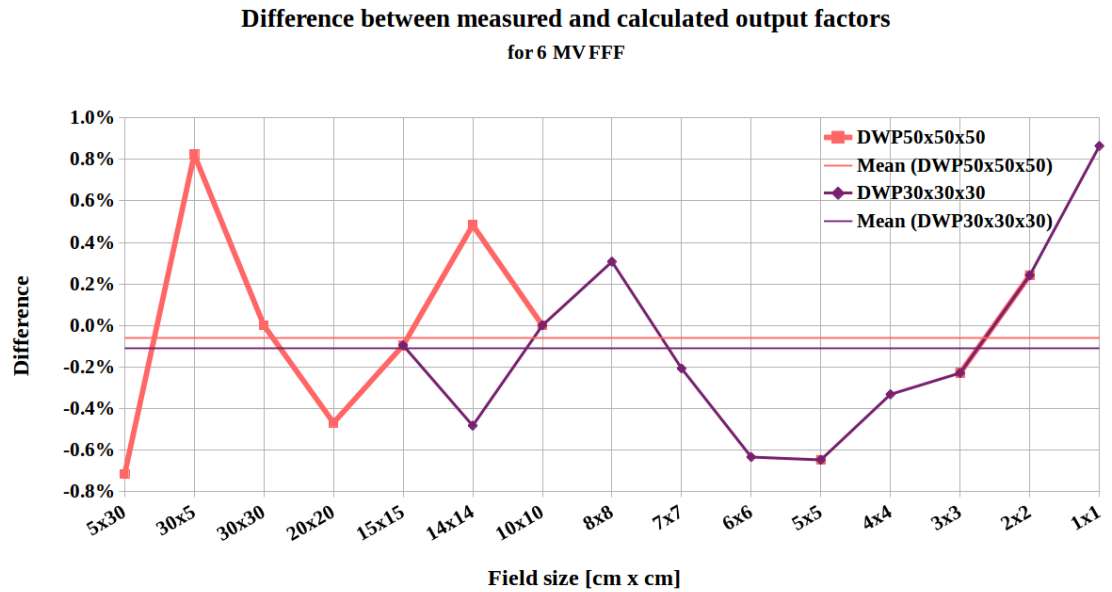


(a) 6 MV FF. Blue: differences based on dose calculation performed on the 50 cm × 50 cm × 50 cm digital water phantom (DWP) along with the respective mean value. Red: differences based on dose calculation performed on the 30 cm × 30 cm × 30 cm digital water phantom (DWP) along with the respective mean value.

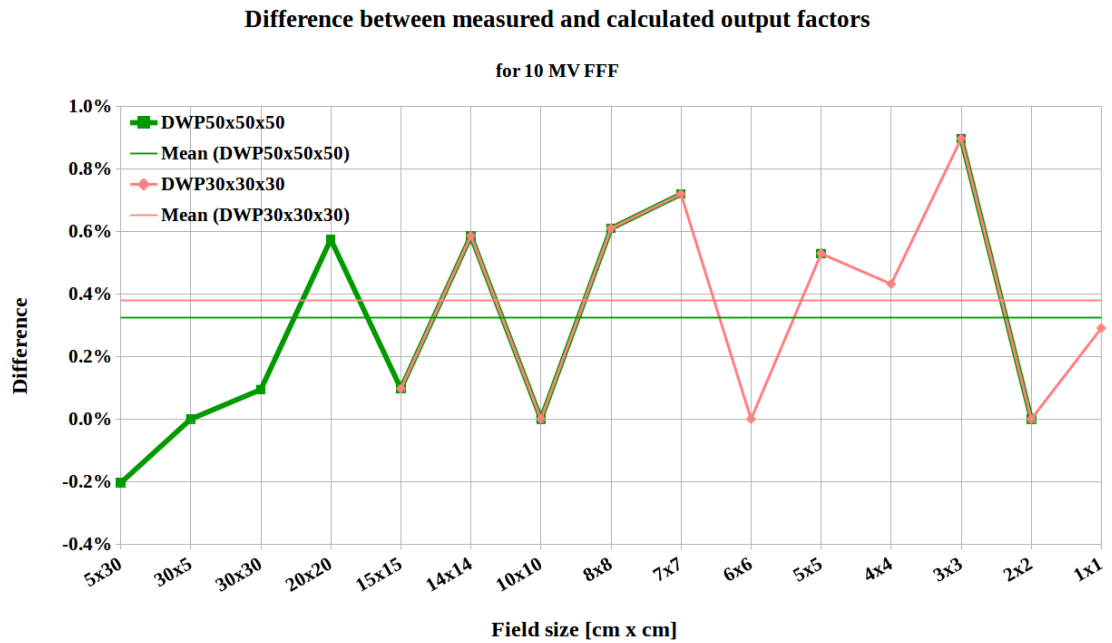


(b) 10 MV FF. Yellow: differences based on dose calculation performed on the 50 cm × 50 cm × 50 cm digital water phantom (DWP) along with the respective mean value. Purple: differences based on dose calculation performed on the 30 cm × 30 cm × 30 cm digital water phantom (DWP) along with the respective mean value.

Figure 3.6: Differences between measured and calculated output factors for the FF linac models.



(a) 6 MV FFF. Salmon: differences based on dose calculation performed on the 50 cm × 50 cm × 50 cm digital water phantom (DWP) along with the respective mean value. Purple: differences based on dose calculation performed on the 30 cm × 30 cm × 30 cm digital water phantom (DWP) along with the respective mean value.



(b) 10 MV FFF. Green: differences based on dose calculation performed on the 50 cm × 50 cm × 50 cm digital water phantom (DWP) along with the respective mean value. Pink: differences based on dose calculation performed on the 30 cm × 30 cm × 30 cm digital water phantom (DWP) along with the respective mean value.

Figure 3.7: Differences between measured and calculated output factors for the FFF linac models.

3.3 Treatment-Delivery Verification

The results of the treatment-delivery verification for the LR prostate carcinoma (PC) indication are summarized by Table 3.5 in the form of average median dose deviations and local GPRs (averaged over the number of plans/measurements that were delivered/made per beam model). The mean local GPRs for all but one model (6 MV FF) are $>95\%$ and the mean local GPRs of the FFF beam models are higher than their corresponding FF beam models (i.e. 6 MV: $98.24\% \pm 1.43\%$ FFF $> 94.49\% \pm 1.71\%$ FF and 10 MV: $96.47\% \pm 1.87\%$ FFF $> 95.13\% \pm 2.32\%$ FF).

For the much smaller group of HR patients (2 patients only, each with 2 plans - an FB plan and an mVMAT plan), the delivery of the QA plans merely with the 6 MV FF beam model produced an average median dose deviation [%] of -1.38 ± 0.31 and an average local GPR [%] of 97.28 ± 1.34 .

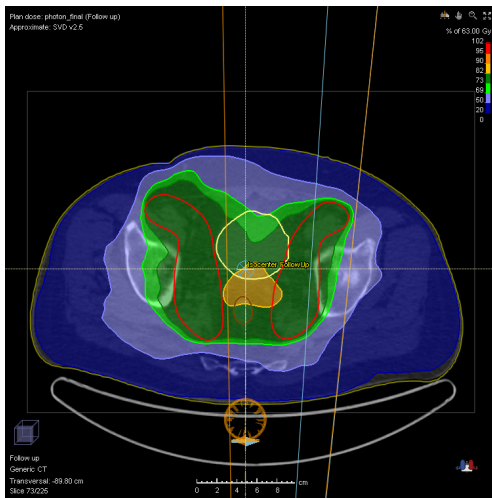
The complete (individual) results can be found in the Appendix, section C.

The individual local GPRs resulting from the treatment-delivery verification of the FF beam models were all but one above the 90% threshold (see Tables C.1, C.2, C.3, C.4 and C.5), in conformity with the general requirements for clinical implementation. For the FFF models, the treatment-delivery verification revealed that all but two individual local GPRs were above 95%, with both of those two exceptions manifesting for the 10 MV FFF beam model and still being above the 90% threshold. This obviously translates to higher average local GPRs for the FFF models as compared to those pertaining to the FF models (Table 3.5).

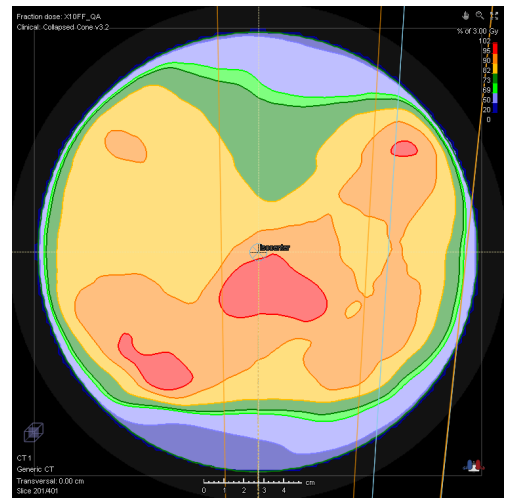
Table 3.5: Average median dose deviation and local GPR for LR patients.

Beam quality + mode	Med. Dose Dev. [%]	local GPR [%]	# of measurements
10 MV FF	-1.60 ± 0.64	95.13 ± 2.32	20
6 MV FF	-2.02 ± 0.20	94.49 ± 1.71	13
10 MV FFF	-0.85 ± 0.29	96.47 ± 1.87	10
6 MV FFF	-0.95 ± 0.33	98.24 ± 1.43	10

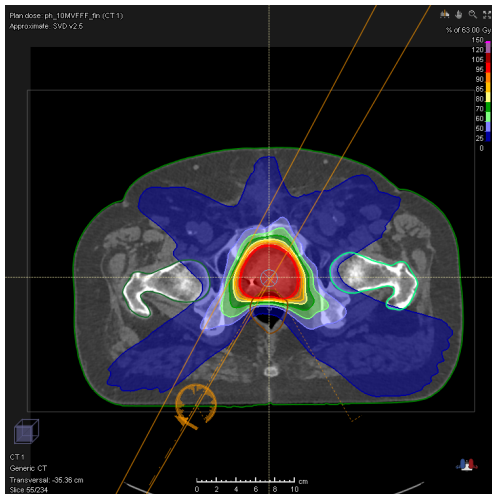
Figure 3.8 exemplifies isodose distributions of delivered plans, i.e. for an HR plan (a) and an LR plan (c), along with their respective QA plans (b and d).



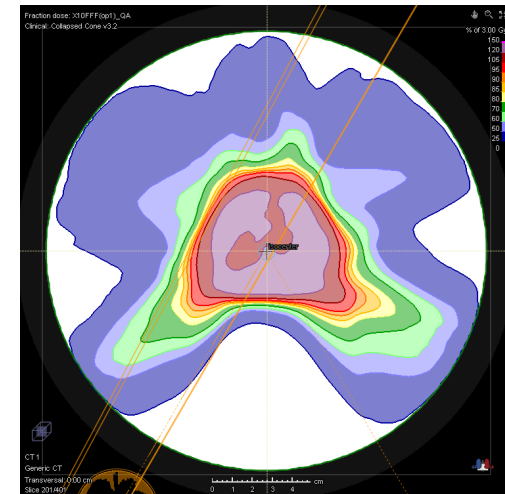
(a) Isodose distribution of an HR 6 MV FF mV-MAT plan (patient HR12).



(b) Isodose distribution of the QA version of the plan in sub-figure a).



(c) Isodose distribution of an LR 10 MV FFF mV-MAT plan (patient LR09).



(d) Isodose distribution of the QA version of the plan in sub-figure c).

Figure 3.8: Example of isodose distributions of plans used in the treatment-delivery verification.

The LR results are statistically analyzed in Table 3.6, by means of an ANOVA performed simultaneously on all beam models using a Fischer (F)-test, six t-tests performed pairwise on all models and six U-tests also performed pairwise on all beam models.

The ANOVA rejected the null hypothesis of equal mean median dose deviation and equal mean local GPR among the four beam models, with p-values being very close to 0 in both cases. Furthermore, the beam models from the FFF group have values that are better compared to the FF beam models on a statistically significant level, yet a further t-test (for the results obtained with each of the two FFF models) reveals there is no clear indication which of the two beam models is better (median dose deviation p-value of 48.3%). The U-test comes in support of the previously mentioned and additionally facilitates the conclusion that there can also be no differentiation between the two FF models (GPR p-value of 29.3% - see Table 3.6).

Table 3.6: Statistical analysis of LR results.

Beam models used	p-value [%] (MDD)		p-value [%] (GPR)
all	ANOVA: 0.0		ANOVA: 0.0
	t-test	U-test	U-test
6 MV FF & 10 MV FF	1.2	1.3	29.3
6 MV FF & 10 MV FFF	0.0*	0.0*	1.8
6 MV FF & 6 MV FFF	0.0*	0.0*	0.0*
10 MV FF & 6 MV FFF	0.1*	0.0*	0.0*
10 MV FF & 10 MV FFF	0.0*	0.0*	4.5
10 MV FFF & 6 MV FFF	48.3	32.1	3.1

MDD: Median dose deviation

GPR: local γ -passing rate

* : statistical significance (null hypothesis rejected at a 5/6% level of statistical significance)

Finally, Table 3.7 shows individual median dose deviations and local GPRs for the plans that were re-calculated on the density-overwritten Delta⁴-phantom, along with the initial value. For the FF models, it was found that adding doses planned on the phantom overwritten with a mass density of 1.19 g/cm³ to the Delta⁴-software yielded local GPRs higher by $\sim 3\%$ for the worst plans per model, while no significant change was noticed for the best plans per model (which coincidentally were all FB plans). For the FFF models the same applied for the best plans per model, while an increase in the local GPRs by 1% (6 MV FFF) and 3% (10 MV FFF) of the worst plans per model was observed.

For the median dose deviations obtained after adding the dose planned on the density-overwritten Delta⁴ phantom a general reduction of the absolute value was observed in all but one plan.

Table 3.7: Median dose deviations and local GPRs for plans calculated on the Delta⁴ of a mass density of 1.19 g/cm³.

Beam model	Plan	Med. Dose Dev. [%]		local GPR [%]	
		Initial density	1.19 g/cm ³	Initial density	1.19 g/cm ³
10 MV FF	best	0.0	0.0	99.8	99.8
	worst	-2.2	-1.6	91.8	94.7
6 MV FF	best	-1.1	-0.8	98.6	98.7
	worst	-2.1	-1.9	91.2	94.3
10 MV FFF	best	-0.7	-0.2	98.6	98.6
	worst	-1.2	-0.7	93.4	96.2
6 MV FFF	best	-0.8	-0.5	99.6	99.6
	worst	-1.2	-1.0	95.3	96.4

3.4 Beam Model Comparison

Table 3.8 shows the average median dose deviations and local GPRs (averaged over the number of plans delivered per indication) obtained after QA plan irradiation with each of the two machines, Elekta's Versa HD and Varian's Clinac120. The individual values (i.e. for each irradiated plan) can

be found in Tables D.1 and D.2. The individual local GPRs deriving from irradiation with the Versa HD are all $>90\%$ (for both indications), whereas for the Clinac120 the local GPRs resulting from irradiations are higher for all individual LR plans (with all values above 97%). For HR plans the situation appears to be slightly different, with one value being as low as 78.3% for a Clinac120 HR mVMAT plan, well below the acceptable threshold of 90%, which logically affected the mean local GPR for the Varian machine. All other HR plans, however, stayed well above the 90% threshold. Delivery with the Clinac120 also produced the only local GPR of 100% for a LR FB plan.

The average local GPR values of LR plans are thus higher for the Clinac120 (99.15%), while the Versa HD linear accelerator seems to have performed better with HR plans (average local GPR of 97.28%).

As far as the individual median dose deviations are concerned, those corresponding to the Versa HD are all negative, whereas the opposite applies for the median dose deviations obtained by irradiation with the Clinac120. This implies that the Versa HD slightly underestimates the dose whereas the Clinac120 tends to slightly overestimate the dose.

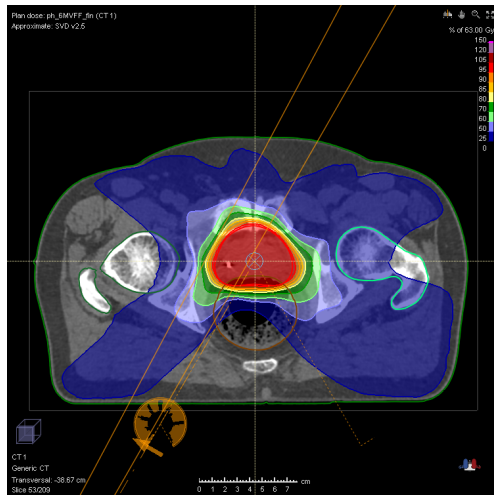
Both models perform very well for plans from the LR group. For the HR indication, however, the Versa HD plans present high mean GPRs and low variation, whereas the Clinac120 plans exhibit a low mean GPR and high variation, thus being an indicative of the superiority of the Versa HD beam model in more complex cases.

Table 3.8: Average median dose deviation and local GPR for Elekta’s Versa HD and Varian’s Clinac120

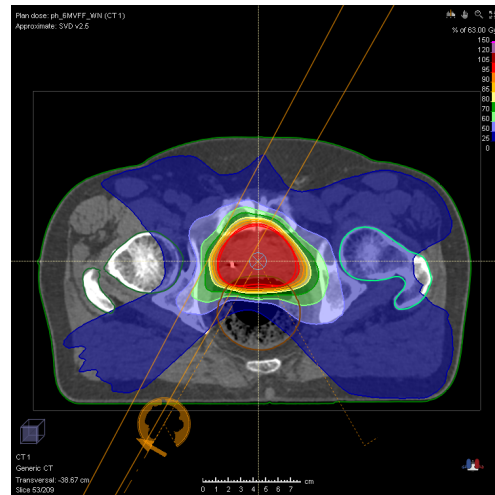
Indication	# of measurements	Med. Dose Dev. [%]		local GPR [%]	
		Versa HD	Clinac120	Versa HD	Clinac120
LR PC	6	-1.92±0.16	1.53±0.19	94.60±1.72	99.15±0.88
HR PC	4	-1.38±0.31	1.68±0.57	97.28±1.34	92.80±9.72

A comparison of dose distributions for plans created with the Versa HD and the Clinac120 beam models can be found in Figure 3.9. The dose distributions of the actual (clinical) plans is depicted in sub-figures (a) and (b) and the dose distributions of their corresponding QA plans is shown in sub-figures (c) and (d). The plans were created for the same patient of the LR group (LR05), with beam models of the same beam quality and mode (6 MV FF) and using the same treatment technique (VMAT).

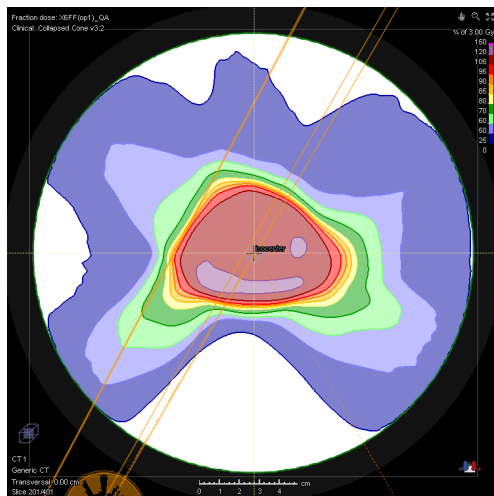
Figure 3.10 gives a DVH plot for two 6 MV FF HR FB plans performed with the Versa HD beam model and the Clinac120 generic beam model, respectively. The figure reveals a slightly steeper fall-off of the target volume curves for the plan created with the Clinac120. As far as OARs are concerned, no clear difference can be perceived from the DVH. The possibility of the overall minor differences between the plans created with the two different beam models being attributed to optimization effects cannot be discarded.



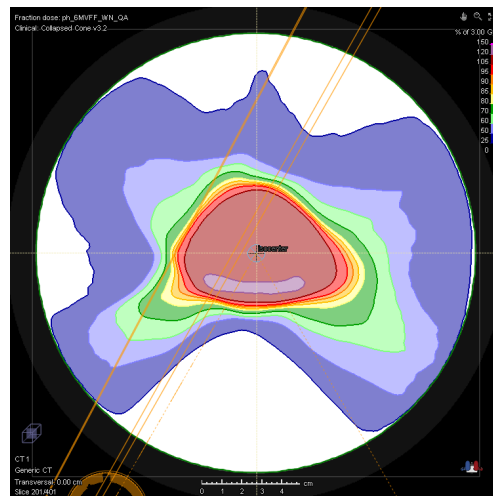
(a) Dose distribution of a 6 MV FF LR mVMAT plan delivered with the Versa HD (patient LR05).



(b) Dose distribution of a 6 MV FF LR mVMAT plan delivered with the Clinac120 (patient LR05).



(c) Dose distribution of the QA plan corresponding to the plan from a).



(d) Dose distribution of the QA plan corresponding to the plan from b).

Figure 3.9: Transversal view of dose distributions of LR plans created with the Versa HD beam model (a and c) and the Clinac120 generic beam model (b and d).

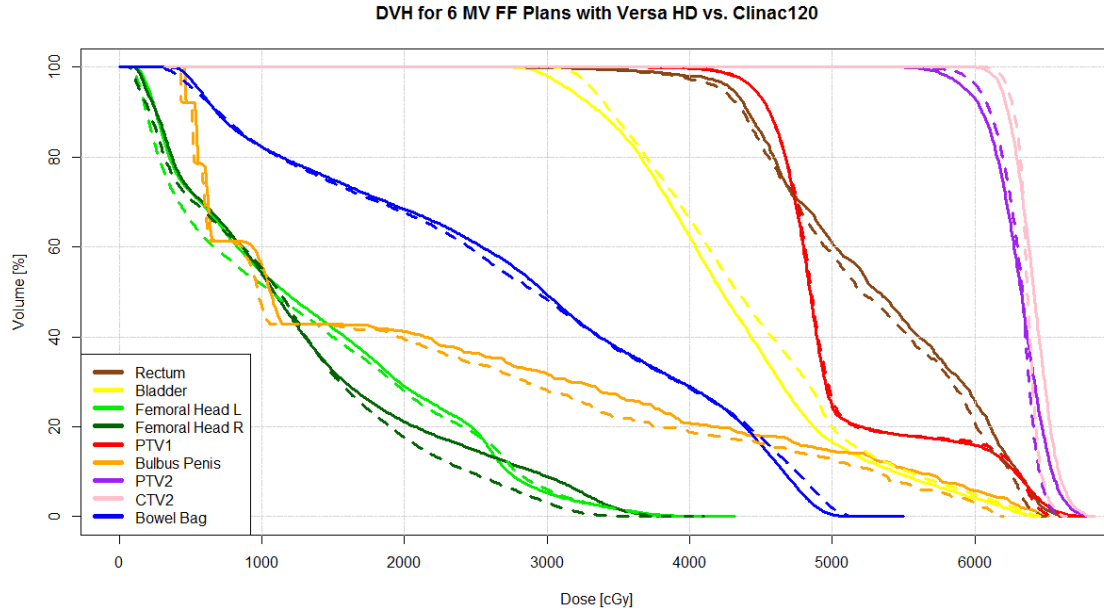


Figure 3.10: DVH of Versa HD (VHD) plan vs. Clinac120 (C120) plan for an HR patient (HR12). Continuous lines represent the plan created with the Versa HD beam model and dashed lines represent the plan created with the Clinac120 beam model.

The results obtained from irradiation of the QA plans created with the two different beam models are statistically analyzed in Table 3.9, by means of t-tests and U-tests.

A t-test and a U-test do indeed confirm the Versa HD and the Clinac120 results to differ from one another on a statistically significant level at least for the LR indication (median dose deviation p-value of 0.0% for the t-test and median dose deviation p-value of 0.5% and GPR p-value of 0.2% for the U-test). Given the fact that the median dose deviations are either above or below zero, depending on the machine that was used for delivery, a statistically significant difference was indeed expected. When t-testing only the absolute values, however, the same conclusion emerged.

For the results following irradiation of plans from the HR indication a t-test performed on the median dose deviations and a U-test performed on both the median dose deviations and the local GPRs revealed contradictory results. Both t-test and U-test on the median dose deviations suggest the results to differ on a statistically significant level (p-values of 0.0% and 2.9% for t-test and U-test, respectively), while the U-test on the local GPRs reveals no statistically significant difference (p-value of 88.5%).

Table 3.9: Statistical analysis of beam model comparison results.

Test performed on	p-value [%] (MDD)		p-value [%] (GPR)
	t-test	U-test	U-test
VHD LR & C120 LR	0.0*	0.5*	0.2*
VHD HR & C120 HR	0.0*	2.9*	88.5

MDD: median dose deviation,

GPR: local γ -passing rate,

VHD: Versa HD,

C120: Clinac120,

* : statistical significance.

3.5 FB vs. mVMAT Plan Comparison

As previously announced, this section contains the results of the QA-plan measurements averaged over the number of delivered plans and grouped per plan type and beam quality. For the LR patient cohort this can be found in Table 3.10. A comparison of FB and mVMAT plans for HR patients can be found in Table 3.11.

While a direct comparison between FB plan and mVMAT plan for each patient unanimously revealed higher local GPRs of the FB plans, no remarkable difference could be observed between the average local GPRs of FB and mVMAT plans.

Table 3.10: Average median dose deviation and local GPR for LR FB and LR mVMAT plans.

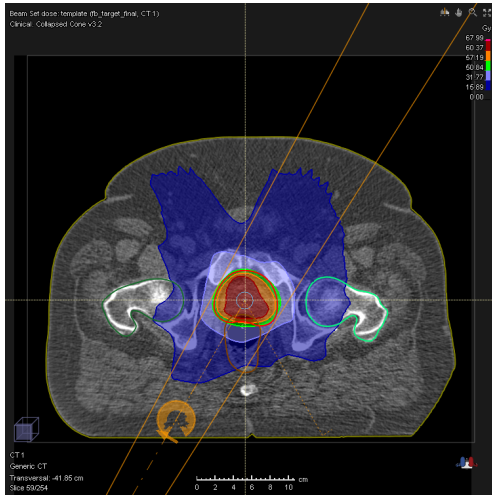
Beam model	# of verified plans		Med. Dose Dev. [%]		local GPR [%]	
	FB	mVMAT	FB plans	mVMAT plans	FB plans	mVMAT plans
10 MV FF	10	10	-1.49±0.63	-1.70±0.67	95.90±1.44	94.36±2.83
6 MV FF	3	10	-1.83±0.06	-2.07±0.19	94.77±0.47	94.41±1.95

Table 3.11: Average median dose deviation and local GPR for HR patients, 6 MV FF

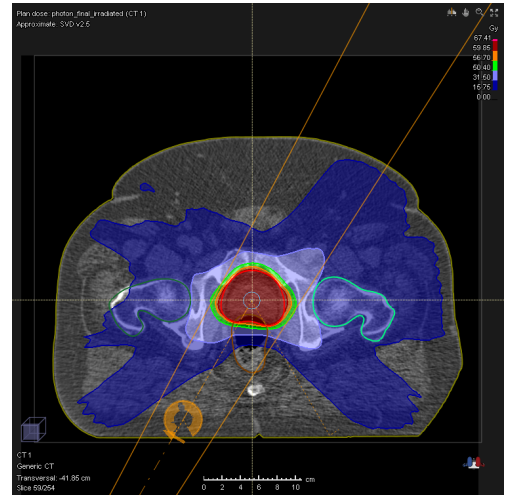
Plan type	# of verified plans	Med. Dose Dev. [%]	local GPR [%]
FB	2	-1.15±0.07	98.4±0.28
mVMAT	2	-1.60±0.28	96.15±0.49

Judging from the individual GPRs one would be tempted to think the FB plans to be better, however, a closer look at the plans (which was the object of Florine Enengl’s bachelor’s thesis [43]) and especially at their dose distributions, DVHs and delivery reveals a few interesting facts and puts this first conclusion into perspective. Figure 3.11 shows the dose distributions of a FB plan compared to that of an mVMAT plan (for the same LR patient, LR01), along with those of their respective QA plans. When looking only at sub-figures (a) and (b), the differences in target coverage are indisputable: the FB plan does not fully cover the target volume, even at the “Target vs. OAR ratio” that puts all emphasis on the target alone.

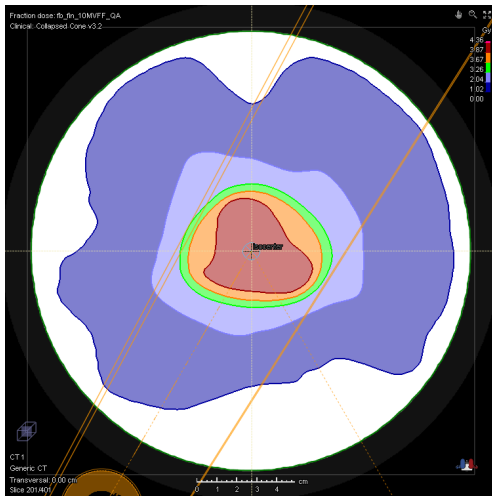
The DVH for the same plans covered in the dose distribution shows the exact same conclusion (see Figure 3.12). Therein one can see not only the steeper fall-off of the dose in the target volume for the manually created VMAT, but also how the same curve starts to fall off at ~ 52 Gy for the FB plan, as opposed to the ~ 62 Gy of the mVMAT plan.



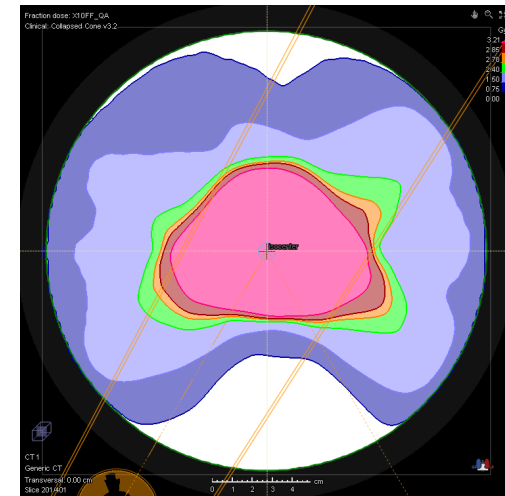
(a) Dose distribution of a delivered LR FB plan created with the 10 MV FF beam model (patient LR01).



(b) Dose distribution of a delivered LR mVMAT plan created with the 10 MV FF beam model (patient LR01).



(c) Dose distribution of the QA plan corresponding to the FB plan from a).



(d) Dose distribution of the QA plan corresponding to the mVMAT plan from b).

Figure 3.11: Transversal view of dose distributions of LR FB and mVMAT plans.

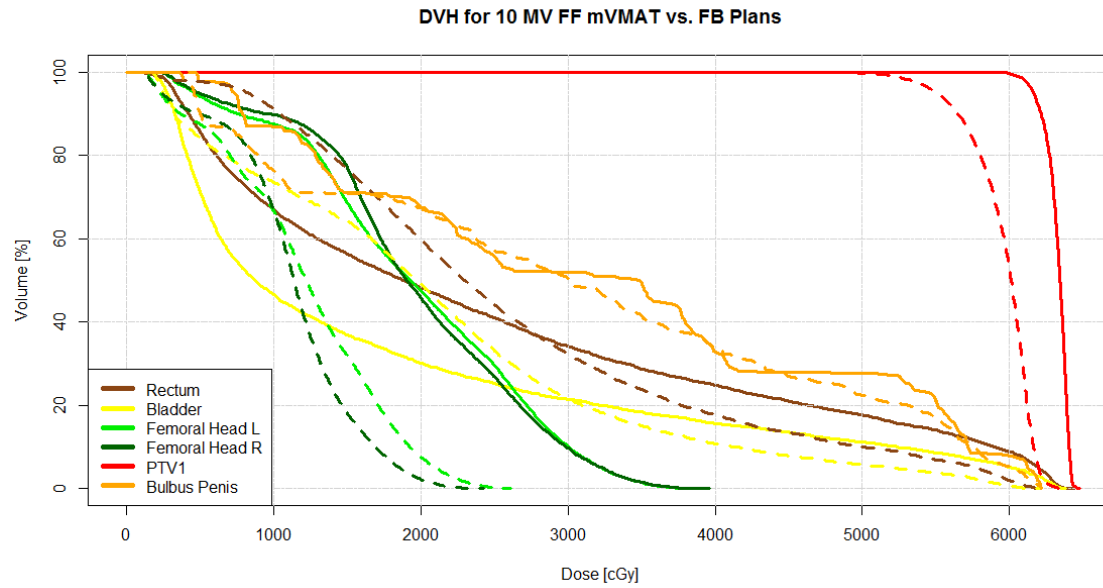


Figure 3.12: DVH of FB plan vs. mVMAT plan for a LR patient (LR01). Continuous lines represent the mVMAT plan and dashed lines represent the FB plan.

There seem to be clear differences in the way the MLC leaves move per segment for each plan type. The openings/windows created by the movement of the leaves are smaller for the segments of the FB plans: the maximum opening of FB plans is smaller by 5.6%-15.4% relative to that of mVMAT plans. This is supported by the fact that the delivery time per segment and the gantry speed per segment are lower by 16%-20% and higher by 18.5%-25%, respectively, for FB plans. Such behaviour can be deduced from Tables 3.12 and 3.13.

Table 3.12: Delivery time/segment [s] and gantry speed/segment [deg/s] for LR plans.

Machine	Beam model	Patient #	Plan type	Delivery time [s] /segment of beam	Gantry speed [deg/s] /segment of beam
VHD ^b	6 MV FF	all ^d	FB	0.96	4.16
			mVMAT	1.2	3.33
	10 MV FF	all ^d	FB	0.96	4.16
			mVMAT	1.2	3.33
C120 ^c	6 MV FF	5	FB	0.87 ^a	4.53 ^a
			mVMAT	0.95 ^a	4.21 ^a
		7	FB	0.83 ^a	4.73 ^a
			mVMAT	0.97 ^a	4.30 ^a
		10	FB	0.82 ^a	4.71 ^a
			mVMAT	0.89 ^a	4.45 ^a

a) Average values - averaged over the number of segments.

b) Versa HD

c) Clinac120

d) those exact values were found for all patients (LR05, LR07, LR10).

Table 3.13: Delivery time/segment [s] and gantry speed/segment [deg/s] for HR plans.

Machine	Beam model	Patient #	Plan type	Beam #	Delivery time [s] /segment of beam	Gantry speed [deg/s] /segment of beam	
VHD ^b	10 MV FF	6	FB	1	0.82	4.86	
				2	0.82	-4.88	
			mVMAT	1	0.98	4.10	
				2	0.98	-4.07	
		12	FB	1	0.81	4.93	
				2	0.81	-4.93	
			mVMAT	1	1.00	4.00	
				2	1.00	-4.00	
	6 MV FF	6	FB	1	0.81	4.92	
				2	0.82	-4.88	
			mVMAT	1	1.00	4.00	
				2	1.00	-4.00	
		12	FB	1	0.81	4.94	
				2	0.81	-4.94	
			mVMAT	1	1.00	4.00	
				2	1.00	-4.00	
C120 ^c	6 MV FF	6	FB	1	0.82 ^a	4.75 ^a	
				2	0.82 ^a	-4.75 ^a	
			mVMAT	1	0.84 ^a	4.62 ^a	
				2	0.87 ^a	-4.52 ^a	
			12	FB	1	0.82 ^a	4.75 ^a
					2	0.82 ^a	-4.75 ^a
		mVMAT		1	0.82 ^a	4.74 ^a	
				2	0.82 ^a	-4.74 ^a	

a) Average values - averaged over the number of segments.

b) Versa HD

c) Clinac120

A correlation between the delivery time per segment, the gantry speed per segment and the maximum delivery time entered at plan creation was hypothesized, so their dependency was studied by selecting one patient from each contingent and creating both FB and mVMAT plans with higher maximum delivery time (i.e. 180 s) using one of the models (10 MV FF) - see Table 3.14 - and by looking at the estimated delivery times per plan reported by the TPS - see Table 3.15.

Setting the maximum delivery time at twice its initial value also doubled the delivery time per segment and halved the gantry speed for both plan types, as can be seen by comparing the values from Table 3.14 with the values in the cells of light-gray background from Tables 3.12 and 3.13. The differences between mVMAT and FB plans were thus maintained.

Table 3.14: Segmentation differences with maximum delivery time (MDT) set at 180 s on the Versa HD for a selected patient from each indication.

Indication + Patient #	Beam model	Plan type	Beam #	Delivery time [s] /segment of beam	Gantry speed [deg/s] /segment of beam
LR 7	10 MV FF	FB	1	1.92	2.08
		mVMAT	1	2.40	1.67
HR 12	10 MV FF	FB	1	1.60	2.50
			2	1.60	-2.50
		mVMAT	1	2.00	2.00
			2	2.00	-2.00

For plans created with the Versa HD beam models and delivered with the respective treatment machine, Fallback LR plans mostly have estimated delivery times below 75 s per arc, while HR FB plans take ~ 150 s to be delivered (since they are composed of two arcs). Delivery of single-arc mVMAT plans almost unanimously takes 90 s and of double-arc mVMAT plans twice as much. The estimated delivery time also doubles when double the initial maximum delivery time is entered, with FB plans still taking less until delivered .

No clear pattern is immediately apparent for plans created with the Clinac120 beam model and delivered with the respective treatment machine, except for the observation that the difference in estimated delivery time between FB and mVMAT plans appears to be smaller, with mVMAT plans generally taking slightly longer to be delivered (i.e. maximally 80 s), or on some occasions an equal amount of time (see Table 3.15).

Table 3.15: Estimated delivery time [s] for plans created with the Versa HD (VHD) and the Clinac120 (C120).

Patient #	Beam #	VHD				C120	
		6 MV FF		10 MV FF		6 MV FF	
		FB	mVMAT	FB /FB ^a	mVMAT/mVMAT ^a	FB	mVMAT
LR05	1	72	90	72	90	66	73
LR07	1	72	90	72/144	90/180	64	73
LR10	1	72	90	72	90	63	68
HR06	1	73	90	74	88	75	77
	2	74	90	74	88	75	80
HR12	1	73	90	73/144	90/180	75	75
	2	73	90	73/144	90/180	75	75

a) with maximum delivery time (MDT) set at 180 s

This matter is further addressed in section 4.3.

4 Discussion

4.1 Beam Modeling

During the beam modeling process, several observations regarding the capabilities and limitations of the RayPhysics beam commissioning module were made, which will be discussed here. Up to the version used in this thesis (v4.99.1.3) RayPhysics does not support the import of diagonally scanned curves, so all imported curves (lateral profiles) had both gantry and collimator angle set to 0.00 in their respective .mcc-files, where NOT_DIAGONAL was additionally mentioned. Furthermore, the majority of the imported curves were both centered and symmetrical. Since all modeled beams (their respective lateral profiles) are also centered and symmetrical, this eased the commissioning process, although the lateral profiles of the FFF beams (and hence their respective measured curves) have proven a slight asymmetrical behaviour. This asymmetry is exhibited by Elekta linacs for beams of energies up to 10 MV (as were all beams modeled throughout this thesis) and is attributed to such linacs not being equipped with a phase shifter. This behaviour is no longer found for linacs producing beams with an energy of 18 MV. A 100% agreement between measured and computed lateral profiles of both FFF beam models was therefore never expected.

Because of the forward-peaked shape of the FFF lateral profiles, the usual definition of the penumbra as the distance between the 20% and 80% dose levels, with the dose normalized to 100% on the central beam axis, can no longer be applied. In order to provide a satisfactory definition for the penumbra the FF and FFF profiles need to be mutually normalized to make them superimpose at their field edges [44]. Two methods of achieving this have so far been introduced: the inflection point normalization proposed by Pönisch in [18] and the renormalization value method proposed by Fogliata in [44, 45].

In [18] the penumbra is defined as the spatial distance between the positions of 20% and 80% of the normalized dose $D_n = \frac{D_u}{D_f} \cdot D_{CAX}$, where D_u and D_f are the doses at the inflection points of the penumbrae of the unflattened and the flattened profile, respectively, and D_{CAX} is the central axis dose of the flattened beam.

Because the inflection point normalization comes with an inarguable uncertainty, a new method was introduced in [44]. Therein the so-called “shoulder point” of FF beam lateral profiles is used to renormalize the corresponding FFF beam to the same dose level exhibited by the FF beam at that point. The shoulder point is located in a region of shallow dose gradient and is a maximum in the third derivative of the profile. Its position in the shallow dose gradient region ultimately results in the reduction of the uncertainty which was inherent in the inflection point method. The latter, on the other hand, can be used without an FF reference beam, which makes it valuable for machines that can only produce FFF beams (e.g. CyberKnife, TomoTherapy and MR-linac).

It is, however, unknown which of the two methods is used by RayPhysics to define the penumbra since the only definition offered in the RayPhysics Manual [20] is the one already given in the introductory section of this thesis (section 1.4.3) and the only steps that differed from the procedure followed for FF beam commissioning were setting all off-axis values to zero, ticking the “Flattening filter free” checkbox in the fluence tab and setting a reduced yet non-zero value for the weight of the flattening filter photon source. The matter was, of course, raised with RaySearch Laboratories AB, yet up to the time this issue was addressed in this thesis, no reply was received.

Modeling the MLC was undertaken in two separate steps: first, values available from the machine vendor were entered (after having worked on the beam parameters in the energy spectrum, off-axis and output factor correction tabs) and the remaining parameters in the fluence tab concerning the MLC were then entered according to calculations and/or the independent verification process. The leaf tip width was long dwelled on, seeing as according to the RayPhysics Manual, modeling should start with the leaf tip width projection at isocenter [20], yet its actual value was calculated at 0.65 cm and consequently its projection at isocenter at 1.85 cm. The RayPhysics application, however, only allowed values between 0.00 cm – 1.00 cm. This matter was raised with RaySearch Laboratories AB (Stockholm, Sweden), who up to the time this issue was addressed in this thesis had not yet provided an explanatory reply. Three values were tested for the leaf tip width: 0.1 cm, 0.65 cm and

1.0 cm, the changes in the modeled lateral profiles were carefully observed and a final value was chosen accordingly. Entering various values for the leaf tip width only affected the crossplane (CR) lateral profiles, as was expected, since that is the direction of leaf motion. The value of 0.1 cm was quickly discarded, since it represented only the default value of the copied template machine and clearly did not reflect neither actual or projected value. With a value of 1.0 cm the tails in the out-of-field region of the FF CR profiles were raised and a diminished agreement between measured and calculated CR profiles for the small field sizes of the FFF beam models was observed. In the end a leaf tip width of 0.65 cm (corresponding to the actual value of the leaf tip width) was entered for all four beam models, which as previously stated has only influenced the agreement between measured and computed lateral profiles in the crossline (CR) direction.

4.2 Beam Model Verification

The RMS differences reported by RayPhysics for the PDDs and the lateral profile curves and their occasional exceedance of their respective limits per curve region (given in section 3.1) has also been documented in [35], with similar exceedances observed for the same type of field sizes, i.e. in the out-of-field region for larger field sizes (where a maximum RMS difference of 5.3% and 7.9% was found for the FFF and FF beam models, respectively) and the in-field region for small field sizes (maximum RMS difference of 3.4% and 3.8% for the FFF and FF beam models, respectively). An exceedance of the 3% in-field region tolerance (by as much as 1.4%) was, however, additionally observed for the largest depth of the larger field sizes of the FF beams modeled throughout the course of this master's thesis. The tolerance for the build-up region was exceeded for small field sizes in the present thesis (by 0.2%-0.6% and only for the 10 MV FFF beam model), as opposed to the same effect occurring for large field sizes in [35].

The impossibility of reaching good agreement for the out-of-field region of larger field sizes, reported also in [35], can be partially explained by the fact that RayStation uses a no-tilt approximation, which leads to narrower dose distributions that are additionally more intense along the beam axis compared to dose distributions resulting from kernel tilt computations [21]. Although RayStation does apply a correction, the beam's dose distribution still remains narrower than it would have been, if computed with a kernel tilt. Another possible explanation for out-of-field disagreements between measured and computed curves could be the limits of the collapsed cone convolution algorithm itself, which is said to lose accuracy when used for either small or large field sizes, small SSDs, high energies and off-axis fields, according to [21]. This is supported by the findings in [39], where the CCC algorithm seems to overestimate doses in the build-up regions of small field sizes and underestimate doses for large field sizes.

Poor agreement between measured and computed curves for other regions may be caused by modeling limitations of RayPhysics, such as the fact that only an average transmission can be entered for the MLC or the energy spectrum is made up of discrete energy bins (as opposed to e.g. the continuous energy spectrum in Monaco) or the electron contamination can only be modeled by changing two parameters. Most disagreements were found for large field sizes and since at the Department of Radiation Oncology of the AKH Wien/Medical University of Vienna it is common practice to focus on optimizing for smaller field sizes (in order to increase model accuracy for IMRT, VMAT and stereotactic applications), while compromising the larger field sizes, such disagreements were tolerated.

In case of the 6 MV FF and the 6 MV FFF beam models, the results obtained during the verification stage can be compared to the results reported in [31], since the models of the exact same machine yet created with another TPS were verified therein. The results for both models seem to be comparable as far as both the independent GPR analysis and the output factor verification are concerned. The GPR-analysis performed in [31] revealed mean γ_{mean} -values (for every field size) between 0.22 and 0.63 for the 6 MV FF beam model and between 0.16 and 0.33 for the 6 MV FFF model. In this thesis the mean γ_{mean} -values were obtained differently, namely for every model per profile type, i.e. mean γ_{mean} -values of 0.19 ± 0.06 and 0.16 ± 0.06 for the PDDs, 0.41 ± 0.25 and 0.37 ± 0.16 for the CR profiles, 0.48 ± 0.33 and 0.39 ± 0.18 for the IN profiles were obtained for the 6 MV FF and the

6 MV FFF beam models, respectively. There is no real difference between the models created for this thesis and the models based on the pencil beam algorithm from [31].

The average deviations of the calculated output factors from the measured ones do seem to be slightly smaller than those reported in [31], however, this might be due to the larger number of field sizes being considered in the present thesis (15, as opposed to 13 considered for output factor verification in [31]). For this thesis, the two average output factor deviations were calculated at -0.05 ± 0.57 and -0.06 ± 0.49 for the 6 MV FF and the 6 MV FFF beam model, respectively, showing almost no variation between the two models.

The average local GPR of $(95.15 \pm 2.00)\%$ obtained for the 6 MV FF beam model alone is in fair agreement with that disclosed by [33], $(95.2 \pm 2.8)\%$, where the Agility MLC was modeled with Pinnacle³ and the model was then verified with 6 MV FF VMAT QA plans.

However, of the four beam models created over the course of this thesis, the 6 MV FF seems to be the weakest, since first the ANOVA revealed the FF models to differ from the FFF models on a statistically significant level (p-values of 0.0% for both median dose deviation and local GPR) and the mean local GPRs of the FF models were shown to be lower compared to the values for the FFF models in section 3.3. Secondly, a further look at the mean median dose deviation and the mean local GPR reveals the lowest values for the 6 MV FF beam model ($-2.02\% \pm 0.20\%$ and $94.49\% \pm 1.71\%$), establishing it as the weakest of the two FF models.

The higher $\gamma_{<1}$ percentages of CR profiles relative to those of the IN profiles obtained during the MATLAB verification might be attributed to the additional option of MLC modeling, whose leaf motion occurs along the x-direction (crossline/CR), indicating that the chosen value for the leaf tip width was reasonable. Since the same observation was made in [35], where only MLC modeling was undertaken with RayStation, this explanation is justified.

The average results of the treatment-delivery verification (QA plan delivery) - see Table 3.5 - were found to be between $(99.2 \pm 1.5)\%$ and $(85.3 \pm 7.5)\%$, disclosed in [35] and $(90.1 \pm 4.0)\%$, disclosed in [34] which seems reasonable since the pass/fail criteria used herein are a combination of those used in the two abovementioned publications, i.e. (3% G/3 mm) and (2% L/2 mm) in [35] and (2% L/2 mm) in [34].

As far as the FFF models are concerned, they appear to slightly outperform their flattened counterparts during the verification procedures, exhibiting higher GPRs during the QA plan delivery verification (thus yielding the mean local GPR of $97.36\% \pm 1.86\%$, higher than the $95.14\% \pm 2.15\%$ obtained for the FF models) and lower average point dose differences from measured point doses (as showed in Table 3.3). This can be presumably attributed to the reduction of treatment head scatter radiation and of scatter radiation variation with field size attained by flattening filter removal [46].

The F- and t-tests assume normally distributed data, therefore the validity of the p-values for the local GPR is questionable, given that the local GPRs are and cannot be normally distributed, as they are restricted to the closed interval [0,100]. For instance the t-test performed for the median dose deviations of the 6 MV FF & 10 MV FF beam models implies statistically relevant differences (p-value=1.2%) whereas the t-test performed for the local GPRs of the same two models states the opposite (p-value=37.1%). However, given that the local GPRs are not normally distributed (and a test of normality has indeed been performed on the local GPR-values obtained for the 10 MV FF beam model, for which the largest data sample was available), the t-test results for the local GPR values cannot be relied on, thus increasing the significance of the t-test results for the median dose deviation. This is the reason why a Mann-Whitney-Wilcoxon U-test (which does not assume any parametric distribution of the observations) was used for both median dose deviation data (as a means of control) and local GPR data.

The slight superiority of the FFF models is also supported by the ANOVA performed on the results of the LR treatment-delivery verification. However, an individual FFF model could not be shown to be better than the other since a t-test on the median dose deviation values resulting from QA plan delivery showed no statistically significant difference (p-value 48.3%). This conclusion was based on the student's t-test performed on the median dose deviations and the U-test performed

on both median dose deviation data and local GPR data.

The overall mean local GPR for FFF plans of $(97.36 \pm 1.86)\%$ is similar to the mean GPR-value of 95.90% from [40], where the FFF beams of Varian TrueBeam linacs were modeled with a TPS also based on the CCC algorithm, Pinnacle³. The median GPR of 97.0% reported in [22], where both RayStation and Monaco were used to model the FFF beams of an Elekta Versa HD linac, is equally similar to the values obtained in this study. The fact that the difference to the median GPR from [22] seems to be negligible is encouraging, given that the linac/TPS combination is the same as the one employed for the work related to this thesis.

Average point dose differences from measured point doses are below 1%, just as those disclosed in [32], where the beams (including FFF) of a Versa HD linac were commissioned with Pinnacle³.

The output factors of FFF beams are higher than those of their corresponding flattened beams for field sizes below $10 \text{ cm} \times 10 \text{ cm}$ and smaller for field sizes above $10 \text{ cm} \times 10 \text{ cm}$ (a behaviour which can be observed by comparing Table B.9 with Table B.11 and Table B.10 with Table B.12), which is in agreement with the observations made in [40]. The best modeling results have indeed been observed for small fields, confirming the findings of [22]. Another discovery shared with [22] for FFF beams involves the out-of-field region, where less agreement with measured curves has been noticed, especially for larger field sizes (i.e. $\geq 20 \text{ cm} \times 20 \text{ cm}$) and more so for the 6 MV FFF beam model. This may be due to the fact that in RayPhysics the off-axis softening is completely eliminated during the FFF modeling process.

The delivery of FFF plans took place with a time-lag relative to that of FF plans on grounds of additional Delta⁴-phantom calibrations and linear accelerator tuning necessary for FFF mode irradiation. Machine tuning was required because of the differences between the two irradiation modes and the fact that the machine is routinely being used in FF mode, but rather seldomly for dynamic treatments in FFF mode. FFF beams are mainly characterized by higher dose rates and hence faster and shorter delivery times, and somewhat modified energy spectra and dose profiles, particularly in the out-of-field region. This last characteristic feature of FFF beams would explain the smaller out-of-field disagreement hereby observed for the $40 \text{ cm} \times 40 \text{ cm}$ field size of the FFF models.

FFF plan delivery was further prolonged by repeated dose rate errors occurring throughout the irradiation of most plans and for the most part in the quadrant between 180° and 270° , suggesting that machine/linac readjustments might be required.

Given the improvement observed in the local GPRs of each beam model's worst plans when using a digital Delta⁴ phantom of mass density 1.19 g/cm^3 and the absence of any significant change in the GPRs of the best plans, the recommendation would be to continue using the universal value of 1.19 g/cm^3 for both beam qualities. The convolution-superposition step in the CCC algorithm is effective density-dependent and therefore mass density-dependent and since below 10 MV the dominating interaction process is the Compton effect, a mass density of 1.19 g/cm^3 shared by both beam qualities is justified [21].

4.3 FB vs. mVMAT Plan Comparison

Since the windows created per segment by the MLC are smaller for the FB plans and judging from the information gathered from Tables 3.12 and 3.13, i.e. the lower delivery time/segment and higher gantry speed/segment of FB plans, a reasonable conclusion would be that the leaves move less and consequently faster when delivering FB plans. This translates to less dose modulation and consequently lower plan quality, in agreement with the observations regarding the dose distributions and DVH curves from section 3.5.

A possible explanation for the lower delivery times per segment and higher gantry speeds per segment of FB plans involves the maximum delivery time set for each plan type (90 seconds) and the way it is dealt with by every plan type. This is plausible since the VMAT treatment technique

is used in both plan types and the VMAT optimization process and therefore the resulting VMAT plans are influenced by the entered maximum delivery time [47].

The mVMAT plans seem to take the maximum delivery time for granted and simply divide it evenly by the total number of segments, thus giving a constant number for the delivery time per segment (i.e. 1.2 s for LR plans and on average 0.995 s for HR plans) and the gantry speed per segment (i.e. 3.33 deg/s for LR plans and on average ± 4.05 deg/s for HR plans). The FB plans, on the other hand, treat the maximum delivery time as a real upper limit that should preferably not be reached, meaning they strive to deliver the dose faster (i.e. in 0.96 s for LR plans and 0.81 s for HR plans), with a higher gantry speed (i.e. 4.16 deg/s for LR plans and on average ± 4.91 deg/s for HR plans), giving them less time to make significant leaf movements.

The hypothesis connecting the maximum delivery time with the segmentation differences between manually created VMAT plans and FB plans is supported by the fact that those differences were noted to be smaller for the Clinac120, which did not allow a maximum delivery time setting, for either plan type. This is also the reason why the delivery time per segment and the gantry speed per segment were tabularized as average values for the Clinac120 (Tables 3.12 and 3.13), since the constant values per segment observed for the Versa HD, which did allow a maximum delivery time setting, no longer occur.

4.4 Beam Model Comparison

The plans created at MedAustron with RayStation were imported into the oncology information system at the LKH Wiener Neustadt as created. The transfer and import processes were executed by representatives of the two facilities and were therefore not witnessed by the author of this thesis. This procedure also proved the possibility of successfully transferring plans from MedAustron to the LKH Wiener Neustadt in spite of the two treatment locations relying on different TPSs. Since the ultimate goal of Fallback Planning will be to temporarily and above all rapidly enable treatment with photons in case of a synchronon breakdown at MedAustron and a plan transfer has been achieved, the abovementioned procedure could become standard practice in contingency situations, provided the Fallback Planning Module is approved for clinical use.

The fact that the Versa HD model consistently underestimates the dose and the Clinac120 consistently overestimates the dose is an indicative of systematic errors of dose calculation affecting both the Versa HD beam model and the Clinac120 beam model. The absolute values of either deviations, however, are within acceptable ranges and may be caused by calibration uncertainties of either the linac or the detector or both.

Given that LR plans are of low complexity, a very good performance of both beam models was hereby expected. The quality of both beam models and their possible limitations was therefore revealed through their respective performances with the more complex HR plans. The somewhat poorer performance of the Clinac120 revealed in section 3.4 would suggest a need for optimization in case of the Clinac's generic model.

Though a statistically significant difference was found between the LR results of Versa HD and Clinac120, no immediate statistical conclusion could be drawn for the HR indication since a t-test and a U-test on the obtained median dose deviations values revealed a difference on a statistically significant level (p-values of 0.0% and 2.9% for the t-test and U-test, respectively), yet a U-test performed on the local GPRs resulting from HR plan irradiation contradicted the findings provided by the tests on the median dose deviations (p-value of 88.5%). However, this may be attributed to the very large differences between the standard deviations of the two data sets. The U-test was again required due to the fact that the local GPRs were not normally distributed, as a t-test automatically assumes. Of course, having such a small sample (at least from a statistical perspective) for both indications (6 plans and 4 plans, respectively) and even a significant outlier among those 4 plans, raises the question of whether a conclusion can be drawn at this moment at all. Therefore any observation made concerning the performance of the two treatment machines relative to one another should be carefully considered.

5 Conclusions and Outlook

Four beam models - both flattened and unflattened modes of the 6 MV and 10 MV beam qualities - were created in RayPhysics following the procedure recommended by RayStation. The models were verified both during the commissioning process - using the RayPhysics in-built fit quality calculator - and after having reached acceptable beam parameters - using an in-house developed MATLAB code to perform a γ -index analysis with 2 mm DTA/2% DD acceptance criteria. Testing the clinical performance of the new beam models as part of the verification process was achieved by creating a total number of 57 clinical treatment plans with the models and transforming those plans into QA plans which were later delivered to a Delta⁴ phantom, whose software performed a local GPR analysis with 3mm DTA/3% local DD acceptance criteria. One of the four models (the 6 MV FF beam model) was also subsequently compared to a model of corresponding beam quality and mode of a Varian machine - the Clinac120. The FF models were also used to assess the capabilities and limitations of RayStation's Fallback Planning Module (a work performed by bachelor student Florine Enengl in her bachelor's thesis [43]) and to compare plans obtained using the Fallback protocol with manually created plans (a task that was shared with the previously mentioned bachelor student).

The four beam models created over the course of this master's thesis have proven to be accurate enough for clinical implementation, having generally passed the independent γ -index analysis. Acceptable deviations from point dose measurements were observed, as well as low differences between measured and computed output factors and local GPR values higher than the 90% threshold, in general, during the treatment-delivery verification.

The weakest of the models appears to be the 6 MV FF model, which exhibited the lowest $\gamma_{<1}$ -values during the MATLAB verification (see Table 3.2) as well as the highest mean median dose deviation and the only average local GPR slightly lower than 95% during the treatment-delivery verification (see Table 3.5). Its somewhat weaker performance with the LR indication in direct comparison with the Clinac120's supports this assessment. In conclusion, a revision and subsequent additional fine tuning might be recommendable for the 6 MV FF beam model.

A comparison between the VMAT plans obtained with the Fallback Planning Module and the manually created VMAT plans revealed clear segmentation differences which have been attributed to the way each plan type interprets the maximum delivery time entered by the planner.

Although the FB plans exhibited higher individual local GPR values and thus more accuracy in delivering planned doses, due to the lower degree of modulation, after having compared the dose distributions and DVHs of FB and mVMAT plans the question of whether the FB plans manifested sufficient target coverage to make them clinically acceptable still stands and was adequately addressed in the bachelor's thesis of Florine Enengl [43]. A possible outlook, therefore, may involve testing the performance of FB planning against manual planning for indications of even higher complexity than that of the HR prostate carcinoma indication and/or other treatment techniques and modalities and placing a special emphasis on treatment plan quality. As far as could be established throughout the work performed for this master's thesis, the performance of the Fallback Planning Module as compared with manually created plans leads to the conclusion of additional optimization of the FB Planning module being required.

An outlook on possible ways of expansion of the models might include adding beam modifiers, such as wedges, i.e. creating wedge models, since the object of this thesis has only been to create the open beam models and given that open models are always the starting point for their wedged counterparts. The TPS also supports modeling of blocks or cones, giving a further possibility of extension of this work. The hereby created beam models thus represent the cornerstone for all other additions.

Furthermore, though the entered leaf tip width seems to have given satisfactory results, it still represents the actual, physical value and this is in contradiction of the recommendation made in the RayPhysics Manual. The author of this thesis therefore recommends deeper enquiries and eventual

subsequent adjustments to the models.

Finally, as far as the generic model of Clinac120 is concerned, its performance with the more complex cases of the HR indication led to the conclusion of its imperative revision and improvement being required so as to make it acceptable for clinical practice. Measurements with the same detector for both the Versa HD and the Clinac120 are recommended in the future, in order to dismiss the possibility of the median dose deviations being attributed to detector calibration uncertainties.

References

- [1] Philip P. Connell and Samuel Hellman. Advances in Radiotherapy and Implications for the Next Century: A Historical Perspective. *Cancer Research*, 69(2):383–392, 2009. v, 2, 3, 4, 5
- [2] Faiz M. Khan and John P. Gibbons. *The Physics of Radiation Therapy*. LIPPINCOTT WILLIAMS & WILKINS, fifth edition, 2014. v, 7, 8, 14, 27, 28, 29, 30
- [3] P. Mayles, A. Nahum, J. C. Rosenwald, and Niko Papanikolaou. *Handbook of Radiotherapy Physics: Theory and Practice*. Taylor & Francis Group, 2008. v, 2, 3, 4, 7, 8, 9, 12, 13, 14, 15, 16, 17, 18, 19, 20, 21, 22, 23
- [4] David R. Tobergte and Shirley Curtis. *Textbook of Radiotherapy*. 2013. v, 9, 10, 11, 14, 15, 16, 22, 23, 27, 28
- [5] Ervin B. Podgoršak. *Radiation Physics for Medical Physicists*. Springer-Verlag Berlin Heidelberg GmbH, second edition, 2010. v, 2, 4, 6, 7, 8, 9, 10, 11, 12, 13, 14, 15, 16, 17, 18, 19, 20
- [6] Wolfgang Lechner. *Dosimetric evaluation of flattening filter free photon beams*. PhD thesis, 2014. v, 20
- [7] International Atomic Energy Agency. *Radiation Oncology Physics: A Handbook for Teachers and Students*. International Atomic Energy Agency, 2008. v, 2, 21, 22, 23, 24, 27
- [8] H.D. Kogelnik. The History and Evolution of Radiotherapy and Radiation Oncology in Austria. *International Journal of Radiation Oncology*Biophysics*, 35(2):219–226, 1996. 2
- [9] Ronald C. McGarry, Lech Papiez, Mark Williams, Tia Whitford, and Robert D. Timmerman. Stereotactic Body Radiation Therapy of Early-Stage Non-Small-Cell Lung Carcinoma: Phase I Study. *International Journal of Radiation Oncology*Biophysics*, 63(4):1010–1015, 2005. 3
- [10] Esam M. A. Hussein. *Radiation Mechanics: Principles and Practice*. Elsevier, 2007. 13
- [11] S Jayaraman and L H Lanzl. *Clinical Radiotherapy Physics*. Springer-Verlag Berlin Heidelberg GmbH, second edition, 2003. 17
- [12] Dietmar Georg, Gabriele Kragl, Sacha af Wetterstedt, Patrick McCavana, Brendan McClean, and Tommy Knöös. Photon Beam Quality Variations of a Flattening Filter Free Linear Accelerator. *Medical physics*, 37(1):49–53, January 2010. 20
- [13] Gabriele Kragl, Sacha af Wetterstedt, Barbara Knäusl, Märten Lind, Patrick McCavana, Tommy Knöös, Brendan McClean, and Dietmar Georg. Dosimetric characteristics of 6 and 10MV unflattened photon beams. *Radiotherapy and Oncology*, 93(1):141–146, 2009. 20
- [14] Jason Cashmore. The Characterization of Unflattened Photon Beams from a 6 MV Linear Accelerator. *Physics in medicine and biology*, 53(7):1933–46, April 2008. 20
- [15] Sotirios Stathakis, Carlos Esquivel, Alonso Gutierrez, Courtney R. Buckey, and Niko Papanikolaou. Treatment Planning and Delivery of IMRT Using 6 and 18MV Photon Beams without Flattening Filter. *Applied Radiation and Isotopes*, 67(9):1629–1637, 2009. 20
- [16] Oleg N Vassiliev, Uwe Titt, Falk Pönisch, Stephen F Kry, Radhe Mohan, and Michael T Gillin. Dosimetric properties of photon beams from a flattening filter free clinical accelerator. *Physics in medicine and biology*, 51(7):1907–17, April 2006. 20
- [17] Weihua Fu, Jianrong Dai, Yimin Hu, Dongsheng Han, and Yixin Song. Delivery time comparison for intensity-modulated radiation therapy with/without flattening filter: a planning study. *Physics in Medicine and Biology*, 49(8):1535–1547, April 2004. 20

- [18] Falk Pönisch, Uwe Titt, Oleg N. Vassiliev, Stephen F. Kry, and Radhe Mohan. Properties of Unflattened Photon Beams Shaped by a Multileaf Collimator. *Medical Physics*, 33(6):1738–1746, 2006. [20](#), [66](#)
- [19] Gabriele Kragl, David Albrich, and Dietmar Georg. Radiation Therapy with Unflattened Photon Beams: Dosimetric Accuracy of Advanced Dose Calculation Algorithms. *Radiotherapy and Oncology*, 100(3):417–423, 2011. [20](#)
- [20] RaySearch Laboratories. *RayStation 5 RayPhysics Manual*. [20](#), [22](#), [23](#), [24](#), [34](#), [35](#), [36](#), [66](#)
- [21] RaySearch Laboratories. *Raystation 5 Reference Manual*. [21](#), [22](#), [26](#), [27](#), [67](#), [69](#)
- [22] S Valdenaire, H Mailleux, and P Fau. Modeling of Flattening Filter Free Photon Beams with Analytical and Monte Carlo TPS. *Biomedical Physics & Engineering Express*, 2(3):035010, 2016. [24](#), [32](#), [69](#)
- [23] Wen-Zhou Chen, Ying Xiao, and Jun Li. Impact of Dose Calculation Algorithm on Radiation Therapy. *World Journal of Radiology*, 6(11):874–80, 2014. [25](#), [26](#)
- [24] A Ahnesjö. Collapsed Cone Convolution of Radiant Energy for Photon Dose Calculation in Heterogeneous Media. *Medical Physics*, 16(4):577–592, 1989. [26](#)
- [25] *Prescribing, recording, and reporting photon beam therapy; issued: 1 September 1993*. ICRU report ; 50. ICRU Publ., Bethesda, Md., 1993. [28](#)
- [26] *Prescribing, recording, and reporting photon beam therapy; issued: 1 November 1999 (supplement to ICRU Report 50)*. ICRU report ; 62. ICRU Publ., Bethesda, Md., 1999. [28](#)
- [27] F.M. Khan. *Treatment Planning in Radiation Oncology*. LWW medical book collection. Lippincott Williams & Wilkins, 2007. [28](#)
- [28] RaySearch Laboratories. *Raystation 5 User Manual*. [31](#)
- [29] Daniel A. Low, William B. Harms, Sasa Mutic, and James A. Purdy. A Technique for the Quantitative Evaluation of Dose Distributions. *Medical Physics*, 25(5):656, 1998. [31](#)
- [30] Markus Stock, Bernhard Kroupa, and Dietmar Georg. Interpretation and Evaluation of the Gamma Index and the Gamma Index Angle for the Verification of IMRT Hybrid Plans. *Physics in Medicine and Biology*, 50(3):399–411, 2005. [32](#)
- [31] Alexander Primežnig. Validation of 6 MV flattening filter free and flattening filter beam models in iPlan, 2016. [32](#), [67](#), [68](#)
- [32] Daniel L. Saenz, Ganesh Narayanasamy, Wilbert Cruz, Nikos Papanikolaou, and Sotirios Stathakis. Pinnacle3 Modeling and End-to-End Dosimetric Testing of a Versa HD Linear Accelerator with the Agility Head and Flattening Filter-Free Modes. *Journal of Applied Clinical Medical Physics*, 17(1):192–206, 2016. [32](#), [69](#)
- [33] James L. Bedford, Michael D. R. Thomas, and Gregory Smyth. Beam Modeling and VMAT Performance with the Agility 160-Leaf Multileaf Collimator. *Journal of Applied Clinical Medical Physics / American College of Medical Physics*, 14(2):4136, 2013. [32](#), [68](#)
- [34] A Savini, F Bartolucci, C Fidanza, F Rosica, and G Orlandi. Optimisation and Assessment of the MLC Model in the RayStation Treatment Planning sSstem. *ESTRO 35, 29 April - 3 May 2016, Turin, Italy*, 119:S380–S381, 2016. [32](#), [68](#)
- [35] Bongile Mzenda, Koki V Mugabe, Rick Sims, Guy Godwin, and Dayan Loria. Modeling and Dosimetric Performance Evaluation of the RayStation Treatment Planning System. *Journal of Applied Clinical Medical Physics / American College of Medical Physics*, 15(5):29–46, 2014. [32](#), [33](#), [67](#), [68](#)

- [36] B Mzenda, K V Mugabe, R Sims, and D Loria. RayStation vs Pinnacle Modelling and System Performance: Implications for Small Field Dosimetry. In *ESTRO 33, 2014*, volume 111, page S67. Elsevier Masson SAS, 2014. [32](#), [33](#)
- [37] S. Lim and T. LoSasso. Beam and MLC Commissioning and Assessment of Three Commercial Treatment Planning Systems. In *Medical Physics*, volume 39, page 3828. American Association of Physicists in Medicine. [32](#), [33](#)
- [38] P Francescon, C Cavedon, S Reccanello, and S Cora. Photon Dose Calculation of a Three-Dimensional Treatment Planning System Compared to the Monte Carlo Code BEAM. *Medical Physics*, 27(7):1579–1587, 2000. [33](#)
- [39] Woong Cho, Jeong-hoon Park, Won-gyun Jung, Jeong-woo Lee, Lei Xing, and Tae-suk Suh. Practical Implementation of the Collapsed Cone Convolution Algorithm for a Radiation Treatment Planning System. *Journal of the Korean Physical Society*, 61(12):2073–2083, 2012. [33](#), [67](#)
- [40] Ryan D. Foster, Michael P. Speiser, and Timothy D. Solberg. Commissioning and Verification of the Collapsed Cone Convolution Superposition Algorithm for SBRT Delivery Using Flattening Filter-Free Beams. *Journal of Applied Clinical Medical Physics / American College of Medical Physics*, 15(2):4631, 2014. [33](#), [69](#)
- [41] RaySearch Laboratories. *Raystation 5 Beam Commissioning Data Specification*. [34](#), [35](#)
- [42] PTW Freiburg. IONIZING RADIATION DETECTORS: Including Codes of Practice. Technical report, 2016. [35](#)
- [43] Florine Enengl. Automated Photon Plan Generation Based on a Proton Distribution - work in progress, 2016. [61](#), [71](#)
- [44] A Fogliata, R Garcia, T Knöös, G Nicolini, A Clivio, E Vanetti, C Khamphan, and L Cozzi. Definition of Parameters for Quality Assurance of Flattening Filter Free (FFF) Photon Beams in Radiation Therapy. *Medical Physics*, 39(10):6455–6464, 2012. [66](#)
- [45] Antonella Fogliata, Jens Fleckenstein, Frank Schneider, Marc Pachoud, Sarah Ghandour, Harald Krauss, Giacomo Reggiori, Antonella Stravato, Frank Lohr, Marta Scorsetti, Luca Cozzi, Harald Krauss, and Frank Lohr. Flattening Filter Free Beams from TrueBeam and Versa HD Units : Evaluation of the Parameters for Quality Assurance. *Medical Physics*, 43(1):205–212, 2016. [66](#)
- [46] Dietmar Georg, Tommy Knöös, and Brendan McClean. Current Status and Future Perspective of Flattening Filter Free Photon Beams. *Medical Physics*, 38(3):1280–93, 2011. [68](#)
- [47] RaySearch Laboratories. *RayStation 5 A Guide to Optimization*. [70](#)

A Machine Reports

A.1 FF Machine

Machine Report

Machine Properties

General

Name	VersaHD_FF (2)
Comment	Elekta VersaHD with Agility.
Commission time	15 Apr 2016, 16_05_08 (hr_min_sec)
Commissioned by	MEDAUSTRON\GMI
Dose curves computed with dose algorithm	Photon energy 6 MV: CCDose v3.2 Photon energy 10 MV: CCDose v3.2
Is machine commissioned	Yes
Photon energy definition	
Is machine deprecated	No
Electron beam capable	No
DMLC capable	Yes
Static arc capable	Yes
Modulated arc capable	Yes
Couch coordinate system definition	IEC 61217
Gantry and collimator coordinate system definitions	IEC 61217
Field coordinate system definition	IEC 61217
Jaw labeling standard	IEC 61217

Geometric

SAD [cm]	100.00
Allow all collimator angles	Yes
Allow all couch angles	Yes
Allow all gantry angles	No
Supported gantry angles start [deg]	180.1
Supported gantry angles, stop [deg]	180.0
Replace couch rotation by ring rotation	No
All angles are specified in the coordinate systems specified in the general section.	
Room view model	Schematic linac

Jaws

Maximum Y2 jaw position [cm]	20.00
Maximum jaw speed [cm/s]	8.50
Minimum Y2 jaw position [cm]	-12.00
No backup jaw	Yes
Reference field size X1/X2 [cm]	10.000
Reference field size Y1/Y2 [cm]	10.000
Jaw movement rule	Per segment
Source to Y1/Y2 jaw bottom distance [cm]	50.90
Thickness Y1/Y2 jaw [cm]	7.70

MLC

Has MLC	Yes
The machine has carriage	No
Allow interdigitation	Yes
Maximum leaf speed [cm/s]	3.50
Maximum tip difference [cm]	20.00
Maximum tip position [cm]	20.00
Minimum dynamic tip gap [cm]	0.30
Minimum static tip gap [cm]	0.30
Minimum tip position [cm]	-15.00
Source to MLC bottom distance [cm]	39.57
Thickness [cm]	9.28
MLC type	X
Use minimum dynamic tip gap for static fields	Yes

Leaf center position [cm]	Width [cm]
-19.75000	0.5000
-19.25000	0.5000
-18.75000	0.5000
-18.25000	0.5000
-17.75000	0.5000
-17.25000	0.5000
-16.75000	0.5000
-16.25000	0.5000
-15.75000	0.5000
-15.25000	0.5000
-14.75000	0.5000
-14.25000	0.5000
-13.75000	0.5000
-13.25000	0.5000
-12.75000	0.5000
-12.25000	0.5000
-11.75000	0.5000
-11.25000	0.5000
-10.75000	0.5000
-10.25000	0.5000
-9.75000	0.5000
-9.25000	0.5000
-8.75000	0.5000
-8.25000	0.5000
-7.75000	0.5000
-7.25000	0.5000
-6.75000	0.5000
-6.25000	0.5000
-5.75000	0.5000
-5.25000	0.5000
-4.75000	0.5000
-4.25000	0.5000
-3.75000	0.5000
-3.25000	0.5000
-2.75000	0.5000
-2.25000	0.5000
-1.75000	0.5000
-1.25000	0.5000
-0.75000	0.5000
-0.25000	0.5000
0.25000	0.5000
0.75000	0.5000
1.25000	0.5000
1.75000	0.5000
2.25000	0.5000
2.75000	0.5000
3.25000	0.5000
3.75000	0.5000
4.25000	0.5000
4.75000	0.5000
5.25000	0.5000
5.75000	0.5000
6.25000	0.5000
6.75000	0.5000
7.25000	0.5000
7.75000	0.5000
8.25000	0.5000
8.75000	0.5000
9.25000	0.5000
9.75000	0.5000
10.25000	0.5000
10.75000	0.5000
11.25000	0.5000
11.75000	0.5000



Machine Name
Commissioned by

VersaHD_FF (2)
MEDAUSTRON\GMI

Report creation time
Commission time

03 Sep 2016, 21:15:47 (hr:min:sec)
15 Apr 2016, 16:05:08 (hr:min:sec)

Leaf center position [cm]	Width [cm]
12.25000	0.5000
12.75000	0.5000
13.25000	0.5000
13.75000	0.5000
14.25000	0.5000
14.75000	0.5000
15.25000	0.5000
15.75000	0.5000
16.25000	0.5000
16.75000	0.5000
17.25000	0.5000
17.75000	0.5000
18.25000	0.5000
18.75000	0.5000
19.25000	0.5000
19.75000	0.5000

Dose rate

Maximum DMLC dose rate [MU/min]	500.00
Maximum static arc dose rate [MU/min]	500.00
Minimum MU per leaf travel distance [MU/cm]	0.30
Minimum static arc dose rate [MU/min]	50.00
Modulated arc dose rate	Variable

Beam quality specific dose rate settings

Maximum dose rate [MU/min]	Minimum dose rate [MU/min]	Nominal energy [MV]
500.00	0.00	6
450.00	0.00	10

Arc properties

Constant control point spacing (in arcs)	No
Limit MU per gantry degree	Yes
Maximum gantry angle speed [deg/s]	6.00
Maximum MU per gantry degree [MU/deg]	10.00
Minimum gantry angle speed [deg/s]	1.00
Minimum MU per arc segment [MU]	1.00
Minimum MU per gantry degree [MU/deg]	0.10
Supported gantry rotation direction (facing gantry)	Clockwise and counter clockwise
Supports variable couch angles	No
Use Arc burst mode	No
Use maximum gantry angle speed or maximum dose rate for each control point	No

Allowed arc gantry spacing

Arc spacing [deg]	Allowed
2.0	Yes
3.0	Yes
4.0	Yes

Block

Support blocks	No
----------------	----

Wedge

Wedge orientation coordinate system	IEC 61217
Elekta Motorized Wedge	No
Siemens Virtual Wedge	No
Standard Wedge	No
Varian Enhanced Dynamic Wedge	No

Cone

Nominal energy 6 MV

Photon Beam Quality, 6 MV

Output factors

Output factor depth [cm] 10.00

Output factors

Field size [cm]	Factor
1x1	0.66500
2x2	0.80100
3x3	0.84400
4x4	0.87900
5x5	0.90500
5x30	0.97700
6x6	0.93000
7x7	0.95100
8x8	0.97000
10x10	1.00000
14x14	1.04800
15x15	1.05800
20x20	1.09700
30x5	0.96900
30x30	1.14400
40x40	1.16400

Calibration

Resolution [cm] 0.20
 Calibration point
 SSD [cm] 90.00
 Depth [cm] 10.00
 Dose/MU [[Gy]/MU] 0.010000
 Measurement conditions
 Phantom size [cm] 55.00

Collimation settings

Field collimation	Modulation					
Jaws and MLC collimated	Open	Field size [cm]	Type	Depth offset [cm]	Detector height [cm]	Detector width [cm]
		1x1	Depth	0.00	0.01	0.11
		1x1	Profile	0.00	0.01	0.11
		2x2	Depth	0.00	0.01	0.11
		2x2	Profile	0.00	0.01	0.11
		3x3	Depth	0.00	0.01	0.11
		3x3	Profile	0.00	0.01	0.11
		4x4	Depth	0.00	0.55	0.55
		4x4	Profile	0.00	0.01	0.11
		5x5	Depth	0.00	0.55	0.55
		5x5	Profile	0.00	0.01	0.11
		5x30	Depth	0.00	0.55	0.55
		5x30	Profile	0.00	0.01	0.11
		6x6	Depth	0.00	0.55	0.55
		6x6	Profile	0.00	0.01	0.11
		7x7	Depth	0.00	0.55	0.55
		7x7	Profile	0.00	0.01	0.11
		8x8	Depth	0.00	0.55	0.55
		8x8	Profile	0.00	0.01	0.11
		10x10	Depth	0.00	0.55	0.55
		10x10	Profile	0.00	0.01	0.11
		14x14	Depth	0.00	0.55	0.55
		14x14	Profile	0.00	0.01	0.11
		15x15	Depth	0.00	0.55	0.55
		15x15	Profile	0.00	0.01	0.11
		20x20	Depth	0.00	0.55	0.55
		20x20	Profile	0.00	0.01	0.11
		30x5	Depth	0.00	0.55	0.55
		30x5	Profile	0.00	0.01	0.11
		30x30	Depth	0.00	0.55	0.55
		30x30	Profile	0.00	0.01	0.11
		40x40	Depth	0.00	0.55	0.55
		40x40	Profile	0.00	0.01	0.11

Curve quality

Field size [cm]	Dose curve type	Depth [cm]	Modulation	Build up	Fall off	Flatness	Symmetry	Penumbra width [cm]	In field	Penumbra	Out of field
1x1	Depth	0.00		8.3	0.9						
1x1	X	1.30					0.0	0.38	1.0	2.0	0.5
1x1	X	10.00					0.0	0.43	1.2	2.0	0.4
1x1	X	20.00					0.0	0.49	3.8	2.5	0.3
1x1	Y	1.30					0.0	0.26	2.1	5.2	0.6
1x1	Y	10.00					0.0	0.29	0.8	3.1	0.8
1x1	Y	20.00					0.0	0.32	3.4	2.9	1.0
2x2	Depth	0.00		7.2	0.5						
2x2	X	1.50					0.0	0.42	0.8	1.6	0.4
2x2	X	5.00					0.0	0.46	0.5	1.5	0.3
2x2	X	10.00					0.0	0.49	1.4	1.4	0.4
2x2	X	20.00					0.0	0.57	2.1	2.1	0.4
2x2	X	30.00					0.0	0.63	3.4	2.7	0.7
2x2	Y	1.50					0.0	0.28	1.8	0.5	0.7
2x2	Y	5.00					0.0	0.30	1.3	2.4	0.8
2x2	Y	10.00					0.0	0.33	0.4	2.7	0.9
2x2	Y	20.00					0.0	0.37	1.1	2.4	1.1
2x2	Y	30.00					0.0	0.41	2.1	2.1	1.2
3x3	Depth	0.00		7.1	0.4						
3x3	X	1.60					0.0	0.45	0.9	3.0	0.4

Field size [cm]	Dose curve type	Depth [cm]	Modulation	Build up	Fall off	Flatness	Symmetry	Penumbra width [cm]	In field	Penumbra	Out of field
3x3	X	5.00					0.0	0.49	0.9	2.5	0.4
3x3	X	10.00					0.0	0.55	1.6	2.6	0.3
3x3	X	20.00					0.0	0.62	2.1	3.3	0.3
3x3	X	30.00					0.0	0.74	3.6	4.6	0.4
3x3	Y	1.60					0.0	0.29	1.1	3.8	0.6
3x3	Y	5.00					0.0	0.32	0.8	4.0	0.7
3x3	Y	10.00					0.0	0.35	0.9	1.4	0.8
3x3	Y	20.00					0.0	0.40	0.6	2.6	0.9
3x3	Y	30.00					0.0	0.45	1.4	1.6	1.1
4x4	Depth	0.00		6.9	0.2						
4x4	X	1.60				0.4	0.0	0.44	0.6	1.6	0.4
4x4	X	10.00				1.2	0.0	0.55	0.9	1.9	0.5
4x4	X	20.00				1.1	0.0	0.63	0.8	1.8	0.5
4x4	Y	1.60				0.3	0.0	0.30	0.8	4.1	0.9
4x4	Y	10.00				0.7	0.0	0.37	0.7	2.5	1.0
4x4	Y	20.00				1.3	0.0	0.43	0.5	2.6	1.1
5x5	Depth	0.00		5.5	0.2						
5x5	X	1.50				0.5	0.0	0.44	0.6	1.7	0.5
5x5	X	1.60				0.5	0.0	0.45	0.7	1.7	0.5
5x5	X	5.00				1.1	0.0	0.50	0.5	1.4	0.5
5x5	X	10.00				1.7	0.0	0.56	0.7	1.4	0.5
5x5	X	20.00				2.4	0.0	0.67	0.8	1.5	0.5
5x5	X	30.00				2.9	0.0	0.77	0.8	1.9	0.6
5x5	Y	1.50				0.5	0.0	0.29	1.3	2.2	0.6
5x5	Y	1.60				0.4	0.0	0.30	1.1	2.0	0.6
5x5	Y	5.00				0.9	0.0	0.34	1.0	3.2	0.8
5x5	Y	10.00				1.5	0.0	0.38	0.9	2.7	0.9
5x5	Y	20.00				1.9	0.0	0.45	1.0	3.1	1.1
5x5	Y	30.00				2.3	0.0	0.52	1.1	3.8	1.2
5x30	Depth	0.00		4.6	0.2						
5x30	X	1.50				0.3	0.0	0.46	0.5	1.6	1.1
5x30	X	5.00				1.4	0.0	0.53	0.3	1.2	0.8
5x30	X	10.00				1.9	0.0	0.64	0.5	1.1	0.6
5x30	X	20.00				2.5	0.0	0.88	0.7	1.0	0.3
5x30	X	30.00				3.4	0.0	1.23	1.3	1.4	0.9
5x30	Y	1.50				6.1	0.0	0.28	0.6	11.2	2.2
5x30	Y	5.00				4.4	0.0	0.34	0.9	10.2	0.9
5x30	Y	10.00				2.8	0.0	0.40	1.7	7.8	1.2
5x30	Y	20.00				5.5	0.0	0.54	2.6	4.2	2.2
5x30	Y	30.00				9.8	0.0	0.73	4.2	3.3	3.0
6x6	Depth	0.00		4.7	0.2						
6x6	X	1.50				0.6	0.0	0.45	0.7	2.2	0.6
6x6	X	10.00				2.4	0.0	0.58	0.5	1.7	0.4
6x6	X	20.00				3.2	0.0	0.70	0.6	1.6	0.4
6x6	Y	1.50				0.5	0.0	0.30	0.7	2.4	0.6
6x6	Y	10.00				2.1	0.0	0.40	0.5	2.4	0.9
6x6	Y	20.00				2.7	0.0	0.48	0.9	2.6	1.2
7x7	Depth	0.00		4.3	0.2						
7x7	X	1.50				0.5	0.0	0.45	0.7	2.6	0.8
7x7	X	5.00				1.8	0.0	0.52	0.6	2.1	0.6
7x7	X	10.00				2.7	0.0	0.60	0.7	1.7	0.5
7x7	X	20.00				3.7	0.0	0.73	0.6	1.4	0.5
7x7	X	30.00				4.9	0.0	0.88	1.2	1.8	0.6
7x7	Y	1.50				0.6	0.0	0.30	0.3	4.4	0.5
7x7	Y	5.00				1.1	0.0	0.35	0.7	1.2	0.6
7x7	Y	10.00				2.5	0.0	0.41	0.6	1.7	0.7
7x7	Y	20.00				3.4	0.0	0.52	0.8	2.2	0.9
7x7	Y	30.00				4.2	0.0	0.62	1.5	2.9	1.2
8x8	Depth	0.00		4.2	0.2						
8x8	X	1.50				0.6	0.0	0.45	0.6	1.6	0.8
8x8	X	10.00				3.0	0.0	0.60	0.3	1.3	0.5
8x8	X	20.00				4.9	0.0	0.76	0.5	1.4	0.5

Field size [cm]	Dose curve type	Depth [cm]	Modulation	Build up	Fall off	Flatness	Symmetry	Penumbra width [cm]	In field	Penumbra	Out of field
8x8	X	30.00				5.2	0.0	0.91	1.1	2.0	0.6
8x8	Y	1.50				1.0	0.0	0.30	0.5	5.8	0.3
8x8	Y	10.00				2.3	0.0	0.42	0.6	2.8	0.6
8x8	Y	20.00				4.1	0.0	0.55	0.8	1.9	1.0
8x8	Y	30.00				5.2	0.0	0.66	1.5	2.2	1.3
10x10	Depth	0.00		4.6	0.1						
10x10	X	1.50				1.1	0.0	0.47	0.7	2.7	1.1
10x10	X	1.50				0.8	0.0	0.46	0.7	2.9	1.1
10x10	X	5.00				2.3	0.0	0.54	0.4	2.0	0.8
10x10	X	10.00				3.9	0.0	0.63	0.5	1.5	0.6
10x10	X	20.00				6.2	0.0	0.84	0.9	1.0	0.4
10x10	X	30.00				7.0	0.0	1.04	1.5	1.6	0.7
10x10	Y	1.50				1.6	0.0	0.32	0.5	4.9	0.4
10x10	Y	1.50				1.2	0.0	0.32	0.3	4.9	0.4
10x10	Y	5.00				1.7	0.0	0.37	0.6	2.4	0.4
10x10	Y	10.00				3.4	0.0	0.45	0.8	2.4	0.6
10x10	Y	20.00				5.2	0.0	0.61	1.6	2.2	1.1
10x10	Y	30.00				6.1	0.0	0.79	2.2	2.7	1.5
14x14	Depth	0.00		4.3	0.2						
14x14	X	1.50				1.4	0.0	0.47	0.6	3.0	1.7
14x14	X	10.00				4.4	0.0	0.68	0.4	1.5	0.8
14x14	X	20.00				7.1	0.0	0.99	1.3	1.3	0.6
14x14	Y	1.50				2.0	0.0	0.32	0.3	6.8	0.7
14x14	Y	10.00				3.9	0.0	0.49	1.0	2.9	0.6
14x14	Y	20.00				6.5	0.0	0.75	1.6	2.2	1.4
15x15	Depth	0.00		4.2	0.2						
15x15	X	1.40				1.5	0.0	0.47	0.8	3.2	1.8
15x15	X	1.50				1.5	0.0	0.47	0.6	3.7	1.8
15x15	X	5.00				2.3	0.0	0.56	0.5	2.3	1.3
15x15	X	10.00				4.3	0.0	0.69	0.5	1.4	0.8
15x15	X	20.00				7.4	0.0	1.02	1.0	1.0	0.7
15x15	X	30.00				9.1	0.0	1.44	2.7	2.3	1.5
15x15	Y	1.40				1.9	0.0	0.32	0.6	5.2	0.8
15x15	Y	1.50				1.8	0.0	0.32	0.6	5.4	0.8
15x15	Y	5.00				1.9	0.0	0.39	0.9	1.2	0.6
15x15	Y	10.00				3.8	0.0	0.50	1.1	1.7	0.7
15x15	Y	20.00				6.7	0.0	0.78	1.6	2.7	1.5
15x15	Y	30.00				8.4	0.0	1.17	3.2	3.8	2.4
20x20	Depth	0.00		3.9	0.3						
20x20	X	1.45				2.1	0.0	0.46	0.6	3.7	2.2
20x20	X	1.50				2.0	0.0	0.47	0.8	4.0	2.2
20x20	X	5.00				1.6	0.0	0.57	0.4	2.2	1.4
20x20	X	10.00				4.1	0.0	0.73	0.9	1.1	0.8
20x20	X	20.00				8.4	0.0	1.21	1.9	1.9	1.1
20x20	X	30.00				11.4	0.0	1.95	3.9	3.7	2.0
20x20	Y	1.40				2.4	0.0	0.32	0.5	4.1	1.2
20x20	Y	1.50				2.5	0.0	0.32	0.3	5.0	1.2
20x20	Y	5.00				1.9	0.0	0.40	0.9	2.8	0.7
20x20	Y	10.00				3.8	0.0	0.54	1.1	2.5	0.6
20x20	Y	20.00				8.0	0.0	0.97	2.6	3.4	1.8
20x20	Y	30.00				11.0	0.0	1.70	4.1	4.9	2.7
30x5	Depth	0.00		4.2	0.2						
30x5	X	1.40				5.2	0.0	0.42	0.6	4.5	1.5
30x5	X	5.00				3.9	0.0	0.49	0.3	2.8	0.9
30x5	X	10.00				2.3	0.0	0.58	0.9	1.6	0.7
30x5	X	20.00				5.9	0.0	0.78	2.3	1.4	1.3
30x5	X	30.00				10.2	0.0	1.01	3.7	2.6	2.3
30x5	Y	1.40				0.4	0.0	0.31	0.6	4.3	0.3
30x5	Y	5.00				0.9	0.0	0.37	0.6	3.1	0.4
30x5	Y	10.00				1.6	0.0	0.46	0.8	2.2	0.5
30x5	Y	20.00				2.7	0.0	0.68	1.3	1.7	1.0
30x5	Y	30.00				3.1	0.0	0.97	1.7	1.7	1.6

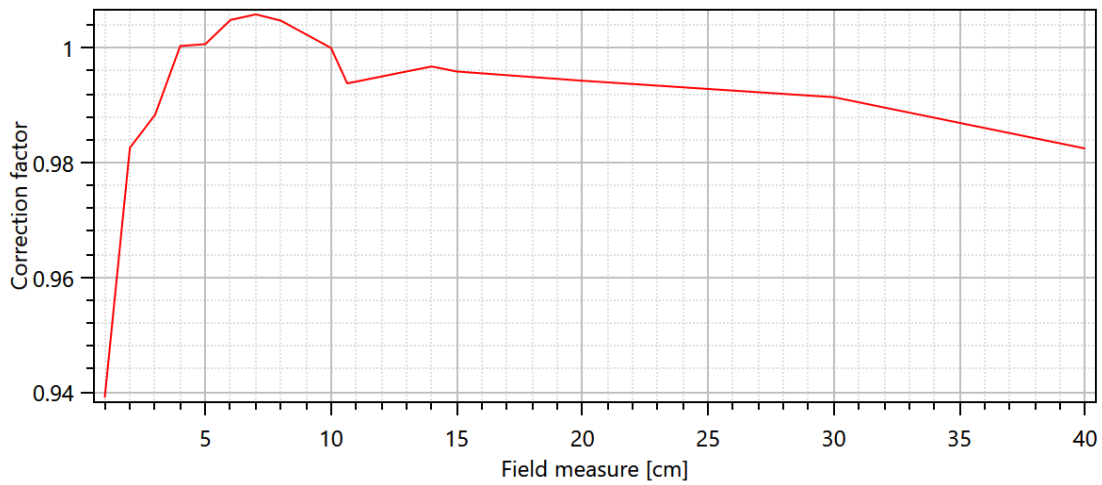
Field size [cm]	Dose curve type	Depth [cm]	Modulation	Build up	Fall off	Flatness	Symmetry	Penumbra width [cm]	In field	Penumbra	Out of field
30x30	Depth	0.00		4.6	0.4						
30x30	X	1.30				4.6	0.0	0.47	0.8	5.5	2.8
30x30	X	5.00				2.8	0.0	0.60	0.3	3.0	1.7
30x30	X	10.00				3.5	0.0	0.83	0.7	1.4	0.9
30x30	X	20.00				10.3	0.0	1.72	2.3	2.4	1.2
30x30	X	30.00				16.2	0.0	3.16	4.2	4.7	2.5
30x30	Y	1.30				4.7	0.0	0.33	0.6	13.0	2.0
30x30	Y	5.00				3.2	0.0	0.43	0.6	8.6	1.0
30x30	Y	10.00				3.7	0.0	0.62	1.1	5.3	0.7
30x30	Y	20.00				10.5	0.0	1.46	2.4	3.4	1.9
30x30	Y	30.00				16.5	0.0	2.94	4.4	5.0	3.0
40x40	Depth	0.00		5.6	0.4						
40x40	X	1.30				5.5	0.0	0.49	0.7	8.5	3.4
40x40	X	1.50				5.2	0.0	0.50	0.9	9.6	3.4
40x40	X	5.00				3.7	0.0	0.61	0.3	7.3	2.6
40x40	X	10.00				5.7	0.0	0.90	0.6	4.5	2.2
40x40	X	20.00				15.6	0.0	2.19	1.8	2.1	4.1
40x40	X	30.00				24.9	0.0	4.72	4.3	4.6	7.9
40x40	Y	1.30				5.5	0.0	0.36	0.8	14.6	2.3
40x40	Y	1.50				5.5	0.0	0.37	0.8	15.5	2.3
40x40	Y	5.00				4.0	0.0	0.40	0.4	14.5	2.2
40x40	Y	10.00				6.1	0.0	0.61	0.8	9.8	1.7
40x40	Y	20.00				15.5	0.0	1.94	2.0	3.8	4.0
40x40	Y	30.00				24.6	0.0	4.49	4.2	4.6	7.5

Output Factor Corrections

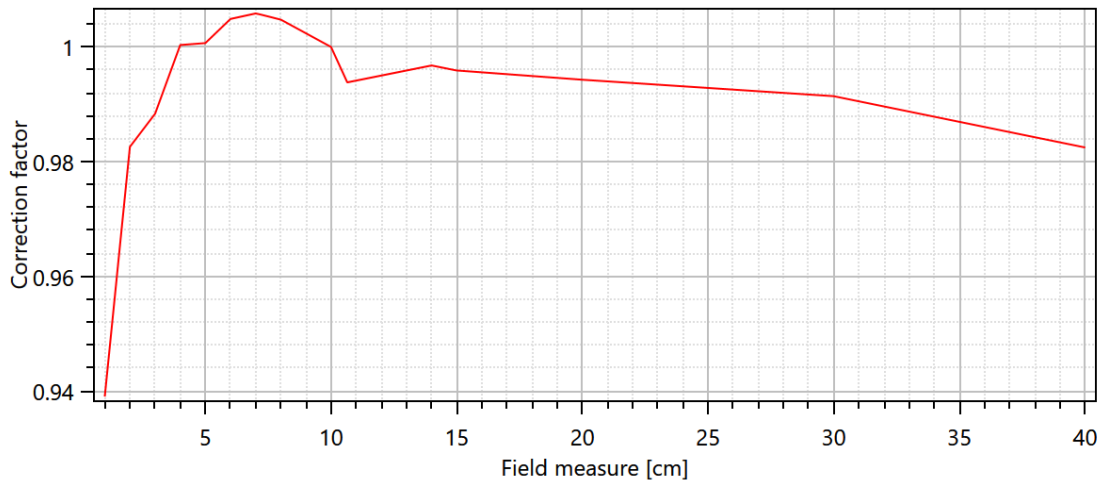
Normalization 4.95537

Field size	Correction factor
1.00	0.93903
2.00	0.98259
3.00	0.98835
4.00	1.00033
5.00	1.00067
6.00	1.00488
7.00	1.00584
7.17	1.00568
8.00	1.00477
10.00	1.00000
10.65	0.99382
14.00	0.99677
15.00	0.99589
20.00	0.99428
30.00	0.99141
40.00	0.98247

Output Factor Corrections



Output Factor Corrections



Off Axis

Beam profile correction

Radius [cm]	Correction factor
0.00	1.000
0.10	1.001
1.00	1.002
2.00	1.002
3.00	1.005
5.00	1.006
7.00	1.007
8.00	1.008
9.00	1.009
10.00	1.010
11.00	1.010
13.00	1.010
15.00	1.009
17.00	1.008

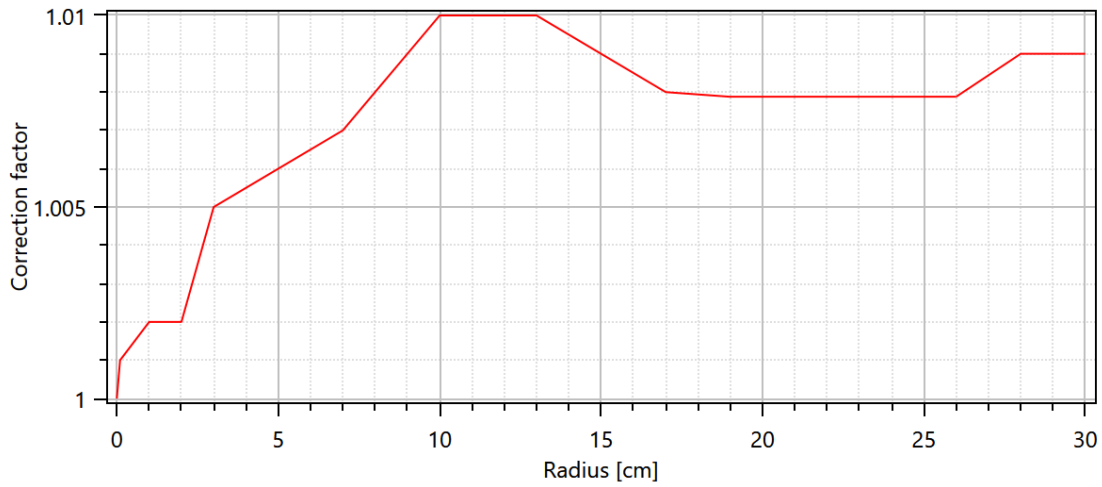
Beam profile correction

Radius [cm]	Correction factor
19.00	1.008
26.00	1.008
28.00	1.009
28.50	1.009
30.00	1.009

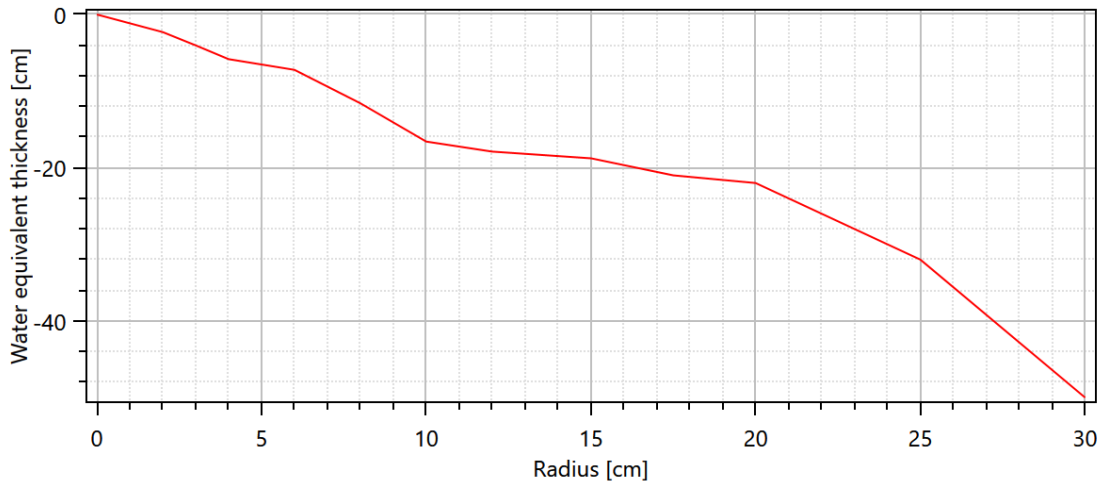
Off Axis Softening

Radius [cm]	Water equivalent thickness [cm]
0.00	0.000
2.00	-2.300
3.00	-4.030
4.00	-5.832
6.00	-7.230
8.00	-11.592
10.00	-16.590
12.00	-17.898
15.00	-18.772
17.50	-21.000
20.00	-22.000
25.00	-32.000
30.00	-50.000

Beam profile



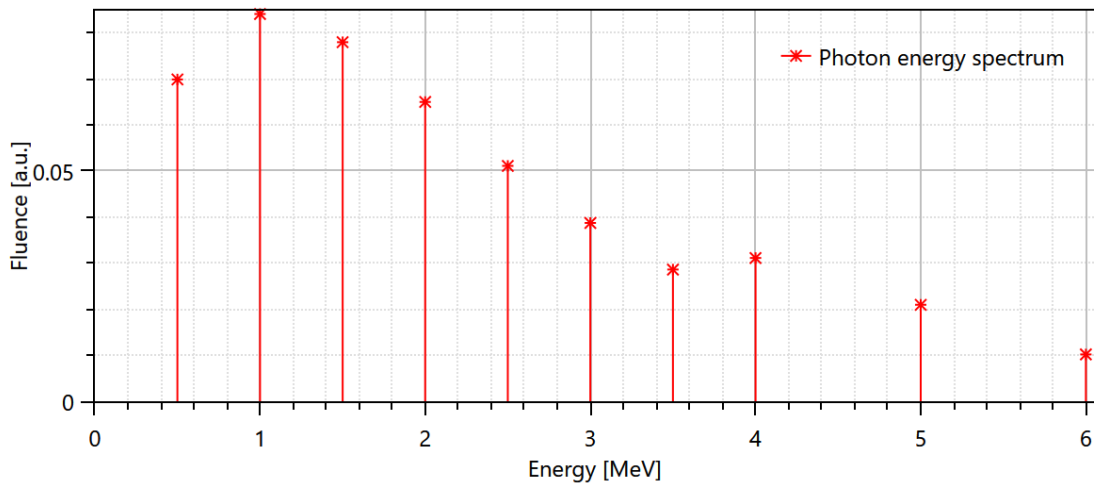
Off-axis softening



Energy Spectrum

Photons	
Energy [MeV]	Fluence [a.u.]
0.50	0.06983
1.00	0.08402
1.50	0.07792
2.00	0.06495
2.50	0.05108
3.00	0.03871
3.50	0.02859
4.00	0.03110
5.00	0.02095
6.00	0.01020

Energy Spectrum

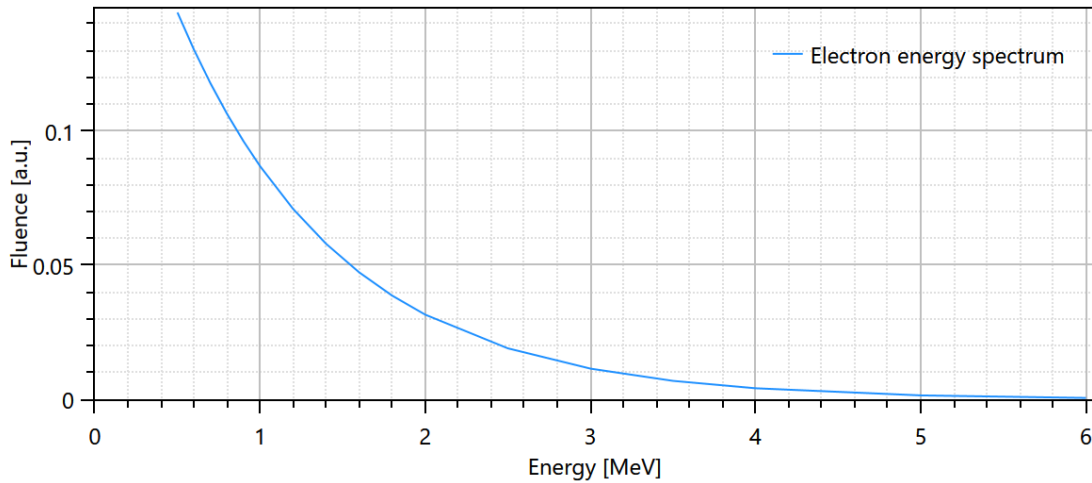


Energy Spectrum

Contamination Electrons

C	0.0000
E [MeV]	0.9880

Energy Spectrum



Fluence

Flattening filter weight for additional electron source	0.605
Flattening filter free	No
Leaf tip width [cm]	0.645
Tongue and groove [cm]	0.100

Collimator calibration

Collimator	Curvature [1/cm]	Gain	Offset [cm]
Y-jaws	0.00022	0.0000	-0.003
MLC x-position	0.00021	0.0000	-0.003
MLC y-position		0.0000	

Collimator position

Collimator	Transmission	Eff. dist. to source [cm]
Y-jaws		50.90
MLC	0.00402	39.57

Sources

Source	Weight	X width [cm]	Y width [cm]	Eff. dist. to source [cm]
Primary		0.099	0.078	
Flattening filter	0.07524	2.446		15.00
Electrons	0.00583	1.190		

Photon Beam Quality, 10 MV

Output factors

Output factor depth [cm]	10.00
--------------------------	-------



Machine Name
Commissioned by

VersaHD_FF (2)
MEDAUSTRON\GMI

Report creation time
Commission time

03 Sep 2016, 21:15:47 (hr:min:sec)
15 Apr 2016, 16:05:08 (hr:min:sec)

Output factors

Field size [cm]	Factor
1x1	0.64400
2x2	0.80700
3x3	0.86200
4x4	0.89600
5x5	0.92000
5x30	0.97900
6x6	0.93800
7x7	0.95600
8x8	0.97100
10x10	1.00000
14x14	1.03800
15x15	1.04700
20x20	1.07600
30x5	0.97000
30x30	1.11100
40x40	1.12400

Calibration

Resolution [cm]	0.20
Calibration point	
SSD [cm]	90.00
Depth [cm]	10.00
Dose/MU [[Gy]/MU]	0.010000
Measurement conditions	
Phantom size [cm]	55.00

Collimation settings

Field collimation	Modulation					
Jaws and MLC collimated	Open	Field size [cm]	Type	Depth offset [cm]	Detector height [cm]	Detector width [cm]
		1x1	Depth	0.00	0.01	0.11
		1x1	Profile	0.00	0.01	0.11
		2x2	Depth	0.00	0.01	0.11
		2x2	Profile	0.00	0.01	0.11
		3x3	Depth	0.00	0.01	0.11
		3x3	Profile	0.00	0.01	0.11
		4x4	Depth	0.00	0.55	0.55
		4x4	Profile	0.00	0.01	0.11
		5x5	Depth	0.00	0.55	0.55
		5x5	Profile	0.00	0.01	0.11
		5x30	Depth	0.00	0.55	0.55
		5x30	Profile	0.00	0.01	0.11
		6x6	Depth	0.00	0.55	0.55
		6x6	Profile	0.00	0.01	0.11
		7x7	Depth	0.00	0.55	0.55
		7x7	Profile	0.00	0.01	0.11
		8x8	Depth	0.00	0.55	0.55
		8x8	Profile	0.00	0.01	0.11
		10x10	Depth	0.00	0.55	0.55
		10x10	Profile	0.00	0.01	0.11
		14x14	Depth	0.00	0.55	0.55
		14x14	Profile	0.00	0.01	0.11
		15x15	Depth	0.00	0.55	0.55
		15x15	Profile	0.00	0.01	0.11
		20x20	Depth	0.00	0.55	0.55
		20x20	Profile	0.00	0.01	0.11
		30x5	Depth	0.00	0.55	0.55
		30x5	Profile	0.00	0.01	0.11
		30x30	Depth	0.00	0.55	0.55
		30x30	Profile	0.00	0.01	0.11
		40x40	Depth	0.00	0.55	0.55
		40x40	Profile	0.00	0.01	0.11

Curve quality

Field size [cm]	Dose curve type	Depth [cm]	Modulation	Build up	Fall off	Flatness	Symmetry	Penumbra width [cm]	In field	Penumbra	Out of field
1x1	Depth	0.00		7.0	0.7						
1x1	X	1.50					0.0	0.38	0.5	3.4	0.9
1x1	X	1.80					0.0	0.39	0.7	2.9	0.8
1x1	X	5.00					0.0	0.42	0.8	2.2	0.7
1x1	X	10.00					0.0	0.45	0.7	2.2	0.6
1x1	X	20.00					0.0	0.50	2.4	2.2	0.5
1x1	X	30.00					0.0	0.55	4.0	2.8	0.5
1x1	Y	1.50					0.0	0.27	2.3	2.9	0.6
1x1	Y	1.80					0.0	0.28	2.6	2.6	0.6
1x1	Y	5.00					0.0	0.30	1.5	3.0	0.7
1x1	Y	10.00					0.0	0.31	0.9	3.6	0.7
1x1	Y	20.00					0.0	0.34	1.8	2.2	0.7
1x1	Y	30.00					0.0	0.38	3.4	1.8	0.8
2x2	Depth	0.00		6.0	0.3						
2x2	X	1.50					0.0	0.42	1.5	3.0	1.1
2x2	X	2.20					0.0	0.44	0.3	2.2	1.0
2x2	X	5.00					0.0	0.47	0.3	2.1	0.9
2x2	X	10.00					0.0	0.50	0.6	1.8	0.8
2x2	X	20.00					0.0	0.57	1.3	1.9	0.7
2x2	X	30.00					0.0	0.62	2.1	1.8	0.6

Field size [cm]	Dose curve type	Depth [cm]	Modulation	Build up	Fall off	Flatness	Symmetry	Penumbra width [cm]	In field	Penumbra	Out of field
2x2	Y	1.50					0.0	0.29	1.0	2.9	0.9
2x2	Y	2.20					0.0	0.31	1.0	2.8	0.9
2x2	Y	5.00					0.0	0.34	1.1	2.5	0.9
2x2	Y	10.00					0.0	0.36	0.9	3.0	0.9
2x2	Y	20.00					0.0	0.40	0.8	3.0	1.0
2x2	Y	30.00					0.0	0.44	1.3	2.5	1.1
3x3	Depth	0.00		5.4	0.3						
3x3	X	1.50					0.0	0.43	1.5	3.5	0.9
3x3	X	2.20					0.0	0.45	0.5	3.0	0.9
3x3	X	5.00					0.0	0.50	0.3	2.4	0.7
3x3	X	10.00					0.0	0.54	0.9	2.6	0.7
3x3	X	20.00					0.0	0.61	1.4	2.9	0.6
3x3	X	30.00					0.0	0.67	1.9	3.0	0.5
3x3	Y	1.50					0.0	0.30	1.4	4.6	0.8
3x3	Y	2.20					0.0	0.32	1.5	4.5	0.9
3x3	Y	5.00					0.0	0.35	2.0	4.6	0.9
3x3	Y	10.00					0.0	0.39	1.1	3.6	0.9
3x3	Y	20.00					0.0	0.43	1.1	3.6	0.9
3x3	Y	30.00					0.0	0.48	1.2	4.0	1.0
4x4	Depth	0.00		6.8	0.2						
4x4	X	1.50				0.5	0.0	0.44	0.7	1.9	0.8
4x4	X	2.20				0.5	0.0	0.46	0.4	1.6	0.8
4x4	X	5.00				0.5	0.0	0.51	0.2	1.5	0.6
4x4	X	10.00				0.9	0.0	0.55	0.3	0.9	0.5
4x4	X	20.00				1.0	0.0	0.63	0.3	1.0	0.5
4x4	X	30.00				1.9	0.0	0.72	1.0	0.4	0.4
4x4	Y	1.50				0.8	0.0	0.31	1.6	3.4	0.9
4x4	Y	2.20				0.6	0.0	0.33	1.4	3.3	0.9
4x4	Y	5.00				0.5	0.0	0.37	0.9	3.0	1.0
4x4	Y	10.00				0.6	0.0	0.41	1.0	3.0	1.0
4x4	Y	20.00				1.1	0.0	0.47	1.5	3.2	1.1
4x4	Y	30.00				1.0	0.0	0.51	1.9	3.3	1.2
5x5	Depth	0.00		6.2	0.1						
5x5	X	1.50				1.0	0.0	0.45	1.2	2.0	0.7
5x5	X	2.20				0.7	0.0	0.47	0.4	1.4	0.6
5x5	X	5.00				1.0	0.0	0.52	0.4	1.3	0.6
5x5	X	10.00				1.3	0.0	0.57	0.3	0.8	0.5
5x5	X	20.00				1.7	0.0	0.66	0.4	0.6	0.4
5x5	X	30.00				2.9	0.0	0.74	0.4	0.3	0.4
5x5	Y	1.50				1.3	0.0	0.32	0.9	3.7	0.6
5x5	Y	2.20				1.1	0.0	0.34	0.5	2.6	0.6
5x5	Y	5.00				0.7	0.0	0.38	0.6	2.1	0.6
5x5	Y	10.00				1.1	0.0	0.42	0.6	2.3	0.8
5x5	Y	20.00				1.4	0.0	0.49	1.0	1.5	0.9
5x5	Y	30.00				2.1	0.0	0.55	1.5	2.2	1.0
5x30	Depth	0.00		4.1	0.1						
5x30	X	2.10				0.5	0.0	0.50	0.4	2.1	1.0
5x30	X	5.00				0.6	0.0	0.55	0.4	1.7	0.7
5x30	X	10.00				1.5	0.0	0.64	0.5	1.3	0.6
5x30	X	20.00				2.7	0.0	0.82	0.9	0.9	0.4
5x30	X	30.00				3.1	0.0	1.02	1.3	0.5	0.7
5x30	Y	2.10				7.7	0.0	0.34	1.1	5.6	1.2
5x30	Y	5.00				6.4	0.0	0.38	1.6	4.1	1.5
5x30	Y	10.00				4.3	0.0	0.44	1.8	3.5	1.9
5x30	Y	20.00				3.5	0.0	0.56	2.7	4.4	2.7
5x30	Y	30.00				6.5	0.0	0.70	3.6	5.7	3.5
6x6	Depth	0.00		5.1	0.1						
6x6	X	1.50				1.0	0.0	0.46	1.0	2.5	0.9
6x6	X	2.20				0.9	0.0	0.48	0.5	2.1	0.8
6x6	X	5.00				1.4	0.0	0.53	0.3	1.7	0.6
6x6	X	10.00				2.2	0.0	0.60	0.2	1.1	0.5
6x6	X	20.00				2.5	0.0	0.69	0.4	0.9	0.4

Field size [cm]	Dose curve type	Depth [cm]	Modulation	Build up	Fall off	Flatness	Symmetry	Penumbra width [cm]	In field	Penumbra	Out of field
6x6	X	30.00				3.9	0.0	0.80	0.9	0.2	0.5
6x6	Y	1.50				1.6	0.0	0.33	0.9	3.1	0.9
6x6	Y	2.20				1.3	0.0	0.35	0.8	3.8	1.0
6x6	Y	5.00				1.2	0.0	0.39	1.1	3.3	1.0
6x6	Y	10.00				2.0	0.0	0.44	0.9	3.5	1.1
6x6	Y	20.00				3.3	0.0	0.52	1.5	3.9	1.3
6x6	Y	30.00				3.5	0.0	0.59	1.3	4.0	1.4
7x7	Depth	0.00		4.7	0.1						
7x7	X	2.20				1.4	0.0	0.49	0.6	2.2	0.8
7x7	X	5.00				2.1	0.0	0.54	0.2	1.9	0.6
7x7	X	10.00				2.6	0.0	0.61	0.3	1.4	0.5
7x7	X	20.00				3.5	0.0	0.73	0.5	0.7	0.4
7x7	X	30.00				4.8	0.0	0.84	1.1	0.5	0.6
7x7	Y	2.20				1.7	0.0	0.36	0.8	3.5	0.8
7x7	Y	5.00				2.0	0.0	0.40	0.7	2.4	0.9
7x7	Y	10.00				2.6	0.0	0.45	0.8	2.7	1.0
7x7	Y	20.00				3.6	0.0	0.54	1.1	2.9	1.3
7x7	Y	30.00				4.2	0.0	0.62	1.9	3.5	1.6
8x8	Depth	0.00		3.9	0.1						
8x8	X	2.30				1.3	0.0	0.50	0.5	2.1	0.8
8x8	X	10.00				3.1	0.0	0.62	0.4	1.3	0.4
8x8	X	20.00				4.2	0.0	0.75	0.6	0.7	0.5
8x8	X	30.00				5.4	0.0	0.88	1.1	0.5	0.7
8x8	Y	2.30				1.7	0.0	0.36	0.9	3.1	0.9
8x8	Y	10.00				2.7	0.0	0.46	1.1	3.9	1.1
8x8	Y	20.00				4.2	0.0	0.56	1.2	4.3	1.4
8x8	Y	30.00				5.2	0.0	0.66	2.0	4.9	1.7
10x10	Depth	0.00		2.9	0.1						
10x10	X	1.50				1.4	0.0	0.49	1.4	2.5	0.8
10x10	X	2.10				1.4	0.0	0.50	0.6	2.0	0.6
10x10	X	5.00				1.9	0.0	0.55	0.4	1.5	0.5
10x10	X	10.00				3.6	0.0	0.64	0.4	1.0	0.4
10x10	X	20.00				5.0	0.0	0.81	0.9	0.6	0.4
10x10	X	30.00				6.0	0.0	0.96	1.3	0.8	0.8
10x10	Y	1.50				1.7	0.0	0.35	1.1	2.8	0.6
10x10	Y	2.10				1.9	0.0	0.37	0.8	3.2	0.6
10x10	Y	5.00				1.5	0.0	0.41	0.9	1.6	0.7
10x10	Y	10.00				3.0	0.0	0.47	1.2	2.6	0.9
10x10	Y	20.00				4.3	0.0	0.61	1.6	2.9	1.2
10x10	Y	30.00				5.1	0.0	0.74	2.3	3.3	1.6
14x14	Depth	0.00		2.9	0.2						
14x14	X	2.10				1.8	0.0	0.51	0.5	2.2	0.8
14x14	X	10.00				2.9	0.0	0.67	0.7	1.1	0.4
14x14	X	20.00				5.4	0.0	0.89	1.1	0.8	0.8
14x14	Y	2.10				2.7	0.0	0.38	1.4	3.4	0.7
14x14	Y	10.00				2.4	0.0	0.51	1.8	3.9	1.2
14x14	Y	20.00				4.9	0.0	0.70	2.1	4.4	1.8
15x15	Depth	0.00		2.9	0.2						
15x15	X	1.50				2.0	0.0	0.50	1.1	2.6	0.9
15x15	X	2.00				2.2	0.0	0.51	0.6	2.2	0.8
15x15	X	5.00				1.8	0.0	0.56	0.8	1.7	0.6
15x15	X	10.00				2.6	0.0	0.67	0.9	1.1	0.4
15x15	X	20.00				5.2	0.0	0.91	1.2	0.9	0.9
15x15	X	30.00				7.0	0.0	1.16	2.3	1.8	1.6
15x15	Y	1.50				2.9	0.0	0.37	1.3	3.2	0.8
15x15	Y	2.00				2.8	0.0	0.38	1.1	2.4	0.7
15x15	Y	5.00				2.5	0.0	0.43	1.5	2.2	1.0
15x15	Y	10.00				2.3	0.0	0.52	1.6	2.8	1.2
15x15	Y	20.00				5.1	0.0	0.72	2.0	3.7	1.9
15x15	Y	30.00				6.4	0.0	0.94	2.7	4.4	2.5
20x20	Depth	0.00		2.9	0.2						
20x20	X	1.50				2.9	0.0	0.52	1.0	2.9	0.7

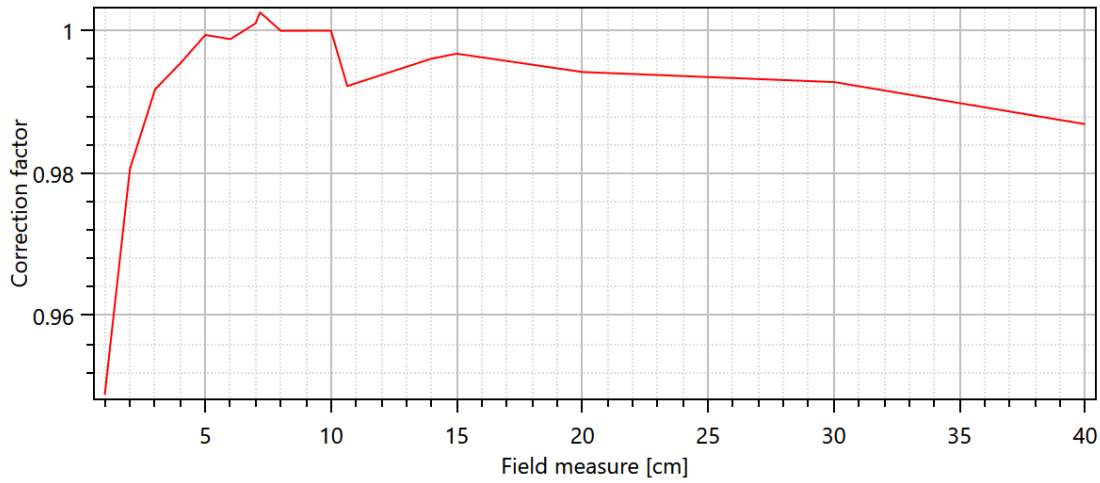
Field size [cm]	Dose curve type	Depth [cm]	Modulation	Build up	Fall off	Flatness	Symmetry	Penumbra width [cm]	In field	Penumbra	Out of field
20x20	X	1.90				2.9	0.0	0.52	0.7	2.7	0.7
20x20	X	5.00				2.8	0.0	0.58	0.9	1.8	0.5
20x20	X	10.00				3.0	0.0	0.71	0.9	1.0	0.4
20x20	X	20.00				5.9	0.0	1.02	1.7	1.8	1.4
20x20	X	30.00				8.5	0.0	1.39	2.2	2.8	2.2
20x20	Y	1.50				3.4	0.0	0.38	1.0	1.6	0.9
20x20	Y	1.90				3.6	0.0	0.38	0.9	3.2	0.7
20x20	Y	5.00				3.3	0.0	0.44	1.6	2.6	1.0
20x20	Y	10.00				2.7	0.0	0.55	1.7	3.2	1.3
20x20	Y	20.00				5.5	0.0	0.82	2.2	4.3	2.3
20x20	Y	30.00				8.2	0.0	1.17	3.0	5.4	3.1
30x5	Depth	0.00		3.3	0.1						
30x5	X	2.10				6.5	0.0	0.45	0.6	2.4	0.8
30x5	X	5.00				5.5	0.0	0.51	1.0	1.9	0.5
30x5	X	10.00				3.4	0.0	0.59	1.2	1.6	0.7
30x5	X	20.00				3.3	0.0	0.74	1.9	3.1	1.5
30x5	X	30.00				6.3	0.0	0.90	2.6	4.5	2.3
30x5	Y	2.10				0.9	0.0	0.36	0.7	2.8	0.7
30x5	Y	5.00				0.8	0.0	0.42	1.2	3.0	0.8
30x5	Y	10.00				1.2	0.0	0.49	1.1	2.8	0.8
30x5	Y	20.00				2.3	0.0	0.65	1.6	2.6	1.2
30x5	Y	30.00				2.3	0.0	0.82	2.0	2.9	1.6
30x30	Depth	0.00		2.7	0.2						
30x30	X	1.50				5.2	0.0	0.52	0.7	3.0	0.6
30x30	X	1.70				5.2	0.0	0.52	0.6	2.8	0.6
30x30	X	5.00				4.2	0.0	0.59	0.9	1.9	0.6
30x30	X	10.00				2.8	0.0	0.76	1.2	1.2	0.7
30x30	X	20.00				6.6	0.0	1.22	2.0	3.4	2.0
30x30	X	30.00				11.3	0.0	1.85	3.2	5.0	2.8
30x30	Y	1.50				5.4	0.0	0.38	0.6	3.7	0.8
30x30	Y	1.70				5.5	0.0	0.38	0.6	3.4	0.7
30x30	Y	5.00				4.4	0.0	0.45	1.2	4.0	1.0
30x30	Y	10.00				3.1	0.0	0.60	1.7	3.3	1.6
30x30	Y	20.00				7.2	0.0	1.01	2.4	4.8	2.7
30x30	Y	30.00				12.0	0.0	1.67	3.3	6.2	3.5
40x40	Depth	0.00		3.4	0.2						
40x40	X	1.50				6.4	0.0	0.54	1.1	3.6	1.3
40x40	X	1.70				6.3	0.0	0.54	0.8	4.2	1.3
40x40	X	5.00				5.1	0.0	0.63	0.6	4.4	1.3
40x40	X	10.00				4.5	0.0	0.84	0.8	4.6	1.5
40x40	X	20.00				11.5	0.0	1.50	1.4	5.4	3.5
40x40	X	30.00				18.4	0.0	2.85	2.6	5.8	6.5
40x40	Y	1.50				6.8	0.0	0.36	1.2	2.8	0.8
40x40	Y	1.70				6.7	0.0	0.36	0.8	3.3	0.7
40x40	Y	5.00				5.5	0.0	0.44	0.5	3.5	0.8
40x40	Y	10.00				4.8	0.0	0.62	0.7	3.0	1.3
40x40	Y	20.00				11.6	0.0	1.29	1.4	3.8	3.5
40x40	Y	30.00				19.3	0.0	2.69	2.7	4.6	6.2

Output Factor Corrections

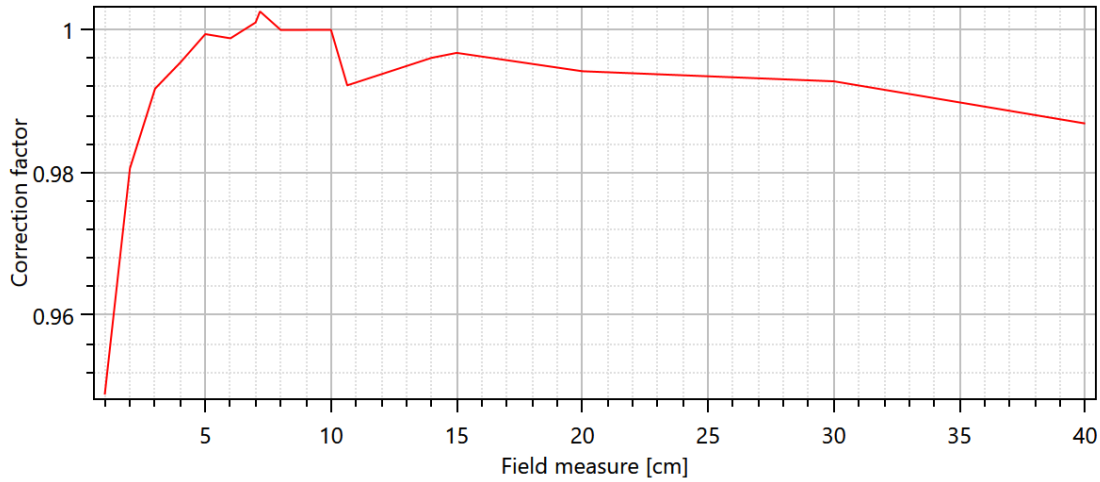
Normalization 5.35310

Field size	Correction factor
1.00	0.94887
2.00	0.98059
3.00	0.99176
4.00	0.99540
5.00	0.99941
6.00	0.99881
7.00	1.00104
7.17	1.00258
8.00	0.99998
10.00	1.00000
10.65	0.99222
14.00	0.99607
15.00	0.99677
20.00	0.99420
30.00	0.99279
40.00	0.98688

Output Factor Corrections



Output Factor Corrections



Off Axis

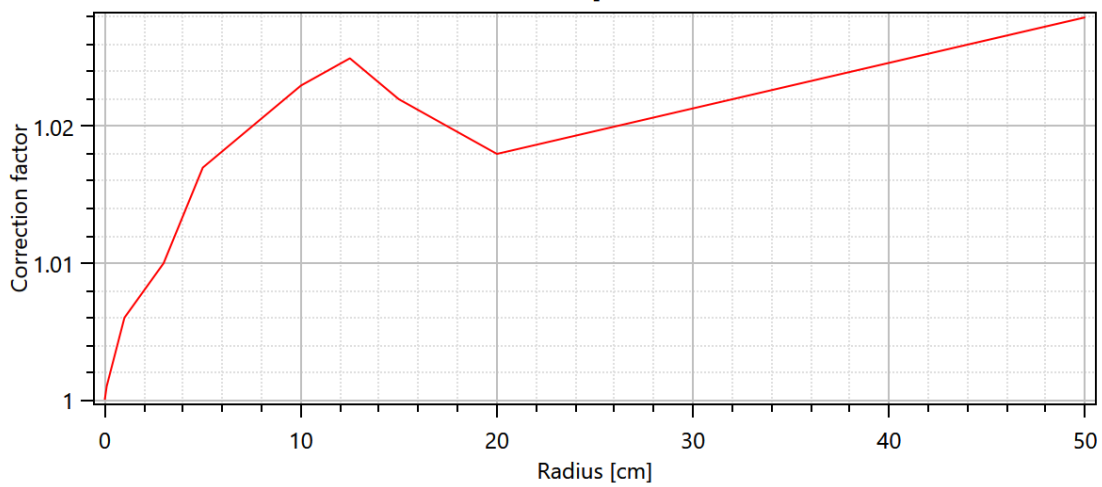
Beam profile correction

Radius [cm]	Correction factor
0.00	1.000
0.10	1.001
1.00	1.006
2.00	1.008
3.00	1.010
5.00	1.017
7.50	1.020
10.00	1.023
12.50	1.025
15.00	1.022
17.50	1.020
20.00	1.018
50.00	1.028

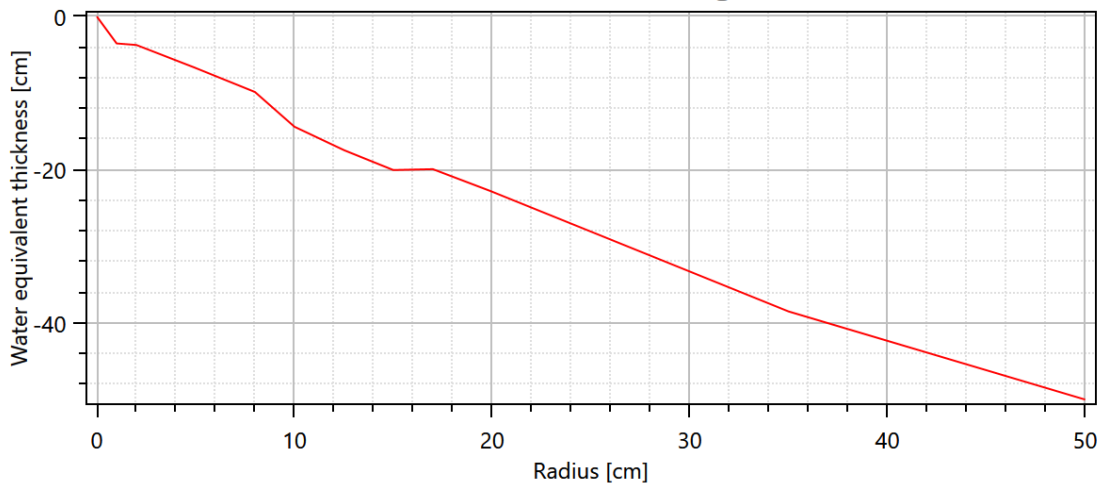
Off Axis Softening

Radius [cm]	Water equivalent thickness [cm]
0.00	0.000
1.00	-3.520
2.00	-3.720
5.00	-6.728
8.00	-9.858
10.00	-14.393
12.50	-17.443
15.00	-20.045
17.00	-19.932
20.00	-22.871
35.00	-38.500
50.00	-50.000

Beam profile



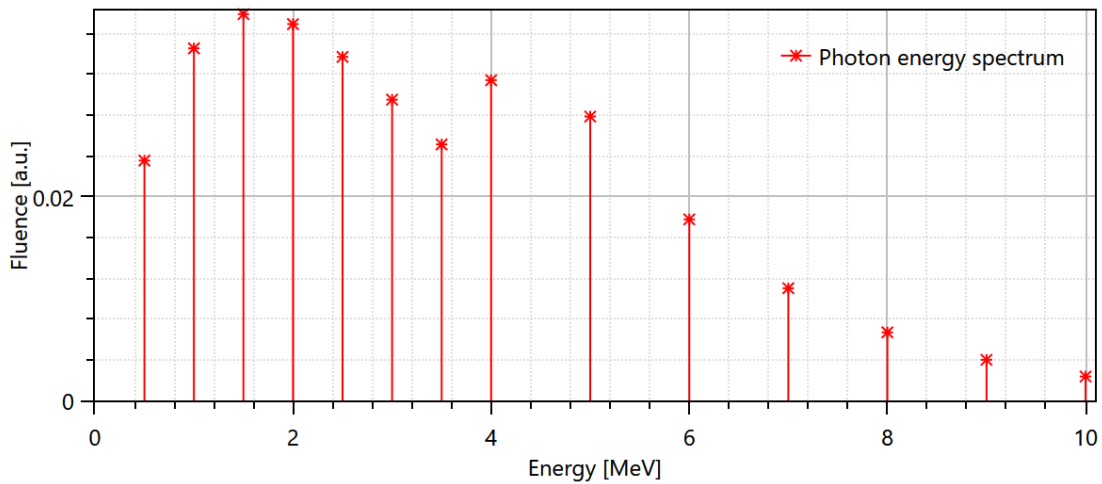
Off-axis softening



Energy Spectrum

Photons	
Energy [MeV]	Fluence [a.u.]
0.50	0.02355
1.00	0.03455
1.50	0.03791
2.00	0.03693
2.50	0.03371
3.00	0.02952
3.50	0.02513
4.00	0.03143
5.00	0.02786
6.00	0.01778
7.00	0.01103
8.00	0.00670
9.00	0.00400
10.00	0.00236

Energy Spectrum

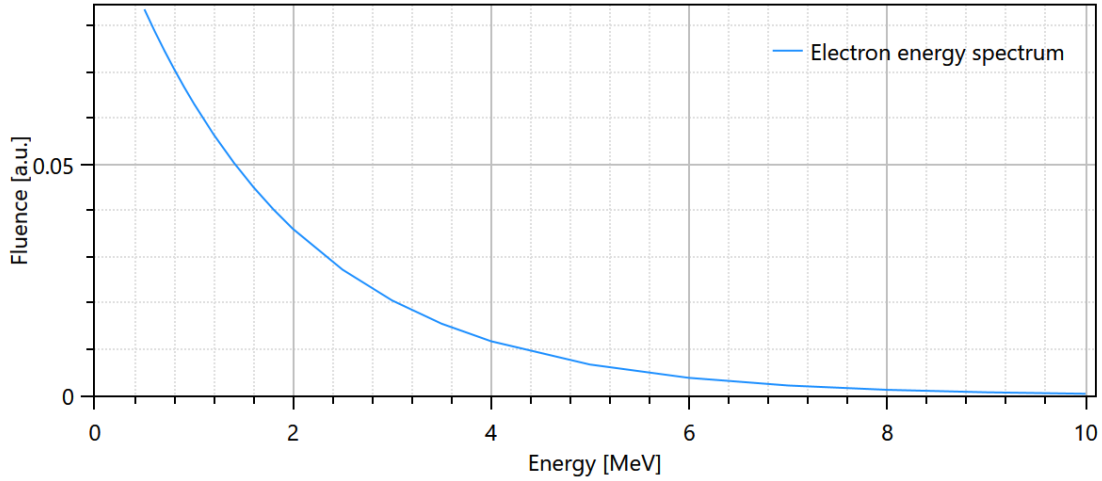


Energy Spectrum

Contamination Electrons

C 0.0000
E₀[MeV] 1.7848

Energy Spectrum



Fluence

Flattening filter weight for additional electron source 4.956E-10
Flattening filter free No
Leaf tip width [cm] 0.645
Tongue and groove [cm] 0.100

Collimator calibration

Collimator	Curvature [1/cm]	Gain	Offset [cm]
Y-jaws	0.00014	0.0000	0.002
MLC x-position	0.00017	0.0000	0.005
MLC y-position		0.0000	

Collimator position

Collimator	Transmission	Eff. dist. to source [cm]
Y-jaws		50.90
MLC	0.00473	39.57

Sources

Source	Weight	X width [cm]	Y width [cm]	Eff. dist. to source [cm]
Primary		0.105	0.041	
Flattening filter	0.07350	2.555		10.00
Electrons	0.00860	3.203		

Signatures

Signature 1 (Name/Signature/Date)

Signature 2 (Name/Signature/Date)

A.2 FFF Machine



Machine Name	Versa_E_FFF	Report creation time	03 Sep 2016, 21:14:15 (hr:min:sec)
Commissioned by	MEDAUSTRON\GMI	Commission time	14 Jun 2016, 11:09:58 (hr:min:sec)

Machine Report

Machine Properties

General

Name	Versa_E_FFF
Comment	Elekta VersaHD with Agility. Only FFF beams.
Commission time	14 Jun 2016, 11_09_58 (hr_min_sec)
Commissioned by	MEDAUSTRON\GMI
Dose curves computed with dose algorithm	Photon energy 6 MV: CCDose v3.2 Photon energy 10 MV: CCDose v3.2
Is machine commissioned	Yes
Photon energy definition	
Is machine deprecated	No
Electron beam capable	No
DMLC capable	Yes
Static arc capable	Yes
Modulated arc capable	Yes
Couch coordinate system definition	IEC 61217
Gantry and collimator coordinate system definitions	IEC 61217
Field coordinate system definition	IEC 61217
Jaw labeling standard	IEC 61217

Geometric

SAD [cm]	100.00
Allow all collimator angles	Yes
Allow all couch angles	Yes
Allow all gantry angles	No
Supported gantry angles start [deg]	180.1
Supported gantry angles, stop [deg]	180.0
Replace couch rotation by ring rotation	No
All angles are specified in the coordinate systems specified in the general section.	
Room view model	Schematic linac

Jaws

Maximum Y2 jaw position [cm]	20.00
Maximum jaw speed [cm/s]	8.50
Minimum Y2 jaw position [cm]	-12.00
No backup jaw	Yes
Reference field size X1/X2 [cm]	10.000
Reference field size Y1/Y2 [cm]	10.000
Jaw movement rule	Per segment
Source to Y1/Y2 jaw bottom distance [cm]	50.90
Thickness Y1/Y2 jaw [cm]	7.70

MLC

Has MLC	Yes
The machine has carriage	No
Allow interdigitation	Yes
Maximum leaf speed [cm/s]	3.50
Maximum tip difference [cm]	20.00
Maximum tip position [cm]	20.00
Minimum dynamic tip gap [cm]	0.30
Minimum static tip gap [cm]	0.30
Minimum tip position [cm]	-15.00
Source to MLC bottom distance [cm]	39.57
Thickness [cm]	9.00
MLC type	X
Use minimum dynamic tip gap for static fields	Yes

Leaf center position [cm]	Width [cm]
-19.75000	0.5000
-19.25000	0.5000
-18.75000	0.5000
-18.25000	0.5000
-17.75000	0.5000
-17.25000	0.5000
-16.75000	0.5000
-16.25000	0.5000
-15.75000	0.5000
-15.25000	0.5000
-14.75000	0.5000
-14.25000	0.5000
-13.75000	0.5000
-13.25000	0.5000
-12.75000	0.5000
-12.25000	0.5000
-11.75000	0.5000
-11.25000	0.5000
-10.75000	0.5000
-10.25000	0.5000
-9.75000	0.5000
-9.25000	0.5000
-8.75000	0.5000
-8.25000	0.5000
-7.75000	0.5000
-7.25000	0.5000
-6.75000	0.5000
-6.25000	0.5000
-5.75000	0.5000
-5.25000	0.5000
-4.75000	0.5000
-4.25000	0.5000
-3.75000	0.5000
-3.25000	0.5000
-2.75000	0.5000
-2.25000	0.5000
-1.75000	0.5000
-1.25000	0.5000
-0.75000	0.5000
-0.25000	0.5000
0.25000	0.5000
0.75000	0.5000
1.25000	0.5000
1.75000	0.5000
2.25000	0.5000
2.75000	0.5000
3.25000	0.5000
3.75000	0.5000
4.25000	0.5000
4.75000	0.5000
5.25000	0.5000
5.75000	0.5000
6.25000	0.5000
6.75000	0.5000
7.25000	0.5000
7.75000	0.5000
8.25000	0.5000
8.75000	0.5000
9.25000	0.5000
9.75000	0.5000
10.25000	0.5000
10.75000	0.5000
11.25000	0.5000
11.75000	0.5000



Leaf center position [cm]	Width [cm]
12.25000	0.5000
12.75000	0.5000
13.25000	0.5000
13.75000	0.5000
14.25000	0.5000
14.75000	0.5000
15.25000	0.5000
15.75000	0.5000
16.25000	0.5000
16.75000	0.5000
17.25000	0.5000
17.75000	0.5000
18.25000	0.5000
18.75000	0.5000
19.25000	0.5000
19.75000	0.5000

Dose rate

Maximum DMLC dose rate [MU/min]	1800.00
Maximum static arc dose rate [MU/min]	1800.00
Minimum MU per leaf travel distance [MU/cm]	0.30
Minimum static arc dose rate [MU/min]	110.00
Modulated arc dose rate	Variable

Beam quality specific dose rate settings

Maximum dose rate [MU/min]	Minimum dose rate [MU/min]	Nominal energy [MV]
1500.00	0.00	6
1800.00	0.00	10

Arc properties

Constant control point spacing (in arcs)	No
Limit MU per gantry degree	Yes
Maximum gantry angle speed [deg/s]	6.00
Maximum MU per gantry degree [MU/deg]	30.00
Minimum gantry angle speed [deg/s]	1.00
Minimum MU per arc segment [MU]	1.00
Minimum MU per gantry degree [MU/deg]	0.10
Supported gantry rotation direction (facing gantry)	Clockwise and counter clockwise
Supports variable couch angles	No
Use Arc burst mode	No
Use maximum gantry angle speed or maximum dose rate for each control point	No

Allowed arc gantry spacing

Arc spacing [deg]	Allowed
2.0	Yes
3.0	Yes
4.0	Yes

Block

Support blocks	No
----------------	----

Wedge

Wedge orientation coordinate system	IEC 61217
Elekta Motorized Wedge	No
Siemens Virtual Wedge	No
Standard Wedge	No
Varian Enhanced Dynamic Wedge	No

Cone

Nominal energy 6 MV

Photon Beam Quality, 6 MV

Output factors

Output factor depth [cm] 10.00

Output factors

Field size [cm]	Factor
1x1	0.69400
2x2	0.82800
3x3	0.87200
4x4	0.90300
5x5	0.92600
5x30	0.97700
6x6	0.94600
7x7	0.96200
8x8	0.97700
10x10	1.00000
14x14	1.03500
15x15	1.04100
20x20	1.06500
30x5	0.97200
30x30	1.09000
40x40	1.09900

Calibration

Resolution [cm] 0.20
 Calibration point
 SSD [cm] 90.00
 Depth [cm] 10.00
 Dose/MU [[Gy]/MU] 0.010000
 Measurement conditions
 Phantom size [cm] 55.00

Collimation settings

Field collimation	Modulation					
Jaws and MLC collimated	Open	Field size [cm]	Type	Depth offset [cm]	Detector height [cm]	Detector width [cm]
		1x1	Depth	0.00	0.22	0.22
		1x1	Profile	0.00	0.22	0.22
		2x2	Depth	0.00	0.22	0.22
		2x2	Profile	0.00	0.22	0.22
		3x3	Depth	0.00	0.22	0.22
		3x3	Profile	0.00	0.22	0.22
		4x4	Depth	0.00	0.55	0.55
		4x4	Profile	0.00	0.22	0.22
		5x5	Depth	0.00	0.55	0.55
		5x5	Profile	0.00	0.22	0.22
		5x30	Depth	0.00	0.55	0.55
		5x30	Profile	0.00	0.22	0.22
		6x6	Depth	0.00	0.55	0.55
		6x6	Profile	0.00	0.22	0.22
		7x7	Depth	0.00	0.55	0.55
		7x7	Profile	0.00	0.22	0.22
		8x8	Depth	0.00	0.55	0.55
		8x8	Profile	0.00	0.22	0.22
		10x10	Depth	0.00	0.55	0.55
		10x10	Profile	0.00	0.22	0.22
		14x14	Depth	0.00	0.55	0.55
		14x14	Profile	0.00	0.22	0.22
		15x15	Depth	0.00	0.55	0.55
		15x15	Profile	0.00	0.22	0.22
		20x20	Depth	0.00	0.55	0.55
		20x20	Profile	0.00	0.22	0.22
		30x5	Depth	0.00	0.55	0.55
		30x5	Profile	0.00	0.22	0.22
		30x30	Depth	0.00	0.55	0.55
		30x30	Profile	0.00	0.22	0.22
		40x40	Depth	0.00	0.55	0.55
		40x40	Profile	0.00	0.22	0.22

Curve quality

Field size [cm]	Dose curve type	Depth [cm]	Modulation	Build up	Fall off	Flatness	Symmetry	Penumbra width [cm]	In field	Penumbra	Out of field
1x1	Depth	0.00		7.4	0.5						
1x1	X	1.30					0.3	0.36	2.0	4.1	1.2
1x1	X	10.00					0.7	0.43	0.9	2.7	0.7
1x1	X	20.00					0.2	0.48	1.2	2.3	0.5
1x1	Y	1.30					0.7	0.24	3.4	3.2	0.9
1x1	Y	10.00					1.5	0.28	1.2	6.4	1.4
1x1	Y	20.00					0.9	0.32	1.5	3.8	1.3
2x2	Depth	0.00		6.4	0.1						
2x2	X	1.60					0.5	0.41	1.1	3.2	0.8
2x2	X	5.00					0.3	0.45	1.1	2.5	0.7
2x2	X	10.00					0.4	0.49	0.5	1.9	0.5
2x2	X	20.00					0.5	0.56	0.4	1.2	0.3
2x2	X	30.00					0.8	0.62	0.8	1.1	0.4
2x2	Y	1.60					1.1	0.28	0.8	4.9	1.1
2x2	Y	5.00					0.6	0.30	1.6	4.4	1.1
2x2	Y	10.00					0.8	0.33	2.0	4.4	1.2
2x2	Y	20.00					0.7	0.37	0.9	5.5	1.7
2x2	Y	30.00					0.8	0.41	1.1	4.6	1.7
3x3	Depth	0.00		5.9	0.2						
3x3	X	1.70					0.7	0.43	0.8	3.3	0.8

Field size [cm]	Dose curve type	Depth [cm]	Modulation	Build up	Fall off	Flatness	Symmetry	Penumbra width [cm]	In field	Penumbra	Out of field
3x3	X	5.00					0.7	0.48	1.0	2.4	0.5
3x3	X	10.00					0.3	0.52	0.6	2.0	0.4
3x3	X	20.00					0.2	0.60	0.4	1.8	0.4
3x3	X	30.00					0.4	0.68	0.5	1.3	0.4
3x3	Y	1.70					0.7	0.28	1.1	3.7	0.7
3x3	Y	5.00					0.8	0.33	1.7	3.9	0.9
3x3	Y	10.00					0.1	0.36	0.9	4.4	1.2
3x3	Y	20.00					0.3	0.41	0.7	3.4	1.1
3x3	Y	30.00					0.6	0.46	0.8	3.6	1.3
4x4	Depth	0.00		10.6	0.1						
4x4	X	1.70				1.3	0.1	0.43	0.9	2.7	0.6
4x4	X	10.00				2.0	0.4	0.54	0.7	1.8	0.4
4x4	X	20.00				2.3	0.5	0.63	0.3	1.2	0.5
4x4	Y	1.70				1.2	0.1	0.29	0.9	4.5	0.8
4x4	Y	10.00				1.7	0.3	0.38	0.8	3.0	1.0
4x4	Y	20.00				2.2	0.4	0.44	0.6	2.5	1.1
5x5	Depth	0.00		10.2	0.1						
5x5	X	1.50				2.1	0.3	0.44	0.5	2.7	0.6
5x5	X	1.70				2.2	0.4	0.45	0.4	2.8	0.6
5x5	X	5.00				2.6	0.2	0.50	0.5	2.2	0.4
5x5	X	10.00				3.6	0.5	0.57	0.3	1.7	0.5
5x5	X	20.00				4.5	0.3	0.68	0.2	1.4	0.6
5x5	X	30.00				5.2	0.9	0.77	0.8	1.0	0.8
5x5	Y	1.50				2.0	0.2	0.30	0.6	4.0	1.0
5x5	Y	1.70				2.0	0.4	0.31	0.4	4.3	1.0
5x5	Y	5.00				2.6	0.3	0.36	0.7	2.7	1.0
5x5	Y	10.00				3.4	0.3	0.41	0.3	3.9	1.2
5x5	Y	20.00				3.5	0.6	0.48	0.5	2.8	1.3
5x5	Y	30.00				4.2	0.4	0.55	0.9	3.2	1.5
5x30	Depth	0.00		7.8	0.1						
5x30	X	1.70				2.1	0.1	0.45	0.8	2.9	0.8
5x30	X	5.00				3.4	0.3	0.53	1.1	2.1	0.7
5x30	X	10.00				3.9	0.2	0.62	0.7	1.7	0.8
5x30	X	20.00				4.7	0.3	0.79	1.0	1.3	1.3
5x30	X	30.00				5.2	0.5	1.00	1.2	1.3	1.8
5x30	Y	1.70				51.0	0.4	7.14	0.3	0.6	1.6
5x30	Y	5.00				52.1	0.6	7.44	0.6	1.1	1.3
5x30	Y	10.00				52.9	0.4	7.83	0.4	0.9	1.7
5x30	Y	20.00				56.5	0.6	8.68	0.5	0.7	2.2
5x30	Y	30.00				61.4	0.8	9.71	0.7	0.7	2.8
6x6	Depth	0.00		9.1	0.1						
6x6	X	1.80				3.6	0.2	0.47	0.4	2.8	0.7
6x6	X	10.00				5.5	0.4	0.61	0.2	1.7	0.6
6x6	X	20.00				6.1	0.4	0.71	0.3	1.1	0.9
6x6	Y	1.80				3.1	0.2	0.32	0.5	2.3	1.1
6x6	Y	10.00				5.2	0.3	0.43	0.5	2.9	1.4
6x6	Y	20.00				5.6	0.5	0.51	0.5	4.1	1.8
7x7	Depth	0.00		8.5	0.1						
7x7	X	1.70				5.0	0.4	0.48	0.5	2.7	0.8
7x7	X	5.00				5.9	0.5	0.55	0.4	2.3	0.6
7x7	X	10.00				7.4	0.6	0.62	0.3	1.7	0.7
7x7	X	20.00				8.9	0.8	0.76	0.4	1.0	1.1
7x7	X	30.00				9.6	0.4	0.88	0.7	1.1	1.4
7x7	Y	1.70				4.6	0.2	0.33	0.6	3.9	1.1
7x7	Y	5.00				5.4	0.2	0.39	0.5	2.9	1.5
7x7	Y	10.00				6.9	0.4	0.45	0.4	4.0	1.7
7x7	Y	20.00				8.0	0.4	0.54	0.6	3.5	2.0
7x7	Y	30.00				9.0	0.8	0.65	0.8	3.8	2.2
8x8	Depth	0.00		7.7	0.1						
8x8	X	1.70				6.9	0.5	0.50	0.5	2.8	0.7
8x8	X	10.00				9.7	0.6	0.67	0.3	1.6	0.8
8x8	X	20.00				11.3	0.6	0.83	0.3	1.0	1.3

Field size [cm]	Dose curve type	Depth [cm]	Modulation	Build up	Fall off	Flatness	Symmetry	Penumbra width [cm]	In field	Penumbra	Out of field
8x8	Y	1.70				6.3	0.2	0.35	0.6	3.2	1.4
8x8	Y	10.00				9.0	0.3	0.49	0.5	3.0	1.7
8x8	Y	20.00				11.1	0.6	0.61	0.4	3.3	2.1
10x10	Depth	0.00		6.3	0.1						
10x10	X	1.50				11.0	0.9	0.55	0.4	2.5	0.6
10x10	X	1.70				11.1	0.9	0.56	0.5	2.3	0.7
10x10	X	5.00				12.4	0.6	0.65	0.3	1.9	0.6
10x10	X	10.00				14.5	0.8	0.79	0.3	1.4	0.8
10x10	X	20.00				15.0	0.9	0.98	0.3	1.0	1.2
10x10	X	30.00				15.6	1.0	1.17	0.7	1.3	1.7
10x10	Y	1.50				10.2	0.3	0.39	0.3	3.1	1.0
10x10	Y	1.70				10.2	0.2	0.40	0.3	3.6	0.9
10x10	Y	5.00				11.9	0.5	0.48	0.3	1.5	1.1
10x10	Y	10.00				13.4	0.2	0.60	0.3	2.3	1.3
10x10	Y	20.00				14.2	0.7	0.78	0.4	2.4	1.8
10x10	Y	30.00				14.7	0.6	0.91	0.7	2.4	2.1
14x14	Depth	0.00		4.8	0.2						
14x14	X	1.70				18.6	1.1	0.86	0.4	1.7	0.9
14x14	X	10.00				21.5	1.2	1.38	0.4	1.0	1.2
14x14	X	20.00				22.4	0.8	1.83	0.7	1.4	2.1
14x14	Y	1.70				17.5	0.4	0.70	0.2	3.3	1.1
14x14	Y	10.00				20.2	0.3	1.17	0.3	1.5	1.8
14x14	Y	20.00				21.7	0.7	1.60	0.8	1.9	2.5
15x15	Depth	0.00		4.5	0.2						
15x15	X	1.50				19.8	1.0	1.06	0.4	1.6	0.8
15x15	X	1.60				19.7	1.0	1.06	0.4	1.5	0.8
15x15	X	5.00				20.9	0.5	1.31	0.3	1.0	0.9
15x15	X	10.00				22.3	0.7	1.66	0.3	0.8	1.3
15x15	X	20.00				24.6	0.7	2.13	0.4	0.9	2.0
15x15	X	30.00				25.6	1.1	2.60	1.2	1.5	2.7
15x15	Y	1.50				18.9	0.2	0.86	0.2	2.2	1.1
15x15	Y	1.60				18.8	0.3	0.87	0.2	2.2	1.2
15x15	Y	5.00				20.4	0.3	1.17	0.3	1.1	1.5
15x15	Y	10.00				22.5	0.4	1.49	0.2	1.5	1.9
15x15	Y	20.00				23.8	0.6	1.98	0.5	1.8	2.6
15x15	Y	30.00				24.8	0.8	2.37	1.6	2.6	3.2
20x20	Depth	0.00		4.1	0.2						
20x20	X	1.50				30.2	1.3	2.90	0.4	1.1	0.6
20x20	X	1.60				29.3	1.1	2.94	0.5	1.1	0.6
20x20	X	5.00				30.1	0.9	3.15	0.4	0.8	1.0
20x20	X	10.00				32.0	1.0	3.50	0.4	0.7	1.5
20x20	X	20.00				34.0	0.9	4.11	0.6	1.1	2.5
20x20	X	30.00				35.0	1.0	4.73	1.6	2.0	3.3
20x20	Y	1.50				29.0	0.3	2.68	0.2	0.6	1.1
20x20	Y	1.60				28.9	0.2	2.68	0.2	0.8	1.1
20x20	Y	5.00				29.9	0.4	2.91	0.2	1.0	1.6
20x20	Y	10.00				31.3	0.3	3.26	0.3	1.1	2.1
20x20	Y	20.00				33.5	0.6	3.88	0.7	1.6	3.0
20x20	Y	30.00				34.5	0.6	4.51	1.5	2.5	3.7
30x5	Depth	0.00		7.1	0.1						
30x5	X	1.70				52.1	1.2	7.38	0.4	0.8	0.8
30x5	X	5.00				53.5	1.3	7.70	0.5	0.7	0.9
30x5	X	10.00				53.3	1.2	8.13	0.3	0.7	1.2
30x5	X	20.00				57.5	1.4	9.06	0.4	0.7	1.9
30x5	X	30.00				61.5	1.2	9.97	0.7	0.6	2.6
30x5	Y	1.70				2.0	0.1	0.32	0.8	4.1	1.5
30x5	Y	5.00				2.4	0.2	0.38	1.1	4.0	1.5
30x5	Y	10.00				3.4	0.2	0.45	0.9	4.6	1.7
30x5	Y	20.00				4.2	0.2	0.61	1.1	4.2	2.0
30x5	Y	30.00				4.8	0.5	0.76	1.8	4.7	2.4
30x30	Depth	0.00		4.4	0.2						
30x30	X	1.70				50.9	1.0	7.18	0.4	0.7	0.8

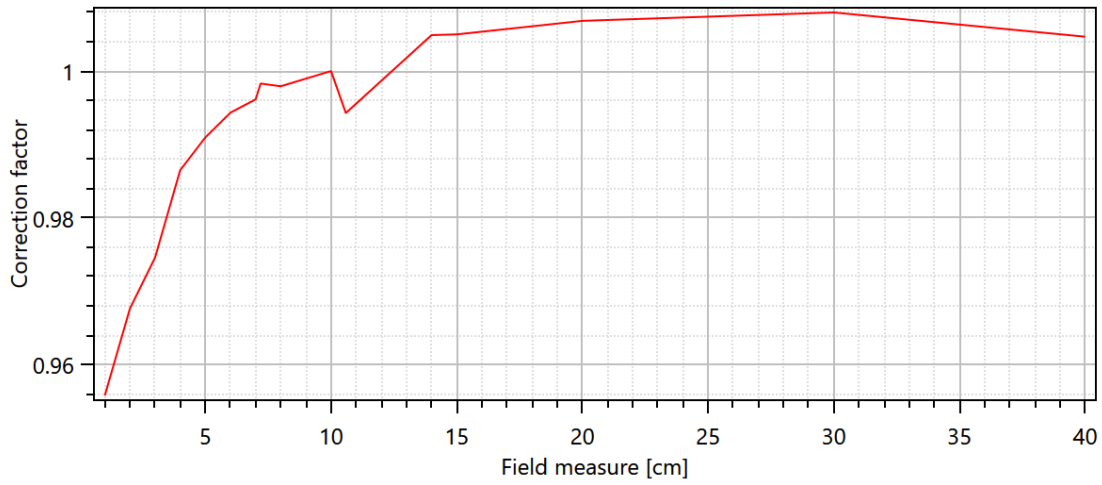
Field size [cm]	Dose curve type	Depth [cm]	Modulation	Build up	Fall off	Flatness	Symmetry	Penumbra width [cm]	In field	Penumbra	Out of field
30x30	X	5.00				51.9	1.1	7.51	0.4	0.7	1.4
30x30	X	10.00				51.8	1.0	7.91	0.3	0.8	1.9
30x30	X	20.00				54.9	1.1	8.76	0.6	1.4	3.2
30x30	X	30.00				58.6	0.8	9.65	1.3	2.4	4.5
30x30	Y	1.70				49.5	0.4	6.95	0.3	1.0	1.2
30x30	Y	5.00				50.6	0.5	7.25	0.3	1.1	1.6
30x30	Y	10.00				52.4	0.3	7.64	0.3	0.8	2.2
30x30	Y	20.00				54.9	0.5	8.53	0.5	1.1	3.4
30x30	Y	30.00				58.1	0.8	9.36	1.7	2.4	4.6
40x40	Depth	0.00		4.6	0.2						
40x40	X	1.50				73.5	0.8	11.69	0.7	1.5	1.4
40x40	X	1.50				73.6	0.8	11.70	0.7	1.1	0.9
40x40	X	5.00				73.5	0.9	12.14	0.4	0.8	1.2
40x40	X	10.00				71.2	0.7	12.65	0.2	0.9	1.8
40x40	X	20.00				72.6	0.8	13.82	0.5	0.8	3.3
40x40	X	30.00				74.0	1.0	15.07	1.1	1.6	5.3
40x40	Y	1.50				73.3	0.4	11.36	0.5	1.4	1.2
40x40	Y	1.50				73.4	0.8	11.36	0.5	1.2	1.1
40x40	Y	5.00				72.3	0.4	11.90	0.4	0.8	1.4
40x40	Y	10.00				71.6	0.5	12.40	0.2	0.7	1.8
40x40	Y	20.00				70.5	0.5	13.60	0.4	0.8	3.3
40x40	Y	30.00				72.4	0.7	14.78	1.5	1.5	5.3

Output Factor Corrections

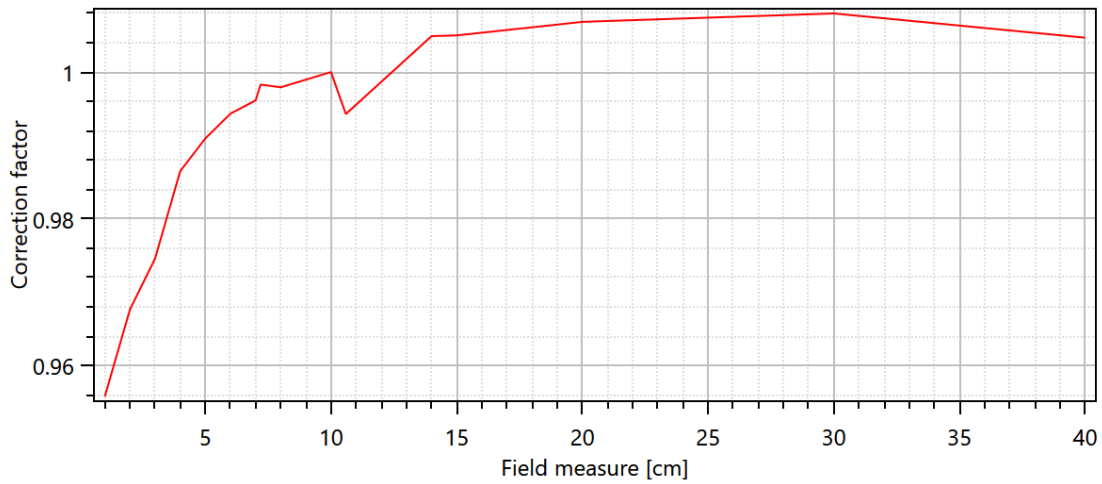
Normalization 4.99661

Field size	Correction factor
1.00	0.95577
2.00	0.96763
3.00	0.97457
4.00	0.98649
5.00	0.99095
6.00	0.99433
7.00	0.99614
7.20	0.99830
8.00	0.99793
10.00	1.00000
10.59	0.99428
14.00	1.00490
15.00	1.00500
20.00	1.00684
30.00	1.00799
40.00	1.00468

Output Factor Corrections



Output Factor Corrections



Off Axis

Beam profile correction

Radius [cm]	Correction factor
0.00	1.000
1.00	0.982
2.00	0.963
3.00	0.939
5.00	0.865
7.00	0.799
8.00	0.766
9.00	0.733
10.00	0.702
11.00	0.673
13.00	0.619
15.00	0.581
17.00	0.539
19.00	0.500

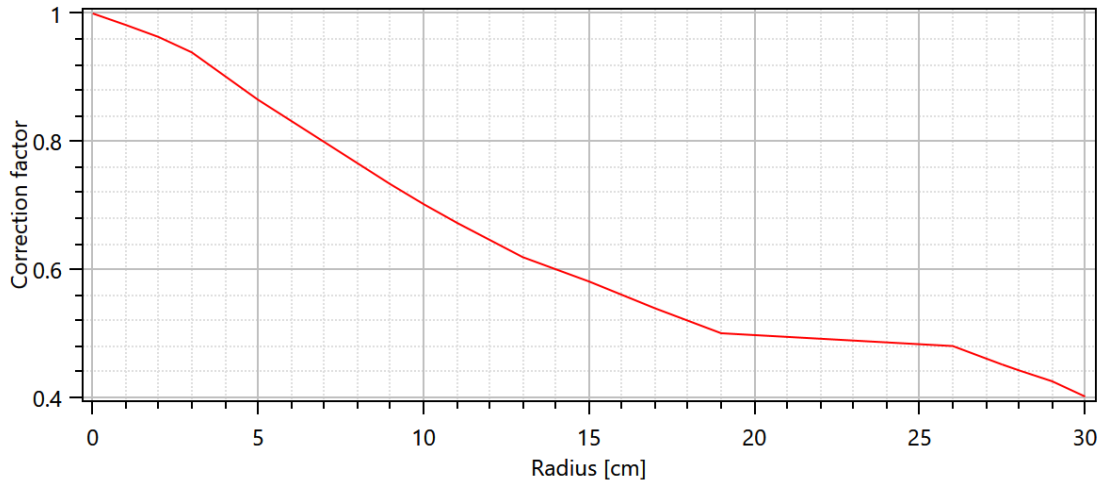
Beam profile correction

Radius [cm]	Correction factor
26.00	0.480
27.50	0.451
28.00	0.442
29.00	0.425
30.00	0.401

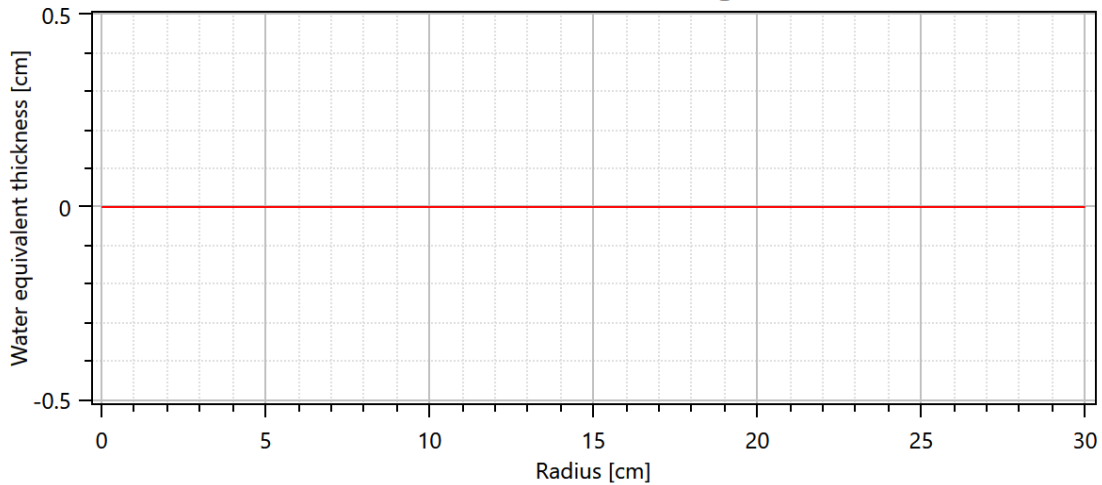
Off Axis Softening

Radius [cm]	Water equivalent thickness [cm]
0.00	0.000
5.00	0.000
10.00	0.000
30.00	0.000

Beam profile



Off-axis softening

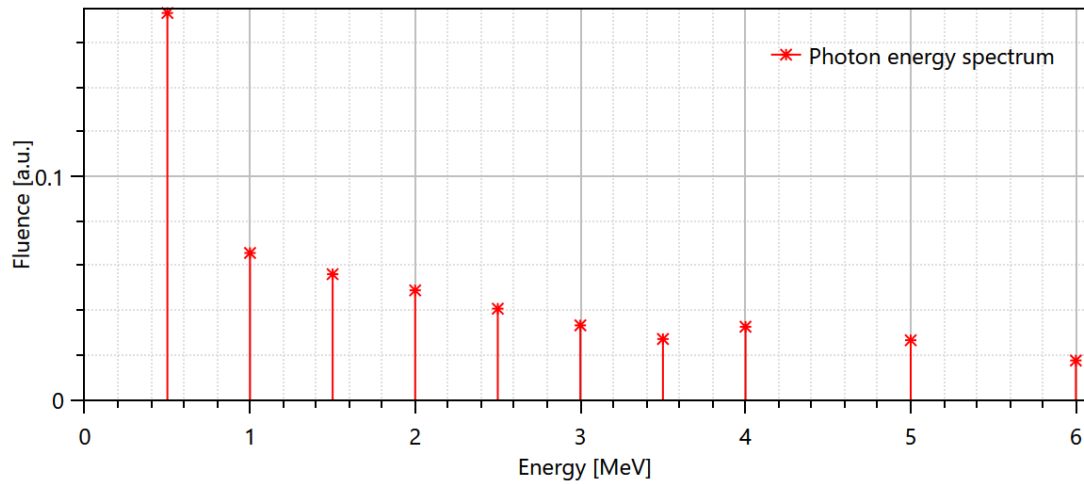


Energy Spectrum

Photons

Energy [MeV]	Fluence [a.u.]
0.50	0.17325
1.00	0.06572
1.50	0.05621
2.00	0.04896
2.50	0.04075
3.00	0.03328
3.50	0.02716
4.00	0.03265
5.00	0.02660
6.00	0.01751

Energy Spectrum

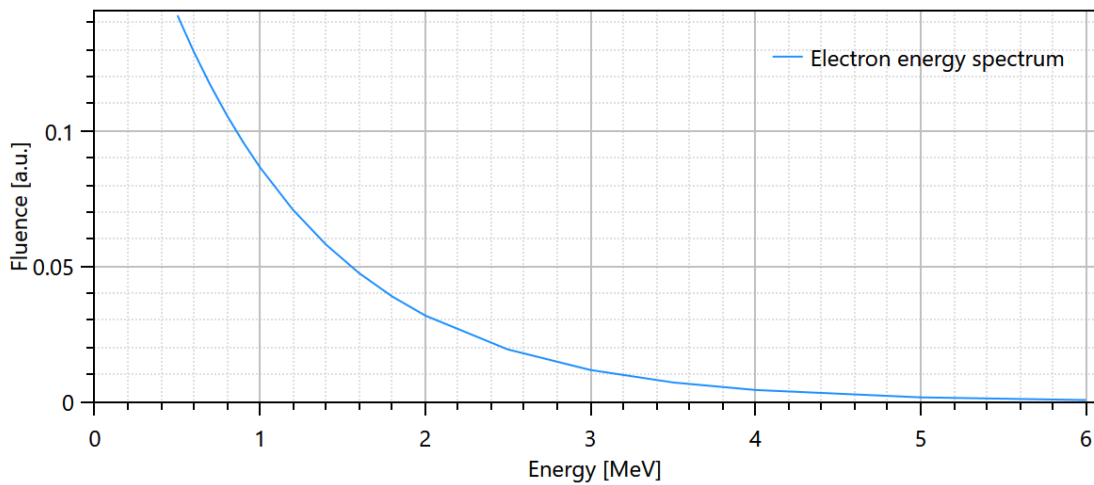


Energy Spectrum

Contamination Electrons

C	0.0000
E ₀ [MeV]	0.9991

Energy Spectrum



Fluence

Flattening filter weight for additional electron source	1.000
Flattening filter free	Yes
Leaf tip width [cm]	0.645
Tongue and groove [cm]	0.100

Collimator calibration

Collimator	Curvature [1/cm]	Gain	Offset [cm]
Y-jaws	0.00020	0.0000	0.004
MLC x-position	0.00015	0.0000	0.011
MLC y-position		0.0000	

Collimator position

Collimator	Transmission	Eff. dist. to source [cm]
Y-jaws		50.90
MLC	0.00268	39.57

Sources

Source	Weight	X width [cm]	Y width [cm]	Eff. dist. to source [cm]
Primary		0.123	0.009	
Flattening filter	0.00800	2.560		15.00
Electrons	0.00471	4.042		

Photon Beam Quality, 10 MV

Output factors

Output factor depth [cm]	10.00
--------------------------	-------

Output factors

Field size [cm]	Factor
1x1	0.68800
2x2	0.84000
3x3	0.89500
4x4	0.92600
5x5	0.94500
5x30	0.98200
6x6	0.96000
7x7	0.97300
8x8	0.98400
10x10	1.00000
14x14	1.02400
15x15	1.02900
20x20	1.04400
30x5	0.98000
30x30	1.05900
40x40	1.06400

Calibration

Resolution [cm]	0.20
Calibration point	
SSD [cm]	90.00
Depth [cm]	10.00
Dose/MU [[Gy]/MU]	0.010000
Measurement conditions	
Phantom size [cm]	55.00

Collimation settings

Field collimation	Modulation					
Jaws and MLC collimated	Open	Field size [cm]	Type	Depth offset [cm]	Detector height [cm]	Detector width [cm]
		1x1	Depth	0.00	0.22	0.22
		1x1	Profile	0.00	0.22	0.22
		2x2	Depth	0.00	0.22	0.22
		2x2	Profile	0.00	0.22	0.22
		3x3	Depth	0.00	0.22	0.22
		3x3	Profile	0.00	0.22	0.22
		4x4	Depth	0.00	0.55	0.55
		4x4	Profile	0.00	0.22	0.22
		5x5	Depth	0.00	0.55	0.55
		5x5	Profile	0.00	0.22	0.22
		5x30	Depth	0.00	0.55	0.55
		5x30	Profile	0.00	0.22	0.22
		6x6	Depth	0.00	0.55	0.55
		6x6	Profile	0.00	0.22	0.22
		7x7	Depth	0.00	0.55	0.55
		7x7	Profile	0.00	0.22	0.22
		8x8	Depth	0.00	0.55	0.55
		8x8	Profile	0.00	0.22	0.22
		10x10	Depth	0.00	0.55	0.55
		10x10	Profile	0.00	0.22	0.22
		14x14	Depth	0.00	0.55	0.55
		14x14	Profile	0.00	0.22	0.22
		15x15	Depth	0.00	0.55	0.55
		15x15	Profile	0.00	0.22	0.22
		20x20	Depth	0.00	0.55	0.55
		20x20	Profile	0.00	0.22	0.22
		30x5	Depth	0.00	0.55	0.55
		30x5	Profile	0.00	0.22	0.22
		30x30	Depth	0.00	0.55	0.55
		30x30	Profile	0.00	0.22	0.22
		40x40	Depth	0.00	0.55	0.55
		40x40	Profile	0.00	0.22	0.22

Curve quality

Field size [cm]	Dose curve type	Depth [cm]	Modulation	Build up	Fall off	Flatness	Symmetry	Penumbra width [cm]	In field	Penumbra	Out of field
1x1	Depth	0.00		6.0	0.5						
1x1	X	1.80					0.6	0.33	2.9	1.9	0.9
1x1	X	10.00					1.0	0.38	1.7	1.6	0.5
1x1	X	20.00					1.2	0.43	1.0	1.6	0.5
1x1	Y	1.80					0.8	0.27	3.3	2.3	0.6
1x1	Y	10.00					0.9	0.31	1.1	2.8	0.8
1x1	Y	20.00					0.9	0.35	1.1	2.6	0.8
2x2	Depth	0.00		4.4	0.2						
2x2	X	2.10					0.5	0.38	1.7	2.2	0.6
2x2	X	5.00					0.3	0.42	1.5	2.3	0.5
2x2	X	10.00					0.3	0.46	0.9	1.8	0.4
2x2	X	20.00					0.3	0.52	0.6	1.4	0.3
2x2	X	30.00					0.3	0.57	0.8	1.1	0.3
2x2	Y	2.10					0.4	0.31	1.6	2.6	0.8
2x2	Y	5.00					0.6	0.34	2.1	3.5	0.9
2x2	Y	10.00					0.7	0.37	2.0	3.7	1.0
2x2	Y	20.00					1.5	0.41	1.5	3.4	1.1
2x2	Y	30.00					0.7	0.45	1.5	3.7	1.2
3x3	Depth	0.00		3.8	0.2						
3x3	X	2.30					0.7	0.42	1.3	2.4	0.5

Field size [cm]	Dose curve type	Depth [cm]	Modulation	Build up	Fall off	Flatness	Symmetry	Penumbra width [cm]	In field	Penumbra	Out of field
3x3	X	5.00					0.7	0.46	1.1	2.2	0.4
3x3	X	10.00					0.2	0.50	0.6	1.6	0.3
3x3	X	20.00					0.2	0.57	0.5	1.3	0.3
3x3	X	30.00					0.2	0.63	0.3	0.7	0.3
3x3	Y	2.30					0.8	0.34	1.5	3.8	0.6
3x3	Y	5.00					1.1	0.38	1.3	3.7	0.7
3x3	Y	10.00					0.5	0.41	1.2	2.1	0.8
3x3	Y	20.00					0.3	0.47	1.1	2.5	0.9
3x3	Y	30.00					0.3	0.51	1.1	3.0	1.0
4x4	Depth	0.00		5.6	0.1						
4x4	X	2.60				2.4	0.9	0.45	1.2	2.8	0.4
4x4	X	10.00				3.3	0.6	0.54	0.9	2.1	0.3
4x4	X	20.00				4.2	0.6	0.62	0.7	1.9	0.4
4x4	Y	2.60				2.1	0.6	0.36	1.7	5.1	0.9
4x4	Y	10.00				2.7	0.5	0.44	1.5	5.0	1.0
4x4	Y	20.00				3.7	0.4	0.51	1.2	4.9	1.1
5x5	Depth	0.00		4.6	0.1						
5x5	X	1.50				3.6	0.5	0.42	0.9	2.4	0.5
5x5	X	2.50				4.1	0.5	0.47	0.9	2.1	0.3
5x5	X	5.00				4.7	0.7	0.52	0.8	2.2	0.3
5x5	X	10.00				5.6	0.4	0.58	0.7	2.0	0.4
5x5	X	20.00				6.8	0.4	0.68	0.7	1.9	0.5
5x5	X	30.00				6.5	0.3	0.75	1.0	2.0	0.6
5x5	Y	1.50				3.4	0.7	0.34	1.2	2.4	0.7
5x5	Y	2.50				3.6	0.6	0.39	1.3	2.4	0.8
5x5	Y	5.00				4.0	0.5	0.43	1.4	3.5	0.9
5x5	Y	10.00				4.8	0.5	0.48	1.1	2.7	1.0
5x5	Y	20.00				5.6	0.5	0.55	1.1	2.9	1.1
5x5	Y	30.00				6.8	0.7	0.61	1.3	3.5	1.2
5x30	Depth	0.00		3.4	0.1						
5x30	X	2.50				3.6	0.6	0.48	1.2	2.6	0.5
5x30	X	5.00				4.0	0.6	0.53	1.3	2.4	0.5
5x30	X	10.00				5.7	0.6	0.61	1.1	2.0	0.6
5x30	X	20.00				6.5	0.4	0.75	1.2	1.8	1.0
5x30	X	30.00				7.7	0.3	0.87	1.2	1.7	1.3
5x30	Y	2.50				72.0	0.6	9.09	0.5	1.1	1.6
5x30	Y	5.00				71.7	0.6	9.35	0.6	1.1	1.7
5x30	Y	10.00				70.0	0.5	9.85	0.5	1.2	1.8
5x30	Y	20.00				69.6	0.8	10.88	0.4	0.9	1.7
5x30	Y	30.00				70.4	1.3	11.96	0.6	0.9	2.2
6x6	Depth	0.00		3.8	0.1						
6x6	X	2.40				7.1	1.3	0.51	0.8	2.5	0.4
6x6	X	10.00				8.5	1.1	0.62	0.6	1.7	0.4
6x6	X	20.00				10.0	0.8	0.73	0.6	1.6	0.7
6x6	Y	2.40				5.7	0.7	0.40	1.2	3.1	0.8
6x6	Y	10.00				7.7	0.9	0.53	1.0	2.9	1.0
6x6	Y	20.00				8.5	0.7	0.61	0.9	2.6	1.2
7x7	Depth	0.00		3.2	0.1						
7x7	X	2.40				9.6	1.3	0.55	0.7	2.4	0.6
7x7	X	5.00				10.6	1.4	0.63	0.5	1.8	0.4
7x7	X	10.00				11.9	1.1	0.70	0.5	1.6	0.6
7x7	X	20.00				13.6	1.1	0.82	0.4	1.2	0.9
7x7	X	30.00				13.5	1.1	0.92	0.6	1.4	1.1
7x7	Y	2.40				8.5	1.1	0.44	0.9	3.5	0.9
7x7	Y	5.00				9.2	0.9	0.51	0.8	1.5	1.0
7x7	Y	10.00				10.3	1.1	0.59	0.8	1.9	1.2
7x7	Y	20.00				11.9	1.1	0.69	0.8	2.2	1.5
7x7	Y	30.00				13.1	0.8	0.79	0.8	2.3	1.7
8x8	Depth	0.00		3.0	0.1						
8x8	X	2.50				12.7	1.4	0.63	0.5	1.8	0.4
8x8	X	10.00				14.4	1.1	0.80	0.4	1.5	0.5
8x8	X	20.00				15.9	1.0	0.94	0.4	1.4	0.8

Field size [cm]	Dose curve type	Depth [cm]	Modulation	Build up	Fall off	Flatness	Symmetry	Penumbra width [cm]	In field	Penumbra	Out of field
8x8	Y	2.50				11.4	1.1	0.51	0.8	2.1	0.9
8x8	Y	10.00				13.6	1.0	0.68	0.7	2.4	1.1
8x8	Y	20.00				15.1	0.9	0.80	0.7	2.4	1.4
10x10	Depth	0.00		3.5	0.1						
10x10	X	1.50				18.6	0.5	0.78	0.8	1.7	0.6
10x10	X	2.40				19.6	1.0	0.89	0.5	1.6	0.5
10x10	X	5.00				21.0	1.1	1.03	0.6	1.3	0.4
10x10	X	10.00				21.9	1.0	1.18	0.5	1.1	0.6
10x10	X	20.00				22.8	1.0	1.39	0.5	1.1	1.0
10x10	X	30.00				22.9	1.0	1.60	0.4	1.2	1.4
10x10	Y	1.50				18.0	1.5	0.63	0.8	2.2	0.9
10x10	Y	2.40				18.7	1.4	0.72	0.6	2.6	0.9
10x10	Y	5.00				19.4	1.1	0.85	0.5	1.5	0.9
10x10	Y	10.00				21.5	1.1	0.99	0.5	1.9	1.1
10x10	Y	20.00				22.0	1.1	1.18	0.5	1.8	1.5
10x10	Y	30.00				22.8	1.0	1.36	0.7	2.0	1.7
14x14	Depth	0.00		4.1	0.1						
14x14	X	2.40				31.0	1.1	2.22	0.5	1.1	0.6
14x14	X	10.00				33.3	1.2	2.61	0.5	0.9	0.8
14x14	X	20.00				34.5	1.4	3.01	0.6	0.9	1.3
14x14	Y	2.40				29.7	1.6	1.92	0.6	1.1	0.9
14x14	Y	10.00				31.2	1.2	2.26	0.6	0.9	1.2
14x14	Y	20.00				32.1	1.2	2.62	0.7	1.0	1.7
15x15	Depth	0.00		3.9	0.1						
15x15	X	1.50				33.0	1.1	2.54	1.0	1.2	0.9
15x15	X	2.40				34.0	1.3	2.62	0.5	1.2	0.7
15x15	X	5.00				35.4	1.3	2.81	0.5	1.0	0.7
15x15	X	10.00				36.1	1.2	3.00	0.5	1.0	1.0
15x15	X	20.00				37.2	1.3	3.41	0.5	1.0	1.6
15x15	X	30.00				38.0	1.3	3.82	1.0	1.3	2.1
15x15	Y	1.50				30.7	1.2	2.21	0.7	1.6	1.1
15x15	Y	2.40				31.5	1.2	2.31	0.7	1.2	1.1
15x15	Y	5.00				32.7	1.3	2.45	0.6	1.1	1.2
15x15	Y	10.00				33.7	1.3	2.67	0.6	1.2	1.5
15x15	Y	20.00				34.8	0.9	3.06	0.6	1.3	2.1
15x15	Y	30.00				35.3	0.9	3.48	1.4	1.8	2.6
20x20	Depth	0.00		3.5	0.1						
20x20	X	1.50				47.5	1.3	4.73	0.8	0.9	1.0
20x20	X	2.30				49.4	1.6	4.86	0.6	0.9	0.8
20x20	X	5.00				51.1	1.6	5.09	0.7	0.9	0.8
20x20	X	10.00				51.9	1.6	5.34	0.6	0.9	1.1
20x20	X	20.00				50.7	1.4	5.91	0.6	0.9	1.8
20x20	X	30.00				50.8	1.6	6.48	0.6	1.0	2.4
20x20	Y	1.50				46.8	1.4	4.31	0.6	0.8	1.3
20x20	Y	2.30				46.5	1.3	4.51	0.7	1.2	1.2
20x20	Y	5.00				47.8	1.2	4.65	0.7	0.9	1.3
20x20	Y	10.00				49.0	1.2	4.94	0.5	0.8	1.6
20x20	Y	20.00				50.3	1.3	5.46	0.6	1.0	2.3
20x20	Y	30.00				51.1	1.1	6.08	0.9	1.2	2.9
30x5	Depth	0.00		3.0	0.1						
30x5	X	2.50				72.6	0.8	9.49	0.4	1.3	1.3
30x5	X	5.00				72.5	0.3	9.79	0.4	1.9	1.9
30x5	X	10.00				71.8	0.7	10.33	0.5	1.8	1.7
30x5	X	20.00				70.8	1.0	11.34	0.5	1.5	1.6
30x5	X	30.00				69.9	0.6	12.35	0.5	1.7	2.2
30x5	Y	2.50				3.7	0.6	0.40	1.5	2.6	1.2
30x5	Y	5.00				3.8	0.4	0.45	1.8	3.6	1.2
30x5	Y	10.00				4.7	0.4	0.51	1.5	2.7	1.3
30x5	Y	20.00				5.8	0.4	0.63	1.6	3.1	1.6
30x5	Y	30.00				7.2	0.5	0.74	1.7	3.6	1.9
30x30	Depth	0.00		2.9	0.1						
30x30	X	2.40				71.0	0.7	9.34	0.4	1.0	1.1

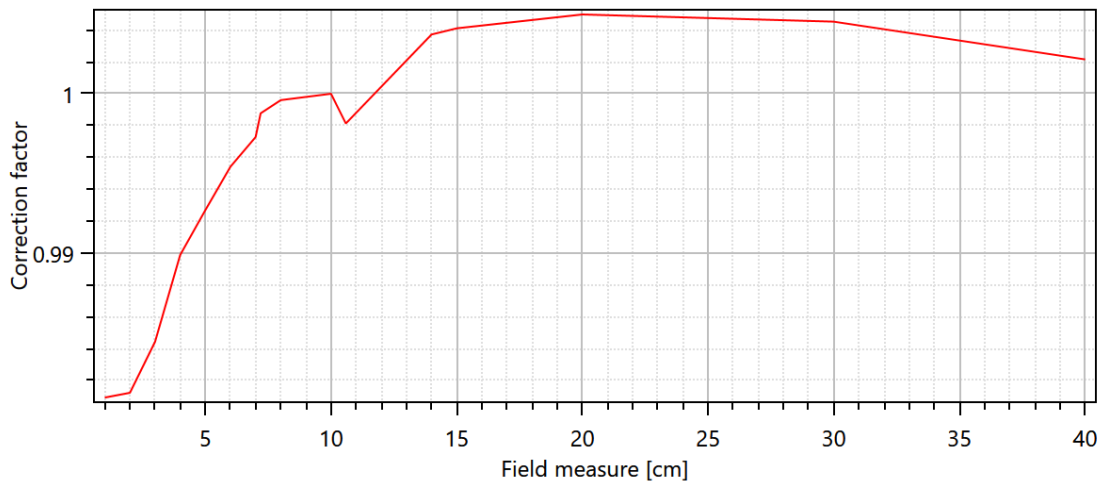
Field size [cm]	Dose curve type	Depth [cm]	Modulation	Build up	Fall off	Flatness	Symmetry	Penumbra width [cm]	In field	Penumbra	Out of field
30x30	X	5.00				70.8	0.6	9.65	0.4	1.2	1.3
30x30	X	10.00				70.5	0.5	10.08	0.4	1.4	1.7
30x30	X	20.00				68.3	0.4	11.01	0.4	1.2	2.2
30x30	X	30.00				68.6	1.0	11.98	0.6	1.1	3.0
30x30	Y	2.40				71.0	0.5	8.97	0.6	1.1	1.7
30x30	Y	5.00				70.6	0.7	9.27	0.6	0.9	1.6
30x30	Y	10.00				70.4	0.7	9.70	0.6	0.9	1.8
30x30	Y	20.00				68.5	0.9	10.62	0.6	1.0	2.5
30x30	Y	30.00				68.1	1.0	11.56	1.0	1.1	3.2
40x40	Depth	0.00		2.9	0.1						
40x40	X	1.50				73.9	0.6	13.70	0.6	1.1	1.3
40x40	X	2.20				73.1	0.2	13.88	0.4	1.2	1.6
40x40	X	5.00				72.9	0.5	14.35	0.3	1.1	1.5
40x40	X	10.00				73.0	0.4	15.01	0.3	1.0	1.6
40x40	X	20.00				73.0	0.6	16.34	0.4	0.7	2.2
40x40	X	30.00				73.5	1.1	17.69	0.8	0.5	3.3
40x40	Y	1.50				72.7	0.4	13.18	0.5	1.5	1.8
40x40	Y	2.20				72.9	0.5	13.46	0.5	1.1	1.5
40x40	Y	5.00				72.8	0.4	13.95	0.6	0.7	1.0
40x40	Y	10.00				72.3	0.4	14.53	0.7	0.6	1.3
40x40	Y	20.00				70.8	0.6	15.91	0.6	0.6	2.2
40x40	Y	30.00				73.9	1.0	17.33	1.0	0.5	3.2

Output Factor Corrections

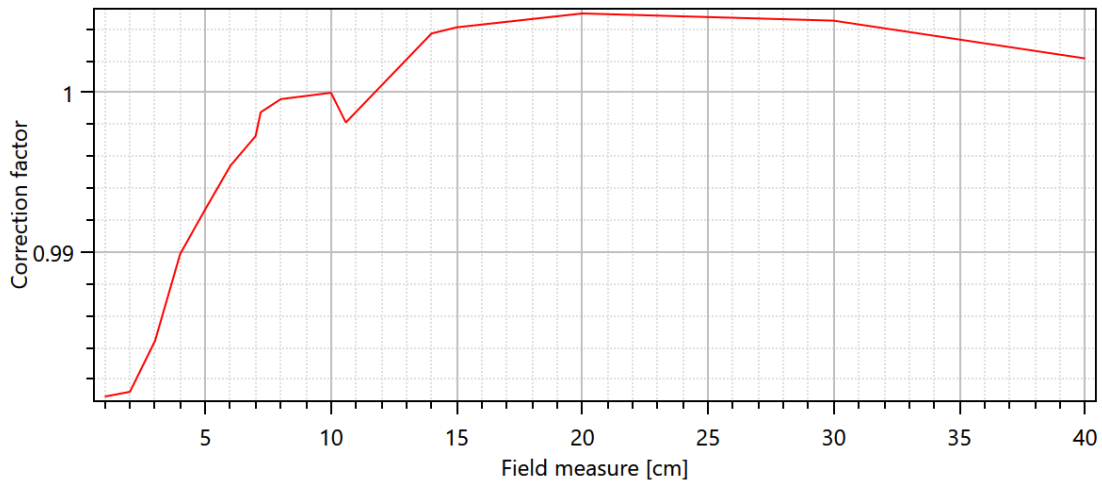
Normalization 5.47311

Field size	Correction factor
1.00	0.98092
2.00	0.98122
3.00	0.98442
4.00	0.98988
5.00	0.99269
6.00	0.99542
7.00	0.99728
7.20	0.99877
8.00	0.99960
10.00	1.00000
10.59	0.99813
14.00	1.00372
15.00	1.00411
20.00	1.00498
30.00	1.00453
40.00	1.00216

Output Factor Corrections



Output Factor Corrections



Off Axis

Beam profile correction

Radius [cm]	Correction factor
0.00	1.000
0.50	0.979
1.00	0.976
2.00	0.925
3.00	0.889
4.00	0.835
5.00	0.784
7.50	0.672
8.00	0.652
9.00	0.626
10.00	0.583
12.50	0.515
15.00	0.454
17.50	0.407

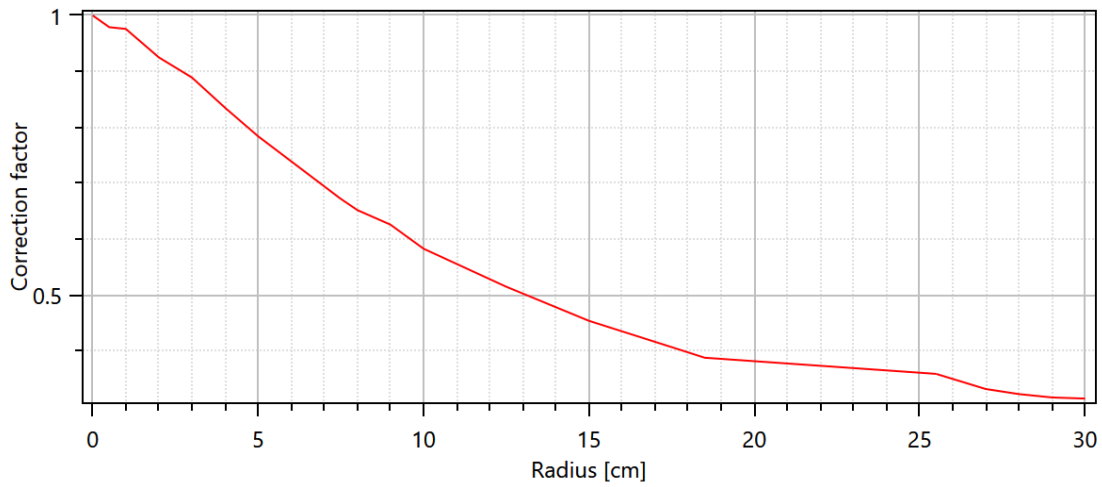
Beam profile correction

Radius [cm]	Correction factor
18.50	0.388
25.50	0.359
27.00	0.332
28.00	0.323
29.00	0.317
30.00	0.315

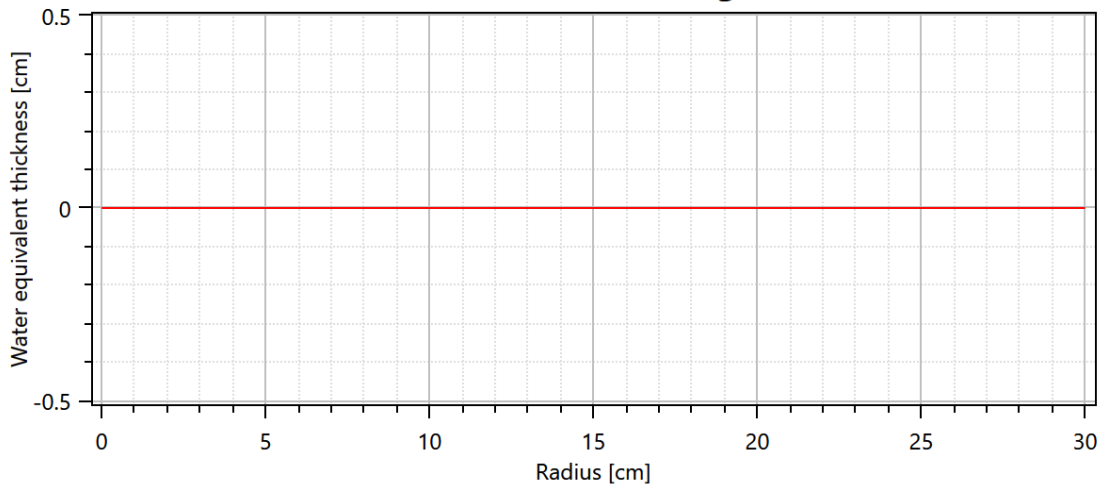
Off Axis Softening

Radius [cm]	Water equivalent thickness [cm]
0.00	0.000
30.00	0.000

Beam profile



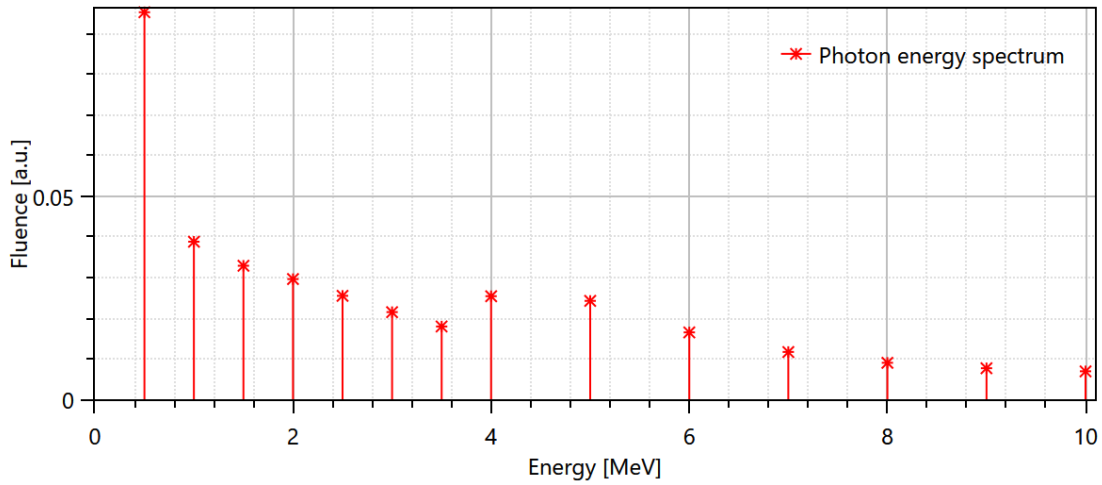
Off-axis softening



Photons

Energy [MeV]	Fluence [a.u.]
0.50	0.09531
1.00	0.03881
1.50	0.03289
2.00	0.02963
2.50	0.02550
3.00	0.02148
3.50	0.01796
4.00	0.02540
5.00	0.02426
6.00	0.01650
7.00	0.01167
8.00	0.00901
9.00	0.00768
10.00	0.00691

Energy Spectrum

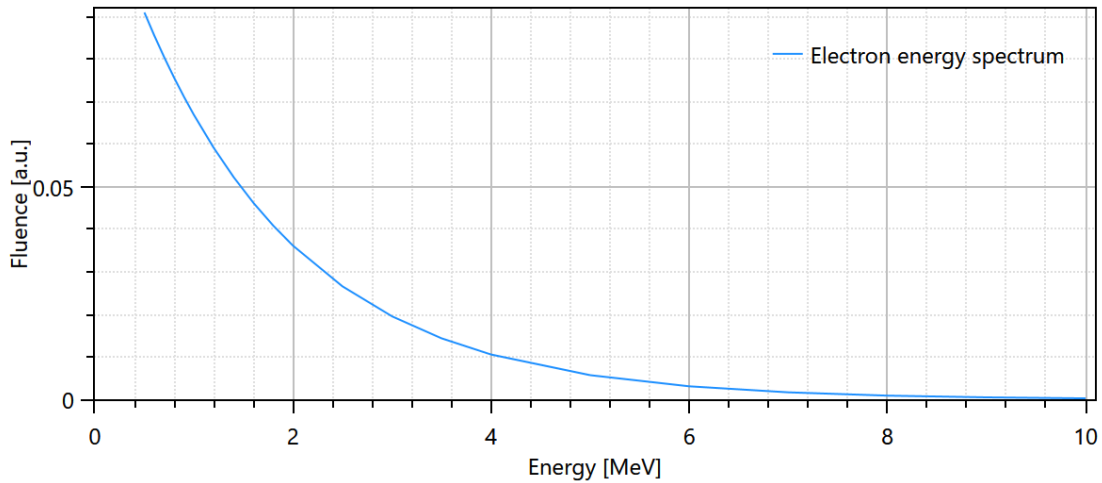


Energy Spectrum

Contamination Electrons

C	0.0000
E ₀ [MeV]	1.6251

Energy Spectrum



Fluence

Flattening filter weight for additional electron source	0.086
Flattening filter free	Yes
Leaf tip width [cm]	0.645
Tongue and groove [cm]	0.100

Collimator calibration

Collimator	Curvature [1/cm]	Gain	Offset [cm]
Y-jaws	0.00016	0.0000	0.005
MLC x-position	0.00030	0.0000	0.004
MLC y-position		0.0000	

Collimator position

Collimator	Transmission	Eff. dist. to source [cm]
Y-jaws		50.90
MLC	0.00257	39.57

Sources

Source	Weight	X width [cm]	Y width [cm]	Eff. dist. to source [cm]
Primary		0.082	0.032	14.00
Flattening filter	0.00782	2.950		
Electrons	0.00591	2.136		

Signatures

Signature 1 (Name/Signature/Date)

Signature 2 (Name/Signature/Date)

B Complete Results of Independent Verification

B.1 MATLAB Verification

The following tables (i.e. Tables B.1, B.2, B.3 and B.4) summarize the results of the verification carried out with the MATLAB code. The notation used denotes: DWP - digital water phantom, CR - crossplane profile, IN - inplane profile, γ_{mean} - the average (mean) γ -value and $\gamma_{<1}$ - the percentage of γ -values that are less than one.

Table B.1: Results of MATLAB verification for 6 MV FF.

Field size [cm × cm]	Curve type - at depth [cm]	30 cm × 30 cm × 30 cm DWP		50 cm × 50 cm × 50 cm DWP	
		γ_{mean}	$\gamma_{<1}$ [%]	γ_{mean}	$\gamma_{<1}$ [%]
1 × 1	PDD	0.68	98.91	-	-
	CR - d_{max}	0.12	100	-	-
	CR - 10	0.16	100	-	-
	CR - 20	0.17	100	-	-
	IN - d_{max}	0.22	100	-	-
	IN - 10	0.24	100	-	-
	IN - 20	0.27	100	-	-
2 × 2	PDD	0.31	100	0.32	99.54
	CR - d_{max}	0.11	100	0.21	100
	CR - 5	0.10	100	0.21	100
	CR - 10	0.10	100	0.20	100
	CR - 20	0.15	100	0.23	100
	CR - 30	0.73	72.67	0.24	100
	IN - d_{max}	0.21	100	0.21	100
	IN - 5	0.21	100	0.24	100
	IN - 10	0.22	100	0.24	100
	IN - 20	0.26	100	0.28	100
3 × 3	PDD	0.18	99.45	0.18	100
	CR - d_{max}	0.14	100	0.20	100
	CR - 5	0.13	100	0.20	100
	CR - 10	0.11	100	0.17	100
	CR - 20	0.19	100	0.23	100
	CR - 30	0.71	75.68	0.21	100
	IN - d_{max}	0.19	100	0.18	100
	IN - 5	0.20	100	0.21	100
	IN - 10	0.27	100	0.26	100
	IN - 20	0.31	100	0.31	100
	IN - 30	0.91	64.86	0.44	100

Field size [cm × cm]	Curve type - at depth [cm]	30 cm × 30 cm × 30 cm DWP		50 cm × 50 cm × 50 cm DWP	
		γ_{mean}	$\gamma_{<1}$ [%]	γ_{mean}	$\gamma_{<1}$ [%]
4 × 4	PDD	0.19	99.45	-	-
	CR - d _{max}	0.12	100	-	-
	CR - 10	0.14	100	-	-
	CR - 20	0.16	100	-	-
	IN - d _{max}	0.17	100	-	-
	IN - 10	0.22	100	-	-
	IN - 20	0.31	100	-	-
5 × 5	PDD	0.22	99.45	0.21	100
	CR - d _{max}	0.17	100	0.22	100
	CR - 1.5	0.17	100	0.21	100
	CR - 5	0.15	100	0.21	100
	CR - 10	0.14	100	0.20	100
	CR - 20	0.10	100	0.15	100
	CR - 30	0.86	63.36	0.32	99.24
	IN - d _{max}	0.15	100	0.15	100
	IN - 1.5	0.17	100	0.18	100
	IN - 5	0.24	100	0.25	100
	IN - 10	0.22	100	0.24	100
	IN - 20	0.43	100	0.43	100
IN - 30	1.11	50.57	0.51	87.79	
6 × 6	PDD	0.13	99.45	-	-
	CR - d _{max}	0.16	100	-	-
	CR - 10	0.14	100	-	-
	CR - 20	0.15	100	-	-
	IN - d _{max}	0.13	100	-	-
	IN - 10	0.16	100	-	-
	IN - 20	0.45	100	-	-
7 × 7	PDD	0.12	99.47	0.11	100
	CR - 1.5	0.19	100	0.23	100
	CR - 5	0.18	100	0.22	100
	CR - 10	0.15	100	0.20	100
	CR - 20	0.19	100	0.24	100
	CR - 30	0.75	62.89	0.43	95.70
	IN - 1.5	0.13	100	0.14	100
	IN - 5	0.18	100	0.19	100
	IN - 10	0.23	100	0.24	100

Field size [cm × cm]	Curve type - at depth [cm]	30 cm × 30 cm × 30 cm DWP		50 cm × 50 cm × 50 cm DWP	
		γ_{mean}	$\gamma_{<1}$ [%]	γ_{mean}	$\gamma_{<1}$ [%]
	IN - 20	0.51	98.34	0.51	98.34
	IN - 30	1.06	44.64	0.68	76.90
8 × 8	PDD	0.13	99.47	-	-
	CR - d_{max}	0.20	100	-	-
	CR - 10	0.19	100	-	-
	CR - 20	0.19	100	-	-
	CR - 30	0.73	70.96	-	-
	IN - d_{max}	0.12	100	-	-
	IN - 10	0.28	100	-	-
	IN - 20	0.49	96.54	-	-
	IN - 30	1.08	47.70	-	-
10 × 10	PDD	0.14	99.47	0.12	99.55
	CR - d_{max}	0.24	100	0.26	100
	CR - 1.5	0.24	100	0.27	100
	CR - 5	0.26	100	0.29	100
	CR - 10	0.27	100	0.30	100
	CR - 20	0.25	100	0.27	100
	CR - 30	0.79	71.21	0.62	90.08
	IN - d_{max}	0.17	100	0.17	100
	IN - 1.5	0.22	100	0.22	100
	IN - 5	0.23	100	0.24	100
	IN - 10	0.29	100	0.30	100
	IN - 20	0.59	84.64	0.60	84.02
IN - 30	1.29	31.31	1.04	41.99	
14 × 14	PDD	0.21	98.36	0.18	100
	CR - 1.5	0.32	100	0.37	100
	CR - 10	0.29	100	0.32	100
	CR - 20	0.40	100	0.43	95.94
	IN - 1.5	0.26	100	0.26	100
	IN - 10	0.40	98.52	0.41	100
15 × 15	IN - 20	0.62	86.67	0.63	84.81
	PDD	0.20	98.36	0.17	100
	CR - d_{max}	0.33	100	0.36	100
	CR - 1.5	0.34	100	0.38	100
	CR - 5	0.32	100	0.35	100
	CR - 10	0.30	100	0.34	100

Field size [cm × cm]	Curve type - at depth [cm]	30 cm × 30 cm × 30 cm DWP		50 cm × 50 cm × 50 cm DWP	
		γ_{mean}	$\gamma_{<1}$ [%]	γ_{mean}	$\gamma_{<1}$ [%]
20 × 20	CR - 20	0.39	100	0.42	97.52
	CR - 30	0.78	69.52	0.59	89.01
	IN - d _{max}	0.25	100	0.23	100
	IN - 1.5	0.26	100	0.26	100
	IN - 5	0.36	100	0.36	100
	IN - 10	0.44	95.74	0.43	97.87
	IN - 20	0.67	75.27	0.66	77.39
	IN - 30	1.19	41.64	0.88	44.52
	PDD	-	-	0.22	99.09
	CR - d _{max}	-	-	0.42	87.61
	CR - 1.5	-	-	0.36	85.45
	CR - 5	-	-	0.44	100
	CR - 10	-	-	0.52	94.24
	CR - 20	-	-	0.57	81.82
	CR - 30	-	-	0.95	54.85
	IN - d _{max}	-	-	0.23	100
IN - 1.5	-	-	0.36	100	
IN - 5	-	-	0.42	97.58	
IN - 10	-	-	0.47	88.18	
IN - 20	-	-	0.89	65.15	
IN - 30	-	-	1.17	34.74	
30 × 30	PDD	-	-	0.21	100
	CR - d _{max}	-	-	0.38	81.86
	CR - 5	-	-	0.33	96.06
	CR - 10	-	-	0.39	96.98
	CR - 20	-	-	0.84	62.38
	CR - 30	-	-	1.10	50.24
	IN - d _{max}	-	-	0.35	91.15
	IN - 5	-	-	0.39	100
	IN - 10	-	-	0.49	90.23
	IN - 20	-	-	0.96	58.24
IN - 30	-	-	1.28	40.71	
40 × 40	PDD	-	-	-	-
	CR - d _{max}	-	-	0.66	74.94
	CR - 1.5	-	-	0.66	75.57
	CR - 5	-	-	0.38	83.68

Table B.2: Results of MATLAB verification for 10 MV FF.

Field size [cm × cm]	Curve type - at depth [cm]	30 cm × 30 cm × 30 cm DWP		50 cm × 50 cm × 50 cm DWP	
		γ_{mean}	$\gamma_{<1}$ [%]	γ_{mean}	$\gamma_{<1}$ [%]
1 × 1	PDD	0.51	98.94	0.77	95.54
	CR - d_{max}	0.15	100	0.17	100
	CR - 1.5	0.16	100	0.18	100
	CR - 5	0.12	100	0.13	100
	CR - 10	0.16	100	0.19	100
	CR - 20	0.18	100	0.21	100
	CR - 30	0.34	100	0.21	100
	IN - d_{max}	0.24	100	0.25	100
	IN - 1.5	0.24	100	0.24	100
	IN - 5	0.23	100	0.23	100
	IN - 10	0.24	100	0.25	100
	IN - 20	0.26	100	0.26	100
	IN - 30	0.50	89.40	0.27	100
2 × 2	PDD	0.14	98.94	0.12	99.55
	CR - d_{max}	0.15	100	0.22	100
	CR - 1.5	0.17	100	0.24	100
	CR - 5	0.14	100	0.21	100
	CR - 10	0.13	100	0.21	100
	CR - 20	0.16	100	0.23	100
	CR - 30	0.60	93.33	0.23	100
	IN - d_{max}	0.22	100	0.22	100
	IN - 1.5	0.27	100	0.26	100
	IN - 5	0.23	100	0.23	100
	IN - 10	0.25	100	0.27	100
	IN - 20	0.29	100	0.30	100
	IN - 30	0.79	66.00	0.33	100
3 × 3	PDD	0.13	98.94	0.16	99.55
	CR - d_{max}	0.13	100	0.19	100
	CR - 1.5	0.15	100	0.20	100
	CR - 5	0.14	100	0.20	100
	CR - 10	0.11	100	0.17	100
	CR - 20	0.17	100	0.22	100
	CR - 30	0.60	89.19	0.20	100
	IN - d_{max}	0.24	100	0.24	100
	IN - 1.5	0.29	100	0.29	100

Field size [cm × cm]	Curve type - at depth [cm]	30 cm × 30 cm × 30 cm DWP		50 cm × 50 cm × 50 cm DWP	
		γ_{mean}	$\gamma_{<1}$ [%]	γ_{mean}	$\gamma_{<1}$ [%]
4 × 4	IN - 5	0.28	100	0.29	100
	IN - 10	0.27	100	0.27	100
	IN - 20	0.29	100	0.31	100
	IN - 30	0.86	63.51	0.39	100
	PDD	0.15	99.34	0.16	99.73
	CR - d_{max}	0.13	100	0.20	100
	CR - 1.5	0.15	100	0.21	100
	CR - 5	0.12	100	0.19	100
	CR - 10	0.12	100	0.19	100
	CR - 20	0.12	100	0.22	100
	CR - 30	0.69	86.39	0.27	100
	IN - d_{max}	0.24	100	0.23	100
	IN - 1.5	0.26	100	0.26	100
	IN - 5	0.25	100	0.28	100
	IN - 10	0.25	100	0.26	100
	IN - 20	0.40	100	0.42	100
IN - 30	1.02	49.47	0.47	100	
5 × 5	PDD	0.12	99.34	0.15	99.73
	CR - d_{max}	0.13	100	0.18	100
	CR - 1.5	0.15	100	0.19	100
	CR - 5	0.14	100	0.18	100
	CR - 10	0.14	100	0.19	100
	CR - 20	0.12	100	0.16	100
	CR - 30	0.63	85.88	0.26	100
	IN - d_{max}	0.18	100	0.18	100
	IN - 1.5	0.23	100	0.22	100
	IN - 5	0.22	100	0.23	100
	IN - 10	0.24	100	0.24	100
	IN - 20	0.47	100	0.48	100
	IN - 30	0.94	59.00	0.52	97.33
6 × 6	PDD	0.10	99.34	0.14	99.73
	CR - d_{max}	0.12	100	0.19	100
	CR - 1.5	0.13	100	0.16	100
	CR - 5	0.12	100	0.18	100
	CR - 10	0.15	100	0.21	100
	CR - 20	0.21	100	0.25	100

Field size [cm × cm]	Curve type - at depth [cm]	30 cm × 30 cm × 30 cm DWP		50 cm × 50 cm × 50 cm DWP	
		γ_{mean}	$\gamma_{<1}$ [%]	γ_{mean}	$\gamma_{<1}$ [%]
7 × 7	CR - 30	0.60	84.78	0.39	100
	IN - d _{max}	0.20	100	0.18	100
	IN - 1.5	0.23	100	0.26	100
	IN - 5	0.23	100	0.22	100
	IN - 10	0.29	100	0.30	100
	IN - 20	0.55	97.83	0.55	96.52
	IN - 30	0.98	45.22	0.53	88.26
	PDD	0.10	99.67	0.11	99.73
	CR - d _{max}	0.13	100	0.20	100
	CR - 5	0.12	100	0.16	100
	CR - 10	0.15	100	0.20	100
	CR - 20	0.23	100	0.31	100
	CR - 30	0.63	92.43	0.42	100
	IN - d _{max}	0.22	100	0.20	100
8 × 8	IN - 5	0.25	100	0.24	100
	IN - 10	0.33	100	0.34	100
	IN - 20	0.45	100	0.46	100
	IN - 30	1.08	45.20	0.71	85.60
	PDD	0.10	99.67	0.10	100
	CR - d _{max}	0.11	100	0.16	100
	CR - 10	0.14	100	0.17	100
	CR - 20	0.23	100	0.29	100
	CR - 30	0.62	94.07	0.41	100
	IN - d _{max}	0.21	100	0.21	100
	IN - 10	0.39	100	0.38	100
	IN - 20	0.40	100	0.41	100
	IN - 30	1.14	44.81	0.79	76.30
	10 × 10	PDD	0.19	99.47	0.16
CR - d _{max}		0.12	100	0.15	100
CR - 1.5		0.10	100	0.14	100
CR - 5		0.16	100	0.17	100
CR - 10		0.20	100	0.22	100
CR - 20		0.26	100	0.28	100
CR - 30		0.75	78.55	0.53	96.69
IN - d _{max}		0.25	100	0.25	100
IN - 1.5		0.25	100	0.28	100

Field size [cm × cm]	Curve type - at depth [cm]	30 cm × 30 cm × 30 cm DWP		50 cm × 50 cm × 50 cm DWP	
		γ_{mean}	$\gamma_{<1}$ [%]	γ_{mean}	$\gamma_{<1}$ [%]
14 × 14	IN - 5	0.31	100	0.29	100
	IN - 10	0.43	96.12	0.43	96.96
	IN - 20	0.54	95.07	0.55	94.20
	IN - 30	1.25	34.35	0.94	55.10
	PDD	0.21	99.67	0.18	99.73
	CR - d_{max}	0.20	100	0.24	100
	CR - 10	0.27	100	0.31	100
	CR - 20	0.42	98.52	0.46	94.46
	IN - d_{max}	0.31	100	0.33	100
	IN - 10	0.60	76.01	0.60	78.97
15 × 15	IN - 20	0.80	72.22	0.81	71.85
	PDD	0.21	99.67	0.18	100
	CR - d_{max}	0.20	100	0.25	100
	CR - 1.5	0.22	100	0.25	100
	CR - 5	0.30	100	0.30	100
	CR - 10	0.33	100	0.35	98.94
	CR - 20	0.46	93.99	0.50	92.58
	CR - 30	0.85	53.93	0.63	86.88
	IN - d_{max}	0.35	100	0.34	100
	IN - 1.5	0.40	99.29	0.40	98.58
20 × 20	IN - 5	0.42	94.33	0.41	96.45
	IN - 10	0.54	81.21	0.54	84.40
	IN - 20	0.79	68.90	0.79	69.96
	IN - 30	1.19	38.66	0.85	52.30
	PDD	-	-	0.21	99.73
	CR - d_{max}	-	-	0.31	100
	CR - 1.5	-	-	0.33	100
	CR - 5	-	-	0.36	100
	CR - 10	-	-	0.42	95.15
	CR - 20	-	-	0.67	78.18
CR - 30	-	-	0.75	65.56	
IN - d_{max}	-	-	0.44	100	
IN - 1.5	-	-	0.42	100	
IN - 5	-	-	0.50	95.15	
IN - 10	-	-	0.72	72.12	
IN - 20	-	-	0.92	52.12	

Field size [cm × cm]	Curve type - at depth [cm]	30 cm × 30 cm × 30 cm DWP		50 cm × 50 cm × 50 cm DWP		
		γ_{mean}	$\gamma_{<1}$ [%]	γ_{mean}	$\gamma_{<1}$ [%]	
30 × 30	IN - 30	-	-	1.13	34.56	
	PDD	-	-	0.14	99.73	
	CR - d _{max}	-	-	0.27	100	
	CR - 1.5	-	-	0.19	100	
	CR - 5	-	-	0.31	97.21	
	CR - 10	-	-	0.47	88.84	
	CR - 20	-	-	0.82	69.95	
	CR - 30	-	-	1.17	44.39	
	IN - d _{max}	-	-	0.32	100	
	IN - 1.5	-	-	0.27	100	
	IN - 5	-	-	0.39	97.91	
	IN - 10	-	-	0.72	79.07	
	IN - 20	-	-	1.04	52.56	
	IN - 30	-	-	1.29	43.16	
	40 × 40	PDD	-	-	0.16	99.73
CR - d _{max}		-	-	0.31	97.18	
CR - 1.5		-	-	0.35	99.37	
CR - 5		-	-	0.28	100	
CR - 10		-	-	0.43	98.69	
CR - 20		-	-	0.85	56.72	
CR - 30		-	-	1.10	44.05	
IN - d _{max}		-	-	0.31	100	
IN - 1.5		-	-	0.36	100	
IN - 5		-	-	0.28	100	
IN - 10		-	-	0.48	99.67	
IN - 20		-	-	0.87	54.48	
IN - 30		-	-	1.20	41.93	
5 × 30		PDD	-	-	0.10	100
		CR - d _{max}	-	-	0.28	100
	CR - 5	-	-	0.36	96.74	
	CR - 10	-	-	0.49	92.33	
	CR - 20	-	-	0.84	69.25	
	CR - 30	-	-	1.03	52.53	
	IN - d _{max}	-	-	0.22	100	
	IN - 5	-	-	0.26	100	
	IN - 10	-	-	0.31	100	

Field size [cm × cm]	Curve type - at depth [cm]	30 cm × 30 cm × 30 cm DWP		50 cm × 50 cm × 50 cm DWP	
		γ_{mean}	$\gamma_{<1}$ [%]	γ_{mean}	$\gamma_{<1}$ [%]
30 × 5	IN - 20	-	-	0.55	97.80
	IN - 30	-	-	0.88	68.68
	PDD	-	-	0.12	100
	CR - d_{max}	-	-	0.24	100
	CR - 5	-	-	0.23	100
	CR - 10	-	-	0.25	100
	CR - 20	-	-	0.31	100
	CR - 30	-	-	0.49	98.90
	IN - d_{max}	-	-	0.51	100
	IN - 5	-	-	0.60	91.86
	IN - 10	-	-	0.72	76.28
	IN - 20	-	-	1.16	35.81
	IN - 30	-	-	1.47	20.99

Table B.3: Results of MATLAB verification for 6 MV FFF.

Field size [cm × cm]	Curve type - at depth [cm]	30 cm × 30 cm × 30 cm DWP		50 cm × 50 cm × 50 cm DWP	
		γ_{mean}	$\gamma_{<1}$ [%]	γ_{mean}	$\gamma_{<1}$ [%]
1 × 1	PDD	0.47	99.45	-	-
	CR - d_{max}	0.15	100	-	-
	CR - 10	0.14	100	-	-
	CR - 20	0.13	100	-	-
	IN - d_{max}	0.20	100	-	-
	IN - 10	0.25	100	-	-
	IN - 20	0.25	100	-	-
2 × 2	PDD	0.13	98.91	0.10	99.53
	CR - d_{max}	0.12	100	0.22	100
	CR - 5	0.13	100	0.21	100
	CR - 10	0.12	100	0.21	100
	CR - 20	0.13	100	0.21	100
	CR - 30	0.64	90.67	0.21	100
	IN - d_{max}	0.19	100	0.22	100
	IN - 5	0.22	100	0.22	100
	IN - 10	0.23	100	0.25	100
	IN - 20	0.26	100	0.29	100
3 × 3	PDD	0.10	98.91	0.07	99.53
	CR - d_{max}	0.13	100	0.18	100
	CR - 5	0.11	100	0.18	100
	CR - 10	0.12	100	0.18	100
	CR - 20	0.13	100	0.21	100
	CR - 30	0.67	85.59	0.24	100
	IN - d_{max}	0.19	100	0.18	100
	IN - 5	0.19	100	0.20	100
	IN - 10	0.24	100	0.26	100
	IN - 20	0.28	100	0.29	100
4 × 4	PDD	0.15	98.91	-	-
	CR - d_{max}	0.15	100	-	-
	CR - 10	0.14	100	-	-
	CR - 20	0.18	100	-	-
	IN - d_{max}	0.21	100	-	-
	IN - 10	0.27	100	-	-

Field size [cm × cm]	Curve type - at depth [cm]	30 cm × 30 cm × 30 cm DWP		50 cm × 50 cm × 50 cm DWP	
		γ_{mean}	$\gamma_{<1}$ [%]	γ_{mean}	$\gamma_{<1}$ [%]
5 × 5	IN - 20	0.31	100	-	-
	PDD	0.12	98.91	0.15	99.54
	CR - d_{max}	0.15	100	0.20	100
	CR - 1.5	0.17	100	0.22	100
	CR - 5	0.13	100	0.20	100
	CR - 10	0.15	100	0.25	100
	CR - 20	0.24	100	0.30	100
	CR - 30	0.89	64.89	0.42	99.24
	IN - d_{max}	0.24	100	0.22	100
	IN - 1.5	0.29	100	0.28	100
	IN - 5	0.23	100	0.25	100
	IN - 10	0.26	100	0.27	100
	IN - 20	0.39	99.24	0.40	100
	IN - 30	1.04	58.14	0.46	92.37
6 × 6	PDD	0.11	98.91	-	-
	CR - d_{max}	0.18	100	-	-
	CR - 10	0.17	100	-	-
	CR - 20	0.29	100	-	-
	IN - d_{max}	0.27	100	-	-
	IN - 10	0.23	100	-	-
	IN - 20	0.47	94.78	-	-
7 × 7	PDD	0.11	98.91	-	-
	CR - d_{max}	0.20	100	-	-
	CR - 5	0.17	100	-	-
	CR - 10	0.20	100	-	-
	CR - 20	0.37	99.20	-	-
	CR - 30	0.98	56.80	-	-
	IN - d_{max}	0.27	100	-	-
	IN - 5	0.25	100	-	-
	IN - 10	0.31	100	-	-
	IN - 20	0.49	90.40	-	-
IN - 30	1.18	52.80	-	-	
8 × 8	PDD	0.12	99.45	-	-
	CR - d_{max}	0.19	100	-	-
	CR - 10	0.21	100	-	-
	CR - 20	0.32	97.04	-	-

Field size [cm × cm]	Curve type - at depth [cm]	30 cm × 30 cm × 30 cm DWP		50 cm × 50 cm × 50 cm DWP		
		γ_{mean}	$\gamma_{<1}$ [%]	γ_{mean}	$\gamma_{<1}$ [%]	
10 × 10	IN - d_{max}	0.25	100	-	-	
	IN - 10	0.36	100	-	-	
	IN - 20	0.48	87.41	-	-	
	PDD	0.13	98.91	0.12	100	
	CR - d_{max}	0.19	100	0.27	100	
	CR - 1.5	0.24	100	0.30	100	
	CR - 5	0.18	100	0.28	100	
	CR - 10	0.25	100	0.35	98.80	
	CR - 20	0.38	86.71	0.46	88.40	
	CR - 30	1.18	56.97	0.66	70.72	
	IN - d_{max}	0.29	100	0.27	100	
	IN - 1.5	0.31	100	0.30	100	
	IN - 5	0.27	100	0.30	100	
	IN - 10	0.33	100	0.35	100	
	IN - 20	0.46	80.81	0.48	82.32	
	IN - 30	1.28	57.93	0.71	64.64	
	14 × 14	PDD	0.16	99.45	0.15	99.54
		CR - d_{max}	0.35	100	0.34	100
CR - 10		0.23	98.46	0.27	98.97	
CR - 20		0.57	76.92	0.62	71.28	
IN - d_{max}		0.42	100	0.42	100	
IN - 10		0.33	95.90	0.35	93.85	
IN - 20		0.51	81.03	0.53	82.05	
15 × 15	PDD	0.17	98.91	0.16	99.54	
	CR - d_{max}	0.26	100	0.26	100	
	CR - 1.5	0.25	100	0.30	100	
	CR - 5	0.20	100	0.31	100	
	CR - 10	0.27	99.29	0.39	94.33	
	CR - 20	0.42	83.69	0.53	80.85	
	CR - 30	1.17	60.15	0.71	70.92	
	IN - d_{max}	0.35	100	0.29	100	
	IN - 1.5	0.32	100	0.29	100	
	IN - 5	0.29	100	0.33	97.87	
	IN - 10	0.36	91.49	0.38	90.07	
	IN - 20	0.56	75.18	0.57	75.89	
IN - 30	1.38	61.19	0.76	65.96		

Field size [cm × cm]	Curve type - at depth [cm]	30 cm × 30 cm × 30 cm DWP		50 cm × 50 cm × 50 cm DWP	
		γ_{mean}	$\gamma_{<1}$ [%]	γ_{mean}	$\gamma_{<1}$ [%]
20 × 20	PDD	-	-	0.17	100
	CR - d _{max}	-	-	0.32	100
	CR - 1.5	-	-	0.30	100
	CR - 5	-	-	0.35	99.39
	CR - 10	-	-	0.42	93.94
	CR - 20	-	-	0.54	78.79
	CR - 30	-	-	0.72	72.73
	IN - d _{max}	-	-	0.39	100
	IN - 1.5	-	-	0.29	100
	IN - 5	-	-	0.34	96.97
	IN - 10	-	-	0.43	87.88
	IN - 20	-	-	0.60	73.33
IN - 30	-	-	0.76	70.30	
30 × 30	PDD	-	-	0.26	99.09
	CR - d _{max}	-	-	0.35	100
	CR - 5	-	-	0.36	97.67
	CR - 10	-	-	0.43	90.23
	CR - 20	-	-	0.60	80.19
	CR - 30	-	-	0.70	81.37
	IN - d _{max}	-	-	0.38	100
	IN - 5	-	-	0.33	96.74
	IN - 10	-	-	0.41	86.98
	IN - 20	-	-	0.59	77.67
IN - 30	-	-	0.84	78.30	
40 × 40	PDD	-	-	0.29	100
	CR - d _{max}	-	-	0.25	100
	CR - 1.5	-	-	0.27	100
	CR - 5	-	-	0.31	100
	CR - 10	-	-	0.38	91.78
	CR - 20	-	-	0.51	83.74
	CR - 30	-	-	0.44	92.06
	IN - d _{max}	-	-	0.23	100
	IN - 1.5	-	-	0.24	100
	IN - 5	-	-	0.25	100
	IN - 10	-	-	0.33	89.80
IN - 20	-	-	0.44	82.76	

Field size [cm × cm]	Curve type - at depth [cm]	30 cm × 30 cm × 30 cm DWP		50 cm × 50 cm × 50 cm DWP	
		γ_{mean}	$\gamma_{<1}$ [%]	γ_{mean}	$\gamma_{<1}$ [%]
5 × 30	IN - 30	-	-	0.48	94.47
	PDD	-	-	0.13	100
	CR - d_{max}	-	-	0.35	100
	CR - 5	-	-	0.34	99.07
	CR - 10	-	-	0.35	97.67
	CR - 20	-	-	0.42	93.40
	CR - 30	-	-	0.42	86.76
	IN - d_{max}	-	-	0.37	100
	IN - 5	-	-	0.42	100
	IN - 10	-	-	0.51	91.21
	IN - 20	-	-	0.78	76.92
	IN - 30	-	-	1.02	59.34
	PDD	-	-	0.13	99.54
	CR - d_{max}	-	-	0.29	100
30 × 5	CR - 5	-	-	0.33	100
	CR - 10	-	-	0.41	100
	CR - 20	-	-	0.62	84.62
	CR - 30	-	-	0.81	69.23
	IN - d_{max}	-	-	0.36	100
	IN - 5	-	-	0.26	100
	IN - 10	-	-	0.31	96.74
	IN - 20	-	-	0.33	92.09
	IN - 30	-	-	0.39	83.49

Table B.4: Results of MATLAB verification for 10 MV FFF.

Field size [cm × cm]	Curve type - at depth [cm]	30 cm × 30 cm × 30 cm DWP		50 cm × 50 cm × 50 cm DWP	
		γ_{mean}	$\gamma_{<1}$ [%]	γ_{mean}	$\gamma_{<1}$ [%]
1 × 1	PDD	0.40	98.94	-	-
	CR - d_{max}	0.14	100	-	-
	CR - 10	0.13	100	-	-
	CR - 20	0.12	100	-	-
	IN - d_{max}	0.16	100	-	-
	IN - 10	0.19	100	-	-
	IN - 20	0.20	100	-	-
2 × 2	PDD	0.14	98.94	0.13	99.55
	CR - d_{max}	0.13	100	0.21	100
	CR - 5	0.13	100	0.20	100
	CR - 10	0.13	100	0.20	100
	CR - 20	0.13	100	0.20	100
	CR - 30	0.59	86.67	0.22	100
	IN - d_{max}	0.18	100	0.17	100
	IN - 5	0.20	100	0.19	100
	IN - 10	0.22	100	0.20	100
	IN - 20	0.26	100	0.25	100
IN - 30	0.73	66.67	0.28	100	
3 × 3	PDD	0.13	99.47	0.11	99.55
	CR - d_{max}	0.13	100	0.19	100
	CR - 5	0.12	100	0.17	100
	CR - 10	0.11	100	0.18	100
	CR - 20	0.12	100	0.19	100
	CR - 30	0.60	86.49	0.20	100
	IN - d_{max}	0.19	100	0.18	100
	IN - 5	0.19	100	0.18	100
	IN - 10	0.23	100	0.23	100
	IN - 20	0.21	100	0.23	100
IN - 30	0.73	72.97	0.28	100	
4 × 4	PDD	0.15	99.47	-	-
	CR - d_{max}	0.13	100	-	-
	CR - 10	0.14	100	-	-
	CR - 20	0.17	100	-	-
	IN - d_{max}	0.22	100	-	-
	IN - 10	0.28	100	-	-

Field size [cm × cm]	Curve type - at depth [cm]	30 cm × 30 cm × 30 cm DWP		50 cm × 50 cm × 50 cm DWP	
		γ_{mean}	$\gamma_{<1}$ [%]	γ_{mean}	$\gamma_{<1}$ [%]
5 × 5	IN - 20	0.30	100	-	-
	PDD	0.16	98.94	0.17	100
	CR - d_{max}	0.14	100	0.21	100
	CR - 1.5	0.19	100	0.23	100
	CR - 5	0.13	100	0.21	100
	CR - 10	0.16	100	0.22	100
	CR - 20	0.21	100	0.28	100
	CR - 30	0.76	72.52	0.34	100
	IN - d_{max}	0.24	100	0.26	100
	IN - 1.5	0.29	100	0.27	100
	IN - 5	0.24	100	0.23	100
	IN - 10	0.26	100	0.26	100
	IN - 20	0.36	100	0.39	100
	IN - 30	0.82	60.47	0.41	99.24
	6 × 6	PDD	0.12	99.47	-
CR - d_{max}		0.19	100	-	-
CR - 10		0.20	100	-	-
CR - 20		0.32	100	-	-
IN - d_{max}		0.26	100	-	-
IN - 10		0.37	100	-	-
IN - 20		0.46	100	-	-
7 × 7	PDD	0.11	99.47	0.13	100
	CR - d_{max}	0.23	100	0.32	100
	CR - 5	0.18	100	0.29	100
	CR - 10	0.21	100	0.31	100
	CR - 20	0.27	100	0.37	100
	CR - 30	0.84	58.40	0.42	97.60
	IN - d_{max}	0.28	100	0.30	100
	IN - 5	0.27	100	0.26	100
	IN - 10	0.34	100	0.32	100
	IN - 20	0.43	100	0.46	100
	IN - 30	0.96	51.20	0.46	89.60
8 × 8	PDD	0.13	99.47	0.13	99.55
	CR - d_{max}	0.20	100	0.25	100
	CR - 10	0.29	98.14	0.33	95.03
	CR - 20	0.31	100	0.36	100

Field size [cm × cm]	Curve type - at depth [cm]	30 cm × 30 cm × 30 cm DWP		50 cm × 50 cm × 50 cm DWP	
		γ_{mean}	$\gamma_{<1}$ [%]	γ_{mean}	$\gamma_{<1}$ [%]
10 × 10	IN - d_{max}	0.33	99.38	0.34	98.14
	IN - 10	0.38	100	0.37	100
	IN - 20	0.47	98.11	0.49	97.52
	PDD	0.16	99.47	0.14	100
	CR - d_{max}	0.20	100	0.29	100
	CR - 1.5	0.27	100	0.31	100
	CR - 5	0.19	100	0.29	100
	CR - 10	0.24	100	0.33	100
	CR - 20	0.33	98.84	0.41	98.90
	CR - 30	0.88	57.58	0.54	84.53
	IN - d_{max}	0.30	100	0.32	100
	IN - 1.5	0.35	100	0.33	100
	IN - 5	0.30	100	0.28	100
	IN - 10	0.31	100	0.31	100
	IN - 20	0.40	94.77	0.41	93.37
	IN - 30	1.02	56.10	0.59	78.45
14 × 14	PDD	0.20	98.94	0.18	100
	CR - d_{max}	0.23	100	0.29	100
	CR - 10	0.26	100	0.30	100
	CR - 20	0.34	90.95	0.45	92.76
	IN - d_{max}	0.33	100	0.34	99.55
	IN - 10	0.35	100	0.36	100
15 × 15	IN - 20	0.39	87.94	0.45	88.69
	PDD	0.20	99.47	0.17	100
	CR - d_{max}	0.25	100	0.35	100
	CR - 1.5	0.30	100	0.37	100
	CR - 5	0.21	100	0.34	100
	CR - 10	0.27	100	0.39	100
	CR - 20	0.38	91.49	0.49	88.65
	CR - 30	0.99	58.65	0.61	77.30
	IN - d_{max}	0.35	100	0.35	100
	IN - 1.5	0.43	100	0.41	100
	IN - 5	0.30	100	0.31	100
	IN - 10	0.36	100	0.37	100
	IN - 20	0.46	85.11	0.49	85.82
IN - 30	1.13	57.46	0.63	71.63	

Field size [cm × cm]	Curve type - at depth [cm]	30 cm × 30 cm × 30 cm DWP		50 cm × 50 cm × 50 cm DWP	
		γ_{mean}	$\gamma_{<1}$ [%]	γ_{mean}	$\gamma_{<1}$ [%]
20 × 20	PDD	-	-	0.22	99.55
	CR - d _{max}	-	-	0.36	100
	CR - 1.5	-	-	0.38	100
	CR - 5	-	-	0.37	100
	CR - 10	-	-	0.43	100
	CR - 20	-	-	0.52	87.88
	CR - 30	-	-	0.61	77.58
	IN - d _{max}	-	-	0.30	100
	IN - 1.5	-	-	0.40	100
	IN - 5	-	-	0.32	100
	IN - 10	-	-	0.35	97.58
	IN - 20	-	-	0.48	81.82
IN - 30	-	-	0.59	71.52	
30 × 30	PDD	-	-	0.21	100
	CR - d _{max}	-	-	0.31	100
	CR - 5	-	-	0.33	100
	CR - 10	-	-	0.40	97.21
	CR - 20	-	-	0.48	85.98
	CR - 30	-	-	0.55	81.55
	IN - d _{max}	-	-	0.30	100
	IN - 5	-	-	0.28	100
	IN - 10	-	-	0.36	94.88
	IN - 20	-	-	0.44	83.72
IN - 30	-	-	0.53	78.30	
40 × 40	PDD	-	-	0.19	100
	CR - d _{max}	-	-	0.28	100
	CR - 1.5	-	-	0.28	100
	CR - 5	-	-	0.32	100
	CR - 10	-	-	0.39	99.67
	CR - 20	-	-	0.45	84.14
	CR - 30	-	-	0.34	95.63
	IN - d _{max}	-	-	0.24	100
	IN - 1.5	-	-	0.30	100
	IN - 5	-	-	0.22	100
IN - 10	-	-	0.29	99.67	
IN - 20	-	-	0.36	84.48	

Field size [cm × cm]	Curve type - at depth [cm]	30 cm × 30 cm × 30 cm DWP		50 cm × 50 cm × 50 cm DWP	
		γ_{mean}	$\gamma_{<1}$ [%]	γ_{mean}	$\gamma_{<1}$ [%]
5 × 30	IN - 30	-	-	0.31	94.09
	PDD	-	-	0.12	100
	CR - d_{max}	-	-	0.25	100
	CR - 5	-	-	0.29	100
	CR - 10	-	-	0.36	100
	CR - 20	-	-	0.40	97.66
	CR - 30	-	-	0.52	92.72
	IN - d_{max}	-	-	0.37	100
	IN - 5	-	-	0.35	100
	IN - 10	-	-	0.41	100
	IN - 20	-	-	0.66	85.71
	IN - 30	-	-	0.78	79.12
	PDD	-	-	0.12	99.55
30 × 5	CR - d_{max}	-	-	0.27	100
	CR - 5	-	-	0.26	100
	CR - 10	-	-	0.30	100
	CR - 20	-	-	0.46	92.31
	CR - 30	-	-	0.63	87.91
	IN - d_{max}	-	-	0.28	100
	IN - 5	-	-	0.27	100
	IN - 10	-	-	0.32	100
	IN - 20	-	-	0.38	95.35
	IN - 30	-	-	0.45	91.98

B.2 Point Dose Verification

The following tables (i.e. Tables B.5, B.6, B.7 and B.8) provide the exhaustive results of the point dose comparison of measured (D_{meas}) and calculated (D_{calc}) dose at various chosen points along the CAX (i.e. at different depths - in cm) and for four different SSDs (90 cm, 100 cm, 85 cm and 80 cm), along with the respective difference percentge (Diff). Once again, “DWP” stands for “digital water phantom” and serves to differentiate the two water phantoms on which the calculations and differences relative to the respective measurements were performed.

Table B.5: Results of point dose verification for 6 MV FF.

SSD [cm]	Field size [cm × cm]	Depth [cm]	D _{meas} [Gy]	30 cm × 30 cm × 30 cm DWP		50 cm × 50 cm × 50 cm DWP	
				D _{calc} [Gy]	Diff [%]	D _{calc} [Gy]	Diff [%]
90	3 × 3	5	1.116	1.16	3.9	1.15	3.0
		10	0.820	0.84	2.5	0.84	2.5
		20	0.445	0.45	1.0	0.45	1.0
	5 × 5	5	1.221	1.22	-0.1	1.22	-0.1
		7	1.084	1.08	-0.4	1.08	-0.4
		10	0.905	0.90	-0.6	0.90	-0.6
		15	0.668	0.67	0.3	0.67	0.3
		20	0.494	0.49	-0.9	0.49	-0.9
	10 × 10	5	1.305	1.30	-0.3	1.31	0.4
		7	1.177	1.18	0.3	1.18	0.3
		10	1.000	1.00	0.0	1.00	0.0
		15	0.757	0.75	-1.0	0.75	-1.0
		20	0.571	0.57	-0.1	0.57	-0.1
	15 × 15	5	1.352	1.36	0.6	1.36	0.6
		10	1.057	1.06	0.3	1.06	0.3
		20	0.624	0.62	-0.6	0.62	-0.6
	30 × 30	5	1.424	-	-	1.43	0.4
		7	1.307	-	-	1.32	1.0
		10	1.143	-	-	1.15	0.6
		15	0.904	-	-	0.91	0.6
		20	0.711	-	-	0.71	-0.1
	5 × 30	5	1.288	-	-	1.28	-0.6
		10	0.978	-	-	0.97	-0.8
		20	0.554	-	-	0.55	-0.7
30 × 5	5	1.270	-	-	1.29	1.6	
	10	0.965	-	-	0.98	1.5	
	20	0.548	-	-	0.55	0.3	
3 × 3	5	0.929	0.95	2.3	0.95	2.3	
	10	0.690	0.70	1.5	0.70	1.5	
	20	0.380	0.38	0.1	0.38	0.1	
5 × 5	5	1.000	1.00	0.0	1.00	0.0	
	7	0.895	0.90	0.6	0.90	0.6	
	10	0.753	0.75	-0.4	0.75	-0.4	
	15	0.562	0.56	-0.3	0.56	-0.3	
	20	0.420	0.42	0.0	0.42	0.0	

SSD [cm]	Field size [cm × cm]	Depth [cm]	D_{meas} [Gy]	30 cm × 30 cm × 30 cm DWP		50 cm × 50 cm × 50 cm DWP	
				D_{calc} [Gy]	Diff [%]	D_{calc} [Gy]	Diff [%]
85	10×10	5	1.068	1.07	0.2	1.07	0.2
		7	0.969	0.97	0.1	0.97	0.1
		10	0.831	0.83	-0.1	0.84	1.1
		15	0.637	0.64	0.5	0.64	0.5
		20	0.486	0.48	-1.2	0.48	-1.2
	15×15	5	1.108	1.12	1.1	1.12	1.1
		10	0.878	0.88	0.2	0.89	1.4
		20	0.530	0.53	-0.1	0.53	-0.1
	30×30	5	1.166	-	-	1.17	0.4
		7	1.075	-	-	1.09	1.4
		10	0.945	-	-	0.96	1.5
		15	0.757	-	-	0.76	0.3
		20	0.601	-	-	0.60	-0.2
	5×30	5	1.055	-	-	1.05	-0.5
		10	0.812	-	-	0.81	-0.2
		20	0.470	-	-	0.47	-0.1
	30×5	5	1.042	-	-	1.06	1.7
		10	0.802	-	-	0.82	2.2
		20	0.466	-	-	0.47	0.9
	3×3	5	1.224	1.28	4.6	1.28	4.6
10		0.896	0.93	3.8	0.93	3.8	
20		0.483	0.49	1.4	0.49	1.4	
5×5	5	1.354	1.35	-0.3	1.35	-0.3	
	7	1.200	1.20	0.0	1.20	0.0	
	10	0.996	1.00	0.4	1.00	0.4	
	15	0.731	0.73	-0.2	0.73	-0.2	
	20	0.538	0.54	0.3	0.54	0.3	
10×10	5	1.449	1.45	0.1	1.45	0.1	
	7	1.303	1.30	-0.3	1.30	-0.3	
	10	1.103	1.10	-0.3	1.10	-0.3	
	15	0.827	0.82	-0.8	0.83	0.4	
	20	0.621	0.62	-0.1	0.62	-0.1	
15×15	5	1.505	1.51	0.4	1.51	0.4	
	10	1.167	1.17	0.3	1.17	0.3	
	20	0.678	0.67	-1.3	0.68	0.2	
30×30	5	1.585	-	-	1.59	0.3	

SSD [cm]	Field size [cm × cm]	Depth [cm]	D_{meas} [Gy]	30 cm × 30 cm × 30 cm DWP		50 cm × 50 cm × 50 cm DWP	
				D_{calc} [Gy]	Diff [%]	D_{calc} [Gy]	Diff [%]
80		7	1.450	-	-	1.46	0.7
		10	1.262	-	-	1.27	0.7
		15	0.992	-	-	0.99	-0.2
		20	0.774	-	-	0.77	-0.5
	5 × 30	5	1.431	-	-	1.42	-0.8
		10	1.078	-	-	1.07	-0.8
		20	0.603	-	-	0.60	-0.4
	30 × 5	5	1.410	-	-	1.43	1.4
		10	1.063	-	-	1.08	1.6
		20	0.596	-	-	0.60	0.6
	3 × 3	5	1.350	1.43	5.9	1.43	5.9
		10	0.985	1.03	4.6	1.03	4.6
		20	0.528	0.54	2.3	0.54	2.3
	5 × 5	5	1.519	1.51	-0.6	1.51	-0.6
		10	1.108	1.10	-0.7	1.11	0.2
		20	0.591	0.59	-0.2	0.59	-0.2
	10 × 10	5	1.627	1.62	-0.4	1.62	-0.4
		10	1.226	1.22	-0.5	1.22	-0.5
		20	0.680	0.67	-1.5	0.68	-0.1
	15 × 15	5	1.689	1.68	-0.5	1.69	0.1
		10	1.299	1.30	0.1	1.30	0.1
		20	0.744	0.73	-1.8	0.74	-0.5
	30 × 30	5	1.780	-	-	1.78	0.0
		10	1.406	-	-	1.41	0.3
20		0.851	-	-	0.84	-1.3	
5 × 30	5	1.606	-	-	1.58	-1.6	
	10	1.200	-	-	1.19	-0.9	
	20	0.662	-	-	0.65	-1.8	
30 × 5	5	1.581	-	-	1.60	1.2	
	10	1.182	-	-	1.20	1.5	
	20	0.655	-	-	0.66	0.8	

Table B.6: Results of point dose verification for 10 MV FF.

SSD [cm]	Field size [cm × cm]	Depth [cm]	D _{meas} [Gy]	30 cm × 30 cm × 30 cm DWP		50 cm × 50 cm × 50 cm DWP	
				D _{calc} [Gy]	Diff [%]	D _{calc} [Gy]	Diff [%]
90	3 × 3	5	1.079	1.14	5.7	1.14	5.7
		10	0.827	0.86	3.9	0.87	5.1
		20	0.487	0.50	2.6	0.50	2.6
	5 × 5	5	1.193	1.19	-0.3	1.19	-0.3
		7	1.077	1.08	0.3	1.08	0.3
		10	0.920	0.92	0.0	0.92	0.0
		15	0.704	0.71	0.9	0.71	0.9
		20	0.542	0.54	-0.3	0.54	-0.3
	10 × 10	5	1.268	1.26	-0.7	1.27	0.2
		7	1.157	1.15	-0.6	1.16	0.3
		10	1.001	1.00	-0.1	1.00	-0.1
		15	0.783	0.78	-0.4	0.78	-0.4
		20	0.611	0.61	-0.2	0.61	-0.2
	15 × 15	5	1.309	1.31	0.1	1.31	0.1
		10	1.048	1.05	0.1	1.05	0.1
		20	0.656	0.65	-1.0	0.65	-1.0
	30 × 30	5	1.363	-	-	1.36	-0.2
		7	1.259	-	-	1.26	0.1
		10	1.113	-	-	1.12	0.6
		15	0.901	-	-	0.90	-0.1
		20	0.725	-	-	0.72	-0.6
	5 × 30	5	1.252	-	-	1.24	-0.9
		10	0.979	-	-	0.97	-1.0
		20	0.595	-	-	0.59	-0.8
	30 × 5	5	1.234	-	-	1.25	1.3
		10	0.969	-	-	0.98	1.2
		20	0.589	-	-	0.59	0.2
	3 × 3	5	0.901	0.94	4.3	0.94	4.3
		10	0.697	0.72	3.4	0.72	3.4
		20	0.416	0.42	1.0	0.42	1.0
5 × 5	5	0.977	0.98	0.3	0.98	0.3	
	7	0.886	0.89	0.5	0.89	0.5	
	10	0.762	0.77	1.0	0.77	1.0	
	15	0.592	0.59	-0.3	0.59	-0.3	
	20	0.459	0.46	0.3	0.46	0.3	

SSD [cm]	Field size [cm × cm]	Depth [cm]	D _{meas} [Gy]	30 cm × 30 cm × 30 cm DWP		50 cm × 50 cm × 50 cm DWP	
				D _{calc} [Gy]	Diff [%]	D _{calc} [Gy]	Diff [%]
85	10 × 10	5	1.034	1.04	0.5	1.04	0.5
		7	0.949	0.96	1.1	0.96	1.1
		10	0.830	0.83	0.0	0.83	0.0
		15	0.656	0.66	0.6	0.66	0.6
		20	0.517	0.52	0.5	0.52	0.5
	15 × 15	5	1.069	1.07	0.1	1.08	1.0
		10	0.868	0.87	0.3	0.87	0.3
		20	0.556	0.55	-1.1	0.56	0.7
	30 × 30	5	1.114	-	-	1.12	0.5
		7	1.034	-	-	1.04	0.5
		10	0.919	-	-	0.93	1.2
		15	0.751	-	-	0.76	1.1
		20	0.612	-	-	0.61	-0.3
	5 × 30	5	1.024	-	-	1.02	-0.4
		10	0.813	-	-	0.81	-0.4
		20	0.503	-	-	0.50	-0.6
	30 × 5	5	1.011	-	-	1.03	1.9
		10	0.803	-	-	0.82	2.1
		20	0.498	-	-	0.50	0.4
	3 × 3	5	1.178	1.26	7.0	1.26	7.0
10		0.901	0.95	5.4	0.95	5.4	
20		0.527	0.54	2.4	0.54	2.4	
5 × 5	5	1.323	1.33	0.5	1.33	0.5	
	7	1.190	1.19	0.0	1.20	0.8	
	10	1.012	1.02	0.8	1.02	0.8	
	15	0.772	0.77	-0.2	0.77	-0.2	
	20	0.590	0.59	-0.1	0.59	-0.1	
10 × 10	5	1.408	1.41	0.2	1.41	0.2	
	7	1.281	1.28	-0.1	1.28	-0.1	
	10	1.105	1.10	-0.4	1.11	0.5	
	15	0.858	0.86	0.3	0.86	0.3	
	20	0.666	0.66	-0.9	0.66	-0.9	
15 × 15	5	1.457	1.45	-0.5	1.46	0.2	
	10	1.158	1.16	0.1	1.16	0.1	
	20	0.715	0.71	-0.7	0.71	-0.7	
30 × 30	5	1.517	-	-	1.51	-0.5	

SSD [cm]	Field size [cm × cm]	Depth [cm]	D_{meas} [Gy]	30 cm × 30 cm × 30 cm DWP		50 cm × 50 cm × 50 cm DWP		
				D_{calc} [Gy]	Diff [%]	D_{calc} [Gy]	Diff [%]	
80		7	1.398	-	-	1.40	0.1	
		10	1.230	-	-	1.23	0.0	
		15	0.989	-	-	0.99	0.1	
		20	0.792	-	-	0.79	-0.2	
		5 × 30	5	1.393	-	-	1.38	-0.9
			10	1.084	-	-	1.07	-1.3
			20	0.649	-	-	0.64	-1.4
		30 × 5	5	1.370	-	-	1.39	1.5
			10	1.068	-	-	1.08	1.1
	20		0.641	-	-	0.65	1.4	
	3 × 3	5	1.305	1.41	8.0	1.41	8.0	
		10	0.996	1.06	6.5	1.06	6.5	
		20	0.579	0.59	1.8	0.59	1.8	
	5 × 5	5	1.492	1.48	-0.8	1.48	-0.8	
		10	1.134	1.13	-0.4	1.13	-0.4	
		20	0.653	0.65	-0.5	0.65	-0.5	
	10 × 10	5	1.593	1.57	-1.5	1.57	-1.5	
		10	1.239	1.23	-0.7	1.23	-0.7	
		20	0.736	0.72	-2.1	0.73	-0.8	
	15 × 15	5	1.647	1.62	-1.6	1.63	-1.0	
		10	1.299	1.29	-0.7	1.29	-0.7	
		20	0.791	0.78	-1.5	0.78	-1.5	
	30 × 30	5	1.717	-	-	1.69	-1.6	
		10	1.381	-	-	1.37	-0.8	
		20	0.878	-	-	0.87	-0.9	
	5 × 30	5	1.574	-	-	1.54	-2.2	
		10	1.216	-	-	1.19	-2.2	
		20	0.717	-	-	0.70	-2.4	
30 × 5	5	1.545	-	-	1.55	0.3		
	10	1.196	-	-	1.20	0.4		
	20	0.708	-	-	0.71	0.3		

Table B.7: Results of point dose verification for 6 MV FFF.

SSD [cm]	Field size [cm × cm]	Depth [cm]	D _{meas} [Gy]	30 cm × 30 cm × 30 cm DWP		50 cm × 50 cm × 50 cm DWP	
				D _{calc} [Gy]	Diff [%]	D _{calc} [Gy]	Diff [%]
90	5 × 5	5	1.249	1.25	0.1	1.26	0.9
		7	1.108	1.10	-0.8	1.1	0.1
		10	0.924	0.92	-0.5	0.92	-0.5
		15	0.681	0.68	-0.2	0.68	-0.2
		20	0.505	0.50	-1.0	0.50	-1.0
	10 × 10	5	1.312	1.32	0.6	1.32	0.6
		7	1.180	1.18	0.0	1.18	0.0
		10	1.000	1.00	0.0	1.00	0.0
		15	0.753	0.75	-0.4	0.75	-0.4
		20	0.567	0.56	-1.3	0.56	-1.3
	15 × 15	5	1.343	1.35	0.5	1.35	0.5
		10	1.040	1.04	0.0	1.04	0.0
		20	0.606	0.60	-0.9	0.60	-0.9
	30 × 30	5	1.383	-	-	1.39	0.5
		7	1.260	-	-	1.27	0.8
		10	1.089	-	-	1.09	0.1
		15	0.846	-	-	0.84	-0.8
		20	0.656	-	-	0.65	-0.9
	5 × 30	5	1.295	-	-	1.29	-0.4
		10	0.976	-	-	0.97	-0.6
20		0.548	-	-	0.54	-1.5	
30 × 5	5	1.286	-	-	1.30	1.1	
	10	0.970	-	-	0.98	1.0	
	20	0.546	-	-	0.55	0.7	
100	5 × 5	5	1.028	1.03	0.2	1.03	0.2
		7	0.918	0.92	0.2	0.92	0.2
		10	0.771	0.77	-0.1	0.77	-0.1
		15	0.574	0.58	1.1	0.58	1.1
		20	0.429	0.43	0.2	0.43	0.2
	10 × 10	5	1.078	1.08	0.2	1.09	1.1
		7	0.975	0.98	0.5	0.98	0.5
		10	0.832	0.83	-0.3	0.83	-0.3
		15	0.635	0.63	-0.8	0.63	-0.8
		20	0.483	0.48	-0.6	0.48	-0.6
15 × 15	5	1.103	1.11	0.6	1.11	0.6	

SSD [cm]	Field size [cm × cm]	Depth [cm]	D _{meas} [Gy]	30 cm × 30 cm × 30 cm DWP		50 cm × 50 cm × 50 cm DWP	
				D _{calc} [Gy]	Diff [%]	D _{calc} [Gy]	Diff [%]
85		10	0.865	0.87	0.5	0.87	0.5
		20	0.515	0.51	-1.0	0.51	-1.0
	30 × 30	5	1.135	-	-	1.15	1.3
		7	1.039	-	-	1.05	1.0
		10	0.905	-	-	0.91	0.6
		15	0.711	-	-	0.71	-0.2
		20	0.556	-	-	0.55	-1.1
		20	0.556	-	-	0.55	-1.1
	5 × 30	5	1.065	-	-	1.07	0.5
		10	0.813	-	-	0.81	-0.4
		20	0.467	-	-	0.46	-1.4
	30 × 5	5	1.058	-	-	1.07	1.1
		10	0.808	-	-	0.82	1.5
		20	0.464	-	-	0.47	1.3
	5 × 5	5	1.388	1.39	0.2	1.39	0.2
		7	1.228	1.23	0.2	1.23	0.2
		10	1.018	1.02	0.2	1.02	0.2
		15	0.746	0.75	0.6	0.75	0.6
		20	0.550	0.55	-0.1	0.55	-0.1
	10 × 10	5	1.456	1.46	0.3	1.46	0.3
7		1.306	1.31	0.3	1.31	0.3	
10		1.101	1.10	-0.1	1.10	-0.1	
15		0.824	0.82	-0.4	0.82	-0.4	
20		0.617	0.61	-1.1	0.61	-1.1	
15 × 15	5	1.491	1.50	0.6	1.50	0.6	
	10	1.145	1.15	0.4	1.15	0.4	
	20	0.658	0.65	-1.2	0.65	-1.2	
30 × 30	5	1.536	-	-	1.55	0.9	
	7	1.394	-	-	1.40	0.4	
	10	1.200	-	-	1.20	0.0	
	15	0.927	-	-	0.92	-0.8	
	20	0.714	-	-	0.71	-0.6	
5 × 30	5	1.437	-	-	1.44	0.2	
	10	1.075	-	-	1.07	-0.5	
	20	0.597	-	-	0.59	-1.3	
30 × 5	5	1.426	-	-	1.44	1.0	
	10	1.068	-	-	1.08	1.1	

SSD [cm]	Field size [cm × cm]	Depth [cm]	D_{meas} [Gy]	30 cm × 30 cm × 30 cm DWP		50 cm × 50 cm × 50 cm DWP	
				D_{calc} [Gy]	Diff [%]	D_{calc} [Gy]	Diff [%]
80		20	0.594	-	-	0.60	1.1
	5×5	5	1.551	1.56	0.6	1.56	0.6
		10	1.129	1.13	0.1	1.13	0.1
		20	0.603	0.60	-0.6	0.60	-0.6
	10×10	5	1.630	1.63	0.0	1.63	0.0
		10	1.221	1.22	-0.1	1.22	-0.1
		20	0.675	0.67	-0.7	0.67	-0.7
	15×15	5	1.670	1.68	0.6	1.68	0.6
		10	1.264	1.27	0.5	1.27	0.5
		20	0.721	0.71	-1.5	0.71	-1.5
	30×30	5	1.720	-	-	1.73	0.6
		10	1.335	-	-	1.33	-0.4
		20	0.784	-	-	0.78	-0.5
	5×30	5	1.610	-	-	1.61	0.0
		10	1.194	-	-	1.19	-0.3
		20	0.655	-	-	0.65	-0.7
	30×5	5	1.596	-	-	1.61	0.9
		10	1.185	-	-	1.19	0.4
		20	0.652	-	-	0.65	-0.2

Table B.8: Results of point dose verification for 10 MV FFF.

SSD [cm]	Field size [cm × cm]	Depth [cm]	D _{meas} [Gy]	30 cm × 30 cm × 30 cm DWP		50 cm × 50 cm × 50 cm DWP	
				D _{calc} [Gy]	Diff [%]	D _{calc} [Gy]	Diff [%]
90	5 × 5	5	1.229	1.24	0.9	1.24	0.9
		7	1.105	1.11	0.4	1.11	0.4
		10	0.941	0.95	0.9	0.95	0.9
		15	0.719	0.72	0.2	0.72	0.2
		20	0.552	0.55	-0.4	0.55	-0.4
	10 × 10	5	1.276	1.28	0.3	1.28	0.3
		7	1.151	1.16	0.7	1.16	0.7
		10	0.997	1.00	0.3	1.00	0.3
		15	0.775	0.78	0.7	0.78	0.7
		20	0.602	0.60	-0.3	0.60	-0.3
	15 × 15	5	1.297	1.31	1.0	1.31	1.0
		10	1.026	1.03	0.4	1.03	0.4
		20	0.630	0.63	-0.1	0.63	-0.1
	30 × 30	5	1.350	-	-	1.33	-1.5
		7	1.211	-	-	1.22	0.7
		10	1.057	-	-	1.06	0.3
		15	0.838	-	-	0.84	0.2
		20	0.663	-	-	0.66	-0.5
	5 × 30	5	1.263	-	-	1.27	0.6
		10	0.979	-	-	0.98	0.1
20		0.586	-	-	0.59	0.7	
30 × 5	5	1.255	-	-	1.27	1.2	
	10	0.974	-	-	0.98	0.6	
	20	0.584	-	-	0.59	1.1	
100	5 × 5	5	1.013	1.02	0.7	1.02	0.7
		7	0.916	0.92	0.4	0.92	0.4
		10	0.784	0.79	0.7	0.79	0.7
		15	0.605	0.61	0.9	0.61	0.9
		20	0.468	0.47	0.3	0.47	0.3
	10 × 10	5	1.050	1.06	0.9	1.06	0.9
		7	0.957	0.96	0.3	0.96	0.3
		10	0.832	0.84	1.0	0.84	1.0
		15	0.653	0.65	-0.5	0.65	-0.5
		20	0.512	0.51	-0.5	0.51	-0.5
15 × 15	5	1.067	1.08	1.2	1.08	1.2	

SSD [cm]	Field size [cm × cm]	Depth [cm]	D _{meas} [Gy]	30 cm × 30 cm × 30 cm DWP		50 cm × 50 cm × 50 cm DWP	
				D _{calc} [Gy]	Diff [%]	D _{calc} [Gy]	Diff [%]
85		10	0.854	0.86	0.7	0.86	0.7
		20	0.535	0.53	-1.0	0.54	0.9
	30 × 30	5	1.088	-	-	1.10	1.1
		7	1.001	-	-	1.01	0.9
		10	0.880	-	-	0.88	0.0
		15	0.705	-	-	0.71	0.7
		20	0.563	-	-	0.56	-0.5
		20	0.563	-	-	0.56	-0.5
	5 × 30	5	1.039	-	-	1.05	1.0
		10	0.816	-	-	0.82	0.5
		20	0.498	-	-	0.50	0.5
	30 × 5	5	1.034	-	-	1.05	1.5
		10	0.812	-	-	0.82	1.0
		20	0.495	-	-	0.50	1.0
	5 × 5	5	1.362	1.38	1.3	1.38	1.3
		7	1.221	1.23	0.7	1.23	0.7
		10	1.035	1.04	0.4	1.04	0.4
		15	0.787	0.79	0.4	0.79	0.4
		20	0.601	0.60	-0.2	0.60	-0.2
	10 × 10	5	1.417	1.43	0.9	1.43	0.9
7		1.282	1.29	0.6	1.29	0.6	
10		1.099	1.10	0.0	1.10	0.0	
15		0.849	0.85	0.1	0.85	0.1	
20		0.656	0.65	-1.0	0.65	-1.0	
15 × 15	5	1.441	1.45	0.6	1.45	0.6	
	10	1.131	1.14	0.8	1.14	0.8	
	20	0.686	0.69	0.6	0.69	0.6	
30 × 30	5	1.469	-	-	1.48	0.7	
	7	1.342	-	-	1.35	0.6	
	10	1.166	-	-	1.17	0.3	
	15	0.919	-	-	0.92	0.1	
	20	0.724	-	-	0.72	-0.6	
5 × 30	5	1.402	-	-	1.41	0.6	
	10	1.080	-	-	1.08	0.0	
	20	0.639	-	-	0.64	0.2	
30 × 5	5	1.392	-	-	1.41	1.3	
	10	1.073	-	-	1.09	1.6	

SSD [cm]	Field size [cm × cm]	Depth [cm]	D_{meas} [Gy]	30 cm × 30 cm × 30 cm DWP		50 cm × 50 cm × 50 cm DWP		
				D_{calc} [Gy]	Diff [%]	D_{calc} [Gy]	Diff [%]	
80	5×5	20	0.636	-	-	0.64	0.6	
		5	1.529	1.54	0.7	1.54	0.7	
		10	1.153	1.16	0.6	1.16	0.6	
	10×10	20	0.663	0.66	-0.4	0.66	-0.4	
		5	1.595	1.59	-0.3	1.59	-0.3	
		10	1.229	1.22	-0.7	1.22	-0.7	
	15×15	20	0.723	0.72	-0.4	0.72	-0.4	
		5	1.622	1.62	-0.1	1.62	-0.1	
		10	1.264	1.26	-0.3	1.26	-0.3	
	30×30	20	0.757	0.75	-0.9	0.75	-0.9	
		5	1.655	-	-	1.66	0.3	
		10	1.303	-	-	1.30	-0.2	
	5×30	20	0.799	-	-	0.79	-1.2	
		5	1.577	-	-	1.58	0.2	
		10	1.205	-	-	1.20	-0.4	
	30×5	20	0.705	-	-	0.70	-0.7	
		5	1.563	-	-	1.58	1.1	
		10	1.195	-	-	1.20	0.4	
			20	1.228	-	-	0.70	-0.1

B.3 Output Factor Verification

The tables of this subsection (B.9, B.10, B.11 and B.12) provide a comparison between output factors obtained from measurements (OF_{meas}) and those obtained from dose calculations using the new beam models. The acronym “OF” understandably stands for “output factor”; all other abbreviations used have the same meaning they had throughout the previous two subsections.

Table B.9: Results of output factor verification for 6 MV FF.

Field size [cm × cm]	OF _{meas}	30 cm × 30 cm × 30 cm DWP			50 cm × 50 cm × 50 cm DWP		
		D _{calc} [Gy]	OF	Diff [%]	D _{calc} [Gy]	OF	Diff [%]
1 × 1	0.665	0.67	0.670	0.7	0.66	0.660	-0.8
2 × 2	0.801	0.80	0.800	-0.1	0.80	0.800	-0.1
3 × 3	0.845	0.84	0.840	-0.6	0.84	0.840	-0.6
4 × 4	0.879	0.88	0.880	0.1	-	-	-
5 × 5	0.905	0.9	0.900	-0.6	0.90	0.900	-0.6
6 × 6	0.930	0.93	0.930	0.0	-	-	-
7 × 7	0.951	0.95	0.950	-0.1	0.95	0.950	-0.1
8 × 8	0.970	0.97	0.970	0.0	-	-	-
10 × 10	1.000	1.00	1.000	0.0	1.00	1.000	0.0
14 × 14	1.048	1.05	1.050	0.2	1.05	1.050	0.2
15 × 15	1.058	1.06	1.060	0.1	1.06	1.060	0.1
20 × 20	1.097	-	-	-	1.10	1.100	0.3
30 × 30	1.144	-	-	-	1.15	1.150	0.5
5 × 30	0.977	-	-	-	0.97	0.970	-0.7
30 × 5	0.969	-	-	-	0.98	0.980	1.1

Table B.10: Results of output factor verification for 10 MV FF.

Field size [cm × cm]	OF _{meas}	30 cm × 30 cm × 30 cm DWP			50 cm × 50 cm × 50 cm DWP		
		D _{calc} [Gy]	OF	Diff [%]	D _{calc} [Gy]	OF	Diff [%]
1 × 1	0.644	0.64	0.640	-0.6	0.64	0.640	-0.6
2 × 2	0.807	0.81	0.810	0.3	0.81	0.810	0.3
3 × 3	0.862	0.86	0.860	-0.2	0.87	0.870	1.0
4 × 4	0.896	0.90	0.900	0.4	0.90	0.900	0.4
5 × 5	0.920	0.92	0.920	0.0	0.92	0.920	0.0
6 × 6	0.938	0.94	0.940	0.2	0.94	0.940	0.2
7 × 7	0.956	0.96	0.960	0.4	0.96	0.960	0.4
8 × 8	0.971	0.97	0.970	-0.1	0.97	0.970	-0.1
10 × 10	1.000	1.00	1.000	0.0	1.00	1.000	0.0
14 × 14	1.038	1.04	1.040	0.2	1.04	1.040	0.2
15 × 15	1.047	1.05	1.050	0.3	1.05	1.050	0.3
20 × 20	1.076	-	-	-	1.08	1.080	0.4
30 × 30	1.111	-	-	-	1.12	1.120	0.8
5 × 30	0.979	-	-	-	0.97	0.970	-0.9
30 × 5	0.970	-	-	-	0.98	0.980	1.1

Table B.11: Results of output factor verification for 6 MV FFF.

Field size [cm × cm]	OF _{meas}	30 cm × 30 cm × 30 cm DWP			50 cm × 50 cm × 50 cm DWP		
		D _{calc} [Gy]	OF	Diff [%]	D _{calc} [Gy]	OF	Diff [%]
1 × 1	0.694	0.70	0.700	0.9	-	-	-
2 × 2	0.828	0.83	0.830	0.2	0.83	0.830	0.2
3 × 3	0.872	0.87	0.870	-0.2	0.87	0.870	-0.2
4 × 4	0.903	0.90	0.900	-0.3	-	-	-
5 × 5	0.926	0.92	0.920	-0.6	0.92	0.920	-0.6
6 × 6	0.946	0.94	0.940	-0.6	-	-	-
7 × 7	0.962	0.96	0.960	-0.2	-	-	-
8 × 8	0.977	0.98	0.980	0.3	-	-	-
10 × 10	1.000	1.00	1.000	0.0	1.00	1.000	0.0
14 × 14	1.035	1.03	1.030	-0.5	1.04	1.040	0.5
15 × 15	1.041	1.04	1.040	-0.1	1.04	1.040	-0.1
20 × 20	1.065	-	-	-	1.06	1.060	-0.5
30 × 30	1.090	-	-	-	1.09	1.090	0.0
5 × 30	0.977	-	-	-	0.97	0.970	-0.7
30 × 5	0.972	-	-	-	0.98	0.980	0.8

Table B.12: Results of output factor verification for 10 MV FFF.

Field size [cm × cm]	D _{meas} [Gy]	30 cm × 30 cm × 30 cm DWP			50 cm × 50 cm × 50 cm DWP		
		D _{calc} [Gy]	OF	Diff [%]	D _{calc} [Gy]	OF	Diff [%]
1 × 1	0.688	0.69	0.690	0.3	-	-	-
2 × 2	0.840	0.84	0.840	0.0	0.84	0.840	0.0
3 × 3	0.892	0.90	0.900	0.9	0.90	0.900	0.9
4 × 4	0.926	0.93	0.930	0.4	-	-	-
5 × 5	0.945	0.95	0.950	0.5	0.95	0.950	0.5
6 × 6	0.960	0.96	0.960	0.0	-	-	-
7 × 7	0.973	0.98	0.980	0.7	0.98	0.980	0.7
8 × 8	0.984	0.99	0.990	0.6	0.99	0.990	0.6
10 × 10	1.000	1.00	1.000	0.0	1.00	1.000	0.0
14 × 14	1.024	1.03	1.030	0.6	1.03	1.030	0.6
15 × 15	1.029	1.03	1.030	0.1	1.03	1.030	0.1
20 × 20	1.044	-	-	-	1.05	1.050	0.6
30 × 30	1.059	-	-	-	1.06	1.060	0.1
5 × 30	0.982	-	-	-	0.98	0.980	-0.2
30 × 5	0.980	-	-	-	0.98	0.980	0.0

C Complete Results of Treatment-Delivery Verification

This section contains the results of the Delta⁴ measurements performed at the AKH in Vienna. To assess how well the planned and measured dose agree with one another, both the median dose deviation (Med. Dose Dev. in %) and the local GPR (also in %) are given for every irradiated plan. The plans are grouped together according to indication and beam quality+mode (e.g. LR 6 MV FF), thus resulting in Tables C.1, C.2, C.3, C.4 and C.5. Since all HR plans are made up of two arcs (beams), the median dose deviation and the local GPR are listed both per plan (total) and per beam (b1 - beam1, b2 - beam2).

Table C.1: Results of treatment-delivery verification for LR 10 MV FF.

Patient #	Plan	Med. Dose Dev. [%]	local GPR [%]
1	FB	0.0	99.8
	mVMAT	0.0	98.8
2	FB	-1.6	95.8
	mVMAT	-2.3	88.4
3	FB	-1.5	94.6
	mVMAT	-1.4	96.7
4	FB	-1.7	95.7
	mVMAT	-2.0	95.2
5	FB	-1.6	95.6
	mVMAT	-2.1	94.9
6	FB	-2.6	96.2
	mVMAT	-1.7	94.1
7	FB	-1.6	95.1
	mVMAT	-1.9	95.4
8	FB	-1.6	95.6
	mVMAT	-1.4	95.3
9	FB	-1.3	95.5
	mVMAT	-2.0	93.0
10	FB	-1.4	95.1
	mVMAT	-2.2	91.8

Table C.2: Results of treatment-delivery verification for LR 6 MV FF.

Patient #	Plan	Med. Dose Dev. [%]	local GPR [%]
1	mVMAT	-1.9	94.3
2	mVMAT	-1.9	93.5
3	mVMAT	-2.0	95.2
4	mVMAT	-2.4	93.9
5	FB	-1.8	95.3
	mVMAT	-2.0	96.4
6	mVMAT	-2.1	96.8
7	FB	-1.9	94.4
	mVMAT	-1.8	95.5
8	mVMAT	-2.3	95.9
9	mVMAT	-2.1	91.2
10	FB	-1.8	94.6
	mVMAT	-2.2	91.4

Table C.3: Results of treatment-delivery verification for LR 6 MV FFF.

Patient #	Plan	Med. Dose Dev. [%]	local GPR [%]
1	mVMAT	-0.2	98.9
2	mVMAT	-1.4	99.2
3	mVMAT	-0.9	99.4
4	mVMAT	-1.0	97.2
5	mVMAT	-1.3	98.3
6	mVMAT	-0.8	99.6
7	mVMAT	-0.9	99.6
8	mVMAT	-1.2	95.3
9	mVMAT	-0.9	96.7
10	mVMAT	-0.9	98.2

Table C.4: Results of treatment-delivery verification for LR 10 MV FFF.

Patient #	Plan	Med. Dose Dev. [%]	local GPR [%]
1	mVMAT	-0.3	97.7
2	mVMAT	-1.0	93.1
3	mVMAT	-0.6	97.2
4	mVMAT	-0.8	96.7
5	mVMAT	-1.0	97.5
6	mVMAT	-0.8	96.8
7	mVMAT	-0.8	98.0
8	mVMAT	-1.2	93.4
9	mVMAT	-0.7	98.6
10	mVMAT	-1.3	95.7

Table C.5: Results of treatment-delivery verification for HR 6 MV FF.

Patient #	Plan	Med. Dose Dev. [%]	local GPR [%]
6	FB	b1: -0.9	b1: 98.6
		b2: -1.2	b2: 98.7
	mVMAT	b1: -1.3	b1: 97.0
		b2: -2.1	b2: 95.3
12	FB	b1: -1.0	b1: 98.4
		b2: -1.4	b2: 97.9
	mVMAT	b1: -1.3	b1: 97.2
		b2: -1.5	b2: 94.3

D Complete Results of Beam Model Comparison

The beam model comparison was, as already mentioned, conducted in the same manner as the treatment delivery verification and therefore the results are listed following the same method used in the previous section. There is again a separation according to indication (leading to Tables D.1 and D.2) and the HR plans have entries per beam (b1, b2) and per plan (total).

Table D.1: Results of beam model comparison for HR 6 MV FF.

Patient #	Plan	Med. Dose Dev. [%]				local GPR [%]			
		VersaHD		Clinac120		VersaHD		Clinac120	
6	FB	b1: -0.9	total: -1.1	b1: 1.6	total: 1.5	b1: 98.6	total: 98.6	b1: 96.7	total: 98.3
		b2: -1.2		b2: 1.3		b2: 98.7		b2: 98.6	
	mVMAT	b1: -1.3	total: -1.8	b1: 2.2	total: 2.5	b1: 97.0	total: 96.5	b1: 81.6	total: 78.3
		b2: -2.1		b2: 2.4		b2: 95.3		b2: 81.6	
12	FB	b1: -1.0	total: -1.2	b1: 1.4	total: 1.5	b1: 98.4	total: 98.2	b1: 96.0	total: 96.2
		b2: -1.4		b2: 1.4		b2: 97.9		b2: 93.9	
	mVMAT	b1: -1.3	total: -1.4	b1: 1.2	total: 1.2	b1: 97.2	total: 95.8	b1: 96.7	total: 98.4
		b2: -1.5		b2: 1.1		b2: 94.3		b2: 98.6	

Table D.2: Results of beam model comparison for LR 6 MV FF.

Patient #	Plan	Med. Dose Dev. [%]		local GPR [%]	
		VersaHD	Clinac120	VersaHD	Clinac120
5	FB	-1.8	1.5	95.3	99.5
	mVMAT	-2.0	1.8	96.4	99.4
7	FB	-1.9	1.5	94.4	99.8
	mVMAT	-1.8	1.4	95.5	98.5
10	FB	-1.8	1.3	94.6	100
	mVMAT	-2.2	1.7	91.4	97.7